DEVELOPING DISEASE-TARGETED PHOTOACOUSTIC IMAGING PROBES

HARNESSING THE SOUND OF LIGHT:
DESIGN, SYNTHESIS & EVALUATION OF PHOTOACOUSTIC IMAGING PROBES FOR THE STUDY OF BONE DISEASE AND BACTERIAL INFECTION

By

ROWAN ELIZABETH SWANN, B.Sc.

A Thesis

Submitted to the School of Graduate Studies

In Partial Fulfillment of the Requirements

For the Degree

Doctor of Philosophy

McMaster University

Doctor of Philosophy (2024); McMaster University, Hamilton, ON.

Department of Chemistry & Chemical Biology

Title: Harnessing the Sound of Light: Design, Synthesis & Evaluation of Photoacoustic Imaging Probes for the Study of Bone Disease and Bacterial Infection

Author: Rowan Elizabeth Swann

Co-Supervised by: Professor Saman Sadeghi & Professor John. F. Valliant

Number of Pages: xvi; 193

Lay Abstract

The work conducted within this thesis aims to outline the process of developing photoacoustic diagnostic agents for the detection of various diseases, including bone disease and bacterial infection. To this end, various small molecule, near-infrared absorbing dyes, disease-targeting molecules, and assembly methods were selected to generate several diagnostic agents. To demonstrate their utility, the diagnostic agents were each evaluated in a series of studies designed to assess their ability to generate detectable photoacoustic signal, interact specifically with disease-markers, and localize the sites of disease in living systems. Significant attention was placed on comprehensively evaluating the diagnostic agents through the development of methodology and generating a standard procedure for photoacoustic data production and reporting, which was practiced throughout the work.

Abstract

To address the paucity of available molecularly targeted photoacoustic imaging probes (PIPs) and to generate meaningful data to support the ongoing effort to refine diagnostic photoacoustic imaging (PAI) applications, the work presented here focuses on the design, synthesis, and evaluation of novel PIPs. To this end, various light-absorbing small molecule dyes, targeting strategies, and disease-targeting molecules were evaluated.

First, a near-infrared photoacoustic probe was used to image bone *in vivo* through active and bioorthogonal pre-targeting strategies by utilizing a coupling between a tetrazine-derived cyanine dye and a *trans*-cyclooctene-modified bisphosphonate. *In vitro* hydroxyapatite binding and *in vivo* bone imaging studies showed significant localization of the agent to the target using both active and pre-targeting strategies.

The tetrazine-dye building block was then used to create a first-generation bacteria-targeting PIP, using a *trans*-cyclooctene-modified Zinc (II)-dipicolylamine (ZnDPA). The PIP demonstrated poor aqueous solubility and overlapping photoacoustic (PA) signal with deoxyhemoglobin. Therefore, a commercially available ZnDPA-derived fluorophore, PSVue794, was then repurposed for use as a PIP. PSVue794 demonstrated the ability to differentiate between bacterial infection, sterile inflammation, and healthy tissue in a mouse model, via PA imaging, which prompted its use in a series of proof-of-concept studies towards the generation of a model of implant infection. The feasibility of detecting the PIP in the presence of a PA signal-emitting metallic implant, which was deemed a significant hurdle due to the intensity of the PA signal of the metal, was verified. Although the work requires some follow-up evaluations to demonstrate the practical use of the model, ZnDPA-based PIPs have remained promising candidates for PAI of bacterial infection.

Finally, a novel general-purpose dye was designed to possess properties ideal for *in vivo* PAI. To evaluate the modifications made, the general-purpose dye was conjugated with ZnDPA, and was tested alongside the non-targeted counterpart and PSVue794. Through the studies conducted, it was evident that the rationale that contributed to the design of the general-purpose dye did lead to highly soluble PIP with promising PA properties, however, the PIP did not demonstrate target-specificity, *in vivo*. Therefore, investigations using the non-targeted PIP with higher affinity targeting vectors for PA-compatible diseases, such as surgical-site/implant infections and prostate cancer, is warranted.

Acknowledgements

To start, I would like to share my appreciation for my supervisors, Dr. Sam Sadeghi and Dr. John Valliant. Thank you for always pushing me to do my best and teaching me how to be a good scientist! It has been an amazing opportunity to be guided by such innovative, intelligent, and influential people, but it has been your kindness, understanding, and patience that have solidified my perceptions of you both. I will always strive to carry myself similarly. Thank you to my committee members, Dr. Alfredo Capretta and Dr. Todd Hoare, for the constant encouragement and support over the years!

Next, I would like to thank past and current VRG and MRG members. I find it downright incredible how any job, no matter how draining, can feel fun in the presence of positive and friendly people. Thank you to each of you who put a smile on my face (perhaps not the most difficult of tasks, but still), who made me laugh (also not a difficult task, but you still deserve some credit), provided me with pep-talks, and endured all the lunch chats that may have gone on a little too long, but hey, I still got everything done and I believe you will too! These small interactions add up to something quite remarkable and I will never forget that! Thank you to Afaf, Mohammed, Rafael, for all the support over the years, this work would not have been possible without you. Thank you 'Mesdooms' for instigating and entertaining my bubble tea addiction and for rounding out this adventure to be something I can look back on with great fondness.

To all my friends and family, thank you for always being there for me and constantly filling my cup! I always know where to go when I need a good laugh, cry, or cry-laugh. Vern, we sure are opposites, but I think that just means we fill each other in . Thank you for all the long life chats and piping hot work tea to distract me when I needed it most! To the Coccaros, grazie per avermi accettato come uno dei vostri, mi sento assolutamente fortunato a chiamarti la mia famiglia! To

FrankyRachyAria, thank you for taking us kids in, for putting up with all our shenanigans, and for all the amazing memories! I think I might just owe all my motivation for finishing this thing to Aria for constantly asking when I'll be done and if it's time to play yet!

To Giovanni, no amount of thanks could ever requite the support you have given me over the last 11 years. We were just wee babies when we started our journey together, the entirety of which, I have been a stressed out student mess. Your patience, willingness to learn, and the level of care that you put into everything you do inspires me every single day. I just can't wait to see how life unfolds from here! I love you.

Dedication

I would like to dedicate this thesis to my wonderful parents, Heather, Clive, Rose, and Terry. I am truly the luckiest cygnet in the world to have been raised by the most hilarious, unconventional, loving, and supportive people! I owe every ounce of creativity, problem solving, resilience, and playfulness that I possess, to the four of you. Thank you from the bottom of my heart.

Table of Contents

List of Figures

List of Tables

List of Schemes

List of Abbreviations

Numerical

^{13}C NMR	Carbon-13 Nuclear Magnetic Resonance
^{1}H NMR	Proton Nuclear Magnetic Resonance
10E-S	10 % Ethanol in Saline
3D	Three-Dimensional

A

Abs	Absorbance
ACN	Acetonitrile
ANOVA	Analysis of Variance
Aq	Aqueous

B

BI	Bioluminescence Imaging
BP	Bisphosphonate

C

CFU	Colony Forming Unit
cm	Centimeters
CPM	Counts per Minute
CT	Computed Tomography

D

DCM	Dichloromethane
DIPEA	N,N-Diisopropylethylamine
DMF	Dimethylformamide
DMSO	Dimethyl Sulfoxide
E	
ε	Molar Absorptivity
EDTA	Ethylenediaminetetraacetic Acid
Em	Emission
EPR	Enhanced Permeability & Retention
ESI	Electrospray Ionization
Ex	Excitation
F	
FA	Formic Acid
FDA	Food & Drug Administration
FDG	Fluorodeoxyglucose
FI	Fluorescence Imaging
G	
γ	Gamma Radiation
g	gram
GUL	Glutamate-Ureido-Lysine
H	
HA	Hydroxyapatite
HAI	Healthcare-Associated Infection
HBSS	Hanks Balanced Salt Solution
H&E	Hematoxylin & Eosin
HOMO	Highest Occupied Molecular Orbital
h P.I.	Hours Post-Injection
HPLC	High Performance Liquid Chromatography
HRMS	High-Resolution Mass Spectrometry
Hz	Hertz
I	
ICG	Indocyanine Green
ID/g	Injected Dose/Gram
IEDDA	Inverse Electron Demand Diels-Alder
IF	Intrafemoral
IgG	Immunoglobulin-G
IM	Intramuscular
IRTz	IR-783-Tetrazine
iTLC	Instant Thin Layer Chromatography
IV	Intravenous Injection

K

kBq	Kilo Becquerel
kDa	Kilo Dalton
keV	Kilo Electron Volts

L

LOD	Limit of Detection
LPS	Lipopolysaccharide
LRMS	Low-Resolution Mass Spectrometry
LUMO	Lowest Unoccupied Molecular Orbital

M

M	Molar
MBq	Mega Becquerel
MeOH	Methanol
mg	Milligram
MHz	Megahertz
µg	Microgram
mJ	Millijoule
µmol	Micromole
µM	Micromolar
MI	Molecular Imaging
mL	Millilitre
mm	Millimetre
mmol	Millimoles
MRI	Magnetic Resonance Imaging
MS	Mass Spectrometry

N

nm	nanometer
nsec	Nanosecond
NIR	Near-Infrared
NMR	Nuclear Magnetic Resonance

O

OD	Optical Density
O/N	Over Night

P

PA	Photoacoustic
PAI	Photoacoustic Imaging
PBS	Phosphate Buffered Saline
PEG	Poly(ethylene) Glycol
PET	Positron Emission Tomography
PIP	Photoacoustic Imaging Probe
PS	Phosphatidylserine
PSMA	Prostate-Specific Membrane Antigen

PyBOP	Benzotriazole-1-yl-oxytripyrrolidinophosphonium hexafluoreophosphate
Q	
φ_f	Fluorescent Quantum Yield
R	
RCP	Radiochemical Purity
RCY	Radiochemical Yield
Rf	Retention Factor
ROI	Region of Interest
Radio-TLC	Radio-Thin-Layer Chromatography
S	
S_0	Singlet Ground State
S_1	First Singlet Excited State
S_2	Second Singlet Excited State
S/B	Signal-to-Background
SEM	Standard Error of the Mean
SPECT	Single Photon Emission Computed Tomography
T	
TCO	*Trans*-Cyclooctene
TCO-NHS	*Trans*-Cyclooctene N-Hydroxy Succinimide
TcO_4^-	Pertechnetate Ion
TFA	Trifluoroacetic Acid
TLC	Thin Layer Chromatography
T/N	Target-to-Non-Target
Tz	Tetrazine
U	
UBI	Ubiquicidin
US	Ultrasound
UV	Ultraviolet
W	
λ	Wavelength
Z	
ZnDPA	Zinc (II)- Dipicolylamine

Declaration of Academic Achievement

All chemistry and radiochemistry, described in this thesis, were carried out by R. Swann, unless otherwise noted. All assays and biological studies were performed by R. Swann, with assistance from L. R. Silva, N. Janzen, and A. Faraday, biologists within the group. Histological analysis was provided by Dr. J. M. Kwiecien from McMaster University's Department of Pathology and Molecular Medicine.

Publications

Peer-Reviewed Journal Articles

Swann, R.; Hernández-Valdés, D.; Silva, L. R.; Marfatia, Y. M.; El-Zaria, M. E.; Genady, A. R.; Kwiecien, J. M.; Valliant, J. F.; & Sadeghi, S. Photoacoustic imaging of a cyanine dye targeting bacterial infection. *Sci. Rep.* **2024**, 14:18322.

Swann, R.; Slikboer, S.; Genady, A. R.; Silva-Mendez, R.; Janzen, N.; Faraday, A.; Valliant, J. F.; Sadeghi, S. A Tetrazine-Derived Near-Infrared Dye for Targeted Photoacoustic Imaging of Bone. *J. Med. Chem*. **2023**, 66, 6025-6036.

Genady, A.; Swann, R.; Slikboer, S. R.; Wyszatko, K.; Janzen, N.; Silva, L. R.; El-Zaria, M, E.; Sadeghi, S.; Valliant, J. F.; A Bioorthogonal Methylene Blue Derived Probe for Targeted Photoacoustic Imaging. *Eur. J. Med. Chem. Rep.* **2022**, 4 100021.

Genady, A.; Fong, D.; Slikboer, S.; El-Zaria, M.; Swann, R.; Janzen, N.; Faraday, A.; McNelles, S.; Rezvani, M.; Sadeghi, S.; Adronov, A.; Valliant, J. F.; ^{99m}Tc-Functionalized Single-Walled Carbon Nanotubes for Bone Targeting. *ACS Appl. Nano Mater*. **2020**, 3 (12), 11819-11824.

Slikboer, S.; Naperstkow, Z.; Janzen, N.; Faraday, A.; Soenjaya, Y.; Le Floc'h, J.; Al-Karmi, S.; Swann, R.; Wyszatko, K.; Demore, C. E. M.; Foster, S.; Tetrazine-Derived Near-Infrared Dye as a Facile Reagent for Developing Targeted Photoacoustic Imaging Agents. *Mol. Pharmaceutics.* **2020**, 17 (9), 3369-3377.

Published Meeting Abstracts

Swann, R.; Hernández-Valdés, D.; El-Zaria, M. E.; Silva, L. R.; Mahmood Marfatia, Y.; Genady, A. R.; Valliant, J.F.; Sadeghi, S. (**September 2022**) A Multimodal SPECT/Photoacoustic Imaging Agent for Bacterial Infection. *The Fourth International Symposium on Technetium and Other Radiometals in Chemistry and Medicine.* Abstract number: 62 (Poster/Communication Presentation).

Chapter 1 : Introduction

1.1 Molecular Imaging:

Molecular imaging (MI) techniques are increasingly becoming an important part of clinical research and medical practice, as they enable the non-invasive visualization of cellular biochemistry. MI has advanced our understanding of disease-specific pathology, elucidating more accurate diagnostic techniques, and contributing to earlier disease staging and the implementation of personalized therapeutics.[1] While modalities such as computed tomography (CT), magnetic resonance imaging (MRI), and ultrasonography (US) are commonly used to address anatomical and structural differences between healthy and diseased states, MI, using optical and nuclear techniques such as fluorescence imaging (FI), positron emission tomography (PET), and single photon emission computed tomography (SPECT), rely on the introduction of contrast agents to image functional processes in the body. With a constant demand for the ability to image specific diseases and cellular processes, the development of molecularly targeted contrast agents remains a prominent focus of research in pathology, diagnostic & therapeutic medicine.

1.1.1 Molecular Targeting

Developing MI strategies begins with identifying biological markers, or biomarkers, of the underlying condition. Biomarkers are objective and quantifiable biochemical or molecular characteristics that can indicate differences between normal and pathogenic biological processes or pharmacological responses to therapeutic intervention.[2,3] Significant research has been done to design high-affinity biomarker-targeting vectors.[4] While the list extends beyond what is mentioned here, substantial attention has been given to small molecules, peptides, and antibodies (**Table 1.1**).

Each class of targeting vector comes with a unique set of assets and challenges, which become important to consider when selecting an appropriate signalling agent and detection method.

Table 1.1. Summary and examples of the commonly used targeting vectors used in synthesizing molecularly targeted imaging agents.

Targeting Vector	**Small Molecules**	**Peptides**	**Antibodies**
Size*	< 1 nm or < 0.5 kDa	~ 1-4 nm or ~ 0.5-2 kDa	~ 15 nm or ~ 150 kDa
Advantages*	▪ Low toxicity ▪ Fast clearance ▪ High tissue penetration	▪ Facile & cheap synthesis ▪ Low toxicity ▪ Moderate specificity	▪ High affinity ▪ High specificity
Disadvantages*	▪ Intensive R&D ▪ Addition of signalling agent can alter targeting potential	▪ Suboptimal biostability	▪ Low tissues penetration ▪ Poor clearance profile ▪ Potential for immunogenicity
Preclinical Examples	Cy7-1-maltotriose (**FI/PAI**)[5] [^{125}I]IMPY (**SPECT**)[6] [^{68}Ga]Ga-DOTA-Olaparib (**PET**)[7]	YC-27 (**FI/PAI**)[6] [^{99m}Tc]Tc-HYNIC-H6F (**SPECT**)[8] [^{18}F]FPRGD4 (**PET**)[9] 9/23/24 4:55:00 PM	BHQ3-Fluorescein Trastuzumab (**FI/PAI**)[10] [^{111}In]In-4497 mAb (**SPECT**)[11] [^{89}Zr]Zr-Trastuzumab (**PET**)[12]
Clinical Examples	[^{18}F]F-FAPI-74 (**PET**)[13] [^{18}F]FDG (**PET**)[14] [^{99m}Tc]Tc-MDP (**SPECT**)[15] OTL38 (**FI**)[16]9/23/24 4:55:00 PM	[^{68}Ga]Ga-PSMA-11 (**PET**)[17] [^{99m}Tc]Tc-UBI-29-41 (**SPECT**)[18] QRH-882260 (**FI**) (ID**: NCT02574858)	[^{89}Zr]Zr-Daratumumab (**PET**) (ID**: NCT03665155) [^{111}In]In-FPI-1547 (**SPECT**) (ID**: NCT03746431) Cetuximab-IRDye800CW (**FI**)[19], **PAI** ID: NCT03923881)

* Information adapted from Weber, *et al* (**2016**).[20]
** ClinicalTrials.gov Identifier.

1.1.2 Signaling Agents & Detection Methods

To detect the biomarker of interest, a suitable signalling agent and imaging modality must be selected. Considerations should be made on instrument parameters, such as depth penetration, spatial resolution, cost of imaging and acquisition time, as well as biological variables such as biodistribution and toxicity. **Table 1.2** reviews some of the instrument parameters that comprise currently available MI modalities.

Table 1.2. Summary of MI instrument parameters.[1,21–29]

Imaging Modality	**Nuclear Imaging Techniques**		**Optical Imaging Techniques**	
	PET	SPECT	Fluorescence Imaging	Photoacoustic Imaging
Energy Detected	511 keV photons	gamma rays	Visible/NIR photons	High frequency sound waves
Spatial Resolution	1-2 mm	≤ 1 mm	2-10 mm	50 μm
Sensitivity	pM	nM	nM	μM
Imaging Depths	whole body	whole body	1-2 cm	≤ 7 cm

Detection methods for nuclear and optical imaging strategies are facilitated by the emission or alteration of electromagnetic energy from a signalling agent.[21] Nuclear imaging strategies like PET and SPECT, for example, leverage the instability of radionuclides and their forms of nuclear decay. For PET imaging, positron-emitting radioisotopes are used, and images are constructed by detecting coincident 511 keV photons that are generated from the annihilation of the emitted positron with an electron in the medium surrounding the radioisotope. For SPECT imaging, gamma ray-emitting radioisotopes are used and images are constructed through the detection of gamma rays by a rotating gamma camera.[4] Because SPECT gamma cameras are equipped with a

collimator, which only allows perpendicular gamma rays to be detected, which results in significantly lower levels of detection, decreased sensitivity and spatial resolution are notable disadvantages as compared with PET instruments.[4,22] Despite this, clinical SPECT remains more widely available and used than clinical PET, a statistic that is expected to change as PET isotope production expands. Similar to nuclear imaging, optical imaging techniques such as FI and photoacoustic imaging (PAI) also exploit the relaxation pathways of unstable energetic states, however, these excited states exist on an atomic and molecular level, rather than a nuclear level, and are generated through the absorption of visible & near-infrared (NIR) light.

1.2 Optical Imaging:

1.2.1 What is Light?

Electromagnetic radiation is a spectrum of energy, transmitted in the form of light or heat and is characterized by its wave-particle duality (**Figure 1.1**). For example, wavelength, amplitude, and frequency are properties that can all be used to contextualize its wave-like characteristics, while the quantized energy of electromagnetic radiation, described as a photon, is used to discern its particle-like nature. The Einstein-Planck equation (**Equation 1.1**) was derived to show the relationship between the energy of a photon and its wavelength and is integral in understanding how we can harness light to facilitate and monitor chemical and biological processes.

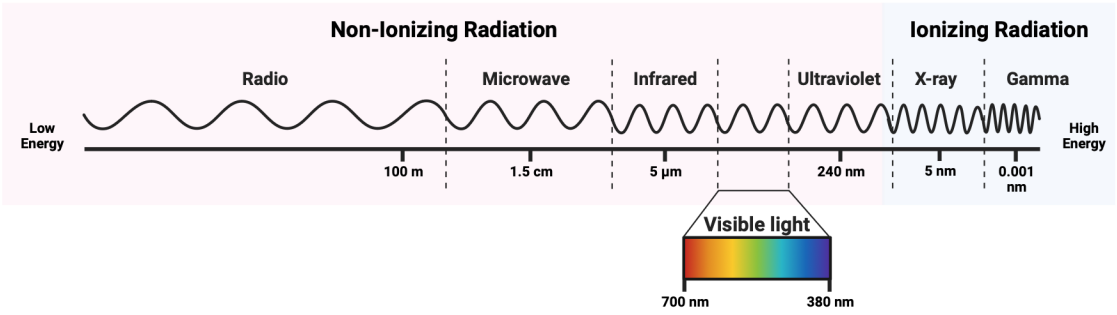

Figure 1.1. The electromagnetic spectrum. (Created with BioRender).

Equation 1.1 $E = hv \qquad \lambda = \frac{c}{v}$

The Einstein-Planck Equation: where E= energy, h= Planck's constant, v= frequency, λ= wavelength, and c= the speed of light.

1.2.2 Light Absorption

Light absorption takes place when photons of a particular energy collide with electrons on a molecule causing the electron to be promoted from the highest occupied molecular orbital (HOMO) to the lowest unoccupied molecular orbital (LUMO).[23] This electronic transition from the singlet ground state (S_0) to a non-zero vibrational level of a singlet excited state (S_1 or S_2), as depicted in **Figure 1.2**, is only possible when the energy of the absorbed photon matches the energy difference between the HOMO and LUMO of the molecule.

1.2.3 Energetic Relaxation & Light Emission

Once the energy is absorbed several non-radiative and/or radiative energetic relaxation processes are possible (**Figure 1.2**). Within a singlet excited state, the absorbed energy must first relax to the 'zeroth' vibrational level (S_{n-0}) through heat generation. Heat is also generated through internal conversion, which describes energy transitioning from a higher to lower singlet excited state. Once the energy reaches the zeroth vibrational level of S_1, it can continue to relax through non-radiative vibrations or the radiative process of fluorescence. As stated by Kasha's Rule, the wavelength of fluorescence emission is independent of the wavelength of the absorbed photon, which is a direct effect of fluorescence occurring only from S_{1-0}.[24] Since the energy difference between S_0 to S_n during absorption is larger than the difference between S_{1-0} back to S_0 during relaxation, the Einstein-Planck equation can be used to show that a bathochromic shift will occur between the wavelength of the absorbed and emitted photon, a phenomenon known as Stokes Shift.

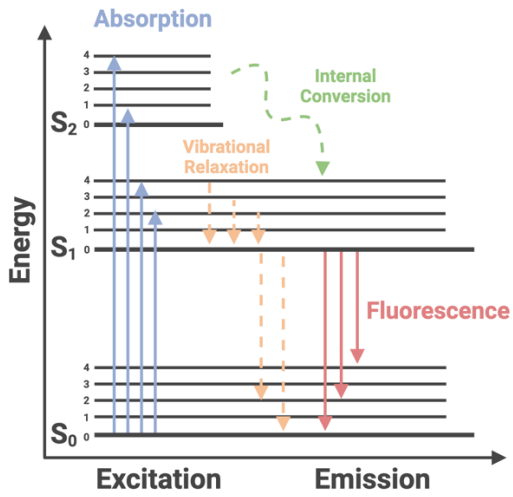

Figure 1.2. Jablonski diagram depicting photon absorption and singlet state energetic relaxation processes. (Created with BioRender).

The emission of a photon, or luminescence, can also occur in cases where light absorption has not taken place. Chemiluminescence, for example, occurs when a chemical reaction produces a molecule in its excited state.[25] A well-documented case of this is the oxidation of luminol. Another form of chemiluminescence, called bioluminescence, pertains to the emission of a photon because of specific biological reactions or processes taking place. A well-known and widely utilized example of this is the luciferase enzymatic reaction that occurs when luciferin interacts with Mg-ATP and molecular oxygen to produce electronically excited oxyluciferin.[26] In the context of molecular imaging, luminescence can be applied as a signalling agent for detection.

1.2.4 Optical Imaging Modalities

Optical imaging strategies, including FI and bioluminescence imaging (BI), rely on the detection of luminescence, or emitted photons, by relaxing optical absorbers or by a biological reaction, respectively. While BI remains prominent in preclinical cellular and small animal imaging, FI has gained some clinical recognition.[27] FI detects photons emitted from a molecule exposed to an external light source. This modality has found diverse applications in imaging

complex biological systems, such as quantification of *in vitro* and *in vivo* inhibition and dissociation constants for pharmacodynamic assessment of therapeutics,[28,29] *in vivo* monitoring of protein activity,[30,31] and longitudinal monitoring of disease progression in small animal models.[32,33] However, the clinical appeal has remained low due to the severe limitations of depth penetration resulting from high photon scattering effects in tissue. Despite this, exogenous dyes such as indocyanine green (ICG) have been successfully employed in clinical intraoperative imaging and laparoscopic surgery for image-guided tumour resection, where imaging depth becomes less critical.[34–36] Considering the disadvantages associated with optical imaging, there remains a precedent for other imaging modalities with applications that extend beyond what can be accomplished using fluorescence imaging. A modality, such as photoacoustic imaging, that shares in the propitious characteristics of fluorescence imaging, such as the exceptional sensitivity and lack of exposure to ionizing radiation, while addressing some of the limitations, namely the insufficient depth resolution, could encourage the clinical application of optical techniques.

1.3 Photoacoustic Imaging:

1.3.1 The History of Photoacoustic Imaging

PAI, while contemporary in reference to MI, is based on a phenomenon that was discovered over a century ago. Initially referred to as the photophonic or radiophonic effect, the photoacoustic (PA) effect describes the generation of acoustic waves through non-radiative relaxation of a molecule upon absorption of light and was first elucidated by Alexander Graham Bell in 1880.[37] Although it was an extraordinary finding for the time, research pertaining to the photoacoustic effect began to wane as signal quantification, via human hearing, became a key obstacle. It was not until several decades later that research began to resurface on the effects of light on gaseous

substances to produce sound,[38] and it wasn't until the late 20th century that experimentation was extended toward liquids and solids.[37,39,40] The invention of the laser in 1960 played a pivotal role in PA research as it became evident that the photoacoustic effect could be useful in biomedical imaging. The first computerized system for photoacoustic microscopy was developed in 1986, by Wada, *et al*.,[41] and *in vivo* studies using laser-induced ultrasound detection began to take place in the mid-1990s. Extensive development of instrumentation and image reconstruction technology took place over the proceeding two decades, allowing for major growth in functional and molecular imaging applications.[42]

1.3.2 The Progression of Photoacoustic Applications

As it currently exists, PAI is typically combined with US and offers several benefits compared to other MI modalities. In comparison to FI, PAI achieves comparable sensitivity while maintaining high-resolution acquisition at greater imaging depths, as a result of the reduced scattering of acoustic waves in tissue compared to light.[20] Additionally, spectral un-mixing, has been made possible by advanced mathematical algorithms implemented into commercial PA machinery, which allows for the visualization of target-specific signals in complicated biological matrices and simultaneous detection of multiple chromophores. In contrast to nuclear imaging techniques like PET and SPECT, PAI provides inexpensive, real-time image acquisition without introducing ionizing radiation.[43] Furthermore, when combined with US, anatomical mapping, through the detection of heterogenous tissue density and compressibility, can supplement PA images by contextualizing signal location.[37] As a result, PA research has emerged as a multidisciplinary field, and significant progress toward clinical translatability is anticipated to be driven by advancements in physical and mathematical technology, as well as the development of molecularly targeted contrast agents.

While PAI was quickly adopted into the preclinical study of disease, for both *in vitro* and *in vivo* research, achieving clinical translatability has posed a significant challenge. The initial step towards improving clinical applicability was the integration with clinically approved US machines. However, concerns for achieving clinically relevant imaging depths persisted. Fortunately, advancements in transducer configurations tailored to specific regions have been made. These include tomographic transducers for breast tissue imaging, handheld transducers with low frequency for imaging abdominal organs and with high frequency for superficial organs, and endocavitary arrays for imaging prostate, ovarian, and rectal tissue. These developments have allowed the prospect of clinical PAI to gain momentum.[44,45]

1.3.3 Photoacoustic Signal Generation & Image Acquisition

PAI (**Figure 1.3**) begins with the absorbance of electromagnetic radiation by a chromophore. However, unlike optical imaging techniques, which rely on the emission of photons for energetic relaxation, PAI is characterized by the non-radiative release of energy.[43] As the chromophore absorbs the photons and vibrationally relaxes, fluctuating pressure waves with megahertz (MHz) frequency are generated when thermal and stress confinement conditions are achieved.[44,46] To detail, thermal confinement occurs when the duration of the laser pulse is shorter than the time it takes for heat to diffuse from the illuminated area. This allows for a rapid and localized temperature increase to occur, which in turn induces a build-up of pressure. If this generated pressure diffuses from the area more slowly than the laser pulse duration, volume expansion of the optical absorber becomes negligible and stress confinement is achieved. When the excitation light duration is less than the thermal and stress relaxation times, a pressure wave with a bipolar shape is generated and the distance between the two peaks, or the PA signal frequency, is proportional to the size of the light-absorbing material.[46] Due to the synonymous

nature of data acquisition between PAI and US imaging, clinical transducers have been customized to include a laser bundle to easily combine the modalities and generate co-registered images.[44] Furthermore, motorized acquisition along an axis permits the generation of three-dimensional images, providing additional information on signal location.

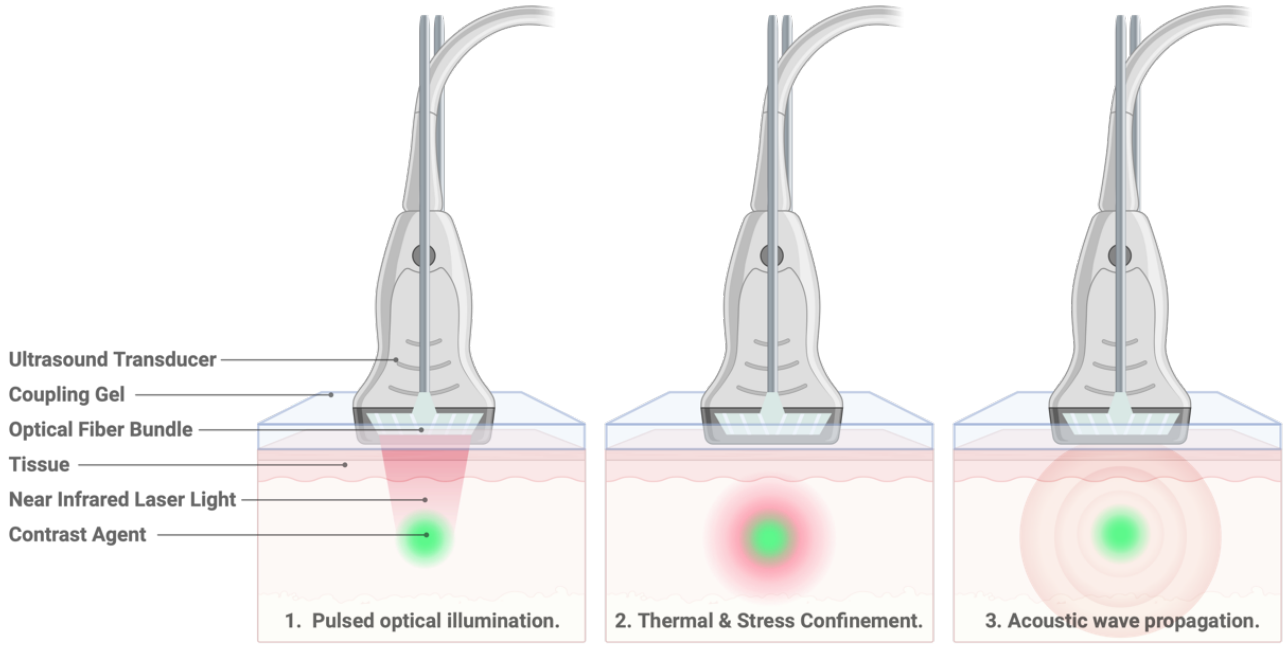

Figure 1.3. A depiction of the generation of photoacoustic signal. (Created with BioRender).

1.3.4 Photoacoustic Imaging Probes (PIPs)

1.3.4.1 Intrinsic Chromophores

Clinical PAI has been advanced by the utilization of 'label-free' imaging techniques (Summarized in **Table 1.3**). This approach involves the detection of endogenous chromophores, particularly those with absorption properties in the near-infrared region, to characterize disease pathology.[43] Hemoglobin, in its oxygenated and deoxygenated states, possesses distinct spectral characteristics with high absorption coefficients, making it easily detectable via PAI. Through quantification of the relative concentrations of these blood chromophores, it is possible to assess

tissue oxygenation levels and elucidate angiogenic or hypoxic conditions.[20] This methodology has proven valuable in the characterization of a diverse array of diseases including, various cancers,[47–49] skeletomuscular conditions,[50] and inflammatory diseases.[51] Melanin, a pigment commonly found in the skin, is a useful biomarker in photoacoustic detection of skin cancers[47,52] and sentinel lymph nodes.[53,54] Additionally, the contents of water and lipids can be quantified using PAI and have been employed to characterize breast[55] and thyroid cancers.[56] These intrinsic chromophores not only provide structural information but also provide functional insight into disease pathology. Notably, their use in PA clinical research is advantageous as they obviate the need for exogenous contrast that would necessitate prior approval from the FDA.

Table 1.3. A non-exhaustive summary of clinical trials utilizing diagnostic PAI.

Disease Target	Trial ID*	Imaging Biomarker	Trial Status
Breast Cancer	NCT03897270 NCT04825444 NCT01807754 NCT04428528 NCT02688257	Endogenous Endogenous Endogenous Endogenous Endogenous	Recruiting In Progress Complete Recruiting Complete
Colorectal Cancer	NCT04339374	Endogenous	Recruiting
Ovarian/Cervical Cancer	NCT04178018 NCT03262818 NCT03923881	Endogenous Endogenous *Exogenous*	Recruiting
Skin Cancer	NCT06379581 NCT04229277	Endogenous Endogenous2024-09-23 4:55:00 PM	Recruiting Complete
Head & Neck Cancer	NCT04428515 NCT04437030 NCT03733210	Endogenous Endogenous *Exogenous*	Recruiting Completed Completed

Prostate Cancer	NCT015515762024-09-23 4:55:00 PM	Endogenous	Completed

* ClinicalTrials.gov Identifier.

1.3.4.2 Exogenous Chromophores

To broaden the applications of PAI, the use of exogenous chromophores has become prevalent in preclinical research. These chromophores enable the detection of biological entities that lack intrinsic light absorption properties.[57,58] Typically, exogenous chromophores are attached to a targeting vector to form a photoacoustic imaging probe (PIP) that is able to selectively bind to a specific biomarker. However, certain chromophores can undergo passive uptake to accumulate in a tissue of interest, negating the requirement of a targeting vector.[20] This form of uptake is often observed in tumours with impaired lymphatic drainage and leaky vasculature.

When designing molecularly targeted PIPs, several criteria pertaining to the photophysical and biological properties of the agent must be considered. In terms of PA characteristics, a unique and sharp absorbance peak should be present in the NIR region. This ensures that the chromophore on the PIP will be identifiable within the wavelength range that most commercially available PA lasers operate in. Additionally, the chromophore should have a high molar extinction coefficient to optimize the amount of light that is capable of being absorbed while maintaining a low quantum yield to minimize the amount of energy released as photons.[20] From a biological perspective, the targeting vector on the PIP should be able to surmount both circulatory and cellular barriers to reach the intended site and should produce a low uptake in non-target organs to produce a low background signal.[20] Overall, the assembled construct should not exhibit any toxic or adverse side effects in the body.

1.3.4.3 Nanoparticle-Based PIPs

The current literature showcases a wide range of PIPs utilized in PAI, including both nanomaterials and small molecule dyes. Nanoparticles, which are particulate materials ranging from 10-100 nm in size, represent a broad category of PIPs used for PAI and are recognized for their tunable photophysical and biochemical properties. They can be synthesized from various elements, such as organic polymers, gold, or carbon, and exhibit distinct characteristics based on variations in size and shape. Notably, their large size enables a high loading capacity of targeting vectors per particle.[20] While nanotechnology has made significant advancements in recent years and shows promise in optimizing the delivery of diagnostic and therapeutic agents to disease sites, refinement in synthesis, purification, and characterization is essential to improve data reproducibility and meet the stringent standards required for clinical translation.[59]

1.3.4.4 Small Molecule Dye-Based PIPs

The integration of small molecule light-absorbing dyes into PAI applications has been warranted by their commercial availability, easily functionalized structures, and biocompatibility. Although there are various classes of light-absorbing dyes, several criteria must be satisfied to continue their use in *in vivo* PAI. These dyes should demonstrate photostability, water solubility, and light absorption in the NIR region.[60] Additionally, their chemical structure must allow for functionalization with a targeting vector.

Cyanine dyes (**Figure 1.4**) are characterized by their backbone of conjugated carbon-carbon double bonds, bordered with symmetrical heterocyclic and aromatic ring systems.[20,23,60] By altering the length of the unsaturated carbon backbone and modifying the ring systems, it is possible to change both the photophysical and chemical properties of these dyes, while also enabling versatile structural functionalization. The heterocyclic groups flanking the conjugated

backbone consist of an electron donor on one side and an acceptor on the other to allow for the delocalization of charge and a reduction in the HOMO to LUMO energy gap. As this gap is decreased, longer wavelengths of absorption and emission are observed and NIR properties can be achieved.[20,23,60]

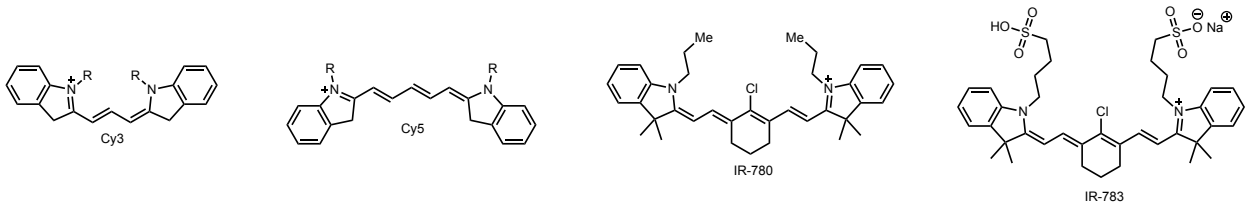

Figure 1.4. Various cyanine dyes. From left to right, Cy3, Cy5, IR-780, and IR-783.

In recent years, the FDA has approved several small-molecule dyes (**Figure 1.5**) for use in humans. Among the approved dyes is indocyanine green (ICG), a heptamethine cyanine dye that absorbs around 785 nm and has been used extensively in clinical fluorescence imaging for determining cardiac output, ophthalmic perfusion and hepatic function.[36,61] However, ICG has a short blood half-life, of approximately 3 minutes, low photostability, and its hydrophobic nature makes its unmodified structure suboptimal for molecular PAI. Similar limitations apply to another FDA-approved dye, methylene blue, which has been used for intraoperative imaging of several conditions.[62–66] This azo dye also experiences accentuated aggregation in aqueous media and exhibits a hypsochromic absorption peak that is not well suited for commercial PAI systems.[20] Despite these challenges, there is still value in exploring the use of small molecule dyes for PAI, namely their small size and modifiable structures.

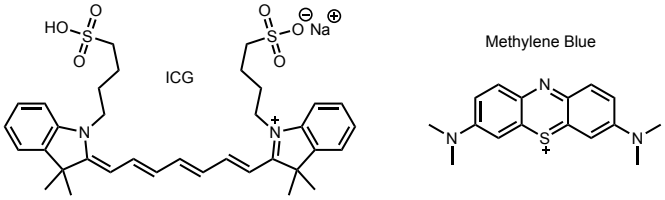

Figure 1.5. FDA-approved dyes for use in humans, ICG and Methylene blue.

1.3.4.5 Molecular Targeting & Assembly of PIPs

In addition to considering the chromophore, it is important to select an appropriate targeting vector and assembly method in the design of molecularly targeted PIPs. The current depth penetration parameters of PAI preclude certain applications, namely systemic or deep tissue diseases, but many suitable and clinically relevant disease targets for PAI remain. For example, imaging diseases that present closer to the surface of the body, such as breast cancer, thyroid cancer, or certain cases of surgical site/medical device infections, or diseases localized to organs accessible via endocavitary arrays, such as colorectal, ovarian, or prostate cancers, are all relevant applications. Several small molecule-, peptide-, and antibody-based targeting vectors for these diseases have been reported in the literature and offer suitable mechanisms of specifically delivering contrast to a site of interest,[13,67–72] some of which have already been utilized in the design of PIPs.[5,73–81]

Direct assembly, which typically involves the use of a linker group, is the simplest approach to joining a targeting vector and a signalling agent. This type of conjugation is quintessential to most PIPs, provided that a chemical means of functionalization is accessible. In cases where the chromophore is hydrophobic or has a structure non-conducive to derivatization, polymeric encapsulations have become a compelling solution.[82] Micelles with a polar exterior and a non-polar interior can be used to improve solubility and biodistribution.[83,84] If passive diffusion is

insufficient for the target of interest, the monomer can be functionalized with a targeting vector of choice prior to micellar assembly.[85,86] Another option is target-activatable contrast, where a chemical alteration of the PIP leads to a 'turn-on' effect when it comes into contact with a specific biomarker.[43,87] Naturally, these probes require well-thought-out chemical design and extensive periods of development, making them a rarity in comparison to the previously discussed forms of assembly.

Despite the progress made in developing exogenous PIPs, one major obstacle to the clinical integration of exogenous contrast for PAI is that the research performed on these exogenous agents has yet to meet the requirements for FDA approval. To overcome this, it is crucial to conduct thorough toxicity profiling, establish reproducible synthetic and characterization methods, and standardize experimental design and data reporting.[20]

1.4 Thesis Overview:

The work conducted within this thesis aims to outline the process of developing exogenous PIPs and the methodology used to validate their utility. To this end, various contrast agents, targeting vectors, and linkers were selected to generate several PIPs, which were then evaluated through a series of photophysical, *in vitro*, and *in vivo* tests to demonstrate their utility. Significant attention was placed on the development of methodology for assessing the *in vivo* potential of the PIPs and a standard procedure for PA data production and reporting was outlined and practiced throughout the work.

Throughout this work, the development of PIPs was pursued to target clinically relevant applications for PAI. Initially, a novel bone-targeted PIP, which could find utility for diagnosing hand and foot microfractures, was developed from a tetrazine-derived near-infrared dye and a *trans*-cyclooctene-derived bisphosphonate and evaluated using active and pre-targeting strategies

(Chapter 2). This work expanded from previous pilot work that focused on the use of the tetrazine-*trans*-cyclooctene pair as a platform for developing PIP building blocks.[88] While the overarching research aim was the development of a proof-of-concept bone-targeted PAI, a focus was placed on characterizing the construct, generating data using standardized protocols for preparation and processing of the images, and showcasing application of the PIP in both active and pre-targeting approaches to probe delivery.

Building on methodologies developed and to expand the scope of applications for the tetrazine-dye PIP building block, a bacteria targeted construct that could be used for diagnosing surgical site and medical implant bacterial infections was pursed. The construct contained the same tetrazine-dye described in Chapter 2 and was functionalized with a *trans*-cyclooctene-derived zinc dipicolylamine (ZnDPA) (Chapter 3.1.1). It has become standard practice to investigate the bacterial specificity of infection imaging agents against states of sterile inflammation.[89] Therefore, a model of bacterial infection and sterile inflammation of the muscle were used alongside a commercially available ZnDPA-fluorophore for proof-of-concept PAI of bacterial infection (Chapter 3.1.2). However, with respect to surgical site and implant-related bacterial infections, the role of cell death was not sufficiently studied, and questions remained surrounding the clinical relevance of using ZnDPA-based probes for targeting bacterial infection. While some studies utilizing ZnDPA-probes have explored cell death in their work,[90–93] the biological relevance of the models used remains under debate. Therefore, the development of a relevant model of medical implant bacterial infection was pursed to aid in determining the clinical utility of ZnDPA-based bacterial infection imaging agents (Chapter 3.2).

In Chapter 4 a novel, general-purpose dye was designed to overcome the challenges faced with PIPs reported in this thesis as well as in the greater field of exogenous PIP development. This

work aimed to address aqueous solubility, which is an ongoing and underrecognized concern pertaining to the use of NIR cyanine dyes *in vivo*.[94,95] Additionally, the use of multiwavelength signal unmixing scans warranted emphasis on the importance of designing PIPs with distinct and strong PA signals, as compared to the signal from endogenous blood chromophores. Standardized protocols in data production and reporting were used to generate a comprehensive analysis of the reported dye's photophysical, solubility, and signal unmixing characteristics. Proof-of-concept work was performed using ZnDPA to target the PIP towards bacterial infection and several clinically relevant disease applications were discussed as a focus for future work.

1.5 References:

(1) Paeng, J. C.; Lee, D. S. Multimodal Molecular Imaging In Vivo. *Open Nucl. Med. J.* **2010**, *2* (1), 145–152. https://doi.org/10.2174/1876388X01002010145.

(2) Strimbu, K.; Tavel, J. A. What Are Biomarkers? *Curr. Opin. HIV AIDS* **2010**, *5* (6), 463–466. https://doi.org/10.1097/COH.0b013e32833ed177.

(3) Mayeux, R. Biomarkers: Potential Uses and Limitations. *Neurotherapeutics* **2004**, *1* (2), 182–188.

(4) Saha, G. B. *Fundamentals of Nuclear Pharmacy*; Springer International Publishing: Cham, 2018. https://doi.org/10.1007/978-3-319-57580-3.

(5) Zlitni, A.; Gowrishankar, G.; Steinberg, I.; Haywood, T.; Sam Gambhir, S. Maltotriose-Based Probes for Fluorescence and Photoacoustic Imaging of Bacterial Infections. *Nat. Commun.* **2020**, *11* (1), 1250. https://doi.org/10.1038/s41467-020-14985-8.

(6) Kung, M.-P.; Hou, C.; Zhuang, Z.-P.; Cross, AlanJ.; Maier, DonnaL.; Kung, HankF. Characterization of IMPY as a Potential Imaging Agent for B-Amyloid Plaques in Double Transgenic PSAPP Mice. *Eur. J. Nucl. Med. Mol. Imaging* **2004**, *31* (8). https://doi.org/10.1007/s00259-004-1487-z.

(7) Wang, X.; Liu, W.; Li, K.; Chen, K.; He, S.; Zhang, J.; Gu, B.; Xu, X.; Song, S. PET Imaging of PARP Expression Using 68Ga-Labelled Inhibitors. *Eur. J. Nucl. Med. Mol. Imaging* **2023**, *50* (9), 2606–2620. https://doi.org/10.1007/s00259-023-06249-6.

(8) Li, L.; Wu, Y.; Wang, Z.; Jia, B.; Hu, Z.; Dong, C.; Wang, F. SPECT/CT Imaging of the Novel HER2-Targeted Peptide Probe ^{99m} Tc-HYNIC-H6F in Breast Cancer Mouse Models. *J. Nucl. Med.* **2017**, *58* (5), 821–826. https://doi.org/10.2967/jnumed.116.183863.

(9) Wu, Z.; Li, Z.-B.; Chen, K.; Cai, W.; He, L.; Chin, F. T.; Li, F.; Chen, X. microPET of Tumor Integrin v 3 Expression Using 18F-Labeled PEGylated Tetrameric RGD Peptide (18F-FPRGD4). *J. Nucl. Med.* **2007**, *48* (9), 1536–1544. https://doi.org/10.2967/jnumed.107.040816.

(10) Maeda, A.; Bu, J.; Chen, J.; Zheng, G.; DaCosta, R. S. Dual in Vivo Photoacoustic and Fluorescence Imaging of HER2 Expression in Breast Tumors for Diagnosis, Margin Assessment, and Surgical Guidance. *Mol. Imaging* **2015**, *14* (1), 7290.2014.00043. https://doi.org/10.2310/7290.2014.00043.

(11) Van Dijk, B.; Hooning Van Duyvenbode, J. F. F.; De Vor, L.; Nurmohamed, F. R. H. A.; Lam, M. G. E. H.; Poot, A. J.; Ramakers, R. M.; Koustoulidou, S.; Beekman, F. J.; Van Strijp, J.; Rooijakkers, S. H. M.; Dadachova, E.; Vogely, H. C.; Weinans, H.; Van Der Wal, B. C. H. Evaluating the Targeting of a Staphylococcus-Aureus-Infected Implant with a Radiolabeled Antibody In Vivo. *Int. J. Mol. Sci.* **2023**, *24* (5), 4374. https://doi.org/10.3390/ijms24054374.

(12) Al-saden, N.; Lam, K.; Chan, C.; Reilly, R. M. Positron-Emission Tomography of HER2-Positive Breast Cancer Xenografts in Mice with ^{89} Zr-Labeled Trastuzumab-DM1: A Comparison with ^{89} Zr-Labeled Trastuzumab. *Mol. Pharm.* **2018**, *15* (8), 3383–3393. https://doi.org/10.1021/acs.molpharmaceut.8b00392.

(13) Huang, R.; Pu, Y.; Huang, S.; Yang, C.; Yang, F.; Pu, Y.; Li, J.; Chen, L.; Huang, Y. FAPI-PET/CT in Cancer Imaging: A Potential Novel Molecule of the Century. *Front. Oncol.* **2022**, *12*, 854658. https://doi.org/10.3389/fonc.2022.854658.

(14) Kaseda, K. Recent and Current Advances in FDG-PET Imaging within the Field of Clinical Oncology in NSCLC: A Review of the Literature. *Diagnostics* **2020**, *10* (8), 561. https://doi.org/10.3390/diagnostics10080561.

(15) Lehman, V. T.; Murphy, R. C.; Maus, T. P. 99mTc-MDP SPECT/CT of the Spine and Sacrum at a Multispecialty Institution: Clinical Use, Findings, and Impact on Patient Management.

Nucl. Med. Commun. **2013**, *34* (11), 1097–1106. https://doi.org/10.1097/MNM.0b013e328364bfa6.

(16) Randall, L. M.; Wenham, R. M.; Low, P. S.; Dowdy, S. C.; Tanyi, J. L. A Phase II, Multicenter, Open-Label Trial of OTL38 Injection for the Intra-Operative Imaging of Folate Receptor-Alpha Positive Ovarian Cancer. *Gynecol. Oncol.* **2019**, *155* (1), 63–68. https://doi.org/10.1016/j.ygyno.2019.07.010.

(17) Wang, Y.; Dong, L.; Zhao, H.; Li, L.; Huang, G.; Xue, W.; Liu, J.; Chen, R. The Superior Detection Rate of Total-Body [68Ga]Ga-PSMA-11 PET/CT Compared to Short Axial Field-of-View [68Ga]Ga-PSMA-11 PET/CT for Early Recurrent Prostate Cancer Patients with PSA < 0.2 Ng/mL after Radical Prostatectomy. *Eur. J. Nucl. Med. Mol. Imaging* **2024**. https://doi.org/10.1007/s00259-024-06674-1.

(18) Gandomkar, M.; Najafi, R.; Shafiei, M.; Mazidi, M.; Goudarzi, M.; Mirfallah, S. H.; Ebrahimi, F.; Heydarpor, H. R.; Abdie, N. Clinical Evaluation of Antimicrobial Peptide [99mTc/Tricine/HYNIC0]Ubiquicidin 29–41 as a Human-Specific Infection Imaging Agent. *Nucl. Med. Biol.* **2009**, *36* (2), 199–205. https://doi.org/10.1016/j.nucmedbio.2008.11.003.

(19) Gao, R. W.; Teraphongphom, N.; De Boer, E.; Berg, N. S. V. D.; Divi, V.; Kaplan, M. J.; Oberhelman, N. J.; Hong, S. S.; Capes, E.; Colevas, A. D.; Warram, J. M.; Rosenthal, E. L. Safety of Panitumumab-IRDye800CW and Cetuximab-IRDye800CW for Fluorescence-Guided Surgical Navigation in Head and Neck Cancers. *Theranostics* **2018**, *8* (9), 2488–2495. https://doi.org/10.7150/thno.24487.

(20) Weber, J.; Beard, P. C.; Bohndiek, S. E. Contrast Agents for Molecular Photoacoustic Imaging. *Nat. Methods* **2016**, *13* (8), 639–650. https://doi.org/10.1038/nmeth.3929.

(21) de la Zerda, A. Photoacoustic Molecular Imaging and Its Biomedical Applications. Doctoral Dissertation, Stanford University, 2011. http://purl.stanford.edu/rc934jq3457.

(22) Rahmim, A.; Zaidi, H. PET versus SPECT: Strengths, Limitations and Challenges. *Nucl. Med. Commun.* **2008**, *29* (3), 193–207. https://doi.org/10.1097/MNM.0b013e3282f3a515.

(23) Watson, A. D. Binding Studies of Near Infrared Cyanine Dyes with Human Serum Albumin and Poly-L-Lysine Using Optical Spectroscopy Methods. Dissertation, Georgia State University, 2008. h9p://scholarworks.gsu.edu/chemistry_diss/15.

(24) Lakowicz, J. R. *Principles of Fluorescence Spectroscopy*, 3rd ed.; Springer: New York, 2006.

(25) Dodeigne, C. Chemiluminescence as Diagnostic Tool. A Review. *Talanta* **2000**, *51* (3), 415–439. https://doi.org/10.1016/S0039-9140(99)00294-5.

(26) Nakatsu, T.; Ichiyama, S.; Hiratake, J.; Saldanha, A.; Kobashi, N.; Sakata, K.; Kato, H. Structural Basis for the Spectral Difference in Luciferase Bioluminescence. *Nature* **2006**, *440* (7082), 372–376. https://doi.org/10.1038/nature04542.

(27) Kosaka, N.; Ogawa, M.; Choyke, P. L.; Kobayashi, H. Clinical Implications of Near-Infrared Fluorescence Imaging in Cancer. *Future Oncol.* **2009**, *5* (9), 1501–1511. https://doi.org/10.2217/fon.09.109.

(28) Luker, G. D.; Pica, C. M.; Song, J.; Luker, K. E.; Piwnica-Worms, D. Imaging 26S Proteasome Activity and Inhibition in Living Mice. *Nat. Med.* **2003**, *9* (7), 969–973. https://doi.org/10.1038/nm894.

(29) Zhang, L.; Lee, K. C.; Bhojani, M. S.; Khan, A. P.; Shilman, A.; Holland, E. C.; Ross, B. D.; Rehemtulla, A. Molecular Imaging of Akt Kinase Activity. *Nat. Med.* **2007**, *13* (9), 1114–1119. https://doi.org/10.1038/nm1608.

(30) Jiang, T.; Olson, E. S.; Nguyen, Q. T.; Roy, M.; Jennings, P. A.; Tsien, R. Y. Tumor Imaging by Means of Proteolytic Activation of Cell-Penetrating Peptides. *Proc. Natl. Acad. Sci.* **2004**, *101* (51), 17867–17872. https://doi.org/10.1073/pnas.0408191101.

(31) Grimm, J.; Kirsch, D. G.; Windsor, S. D.; Kim, C. F. B.; Santiago, P. M.; Ntziachristos, V.; Jacks, T.; Weissleder, R. Use of Gene Expression Profiling to Direct in Vivo Molecular Imaging of Lung Cancer. *Proc. Natl. Acad. Sci.* **2005**, *102* (40), 14404–14409. https://doi.org/10.1073/pnas.0503920102.

(32) Hassan, M.; Klaunberg, B. A. Biomedical Applications of Fluorescence Imaging In Vivo. *Comp. Med.* **2004**, *54* (6), 10.

(33) Hickson, J. In Vivo Optical Imaging: Preclinical Applications and Considerations. *Urol. Oncol. Semin. Orig. Investig.* **2009**, *27* (3), 295–297. https://doi.org/10.1016/j.urolonc.2008.10.030.

(34) Crane, L. M. A.; Themelis, G.; Arts, H. J. G.; Buddingh, K. T.; Brouwers, A. H.; Ntziachristos, V.; van Dam, G. M.; van der Zee, A. G. J. Intraoperative Near-Infrared Fluorescence Imaging for Sentinel Lymph Node Detection in Vulvar Cancer: First Clinical Results. *Gynecol. Oncol.* **2011**, *120* (2), 291–295. https://doi.org/10.1016/j.ygyno.2010.10.009.

(35) Boni, L.; David, G.; Mangano, A.; Dionigi, G.; Rausei, S.; Spampatti, S.; Cassinotti, E.; Fingerhut, A. Clinical Applications of Indocyanine Green (ICG) Enhanced Fluorescence in Laparoscopic Surgery. *Surg. Endosc.* **2015**, *29* (7), 2046–2055. https://doi.org/10.1007/s00464-014-3895-x.

(36) Schaafsma, B. E.; Mieog, J. S. D.; Hutteman, M.; van der Vorst, J. R.; Kuppen, P. J. K.; Löwik, C. W. G. M.; Frangioni, J. V.; van de Velde, C. J. H.; Vahrmeijer, A. L. The Clinical Use of Indocyanine Green as a Near-Infrared Fluorescent Contrast Agent for Image-Guided Oncologic Surgery. *J. Surg. Oncol.* **2011**, *104* (3), 323–332. https://doi.org/10.1002/jso.21943.

(37) Emelianov, S. Y.; Li, P.-C.; O'Donnell, M. Photoacoustics for Molecular Imaging and Therapy. *Phys. Today* **2009**, *62* (8), 34–39. https://doi.org/10.1063/1.3141939.

(38) Veingerov, M. L. An Optical-Acoustic Method of Gas Analysis. *Nature* **1946**, *158*, 28–29.

(39) Rosencwaig, A. Photoacoustic Spectroscopy of Solids. *Opt. Commun.* **1973**, *7*, 305–308.

(40) Harshbarger, W. R.; Robin, M. B. Opto-Acoustic Effect. Revival of an Old Technique for Molecular Spectroscopy. *Acc. Chem. Res. 6*, 329–334.

(41) Wada, K.; Masujima, T.; Yoshida, H.; Murakami, T.; Yata, N.; Imai, H. Application of Photoacoustic Microscopy to Analysis of Biological Compenents in Tissue Sections. *Chem. Pharm. Bull. (Tokyo)* **1986**, *34* (4), 1688–1693.

(42) Beard, P. Biomedical Photoacoustic Imaging. *Interface Focus* **2011**, *1* (4), 602–631. https://doi.org/10.1098/rsfs.2011.0028.

(43) Knox, H. J.; Chan, J. Acoustogenic Probes: A New Frontier in Photoacoustic Imaging. *Acc. Chem. Res.* **2018**, *51* (11), 2897–2905. https://doi.org/10.1021/acs.accounts.8b00351.

(44) Valluru, K. S.; Wilson, K. E.; Willmann, J. K. Photoacoustic Imaging in Oncology: Translational Preclinical and Early Clinical Experience. *Radiology* **2016**, *280* (2), 332–349. https://doi.org/10.1148/radiol.16151414.

(45) Jiang, D.; Zhu, L.; Tong, S.; Shen, Y.; Gao, F.; Gao, F. Photoacoustic Imaging plus X: A Review. *J. Biomed. Opt.* **2023**, *29* (S1). https://doi.org/10.1117/1.JBO.29.S1.S11513.

(46) Xia, J.; Yao, J.; Wang, L. V. Photoacoustic Tomography: Principles and Advances. *Electromagn Wave Camb* **2015**, *147*, 1–22.

(47) Attia, A. B. E.; Chuah, S. Y.; Razansky, D.; Ho, C. J. H.; Malempati, P.; Dinish, U. S.; Bi, R.; Fu, C. Y.; Ford, S. J.; Lee, J. S.-S.; Tan, M. W. P.; Olivo, M.; Thng, S. T. G. Noninvasive

Real-Time Characterization of Non-Melanoma Skin Cancers with Handheld Optoacoustic Probes. *Photoacoustics* **2017**, *7*, 20–26. https://doi.org/10.1016/j.pacs.2017.05.003.

(48) Becker, A.; Masthoff, M.; Claussen, J.; Ford, S. J.; Roll, W.; Burg, M.; Barth, P. J.; Heindel, W.; Schäfers, M.; Eisenblätter, M.; Wildgruber, M. Multispectral Optoacoustic Tomography of the Human Breast: Characterisation of Healthy Tissue and Malignant Lesions Using a Hybrid Ultrasound-Optoacoustic Approach. *Eur. Radiol.* **2018**, *28* (2), 602–609. https://doi.org/10.1007/s00330-017-5002-x.

(49) Yang, M.; Zhao, L.; He, X.; Su, N.; Zhao, C.; Tang, H.; Hong, T.; Li, W.; Yang, F.; Lin, L.; Zhang, B.; Zhang, R.; Jiang, Y.; Li, C. Photoacoustic/Ultrasound Dual Imaging of Human Thyroid Cancers: An Initial Clinical Study. *Biomed. Opt. Express* **2017**, *8* (7), 3449. https://doi.org/10.1364/BOE.8.003449.

(50) Regensburger, A. P.; Fonteyne, L. M.; Jüngert, J.; Wagner, A. L.; Gerhalter, T.; Nagel, A. M.; Heiss, R.; Flenkenthaler, F.; Qurashi, M.; Neurath, M. F.; Klymiuk, N.; Kemter, E.; Fröhlich, T.; Uder, M.; Woelfle, J.; Rascher, W.; Trollmann, R.; Wolf, E.; Waldner, M. J.; Knieling, F. Detection of Collagens by Multispectral Optoacoustic Tomography as an Imaging Biomarker for Duchenne Muscular Dystrophy. *Nat. Med.* **2019**, *25* (12), 1905–1915. https://doi.org/10.1038/s41591-019-0669-y.

(51) Waldner, M. J.; Knieling, F.; Egger, C.; Morscher, S.; Claussen, J.; Vetter, M.; Kielisch, C.; Fischer, S.; Pfeifer, L.; Hagel, A.; Goertz, R. S.; Wildner, D.; Atreya, R.; Strobel, D.; Neurath, M. F. Multispectral Optoacoustic Tomography in Crohn's Disease: Noninvasive Imaging of Disease Activity. *Gastroenterology* **2016**, *151* (2), 238–240. https://doi.org/10.1053/j.gastro.2016.05.047.

(52) Chuah, S. Y.; Attia, A. B. E.; Ho, C. J. H.; Li, X.; Lee, J. S.-S.; Tan, M. W. P.; Yong, A. A.; Tan, A. W. M.; Razansky, D.; Olivo, M.; Thng, S. T. G. Volumetric Multispectral Optoacoustic Tomography for 3-Dimensional Reconstruction of Skin Tumors: A Further Evaluation with Histopathologic Correlation. *J. Invest. Dermatol.* **2019**, *139* (2), 481–485. https://doi.org/10.1016/j.jid.2018.08.014.

(53) Stoffels, I.; Morscher, S.; Helfrich, I.; Hillen, U.; Leyh, J.; Burton, N. C.; Sardella, T. C. P.; Claussen, J.; Poeppel, T. D.; Bachmann, H. S.; Roesch, A.; Griewank, K.; Schadendorf, D.; Gunzer, M.; Klode, J. Metastatic Status of Sentinel Lymph Nodes in Melanoma Determined

Noninvasively with Multispectral Optoacoustic Imaging. *Sci. Transl. Med.* **2015**, *7* (317), 317ra199-317ra199. https://doi.org/10.1126/scitranslmed.aad1278.

(54) Stoffels, I.; Jansen, P.; Petri, M.; Goerdt, L.; Brinker, T. J.; Griewank, K. G.; Poeppel, T. D.; Schadendorf, D.; Klode, J. Assessment of Nonradioactive Multispectral Optoacoustic Tomographic Imaging With Conventional Lymphoscintigraphic Imaging for Sentinel Lymph Node Biopsy in Melanoma. *JAMA Netw. Open* **2019**, *2* (8), e199020. https://doi.org/10.1001/jamanetworkopen.2019.9020.

(55) Diot, G.; Metz, S.; Noske, A.; Liapis, E.; Schroeder, B.; Ovsepian, S. V.; Meier, R.; Rummeny, E.; Ntziachristos, V. Multispectral Optoacoustic Tomography (MSOT) of Human Breast Cancer. *Clin. Cancer Res.* **2017**, *23* (22), 6912–6922. https://doi.org/10.1158/1078-0432.CCR-16-3200.

(56) Roll, W.; Markwardt, N. A.; Masthoff, M.; Helfen, A.; Claussen, J.; Eisenblätter, M.; Hasenbach, A.; Hermann, S.; Karlas, A.; Wildgruber, M.; Ntziachristos, V.; Schäfers, M. Multispectral Optoacoustic Tomography of Benign and Malignant Thyroid Disorders: A Pilot Study. *J. Nucl. Med.* **2019**, *60* (10), 1461–1466. https://doi.org/10.2967/jnumed.118.222174.

(57) Steinberg, I.; Huland, D. M.; Vermesh, O.; Frostig, H. E.; Tummers, W. S.; Gambhir, S. S. Photoacoustic Clinical Imaging. *Photoacoustics* **2019**, *14*, 77–98. https://doi.org/10.1016/j.pacs.2019.05.001.

(58) Sivaramakrishnan, M.; Maslov, K.; Zhang, H. F.; Stoica, G.; Wang, L. V. Limitations of Quantitative Photoacoustic Measurements of Blood Oxygenation in Small Vessels. *Phys. Med. Biol.* **2007**, *52* (5), 1349–1361. https://doi.org/10.1088/0031-9155/52/5/010.

(59) Duncan, R.; Gaspar, R. Nanomedicine(s) under the Microscope. *Mol. Pharm.* **2011**, *8* (6), 2101–2141. https://doi.org/10.1021/mp200394t.

(60) D. Nolting, D.; C. Gore, J.; Pham, W. Near-Infrared Dyes: Probe Development and Applications in Optical Molecular Imaging. *Curr. Org. Synth.* **2011**, *8* (4), 521–534. https://doi.org/10.2174/157017911796117223.

(61) James, N. S.; Chen, Y.; Joshi, P.; Ohulchanskyy, T. Y.; Ethirajan, M.; Henary, M.; Strekowsk, L.; Pandey, R. K. Evaluation of Polymethine Dyes as Potential Probes for Near Infrared Fluorescence Imaging of Tumors: Part - 1. *Theranostics* **2013**, *3* (9), 692–702. https://doi.org/10.7150/thno.5922.

(62) Cwalinski, T.; Polom, W.; Marano, L.; Roviello, G.; D'Angelo, A.; Cwalina, N.; Matuszewski, M.; Roviello, F.; Jaskiewicz, J.; Polom, K. Methylene Blue—Current Knowledge, Fluorescent Properties, and Its Future Use. *J. Clin. Med.* **2020**, *9* (11), 3538. https://doi.org/10.3390/jcm9113538.

(63) Handgraaf, H. J. M.; Boogerd, L. S. F.; Shahbazi Feshtali, S.; Fariña Sarasqueta, A.; Snel, M.; Swijnenburg, R.-J.; Vahrmeijer, A. L.; Bonsing, B. A.; Mieog, J. S. D. Intraoperative Near-Infrared Fluorescence Imaging of Multiple Pancreatic Neuroendocrine Tumors: A Case Report. *Pancreas* **2018**, *47* (1), 130–133. https://doi.org/10.1097/MPA.0000000000000951.

(64) Tummers, Q. R. J. G.; Boonstra, M. C.; Frangioni, J. V.; Van De Velde, C. J. H.; Vahrmeijer, A. L.; Bonsing, B. A. Intraoperative Near-Infrared Fluorescence Imaging of a Paraganglioma Using Methylene Blue: A Case Report. *Int. J. Surg. Case Rep.* **2015**, *6*, 150–153. https://doi.org/10.1016/j.ijscr.2014.12.002.

(65) Delacroix, S.; Winters, J. C. Urinary Tract Injures: Recognition and Management. *Clin. Colon Rectal Surg.* **2010**, *23* (02), 104–112. https://doi.org/10.1055/s-0030-1254297.

(66) Jiang, L.; Liu, T.; Wang, X.; Li, J.; Zhao, H. Real-time Near-infrared Fluorescence Imaging Mediated by Blue Dye in Breast Cancer Patients. *J. Surg. Oncol.* **2020**, *121* (6), 964–966. https://doi.org/10.1002/jso.25874.

(67) Ducharme, M.; Lapi, S. E. Peptide Based Imaging Agents for HER2 Imaging in Oncology. *Mol. Imaging* **2020**, *19*, 153601212096025. https://doi.org/10.1177/1536012120960258.

(68) Munnink, T. H. O.; Nagengast, W. B.; Brouwers, A. H.; Schröder, C. P.; Hospers, G. A.; Hooge, M. N. L. Molecular Imaging of Breast Cancer. *The Breast* **2009**.

(69) Leevy, W. M.; Gammon, S. T.; Johnson, J. R.; Lampkins, A. J.; Jiang, H.; Marquez, M.; Piwnica-Worms, D.; Suckow, M. A.; Smith, B. D. Noninvasive Optical Imaging of Staphylococcus Aureus Bacterial Infection in Living Mice Using a Bis-Dipicolylamine-Zinc(II) Affinity Group Conjugated to a Near-Infrared Fluorophore. *Bioconjug. Chem.* **2008**, *19* (3), 686–692. https://doi.org/10.1021/bc700376v.

(70) Rossin, R.; Robillard, M. S. Pretargeted Imaging Using Bioorthogonal Chemistry in Mice. *Curr. Opin. Chem. Biol.* **2014**, *21*, 161–169. https://doi.org/10.1016/j.cbpa.2014.07.023.

(71) Sharma, S. K.; Nemieboka, B.; Sala, E.; Lewis, J. S.; Zeglis, B. M. Molecular Imaging of Ovarian Cancer. *J. Nucl. Med.* **2016**, *57* (6), 827–833. https://doi.org/10.2967/jnumed.115.172023.

(72) Jadvar, H. Molecular Imaging of Prostate Cancer with 18F-Fluorodeoxyglucose PET. *Nat. Rev. Urol.* **2009**, *6* (6), 317–323. https://doi.org/10.1038/nrurol.2009.81.

(73) Zhang, T.; Cui, H.; Fang, C.-Y.; Cheng, K.; Yang, X.; Chang, H.-C.; Forrest, M. L. Targeted Nanodiamonds as Phenotype-Specific Photoacoustic Contrast Agents for Breast Cancer. *Nanomed.* **2015**, *10* (4), 573–587. https://doi.org/10.2217/nnm.14.141.

(74) Zhang, M.; Kim, H. S.; Jin, T.; Yi, A.; Moon, W. K. Ultrasound-Guided Photoacoustic Imaging for the Selective Detection of EGFR-Expressing Breast Cancer and Lymph Node Metastases. *Biomed. Opt. Express* **2016**, *7* (5), 1920. https://doi.org/10.1364/BOE.7.001920.

(75) Levi, J.; Kothapalli, S.-R.; Bohndiek, S.; Yoon, J.-K.; Dragulescu-Andrasi, A.; Nielsen, C.; Tisma, A.; Bodapati, S.; Gowrishankar, G.; Yan, X.; Chan, C.; Starcevic, D.; Gambhir, S. S. Molecular Photoacoustic Imaging of Follicular Thyroid Carcinoma. *Clin. Cancer Res.* **2013**, *19* (6), 1494–1502. https://doi.org/10.1158/1078-0432.CCR-12-3061.

(76) Wang, Y.; Thompson, J. M.; Ashbaugh, A. G.; Khodakivskyi, P.; Budin, G.; Sinisi, R.; Heinmiller, A.; van Oosten, M.; van Dijl, J. M.; van Dam, G. M.; Francis, K. P.; Bernthal, N. M.; Dubikovskaya, E. A.; Miller, L. S. Preclinical Evaluation of Photoacoustic Imaging as a Novel Noninvasive Approach to Detect an Orthopaedic Implant Infection: *J. Am. Acad. Orthop. Surg.* **2017**, *25*, S7–S12. https://doi.org/10.5435/JAAOS-D-16-00630.

(77) Lesniak, W. G.; Wu, Y.; Kang, J.; Boinapally, S.; Ray Banerjee, S.; Lisok, A.; Jablonska, A.; Boctor, E. M.; Pomper, M. G. Dual Contrast Agents for Fluorescence and Photoacoustic Imaging: Evaluation in a Murine Model of Prostate Cancer. *Nanoscale* **2021**, *13* (20), 9217–9228. https://doi.org/10.1039/D1NR00669J.

(78) Qiu, C.; Bai, Y.; Yin, T.; Miao, X.; Gao, R.; Zhou, H.; Ren, J.; Song, L.; Liu, C.; Zheng, H.; Zheng, R. Targeted Imaging of Orthotopic Prostate Cancer by Using Clinical Transformable Photoacoustic Molecular Probe. *BMC Cancer* **2020**, *20* (1), 419. https://doi.org/10.1186/s12885-020-06801-9.

(79) Tan, H.; Hou, N.; Liu, Y.; Liu, B.; Cao, W.; Zheng, D.; Li, W.; Liu, Y.; Xu, B.; Wang, Z.; Cui, D. CD133 Antibody Targeted Delivery of Gold Nanostars Loading IR820 and Docetaxel for Multimodal Imaging and Near-Infrared Photodynamic/Photothermal/Chemotherapy against Castration Resistant Prostate Cancer. *Nanomedicine Nanotechnol. Biol. Med.* **2020**, *27*, 102192. https://doi.org/10.1016/j.nano.2020.102192.

(80) Levi, J.; Sathirachinda, A.; Gambhir, S. S. A High-Affinity, High-Stability Photoacoustic Agent for Imaging Gastrin-Releasing Peptide Receptor in Prostate Cancer. *Clin. Cancer Res.* **2014**, *20* (14), 3721–3729. https://doi.org/10.1158/1078-0432.CCR-13-3405.

(81) Capozza, M.; Blasi, F.; Valbusa, G.; Oliva, P.; Cabella, C.; Buonsanti, F.; Cordaro, A.; Pizzuto, L.; Maiocchi, A.; Poggi, L. Photoacoustic Imaging of Integrin-Overexpressing Tumors Using a Novel ICG-Based Contrast Agent in Mice. *Photoacoustics* **2018**, *11*, 36–45. https://doi.org/10.1016/j.pacs.2018.07.007.

(82) Wood, C. A.; Han, S.; Kim, C. S.; Wen, Y.; Sampaio, D. R. T.; Harris, J. T.; Homan, K. A.; Swain, J. L.; Emelianov, S. Y.; Sood, A. K.; Cook, J. R.; Sokolov, K. V.; Bouchard, R. R. Clinically Translatable Quantitative Molecular Photoacoustic Imaging with Liposome-Encapsulated ICG J-Aggregates. *Nat. Commun.* **2021**, *12* (1), 5410. https://doi.org/10.1038/s41467-021-25452-3.

(83) Basak, R.; Bandyopadhyay, R. Encapsulation of Hydrophobic Drugs in Pluronic F127 Micelles: Effects of Drug Hydrophobicity, Solution Temperature, and pH. *Langmuir* **2013**, *29* (13), 4350–4356. https://doi.org/10.1021/la304836e.

(84) Pais-Silva, C.; de Melo-Diogo, D.; Correia, I. J. IR780-Loaded TPGS-TOS Micelles for Breast Cancer Photodynamic Therapy. *Eur. J. Pharm. Biopharm.* **2017**, *113*, 108–117. https://doi.org/10.1016/j.ejpb.2017.01.002.

(85) Yue, C.; Liu, P.; Zheng, M.; Zhao, P.; Wang, Y.; Ma, Y.; Cai, L. IR-780 Dye Loaded Tumor Targeting Theranostic Nanoparticles for NIR Imaging and Photothermal Therapy. *Biomaterials* **2013**, *34* (28), 6853–6861. https://doi.org/10.1016/j.biomaterials.2013.05.071.

(86) van Onzen, A. H. A. M.; Rossin, R.; Schenning, A. P. H. J.; Nicolay, K.; Milroy, L.-G.; Robillard, M. S.; Brunsveld, L. Tetrazine— Trans-Cyclooctene Chemistry Applied to Fabricate Self-Assembled Fluorescent and Radioactive Nanoparticles for in Vivo Dual Mode Imaging. *Bioconjug. Chem.* **2019**, *30* (3), 547–551. https://doi.org/10.1021/acs.bioconjchem.9b00038.

(87) Lucero, M.; Chan, J. *Towards Personalized Medicine: Photoacoustic Imaging Enables Companion Diagnosis and Targeted Treatment of Lung Cancer*; preprint; Chemistry, 2020. https://doi.org/10.26434/chemrxiv.11888214.v1.

(88) Slikboer, S.; Naperstkow, Z.; Janzen, N.; Faraday, A.; Soenjaya, Y.; Le Floc'h, J.; Al-Karmi, S.; Swann, R.; Wyszatko, K.; Demore, C. E. M.; Foster, S.; Valliant, J. F. Tetrazine-Derived

Near-Infrared Dye as a Facile Reagent for Developing Targeted Photoacoustic Imaging Agents. *Mol. Pharm.* **2020**, *17* (9), 3369–3377. https://doi.org/10.1021/acs.molpharmaceut.0c00441.

(89) Liu, X.; Cheng, D.; Gray, B. D.; Wang, Y.; Akalin, A.; Rusckowski, M.; Pak, K. Y.; Hnatowich, D. J. Radiolabeled Zn-DPA as a Potential Infection Imaging Agent. *Nucl. Med. Biol.* **2012**, *39* (5), 709–714. https://doi.org/10.1016/j.nucmedbio.2011.12.006.

(90) Thakur, M. L.; Zhang, K.; Paudyal, B.; Devakumar, D.; Covarrubias, M. Y.; Cheng, C.; Gray, B. D.; Wickstrom, E.; Pak, K. Y. Targeting Apoptosis for Optical Imaging of Infection. *Mol. Imaging Biol.* **2012**, *14* (2), 163–171. https://doi.org/10.1007/s11307-011-0490-6.

(91) Smith, B. A.; Gammon, S. T.; Xiao, S.; Wang, W.; Chapman, S.; McDermott, R.; Suckow, M. A.; Johnson, J. R.; Piwnica-Worms, D.; Gokel, G. W.; Smith, B. D.; Leevy, W. M. In Vivo Optical Imaging of Acute Cell Death Using a Near-Infrared Fluorescent Zinc−Dipicolylamine Probe. *Mol. Pharm.* **2011**, *8* (2), 583–590. https://doi.org/10.1021/mp100395u.

(92) Smith, B. A.; Xiao, S.; Wolter, W.; Wheeler, J.; Suckow, M. A.; Smith, B. D. In Vivo Targeting of Cell Death Using a Synthetic Fluorescent Molecular Probe. *Apoptosis* **2011**, *16* (7), 722–731. https://doi.org/10.1007/s10495-011-0601-5.

(93) Smith, B. A.; Xie, B.-W.; Van Beek, E. R.; Que, I.; Blankevoort, V.; Xiao, S.; Cole, E. L.; Hoehn, M.; Kaijzel, E. L.; Löwik, C. W. G. M.; Smith, B. D. Multicolor Fluorescence Imaging of Traumatic Brain Injury in a Cryolesion Mouse Model. *ACS Chem. Neurosci.* **2012**, *3* (7), 530–537. https://doi.org/10.1021/cn3000197.

(94) Usama, S. M.; Park, G. K.; Nomura, S.; Baek, Y.; Choi, H. S.; Burgess, K. Role of Albumin in Accumulation and Persistence of Tumor-Seeking Cyanine Dyes. *Bioconjug. Chem.* **2020**, *31* (2), 248–259. https://doi.org/10.1021/acs.bioconjchem.9b00771.

(95) Thavornpradit, S.; Usama, S. M.; Lin, C.-M.; Burgess, K. Protein Labelling and Albumin Binding Characteristics of the Near-IR Cy7 Fluorophore, QuatCy. *Org. Biomol. Chem.* **2019**, *17* (30), 7150–7154. https://doi.org/10.1039/C9OB01184F.

Chapter 2 : A Tetrazine-Derived Near-Infrared Dye for Targeted Photoacoustic Imaging of Bone

Rowan Swann[†], Samantha Slikboer[†], Afaf Genady [†], Luis Rafael Silva[†], Nancy Janzen[†], Amber Faraday[†], John F. Valliant[†], & Saman Sadeghi[†,*]

[†] Department of Chemistry and Chemical Biology, McMaster University, Hamilton, Ontario, L8S 4L8, Canada

Manuscript Published in ACS Journal of Medicinal Chemistry
DOI: 10.1021/acs.jmedchem.2c01685

2.1 Introduction:

Molecular imaging of bone diseases and injuries such as cancer and microfractures, which are not evident on X-ray or CT, is principally performed using nuclear medicine techniques employing radiolabeled bisphosphonates (BPs).[1,2] Optical imaging has been explored as a means to eliminate the use of ionizing radiation and to improve resolution, particularly for microfractures. While BP-derived fluorescent probes have shown promise, limitations in depth resolution remain a key challenge.[3–7]

Photoacoustic imaging (PAI) is based on the photoacoustic (PA) effect, where acoustic waves are generated through a molecule's thermal expansion and contraction after pulsed light absorption.[8] As compared with fluorescence imaging, PAI has a similar degree of sensitivity; however, the reduced scattering of acoustic waves in tissue facilitates high-resolution acquisition at increased imaging depths.[9] In addition to the anatomical mapping capabilities of ultrasound (US) in dual-mode US-PA systems, which contextualize signal locations, PA spectral unmixing algorithms enable visualization of target-specific signal in complicated biological matrices and simultaneous detection of multiple chromophores.[10]

Reported clinical applications of PAI have largely focused on the use of 'label-free' imaging to characterize disease pathology,[8,11–13] where endogenous PA-active biomolecules, such

as melanin,[14] oxygenated and deoxygenated hemoglobin,[15] and lipids,[16] provide functional information related to disease states without introducing exogenous contrast. However, exogenous PA imaging probes (PIPs) have gained recognition as they facilitate the detection of biological entities that do not possess intrinsic light absorption properties.[12,17,18] Small molecule dyes, due to their commercial availability, easily functionalized structures, and biocompatibility, provide opportunities to create targeted PA contrast and recent examples have demonstrated the application of PAI for bacterial infection and various cancers.[9,18–24]

Literature reported on PAI of bone and related diseases has predominantly consisted of endogenous contrast or passive targeting strategies, such as the enhanced permeability and retention (EPR) effect.[3,25–27] PA monitoring of an exogenous agent, tailored to accumulate at sites of bone injury, could provide high-resolution PA images and have widespread utility in diagnostic medicine. To this end, *trans*-cyclooctene-bisphosphonate (TCOBP), a compound previously demonstrated to localize diagnostic radio-tracers to the bone,[28] was coupled to a tetrazine (Tz)-derived cyanine dye and evaluated for targeted PAI of bone. The photophysical characteristics, PA signal generation properties, and the feasibility of PA signal unmixing from endogenous blood chromophores were assessed. BP-specific hydroxyapatite (HA) binding was evaluated *in vitro* and preclinical validation using local intrafemoral (IF) injection and intravenous (IV) active and pre-targeting strategies, were performed to demonstrate the PIP's ability to localize to the bone with detectable, spectrally verified, *in vivo* PA signal.

2.2 Results & Discussion:

2.2.1 Synthesis & Characterization

A novel Tz-derivative of the cyanine dye IR783 was developed using a two-step synthesis and later conjugated to TCOBP. Commercially available dye IR783 (**2-1**) was coupled to 4-carboxyphenyl boronic acid (**2-2**) via the Suzuki-Miyaura reaction to produce IR783-carboxylic acid (**2-3**, **Scheme 2.1**) in 65% yield. The coupling of **2-3** with tetrazine-amine (**2-4**), using benzotriazole-1-yl-oxytripyrrolidinophosphonium hexafluorophosphate (PyBOP) was carried out, yielding IR783-tetrazine (**2-5**) as a green solid (62%) (**Scheme 2.1**). Compounds **2-3** and **2-5** were fully characterized by HPLC, HRMS, and ^{1}H- and ^{13}C- NMR (**Figure AI-1-8**). Using TCOBP (**2-6**) described by Yazdani *et al*.,[28] the bone-targeted PIP (**2-7**) was synthesized via the inverse electron demand Diels-Alder (IEDDA) reaction between **2-5** and a 3.3× molar excess of **2-6** (**Scheme 2.1**) and the product was confirmed through HPLC and HRMS (**Figure AI-9-10**). The expected formation of multiple IEDDA-products, 4,5-dihyrdopyridazine, 1,4-dihydropyridizine, and pyridazine (**Scheme AI-1**), was evident in the HPLC trace between 6-8 minutes, which is consistent with other comparable Tz-TCO reactions.[29] Previous studies with radiolabeled bisphosphonates, where the ligand is present in large excess, have demonstrated that HA binding sites will not be saturated.[30] Therefore, similar to previous reports, the molar excess of **2-6** was not separated from the desired product.[28,31]

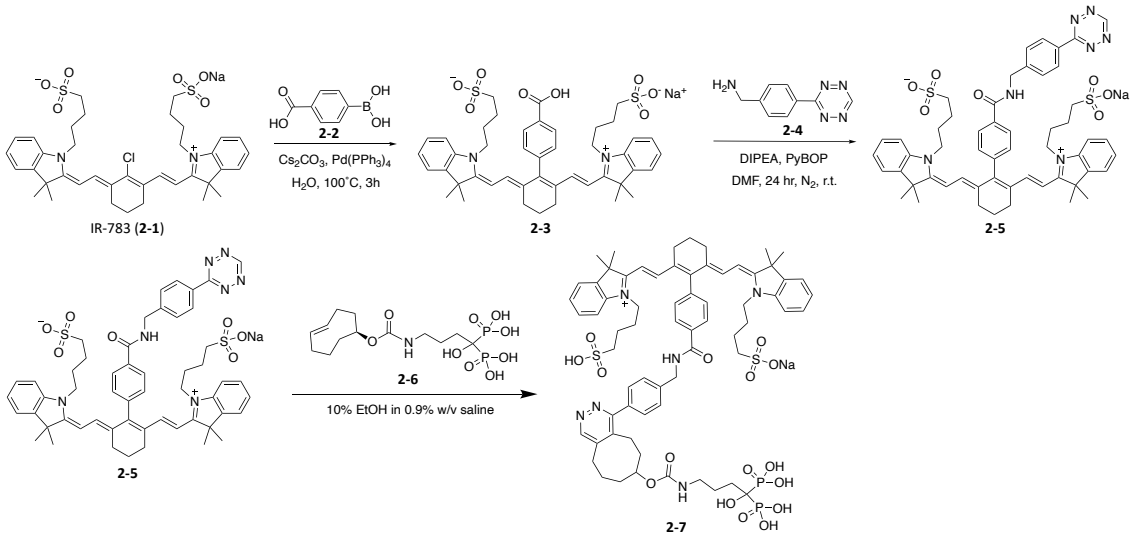

Scheme 2.1. Synthesis of 2-3, 2-5, and 2-7 from commercially available IR783 (2-1).

2.2.2 Photophysical Characterizations of 2-5 & 2-7

The photophysical properties of **2-5** and **2-7** were characterized through the assessment of absorbance and emission spectra, PA signal, quantum yield, molar absorptivity and relative brightness (**Figure 2.1**). The absorbance and PA spectra of **2-5** and **2-7** in **Figure 2.1 (a-d)** show the presence of both monomeric ($\lambda_{max} \cong$ 760-770 nm) and dimeric dye species ($\lambda_{max} \cong$ 690-700 nm). The distinct absorbance peak in the near-infrared (NIR) region can distinguish **2-5** and **2-7** from endogenous chromophores while remaining compatible with commercially available PAI lasers, which operate in the range of 680-970 nm.

The pertinent photophysical properties of **2-5** and **2-7** are summarized in **Table 2.1**. A biocompatible solvent of ten percent (10 %) ethanol in saline was used in all measurements, except when calculating the fluorescence quantum yield where methanol was used to allow for a direct comparison to the literature value found for IR783.[32] Decreases in the molar absorptivity were observed for **2-5** and **2-7** compared to **2-1**, but still fell in the expected range for heptamethine cyanine dyes.[33] The low fluorescence quantum yields indicate that a large portion of the absorbed

energy is converted to thermal or vibrational energy upon relaxation, which is ideal for PA signal generation.[34] Despite possessing a tendency to aggregate in aqueous media, the addition of the BP did not prevent the dye from generating a PA signal.

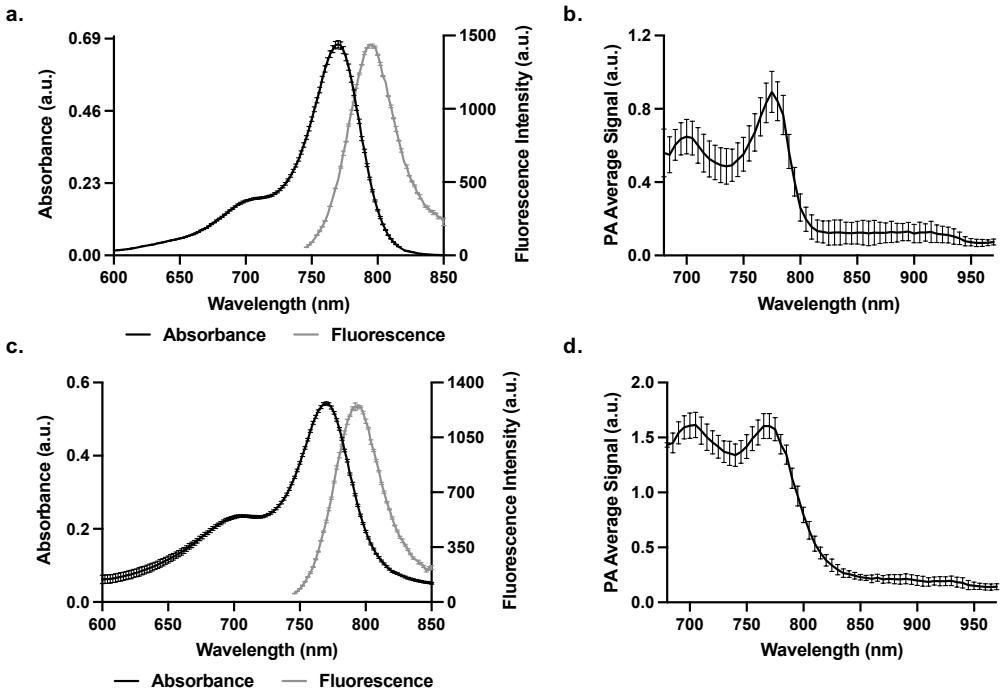

Figure 2.1. Spectral characterization of **2-5** and **2-7**: **a.** Absorbance & emissions spectra of **2-5** (5 μM) in methanol, $\boldsymbol{\lambda_{exc}}$= 736 nm. **b**. PA spectrum of **2-5** (50 μM) in 10% ethanol in saline. **c**. Absorbance & emissions spectra of **2-7** (5 μM) in methanol, $\boldsymbol{\lambda_{exc}}$= 736 nm. **d.** PA spectrum of **2-7** (50 μM) in 10% ethanol in saline. Data were collected in triplicate.

Table 2.1. Photophysical characteristics comparison of **2-1**, **2-5**, & **2-7**.

Construct	Solvent	PA λ_{max} (nm)	Absorbance λ_{max} (nm)	Emission λ_{max} (nm)	Fluorescent Quantum Yield (φ_f)	Molar Absorptivity (ε) ($cm^{-1}M^{-1}$)
2-1	Methanol	760	783	808	0.084*	282 200*
2-5	Methanol	770	766	788	0.055	173 400
	10% Ethanol in Saline	770	760	780	-	-
2-7	Methanol	770	762	786	0.014	150 133
	10% Ethanol in Saline	770	762	778	-	-

*Data derived from James, *et al*., 2013.[32]

The absorbance and PA spectra of the dyes dissolved in 10% ethanol in saline were acquired to characterize the signal at various concentrations (**Figure 2.2a,c** for **2-7**, **Figure AI-11a,c** for **2-5**). Absorbance at 770 nm was used to quantify concentration (**Figure 2.2b** for **2-7**, **Figure AI-12b** for **2-5**). Spectral analysis, where the PA signal is mapped as a function of wavelength ('Spectro scans', as outlined in the 'phantom photoacoustic imaging' section of the methods and materials), was used to characterize the spectral signature of the compounds and multiwavelength unmixing scans were used to quantify the PA signal (**Figure 2.2d** and **AI-12b,d** for **2-7**, **Figure AI-11d** and **AI-12a,c** for **2-5**). Using **Equation AI-3** (Appendix I), the limits of detection for the PA signal from **2-5** and **2-7** were calculated to be 2.5 and 5 µM, respectively. The corresponding PA images depict the change in visual intensity over the concentration series (**Figure 2.2e** for **2-7**, **Figure AI-11e** for **2-5**).

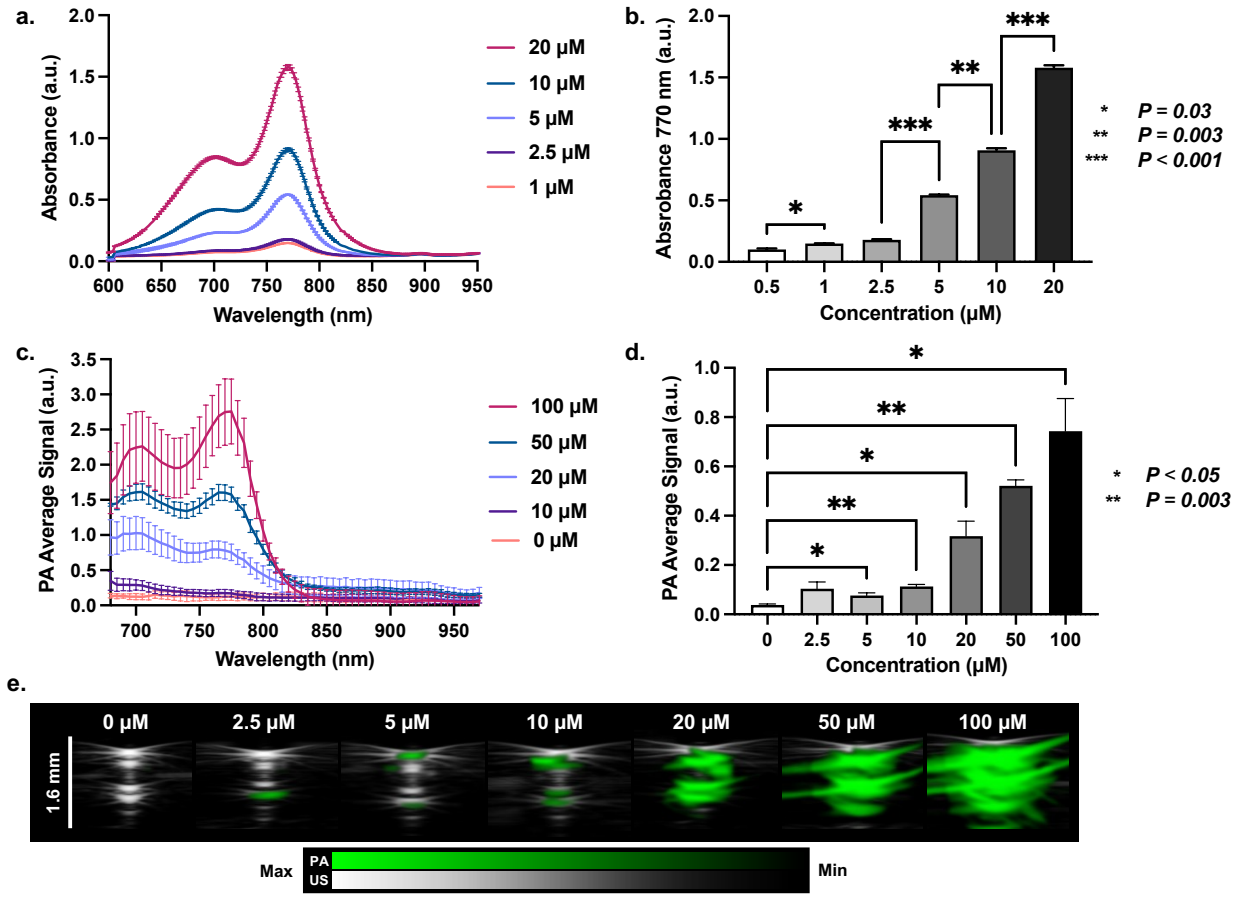

Figure 2.2. Absorbance & photoacoustic signal analysis of **2-7** in 10% ethanol in saline, as a function of concentration: **a**. Absorbance spectra of **2-7. b**. Absorbance intensity of **2-7** at 770 nm. **c**. PA spectra of **2-7**. **d**. PA average signal of **2-7** at 770 nm at each concentration. **e**. Corresponding PA images of **2-7** in a PA phantom.

To assess the ability to detect the modified dyes *in vivo*, the PA signal from **2-5** and **2-7** in murine blood (i.e., in the presence of oxygenated and deoxygenated hemoglobin) was measured. While there was some overlap of the signals with deoxyhemoglobin, the overlaid spectra of **2-5** and **2-7** (**Figure 2.3a**) with blood chromophores depict a unique maximum for the dyes (770 nm) compared to deoxyhemoglobin (760 nm). To assess whether signal unmixing was feasible, the PA signal from different concentrations of the dye in blood was analyzed and the unmixed signals of **2-5** and **2-7** from oxygenated and deoxygenated hemoglobin were quantified (**Figure 2.3b** and **AI-14b,d** for **2-7**, **Figure AI-13a** and **AI-14a,b** for **2-5**). The corresponding PA images of the samples (**Figure 2.3c** for **2-7**, **Figure AI-13b** for **2-5**) depict the change in intensity over the concentration series and the limits of detection (using **Equation AI-3**) were calculated to be 35 µM and 18 µM for **2-5** and **2-7**, respectively.

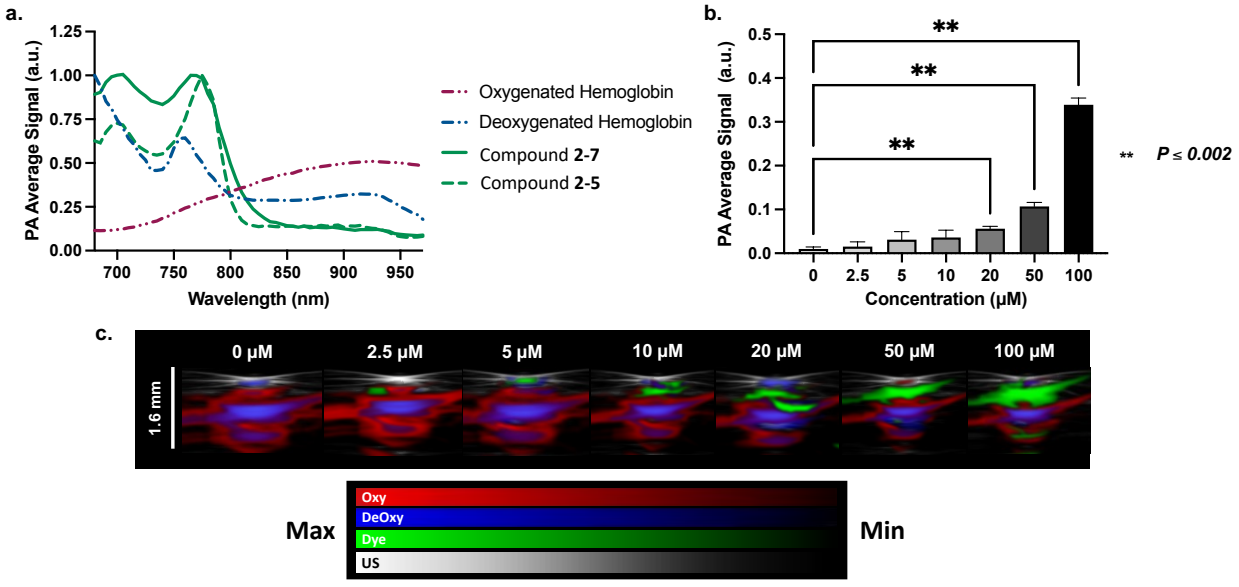

Figure 2.3. Photoacoustic signal analysis of **2-7** in whole murine blood: **a**. Normalized PA spectra of **2-5** and **2-7** (50 µM in 10% ethanol in saline) overlaid with the spectra of blood chromophores;

oxygenated and deoxygenated hemoglobin. **b**. Analysis of the PA average signal of **2-7** unmixed from blood, as a function of concentration. **c**. Corresponding unmixed PA images of the samples in the PA phantom. Red= oxygenated hemoglobin, blue= deoxygenated hemoglobin, green= **2-7**.

2.2.3 Hydroxyapatite (HA) Binding Assay

BPs are widely recognized for their high affinity to HA; a calcium-containing mineral present during bone remodelling and at sites of pathological calcification.[1,35] An established *in vitro* binding assay was used to evaluate the ability of the dyes to bind HA in the presence or absence of the BP targeting vector, where both active and pre-targeting strategies were tested.[36] Absorbance measurements of the supernatant were taken after incubation with HA and were used to calculate the percent binding through comparison with the supernatant of a control sample without HA (**Equation AI-4**). In contrast to the low percent binding exhibited by the non-targeted dye, **2-5** (1 ± 1%), the pre-coupled, actively targeted dye, **2-7**, demonstrated significant BP-specific binding (62 ± 6 %, P= 0.005) (**Figure 2.4a**). Similarly, a high percentage of BP-specific binding was observed using the pre-targeting approach (55 ± 3%, where P< 0.001), where the addition of **2-5** took place 1 hour after incubation of the HA with **2-6**, to form **2-7** *in vitro* (**Figure 2.4a**).

To further demonstrate the interaction between HA and the BP-conjugates, the HA pellets were collected and washed from the described samples, and PA images were taken of the resuspended pellets (**Figure 2.4b**,**c**). There were no significant differences between the HA pellets incubated with the vehicle control (50 mM Tris buffer with HA) (0.44 ± 0.2 a.u.) and **2-5** (0.29 ± 0.04 a.u.), but significant increases in PA signal on the HA pellets were observed when active (6.23 ± 0.3 a.u., P= 0.02) and pre-targeting (5.57 ± 1.7 a.u., where P< 0.001) strategies were used (**Figure 2.4b**).

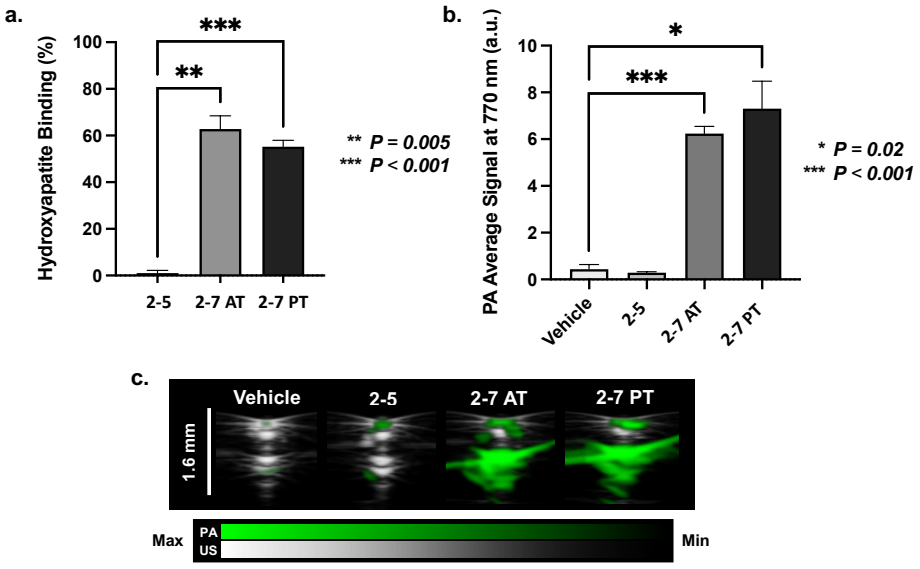

Figure 2.4. Data from a hydroxyapatite binding assay involving **2-5** and **2-7**: **a**. Percent binding of the dyes to HA, based on absorbance maximum ($\boldsymbol{\lambda_{max}}$= 770 nm) of the supernatant. **b**. PA average signal of the washed HA pellet at $\boldsymbol{\lambda_{max}}$= 770 nm. **c**. Corresponding PA images of the suspended pellets in PA phantom. (AT: actively targeted, PT: pre-targeted). Vehicle = Tris Buffer.

2.2.4 Photoacoustic Imaging of Bone using an Intrafemorally Administered Active Targeting Approach

Bone tissue is under constant reconstruction to regulate blood mineral concentrations and remodel bones during periods of growth.[30] As a result, the mineral HA is largely available on bone, and notably around highly strained joints, such as the knee, enabling the use of healthy mice as an *in vivo* model to verify target affinity. Prior to IV injection, IF injection was used to assess the ability of the modified dyes to bind to and be retained at the bone *in vivo*, while eliminating the pharmacokinetic variables associated with IV administration.

Throughout each *in vivo* imaging study, 3D multiwavelength unmixing scans and Spectro scans were performed, as outlined in the '*in vivo* photoacoustic imaging studies' section of the methods and materials. Multiwavelength unmixing scans are used for 3D image rendering while

Spectro scans are used to generate spectral plots for secondary verification that the PA signal originating from the bone matches that of the expected signature of the dye.

3D multiwavelength unmixing scans were acquired pre-injection, to establish background signal, and at 4-, 24-, and 48-hours post-injection (h P.I.), as well as *ex vivo*, following IF administration of **2-5** or **2-7** (**Figure 2.5a**) *In vivo* spectral analysis was performed pre-injection and at 24 h P.I. (**Figure 2.5b,c**). Finally, the spectrally unmixed signals of **2-5** and **2-7**, from the 3D multiwavelength unmixing scans were quantified using 3D regions of interest (ROI) drawn over the femur and joint (**Figure 2.5d**) (see **Figure AI-15** for an example of the 3D ROIs used).

No significant differences were observed between the signal intensities, or the spectral signatures acquired from the pre-and post-injection scans of mice treated with **2-5** (**Figure 2.5a-c**). Meanwhile, significant differences in the PA average signals were observed between pre-injection (0.020 ± 0.003 a.u.), 4 h P.I. (0.23 ± 0.11 a.u., where $P \leq 0.03$ compared to pre-injection signal) and 24 h P.I. (0.27 ± 0.09 a.u., where $P \leq 0.006$ compared to pre-injection signal) of the mice treated with **2-7**. A spectral signature, matching that of **2-7** was acquired 24 h P.I., which verified the detected PA signal. The differences in mice treated with **2-5** (0.04 ± 0.01 a.u. at 4 h P.I., and 0.03 ± 0.01 a.u. at 24 h P.I.) and **2-7** (0.23 ± 0.11 a.u at 4 h P.I., and 0.27 ± 0.09 a.u. at 24 h P.I.) were significant with $P \leq 0.03$ and $P \leq 0.006$ at 4 and 24 h P.I. respectively. The PA signal of **2-7** at 48 h P.I. (0.16 ± 0.08 a.u.) was no longer found to be statistically significant compared with the pre-injection scan or with mice treated with **2-5**, likely due to wash-out of the dye. The specificity of the bone-targeted dye **2-7** compared to its non-targeted counterpart **2-5** was demonstrated through the spectrally verified PA signal observed in **Figure 2.5a-c**, and after quantitative analysis of the signal (**Figure 2.5d**). The results indicated that a wash-out of **2-5** likely

took place before the 4 h imaging time point while the retention of **2-7** was quantitatively maintained out to 24 h P.I., after which, a drop in the PA signal was observed 48 h P.I.

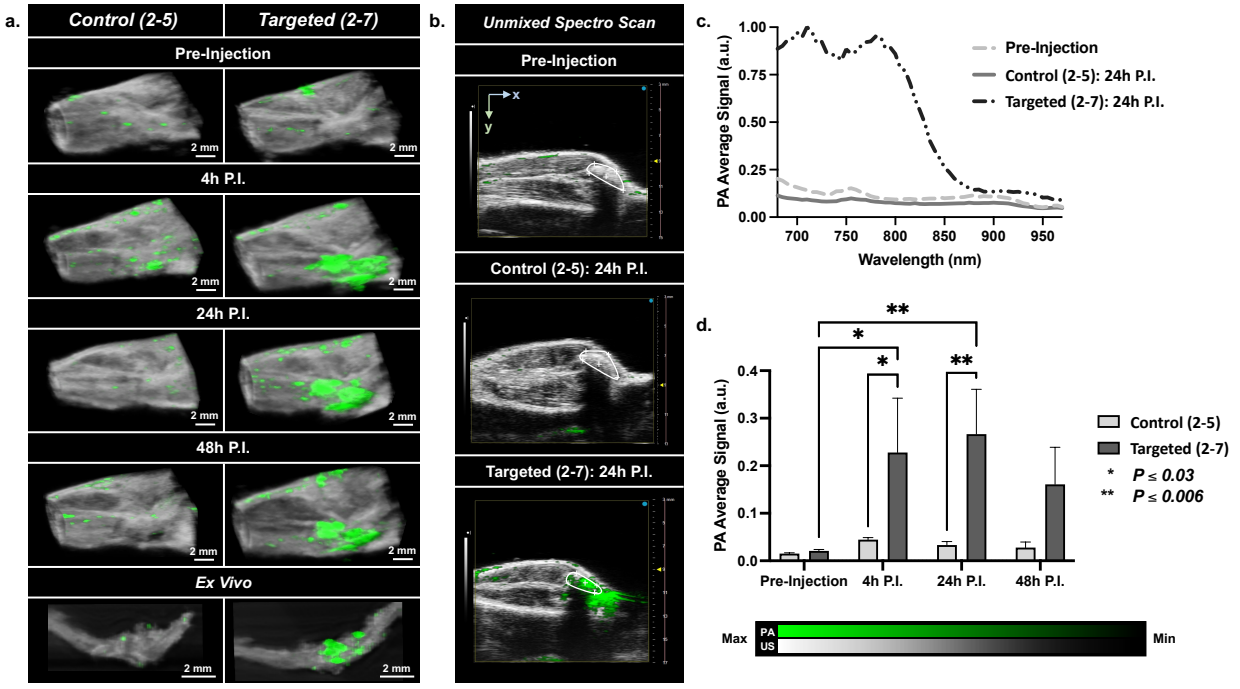

Figure 2.5. Photoacoustic imaging of bone using an intrafemorally (IF) administered active targeting approach: **a**. Representative PA multispectral unmixing images (*in vivo* pre-injection, 4-, 24-, and 48-hours post-injection, and *ex vivo*) of mice injected IF with non-targeted dye **2-5** (control) or targeted dye **2-7**. **b-c**. Spectral analysis of the knee/epiphysis of the femur of treated mice, pre-injection & 24 hours post-injection. ROIs drawn over the bone (white) in the unmixed Spectro scans in **b** indicate the signal from which the spectral curves in **c** were derived. **d**. Bar graph representing the quantified 3D PA average signal within the bone of the mice throughout the study. For all multiwavelength unmixing scans, greyscale= US images overlaid with unmixed PA signal, where green= **2-5** or **2-7**. The signals from oxygenated and deoxygenated hemoglobin have been subtracted from each image.

2.2.5 Photoacoustic Imaging of Bone Using a Systemic, Active Targeting Approach

To determine whether active bone-targeting of the dye could be achieved through systemic circulation, the control dye **2-5** and bone-targeted dye **2-7** were administered IV and photoacoustic analysis of the bone was carried out 4 h P.I. (**Figure 2.6**). Although a non-negligible PA signal was present in the scans of mice treated with **2-5**, above the background signal (0.05 ± 0.01 a.u., and 0.02 ± 0.01 a.u., respectively, where $P \leq 0.03$), the signal detected in mice treated with **2-7** was

found to be statistically significant above both background and the control group (0.18 ± 0.02 a.u., where $P < 0.001$ and $P < 0.0001$, respectively). *Ex vivo* images (**Figure 2.6a**) demonstrated a difference in the signal intensity between the groups and confirmed that **2-7** had localized to the bone. The spectral signature of the *in vivo* signal (**Figure 2.6b-c**) was found to match the expected spectral signature of the exogenous dye in the mice treated with **2-7**, while the signal in the control scans matched the background signal. The non-specific signal was likely due to residually circulating dye and demonstrated the ability of the BP-bound dye to localize to bone and bind to HA, following systemic circulation.

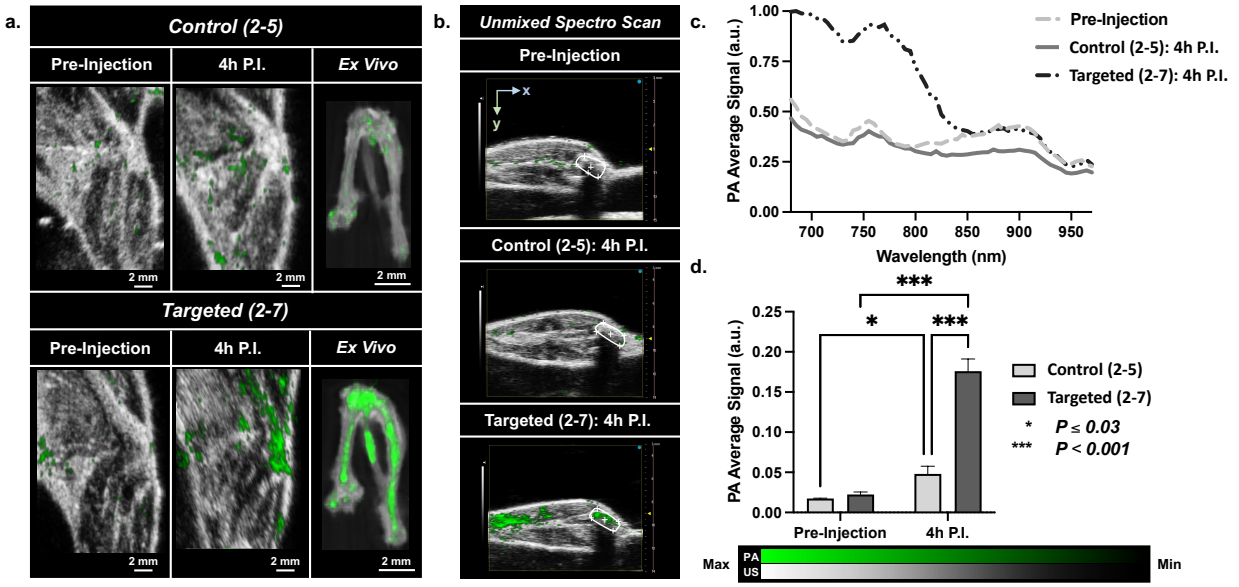

Figure 2.6. Photoacoustic imaging of bone using a systemic, active targeting approach: **a**. Representative PA multispectral unmixing images (*in vivo* pre-injection, 4 hours post-injection, and *ex vivo*) of mice injected IV with non-targeted dye **2-5** (control) or targeted dye **2-7**. **b-c**. Spectral analysis of the knee/epiphysis of the femur of treated mice, pre-injection & 4 hours post-injection. ROIs drawn over the bone (white) in the unmixed Spectro scans in **b** indicate the signal from which the spectral curves in **c** were derived. **d**. Bar graph representing the quantified 3D PA average signal within the bone of the mice throughout the study. For all multiwavelength unmixing scans, greyscale= US images overlaid with unmixed PA signal, where green= **2-5** or **2-7** and signals from oxygenated and deoxygenated hemoglobin have been subtracted from each image.

2.2.6 Photoacoustic Imaging of Bone using a Systemic, Pre-Targeting Approach

The design of the probe incorporated Tz and TCO moieties, a bioorthogonal coupling pair that has been well characterized in the literature and used for *in vivo* pre-targeting.[37–39] In this approach, a diagnostic probe is administered at a pre-determined time after administration of a targeting vector, and the components are allowed to couple *in vivo*.

While BPs have been generally recognized as safe drugs, following routine clinical use, acute liver damage has been reported on several occasions.[40–44] Pharmacokinetic changes due to structural alterations to BPs can result in increased off-target organ and liver uptake. In a previous report that employed a functionalized tetrazine coupled to **2-6** for active bone targeting, an increased propensity for particulate formation was observed, which resulted in higher liver, spleen, and lung uptake of the actively targeted probe.[45] However, it was observed that pre-targeting the probe led to a reduction in uptake for these organs. The tendency for heptamethine cyanine dyes to aggregate in aqueous media, leading to liver accumulations, has been well discussed in the literature.[46,47] A solubility analysis, utilizing absorbance spectra of **2-5** and **2-7** at an extended concentration of 100 μM, demonstrated an increase in aggregate formation (675 nm) of the dye after the addition of **2-6** (**Figure AI-16**). Avoiding particulate formation using a pre-targeting strategy became a compelling alternative for PA bone imaging, without increasing the potential for liver accumulation and toxicity. Previous reports have demonstrated that after 1 hour, ^{99m}Tc-labeled **2-6** was predominantly cleared from the blood and significant uptake of the tracer was achieved in the bone.[28] The interval between the injection of the targeting vector (either vehicle control or **2-6**) and the PA dye (**2-5**) was therefore maintained at 1 hour.

Mice were split into a non-targeted control group and a pre-targeting group, where saline or **2-6**, respectively, were administered IV 1 h before the injection of **2-5**. *In vivo* and *ex vivo*

photoacoustic analysis was carried out pre-injection, to establish a background signal, and at 4 h P.I. of IV-administered **2-5** (**Figure 2.7a-c**). Signal quantification (**Figure 2.7d**) showed that a statistically significant signal, above background (0.026 ± 0.002 a.u.), was observed in the control group (0.058 ± 0.004 a.u., where $P = 0.02$) and the pre-targeting group 4 h P.I. (0.102 ± 0.011 a.u., where $P < 0.001$). The signal present in the pre-targeting group remained significantly higher in comparison to the control group (where $P = 0.001$) at 4 h P.I. At 24 h P.I. the non-targeted control (0.036 ± 0.005 a.u.) was found to be insignificant with respect to the background signal, meanwhile, the significant signal in the pre-targeting group was retained (0.073 ± 0.009 a.u., where $P < 0.001$). *Ex vivo* analysis of the bone supported these findings, and the spectral signature of the *in vivo* signal (**Figure 2.7b-c**) was found to match the expected spectral signature of the exogenous dye in the pre-targeting group at both time points P.I., while the signal in the control group did not differ from the pre-injection background signal by 24 h P.I. The significant differences in the quantified PA signal of the pre-targeting group compared to the background and control group demonstrated the maintained bioorthogonal reaction post-target binding of **2-6** and post-*in vivo* circulation of **2-5**.

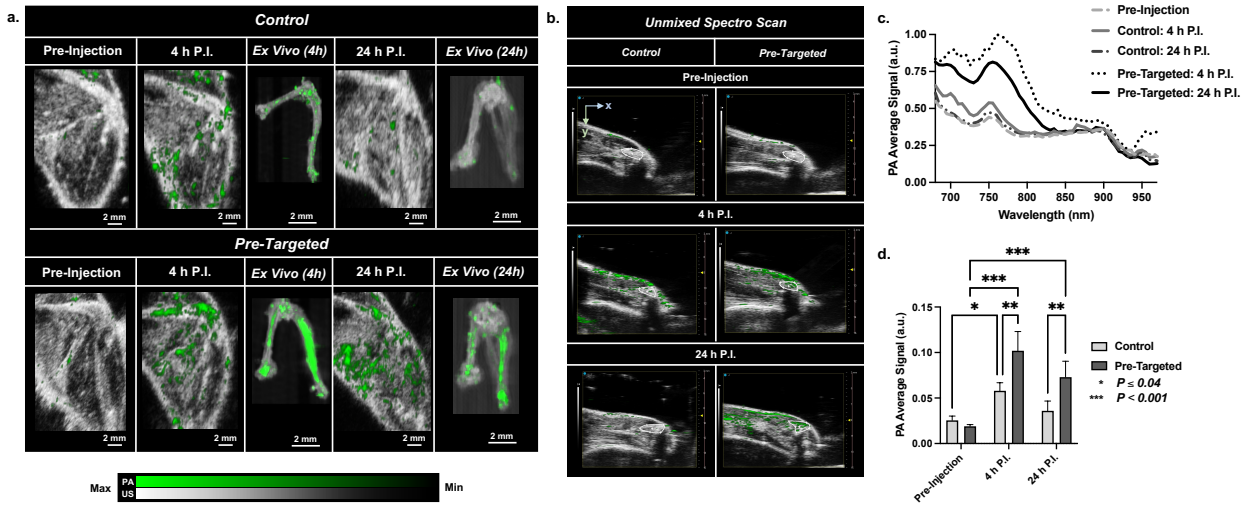

Figure 2.7. Photoacoustic imaging of bone using a systemic, pre-targeting approach: **a**. Representative PA multispectral unmixing images (*in vivo* pre-injection, 4 h P.I., 24 h P.I., and *ex vivo*) of mice injected IV with dye **2-5**. The dye was delivered to the bone using a pre-targeting approach where sterile saline (control group) or **2-6** (pre-targeted group), were injected 1 hour before injection of **2-5**. **b-c**. Spectral analysis of the knee/epiphysis of the femur of treated mice, pre-injection, 4 and 24 h P.I. of **2-5**. ROIs drawn over the bone (white) in the unmixed Spectro scans in **b** indicate the signal from which the spectral curves in **c** were derived. **d**. Bar graph representing the quantified 3D PA average signal within the bone of the mice throughout the study. For all multiwavelength unmixing scans, greyscale= US images overlaid with unmixed PA signal, where green= **2-5**. The signals from oxygenated and deoxygenated hemoglobin have been subtracted from each image.

2.3 Conclusion:

Compound **2-5** is a new near-infrared dye that can be readily derivatized with a BP using the highly efficient reaction between tetrazine and *trans*-cyclooctene. The photophysical properties and PA signal analysis of **2-5** and the BP-conjugate, **2-7**, were suitable for both *in vitro* and *in vivo* PAI. The ability of **2-7** to bind HA compared to **2-5**, was demonstrated *in vitro* using both active and pre-targeting approaches. Subsequently, three different injection strategies were employed to assess the ability of the probe to localize and be retained at sites of active bone metabolism *in vivo*. IF injections demonstrated the specificity of the probe towards bone by showing retention of **2-7** out to 24 h P.I. and washout of **2-5** dye by 4 h P.I. Previous therapeutic studies have been reported on light-assisted phototherapies for bone.[48] Anchoring BP-derived dyes, such as **2-7**, to bone/joint through I.F, or intraarticular injections could provide an approach to administering high concentrations of photothermally active dyes to the bone for therapeutic purposes. Further *in vivo* studies demonstrated IV active and pre-targeting approaches could be used to deliver the dye to regions of active bone turnover for non-invasive imaging. While active targeting resulted in higher bone uptake at 4 h P.I., both active and pre-targeting exhibited significant uptake and retention of the targeted dyes at the bone, where high-intensity contrast was achieved for imaging. Spectral analysis of the observed *in vivo* signal in the knee joint/femur further confirmed the presence of

dye within the bone. Further optimization of the pre-targeting strategy may be possible by adjusting the ratio of tetrazine to TCO compounds, exploring additional time points, and alternative diene and dienophile coupling partners with increased reactivity.[29] To the best of our knowledge, this study is one of the first reports on the use of *in vivo* bioorthogonal chemistry towards pre-targeting a PIP, which could have wide-ranging applications in PAI to mitigate aggregation tendencies of directly functionalized small molecule dyes. The results warrant further studies to assess osseous diseases, including cancer and osteomyelitis, in non-rodent mammalian species.

2.4 Methods & Materials:

General Materials, Instrumentation, & Methods. Unless otherwise noted, all reagents and solvents were ACS grade, purchased from commercial suppliers, and used without further purification. CHT™ Ceramic Hydroxyapatite Type 1 (1570020) was purchased from BioRad. (E)-Cyclooct-4-enyl-2,5-dioxopyrrolidin-1-yl-carbonate (TCO-NHS) and 4-(1,2,4,5-tetrazine-3-yl)phenyl)methanamine hydrochloride (**2-4**) were purchased from Conju-Probe (San Diego, CA). TCOBP (**2-6**) was prepared according to literature methods. Distilled water was used for all experiments requiring the use of water. Deuterated solvents for NMR samples were purchased from Cambridge Isotope Laboratories. All compounds are > 95% pure by HPLC analysis.

Nuclear magnetic resonance (NMR) spectra (^{1}H, ^{13}C) were recorded on a Bruker AV600 MHz spectrometer at ambient temperature. Mass spectrometry analyses were provided by the McMaster Regional Center for Mass Spectrometry on an Agilent 6340 Ion Trap LC/MS mass spectrometer operating in electrospray ionization (ES) mode. High-resolution mass spectrometry (HRMS) was collected on a Waters/Micromass Q-Tof Global Ultima spectrometer. Melting points were analyzed on DigiMelt, SRS (MPQ160) Apparatus. Absorbance and fluorescence scans were collected on a Tecan Infinite M1000 plate reader using Corning 96-well black, clear bottom plates (non-treated surface) (Corning 3631). High-performance liquid chromatography (HPLC) was

performed on a Waters Autopurification SFO Binary HPLC system connected to a 2998 photodiode array detector monitoring at 700 nm. Analytical HPLC was performed using an XSelect CSH C18, 5 µm column, operating at a flow rate of 1 mL/min. Solvents were evaporated using reduced pressure with a rotary evaporator. Compounds were dried using a VirTis Benchtop lyophilizer equipped with an Edwards RV5 pump. Unless otherwise stated, all flash chromatography purifications were carried out on a CombiFlash®Rf+.

HPLC Method A: Solvent A: Water + 0.1% formic acid (FA), Solvent B: Acetonitrile + 0.1% FA. 0-2 min 90% A, 2-5 min 90-40% A, 5-7 min 40% A, 7-13 min 40-20% A, 13-15 min 20% A.

CombiFlash®Rf+ Method A: Using the Prep HPLC Column: C18Aq Dimensions: 30 mm x 150 mm 5µm. Solvent A: Acetonitrile, Solvent B: Water. 1-10 min 100% B, 10-20 min 100-70% B, 20-30 min 70% B, 30-40 min 70-50% B, 40-50 min 50% B.

Synthesis of IR783-Carboxylic Acid (2-3): To a round bottom flask, equipped with a magnetic stir bar, commercially available IR-783 (**2-1**) (0.25 g, 0.33 mmol), 4-carboxyphenylboronic acid (**2-2**) (0.110 g, 0.66 mmol), cesium carbonate (0.055 g, 50 mol%), and Tetrakis(triphenylphosphine) palladium(0) (0.035 g, 8 mol%) were added and dissolved in 25 mL of water. The mixture was stirred under reflux (100˚C) for 4 hours then filtered through a pad of celite and washed with water. CombiFlash®Rf+ purification of the material (dissolved in 4 mL of water) was carried out using the CombiFlash®Rf+ Method A. 0.18 g of green solid (65% yield) was yielded after purification and subsequent lyophilization. mp. 196-198 ˚C. **HPLC** (method A, UV 700 nm) t_r= 14.8 min. **HRMS** (ESI^-) m/z calculated for $C_{45}H_{52}N_2O_8S_2$: 811.3103 $[M-H]^-$, found 811.3082, 405.151 $[M-2H]^{2-}$, found 405.1502. **^{1}H NMR** (600 MHz, CD_3OD) δ= 8.235 (d, J=6.84 Hz, 2H), 7.34 (dt, J=6.42, 0.84 Hz, 2H), 7.31 (t, J=6.84 Hz, 4H), 7.255 (d, J=6.72 Hz, 2H), 7.25 (d, J=12 Hz, 2H), 7.16 (t, J=13.08 Hz, 2H), 6.23 (d, J=12 Hz, 2H), 4.11 (t, J=5.88 Hz, 4H), 2.88 (t, J=6.18 Hz, 4H), 2.75 (t, J=5.22 Hz, 4H), 2.065 (q, J=5.34, 2H), 1.97-1.89 (m, 8H), 1.18 (s, 12H) ppm; **^{13}C NMR** (150 MHz, CD_3OD) δ= 173.5, 172.3, 167.5, 163.4, 159.7, 149.7, 143.9, 143.8, 142.4, 136.5, 134.3, 132.8, 131.3, 131.1, 131, 130.7, 129.9, 129.8, 128.1, 126.1, 123.5, 112, 101.2, 56, 52, 50.1, 49.7, 44.9, 44.2, 43.9, 28.1, 27.3, 25.8, 23.8, 22.7, 12.3 ppm.

Synthesis of IR783-Tz (2-5): To a dry microwave vial equipped with a magnetic stir bar, compound **2-3** (0.035 g, 0.042 mmol), PyBOP (0.048 g, 0.097 mmol) and *N,N*-diisopropylethylamine (DIPEA) (0.015 mL, 0.084 mmol) were added. The vial was capped, and a nitrogen atmosphere was induced. The mixture was dissolved in 2.5 mL of DMF. In a separate, dry microwave vial, tetrazine amine HCl salt (4-(1,2,4,5-Tetrazin-3-yl)phenyl)methanamine) (**2-4**) (0.013 g, 0.061 mmol) was added and dissolved in 2.5 mL of anhydrous DMF once the vial was capped and under nitrogen. Once fully dissolved, the tetrazine amine solution was added dropwise to the vial containing the reaction mixture. The reaction was shielded from light and left to stir at room temperature for 24 hours. The mixture was filtered through a pad of celite, washed with water, and the solvent was evaporated. CombiFlash®Rf+ purification of the material (dissolved in 2 mL of water) was carried out using the CombiFlash®Rf+ Method A. Upon lyophilization, 0.025 g of green solid was obtained (62% yield). mp. 171-173 ˚C. **HPLC** (method A, UV 700 nm) t_r= 14.9 min. **HRMS** (ESI^-) m/z calculated for $C_{54}H_{59}N_7O_7S_2$: 980.3798 $[M-H]^-$, found 980.3851. **^{1}H NMR** (600 MHz, CD_3OD) δ= 10.38 (s, 1H), 8.645 (dt, J=8.46, 1.74 Hz, 2H), 8.19 (d, J= 8.22 Hz, 2H), 7.725 (d, J=8.52 Hz, 2H), 7.405 (d, J=8.22 Hz, 2H), 7.34 (dt, J=7.95, 1.02 Hz, 2H), 7.32 (d, J=7.5 Hz, 2 H), 7.265 (d, J=7.92 Hz, 2H), 7.20 (d, J=14.04 Hz, 2H), 7.165 (t, J=7.44 Hz, 2H), 6.24 (d, J=13.98 Hz, 2H), 4.81 (s, 2H), 4.12 (t, J=6.9 Hz, 4H), 2.875 (t, J=7.32 Hz, 4H), 2.75 (t, J=5.94 Hz, 4H), 2.06 (q, J=5.88 Hz, 2H), 1.97-1.87 (m, 8H), 1.18 (s, 12H) ppm; **^{13}C NMR** (150 MHz, CD_3OD) δ=173.5, 169.2, 167.8, 162.5, 159.5, 149.4, 146.0, 144.7, 142.3, 135.4, 132.9, 132.6, 131.4, 129.9, 129.8, 129.6, 129.0, 126.2, 123.5, 112.1, 101.4, 52.0, 50.1, 50.0, 49.7, 44.9, 44.6, 28.2, 27.4, 25.8, 23.7, 22.7 ppm.

Synthesis of IR783-BP (2-7): A solution of **2-6** (3.3 molar equivalents) in 0.9% w/v saline was added to a solution of **5** (1 molar equivalent) in 10% ethanol/0.9% w/v saline. For each study, the material was reacted for a minimum of 1 hour before use and diluted to the desired concentration using 10% ethanol/0.9% w/v saline. Confirmation of product formation was carried out by HPLC and HRMS. **HPLC** (method A, UV 700 nm) t_r= 15 min. (**AI-9**) **HRMS** (ESI) m/z calculated for $C_{67}H_{84}N_6O_{16}P_2S_2$: 1353.4788 $[M-H]^-$, found 1353.4785, 676.2357 $[M-2H]^{2-}$, found 676.2351 (**AI-10**, 1375.4430 and 1398.4348 are the product with 1 or 2 sodium counter ions, respectively).

Absorption & Emission Spectra: Compounds **2-5** and **2-7** were formulated in 10% ethanol in 0.9% w/v saline to create stock solutions, from which various concentrations, including 0.5, 1, 2.5, 5, 10, and 20 μM, were prepared through dilution with the neat solvent. The samples, including neat solvent for blank subtraction, were aliquoted, in triplicate, into a 96 well plate and the absorption (600-950 nm) and emission (excitation at 736 nm, emission from 746-850 nm) spectra were collected on a Tecan Infinite M1000 plate reader. Absorption coefficients and quantum yields were calculated using procedures that can be found in **AI-1: Supporting Methods**.

Photoacoustic Phantom Imaging: PA phantom work was performed using a Vevo Phantom imaging chamber (see **Figure AI-17**) and the Vevo-3100/LAZR-X (FUJIFILM VisualSonics, Inc., Toronto, ON, Canada) imaging system equipped with a 680-970 nm laser. Samples were injected into Vevo Contrast Agent Phantom tubing (PN52807) that was threaded into the Vevo Phantom chamber. A 30 MHz, linear array US transducer equipped with integrated fibre optic cables (MX400 and LZ-400 [15-30 mJ $(cm^3)^{-1}$], FUJIFILM VisualSonics, Inc., Toronto, ON, Canada) was positioned overtop of the tubes.

Spectral analysis was performed using 'Spectro' scans, where the PA signal of a 2D, x,y-cross-section of a sample is quantified at each wavelength (690-970 nm) and is used to plot the spectral curve or 'spectral signature' from a defined ROI. From this, the signal intensity of the chromophore of interest can be quantified by the signal unmixing algorithm utilized in the VevoLAB software (VisualSonics, Inc., Toronto, ON, Canada). The 2D multispectral unmixing scans (oxygenated and deoxygenated hemoglobin unmixed from the spectra of **2-5** and **2-7**) were taken for each material in triplicate. Signals generated at 680, 700, 734, 778, 810, and 924 nm were utilized in the signal unmixing algorithm. Images from the multiwavelength unmixing scans have been displayed using the render mode with the PA signal overlaid on US B-mode (greyscale) signal of a cross-section of tubing. All image processing was carried out using the VevoLAB software. A ROI was drawn around the US image of the tube and, using ROIs of the same size and shape, a spectrum was generated from the overlaid PA signal. From the generated spectrum, the PA signal intensity was derived from each sample for analysis.

PA signal analysis of 2-5 and 2-7: Stock concentrations of **2-5** and **2-7** (1 mM, formulated in 10% ethanol in 0.9% w/v saline) were used to prepare various concentrations of material, including 2.5, 5, 10, 20, 50 and 100 μM, diluted using the specified solvent. A series of samples were also diluted using whole murine blood (mixed with 10% EDTA in PBS). To ensure the same level of interference from blood chromophores was maintained throughout the study, each concentration was prepared by adding the appropriate amount of stock solution and solvent to reach 20 μL. Solutions were then further diluted with 180 μL of blood. All concentrations and blank controls of the specified solvent and blood (180 μL diluted with 20 μL of solvent) were then analyzed on the Vevo-3100/LAZR-X.

Active & Pre-Targeting Hydroxyapatite Binding Assay: 1.24 mL of HA (1 mg mL^{-1}) in 50 mM Tris buffer (pH 6.9) was combined with 310 μL of **2-5** (100 μM in 1% Tween80 10% ethanol in 0.9% w/v saline) as a negative control, 39.8 μL of **2-6** (2.49 mM in 0.9% w/v saline) for pre-targeting, or **2-7** (100 μM in 1% Tween80 10% ethanol in 0.9% w/v saline) for active targeting. Negative controls consisting of each article in 50 mM Tris (pH 6.9) without the addition of HA were used. After 1 hour of agitation at room temperature, 310 μL of **2-5** (100 μM in 1% Tween80 10% ethanol in 0.9% w/v saline) was added to the vial of **2-6** and the sample was agitated at room temperature for an additional 1 hour. Each sample was then centrifuged at 10, 000 rpm for 5 mins to precipitate the HA. An aliquot (200 μL) of the supernatants was transferred to a 96-well plate and the absorbance at 770 nm was recorded. Each experiment was performed in triplicate and percent binding was calculated using **Equation AI-4**. Following analysis of the supernatant, the HA pellet was washed with 1 mL of buffer and resuspended in 1 mL of buffer and vortexed. An aliquot of the resuspended HA pellets was loaded into the phantom tubing that was threaded into the Vevo Phantom chamber and Spectro scans were taken in triplicate. Using the system's signal unmixing algorithm, the signal from the dye was quantified using ROIs of the same size.

Animal Studies: All procedures were conducted according to the guidelines of the Committee for Research and Ethics Issues of the International Association for the Study of Pain, and guidelines established by the Canadian Council on Animal Care and the McMaster University Animal Research Ethics Board. In each animal study 7-10 week-old female BALB/c mice (Charles River Laboratories, Raleigh, NC), weighing around 20 g, were used. The mice were sterile housed

and maintained at 21 ˚C with a 12-hour light/dark cycle and were provided autoclaved food and water *ad libitum*.

***In Vivo* Photoacoustic Imaging Studies:** PAI was performed using the Vevo-3100/LAZR-X imaging system. Mice were anesthetized, and the fur of their right hindlimb was thoroughly removed before being placed in a prone position on a platform that enabled the monitoring of their respiration and heart rates. A generous amount of US gel was applied before imaging with the transducer (MX400/LX400) positioned overtop of the leg. Spectro scans and 3D multispectral unmixing scans of each right hindlimb were taken at each imaging time point. The transducer was positioned laterally overtop of the hindlimb, corresponding with the femur, knee, and fibula. Scan distances averaged 20 mm and scans were taken every 0.33 mm.

3D multiwavelength unmixing scans were performed to construct images depicting dye-specific PA signal present within the hindlimb. Designated wavelengths (680, 700, 734, 778, 810, and 924 nm), based on notable signals generated within individual chromophore spectra (oxygenated and deoxygenated hemoglobin, **2-5**, and **2-7**), were used by the Vevo-3100/LAZR-X unmixing algorithm. The series of 2D cross-sectional scans collected were then reconstructed by the instrument into a 3D image, where the signals from each chromophore are assigned a colour and overlaid onto a b-mode ultrasound scan. The scans are displayed as either render mode or texture mapping images where the PA signal is overlaid on US B-mode (greyscale) signal for sections of the hindlimb. Signals from oxygenated and deoxygenated hemoglobin were subtracted from the images to reduce visual complexity. All signal unmixing algorithms and image processing was carried out using the VevoLAB software. Image processing consisted of signal optimization, with parameters set the same for each image within the study. Images were displayed as 2D cross-sections of the 3D images or as 3D rendered maximum intensity projections. 3D regions of interest were drawn around the bone, guided by the intrinsic acoustic shadow created by bone in the US images, and were defined from below the knee to the upper portion of the femur (as depicted in **AI-16**). An approximate volume of 30 mm^3 was used for each measurement.

In vivo spectral analysis was performed using ‘Spectro’ scans (as described in the “Photoacoustic Phantom Imaging’ section) and was used to verify whether the spectral signature of the *in vivo* signal matched that of the exogenous dye. The US signal was used as a guide to define the ROI specifically around the bone. The ROI used for each spectral curve was displayed

in a multiwavelength unmixing scan (oxygenated and deoxygenated hemoglobin unmixed from **2-5** or **2-7**) derived from the Spectro scan.

Photoacoustic Imaging of Bone using an Intrafemorally (IF) Administered Active Targeting Approach: 10 healthy mice were imaged, as described in the section titled '*In Vivo* Photoacoustic Imaging Studies', on the Vevo-3100/LAZR X, pre-injection, 4-, 24- and 48-hours post-injection, and *ex vivo*. Following a procedure outlined by Yazdani, *et al*.[49], mice were injected intrafemorally with 5 µL of **2-5** (0.25 mM) or **2-7** (which was prepared 1 h prior to injection by mixing 0.25 mM **2-5** with 3.74 mM of **2-6**) formulated in 10% ethanol/0.9% w/v saline. To detail, mice were anesthetized by isoflurane inhalation and injected subcutaneously with analgesic (Temgesic 0.1 mg kg^{-1}, McMaster University Central Animal Facility). Mice were laid supine with the ipsilateral stifle joint bent at 90° to provide clearance of the patella. A 26-gauge needle was then inserted between the medial and lateral condyles of the distal epiphysis parallel to the longitudinal axis of the femur to penetrate the cortical bone and enter the epiphysis. The dye solution was injected over 30 seconds. To mitigate post-surgery pain, 0.1 mg kg^{-1} Temgesic was administered every 12 hours for the course of the study. Animals tolerated surgery and administration of the PIPs well and no observable changes in behaviour or weight were noted throughout the study. *Ex vivo* images of the bone were taken using a phantom chamber.

Photoacoustic Imaging of Bone using a Systemic, Active Targeting Approach: 6 mice were imaged, as described in the section titled '*In Vivo* Photoacoustic Imaging Studies', on the Vevo-3100/LAZR X, pre-injection, 4 hours post-injection, and *ex vivo*. **2-7** was prepared using a molar equivalence of 1:3.3 of compounds **2-5** and **2-6**. This formulation utilized our approved upper limit of 20 mg/kg for **2-6** and 15 mg/kg of **2-5**, which was based on literature-recommended dosing of a similar dye, indocyanine green, in rats (16 mg/kg, I.V. administration).[50] The mice were injected intravenously with 200 µL of either **2-5** (15 mg kg^{-1} or 1.5 mM, n=3) or **2-7** (which was prepared 1 h prior to injection by mixing 15 mg kg^{-1} or 1.5 mM of **2-5** and 20 mg kg^{-1} or 5 mM of **2-6**, n=3) formulated in 10% ethanol/0.9% w/v saline. Animals tolerated administration of the PIPs well and no observable changes in behaviour or weight were noted throughout the study. *Ex vivo* images of the bone were taken using a phantom chamber.

Photoacoustic Imaging of 2-5 & 2-7 using a Systemic, Pre-Targeting Approach: 7-8 mice were imaged, as described in the section titled '*In Vivo* Photoacoustic Imaging Studies', on the Vevo-3100/LAZR X, pre-injection, 4 and 24 h post-injection, and *ex vivo*. With the improved solubility of **2-5** over **2-7**, and to increase the probability of the *in vivo* reaction occurring between **2-5** and **2-6**, we were able to increase the molar ratio to 1:2.5 of compounds **2-5** and **2-6**, which was the upper limit of our approved dosing for **2-5** (20 mg/kg). The mice were injected intravenously with 50 µL of either 0.9% w/v sterile saline (n=4) or **2-6** (20 mg kg^{-1} or 20 mM in 0.9% w/v sterile saline) (n=4). 1 h post-injection, all mice were injected with 150 µL of **2-5** (20 mg kg^{-1} or 2.65 mM formulated in 10% ethanol in 0.9% w/v sterile saline). Animals tolerated administration of the PIPs well and no observable changes in behaviour or weight were noted throughout the study. *Ex vivo* images of the bone were taken using a phantom chamber.

2.4.5 Statistical Analyses

Data are reported as mean ± standard error of the mean (SEM). Concentration and hydroxyapatite binding data were analyzed by one-way analysis of variance (ANOVA). Differences between test groups and control were assessed using Dunnett's Multiple Comparison Test on GraphPad Prism version 9 (GraphPad Software, San Diego, CA). Each experiment was performed and validated at least 3 times. *In vivo* PAI data were analyzed using a two-way ANOVA. The Tukey Test on GraphPad was used to assess the differences between the test and control groups. Statistical significance was established using * $P \leq 0.05$; ** $P \leq 0.01$; *** $P \leq 0.001$ vs. control or appropriate diluent.

Ancillary Information: Supporting data are available in Appendix I: methods & calculations for molar absorptivity, fluorescence quantum yield, and hydroxyapatite percent binding; HPLC, HRMS, and ^{1}H & ^{13}C-NMR data of all compounds; Absorbance & photoacoustic signal characterizations for **2-5**, available under Appendix I.

Acknowledgements: Technical and financial support by VisualSonics Inc., and review of data by Andrew Heinmiller, M.Sc., is gratefully acknowledged. This work was supported by the Canadian Institutes of Health Research (FRN PJT-165895), the Canada Foundation for Innovation, and the Ontario Institute for Cancer Research through funding provided by the Government of

Ontario. We acknowledge the support of the Natural Sciences and Engineering Research Council of Canada (NSERC). Graphical abstract created with BioRender.com

2.6 References:

(1) Gnanasegaran, G.; Cook, G.; Adamson, K.; Fogelman, I. Patterns, Variants, Artifacts, and Pitfalls in Conventional Radionuclide Bone Imaging and SPECT/CT. *Semin. Nucl. Med.* **2009**, *39* (6), 380–395. https://doi.org/10.1053/j.semnuclmed.2009.07.003.

(2) Kim, S. *Handbook of Nuclear Medicine and Molecular Imaging: Principles and Clinical Applications: Chapter 12: Bone and Joint Nuclear Imaging*; World Scientific, 2012.

(3) Park, E.-Y.; Lee, D.; Lee, C.; Kim, C. Non-Ionizing Label-Free Photoacoustic Imaging of Bones. *IEEE Access* **2020**, *8*, 160915–160920. https://doi.org/10.1109/ACCESS.2020.3020559.

(4) Sun, S.; Błażewska, K. M.; Kadina, A. P.; Kashemirov, B. A.; Duan, X.; Triffitt, J. T.; Dunford, J. E.; Russell, R. G. G.; Ebetino, F. H.; Roelofs, A. J.; Coxon, F. P.; Lundy, M. W.; McKenna, C. E. Fluorescent Bisphosphonate and Carboxyphosphonate Probes: A Versatile Imaging Toolkit for Applications in Bone Biology and Biomedicine. *Bioconjug. Chem.* **2016**, *27* (2), 329–340. https://doi.org/10.1021/acs.bioconjchem.5b00369.

(5) Bhushan, K. R.; Misra, P.; Liu, F.; Mathur, S.; Lenkinski, R. E.; Frangioni, J. V. Detection of Breast Cancer Microcalcifications Using a Dual-Modality SPECT/NIR Fluorescent Probe. *J. Am. Chem. Soc.* **2008**, *130* (52), 17648–17649. https://doi.org/10.1021/ja807099s.

(6) Rudnick-Glick, S.; Corem-Salkmon, E.; Grinberg, I.; Yehuda, R.; Margel, S. Near IR Fluorescent Conjugated Poly(Ethylene Glycol)Bisphosphonate Nanoparticles for in Vivo Bone Targeting in a Young Mouse Model. *J. Nanobiotechnology* **2015**, *13* (80). https://doi.org/10.1186/s12951-015-0126-0.

(7) Hyun, H.; Wada, H.; Bao, K.; Gravier, J.; Yadav, Y.; Laramie, M.; Henary, M.; Frangioni, J. V.; Choi, H. S. Phosphonated Near-Infrared Fluorophores for Biomedical Imaging of Bone. *Angew. Chem. Int. Ed.* **2014**, *53* (40), 10668–10672. https://doi.org/10.1002/anie.201404930.

(8) Knox, H. J.; Chan, J. Acoustogenic Probes: A New Frontier in Photoacoustic Imaging. *Acc. Chem. Res.* **2018**, *51* (11), 2897–2905. https://doi.org/10.1021/acs.accounts.8b00351.

(9) Weber, J.; Beard, P. C.; Bohndiek, S. E. Contrast Agents for Molecular Photoacoustic Imaging. *Nat. Methods* **2016**, *13* (8), 639–650. https://doi.org/10.1038/nmeth.3929.

(10) Emelianov, S. Y.; Li, P.-C.; O'Donnell, M. Photoacoustics for Molecular Imaging and Therapy. *Phys. Today* **2009**, *62* (8), 34–39. https://doi.org/10.1063/1.3141939.

(11) Valluru, K. S.; Wilson, K. E.; Willmann, J. K. Photoacoustic Imaging in Oncology: Translational Preclinical and Early Clinical Experience. *Radiology* **2016**, *280* (2), 332–349. https://doi.org/10.1148/radiol.16151414.

(12) Steinberg, I.; Huland, D. M.; Vermesh, O.; Frostig, H. E.; Tummers, W. S.; Gambhir, S. S. Photoacoustic Clinical Imaging. *Photoacoustics* **2019**, *14*, 77–98. https://doi.org/10.1016/j.pacs.2019.05.001.

(13) Attia, A. B. E.; Balasundaram, G.; Moothanchery, M.; Dinish, U. S.; Bi, R.; Ntziachristos, V.; Olivo, M. A Review of Clinical Photoacoustic Imaging: Current and Future Trends. *Photoacoustics* **2019**, *16*, 100144. https://doi.org/10.1016/j.pacs.2019.100144.

(14) Oh, J.-T.; Li, M.-L.; Zhang, H. F.; Maslov, K.; Stoica, G.; Wang, L. V. Three-Dimensional Imaging of Skin Melanoma in Vivo by Dual-Wavelength Photoacoustic Microscopy. *J. Biomed. Opt.* **2006**, *11* (3), 034032. https://doi.org/10.1117/1.2210907.

(15) Hu, S.; Wang, L. V. Photoacoustic Imaging and Characterization of the Microvasculature. *J. Biomed. Opt.* **2010**, *15* (1), 011101. https://doi.org/10.1117/1.3281673.

(16) Guggenheim, J. A.; Allen, T. J.; Plumb, A.; Zhang, E. Z.; Rodriguez-Justo, M.; Punwani, S.; Beard, P. C. Photoacoustic Imaging of Human Lymph Nodes with Endogenous Lipid and Hemoglobin Contrast. *J. Biomed. Opt.* **2015**, *20* (05), 1. https://doi.org/10.1117/1.JBO.20.5.050504.

(17) Sivaramakrishnan, M.; Maslov, K.; Zhang, H. F.; Stoica, G.; Wang, L. V. Limitations of Quantitative Photoacoustic Measurements of Blood Oxygenation in Small Vessels. *Phys. Med. Biol.* **2007**, *52* (5), 1349–1361. https://doi.org/10.1088/0031-9155/52/5/010.

(18) Zlitni, A.; Gowrishankar, G.; Steinberg, I.; Haywood, T.; Sam Gambhir, S. Maltotriose-Based Probes for Fluorescence and Photoacoustic Imaging of Bacterial Infections. *Nat. Commun.* **2020**, *11* (1), 1250. https://doi.org/10.1038/s41467-020-14985-8.

(19) St. Lorenz, A.; Buabeng, E. R.; Taratula, O.; Taratula, O.; Henary, M. Near-Infrared Heptamethine Cyanine Dyes for Nanoparticle-Based Photoacoustic Imaging and Photothermal

Therapy. *J. Med. Chem.* **2021**, *64* (12), 8798–8805. https://doi.org/10.1021/acs.jmedchem.1c00771.

(20) Wang, Y.; Thompson, J. M.; Ashbaugh, A. G.; Khodakivskyi, P.; Budin, G.; Sinisi, R.; Heinmiller, A.; van Oosten, M.; van Dijl, J. M.; van Dam, G. M.; Francis, K. P.; Bernthal, N. M.; Dubikovskaya, E. A.; Miller, L. S. Preclinical Evaluation of Photoacoustic Imaging as a Novel Noninvasive Approach to Detect an Orthopaedic Implant Infection: *J. Am. Acad. Orthop. Surg.* **2017**, *25*, S7–S12. https://doi.org/10.5435/JAAOS-D-16-00630.

(21) Levi, J.; Kothapalli, S.-R.; Bohndiek, S.; Yoon, J.-K.; Dragulescu-Andrasi, A.; Nielsen, C.; Tisma, A.; Bodapati, S.; Gowrishankar, G.; Yan, X.; Chan, C.; Starcevic, D.; Gambhir, S. S. Molecular Photoacoustic Imaging of Follicular Thyroid Carcinoma. *Clin. Cancer Res.* **2013**, *19* (6), 1494–1502. https://doi.org/10.1158/1078-0432.CCR-12-3061.

(22) Capozza, M.; Blasi, F.; Valbusa, G.; Oliva, P.; Cabella, C.; Buonsanti, F.; Cordaro, A.; Pizzuto, L.; Maiocchi, A.; Poggi, L. Photoacoustic Imaging of Integrin-Overexpressing Tumors Using a Novel ICG-Based Contrast Agent in Mice. *Photoacoustics* **2018**, *11*, 36–45. https://doi.org/10.1016/j.pacs.2018.07.007.

(23) Zhang, H. K.; Chen, Y.; Kang, J.; Lisok, A.; Minn, I.; Pomper, M. G.; Boctor, E. M. Prostate-Specific Membrane Antigen-Targeted Photoacoustic Imaging of Prostate Cancer *in Vivo*. *J. Biophotonics* **2018**, *11* (9), e201800021. https://doi.org/10.1002/jbio.201800021.

(24) Chatni, M. R.; Xia, J.; Sohn, R.; Maslov, K.; Guo, Z.; Zhang, Y.; Wang, K.; Xia, Y.; Anastasio, M.; Arbeit, J.; Wang, L. V. Tumor Glucose Metabolism Imaged in Vivo in Small Animals with Whole-Body Photoacoustic Computed Tomography. *J. Biomed. Opt.* **2012**, *17* (7), 0760121. https://doi.org/10.1117/1.JBO.17.7.076012.

(25) Han, S. H. Review of Photoacoustic Imaging for Imaging-Guided Spinal Surgery. *Neurospine* **2018**, *15* (4), 306–322. https://doi.org/10.14245/ns.1836206.103.

(26) Shubert, J.; Lediju Bell, M. A. Photoacoustic Imaging of a Human Vertebra: Implications for Guiding Spinal Fusion Surgeries. *Phys. Med. Biol.* **2018**, *63* (14), 144001. https://doi.org/10.1088/1361-6560/aacdd3.

(27) Hu, J.; Yu, M.; Ye, F.; Xing, D. In Vivo Photoacoustic Imaging of Osteosarcoma in a Rat Model. *J. Biomed. Opt.* **2011**, *16* (2), 020503. https://doi.org/10.1117/1.3544502.

(28) Yazdani, A.; Bilton, H.; Vito, A.; Genady, A. R.; Rathmann, S. M.; Ahmad, Z.; Janzen, N.; Czorny, S.; Zeglis, B. M.; Francesconi, L. C.; Valliant, J. F. A Bone-Seeking Trans-

Cyclooctene for Pretargeting and Bioorthogonal Chemistry: A Proof of Concept Study Using 99mTc- and 177Lu-Labeled Tetrazines. *J. Med. Chem.* **2016**, *59* (20), 9381–9389. https://doi.org/10.1021/acs.jmedchem.6b00938.

(29) Oliveira, B. L.; Guo, Z.; Bernardes, G. J. L. Inverse Electron Demand Diels–Alder Reactions in Chemical Biology. *Chem. Soc. Rev.* **2017**, *46* (16), 4895–4950. https://doi.org/10.1039/C7CS00184C.

(30) Calvo, M. S.; Eyre, D. R.; Gundberg, C. M. Molecular Basis and Clinical Application of Biological Markers of Bone Turnover. *Endocr. Rev.* **1996**, *17* (4), 36.

(31) Slikboer, S. R. Synthesis and Evaluation of Multimodal Near-Infrared/Technetium-99m Probes for Imaging Cancer and Bone Injury. Doctoral Dissertation, McMaster University, 2019.

(32) James, N. S.; Chen, Y.; Joshi, P.; Ohulchanskyy, T. Y.; Ethirajan, M.; Henary, M.; Strekowsk, L.; Pandey, R. K. Evaluation of Polymethine Dyes as Potential Probes for Near Infrared Fluorescence Imaging of Tumors: Part - 1. *Theranostics* **2013**, *3* (9), 692–702. https://doi.org/10.7150/thno.5922.

(33) Chapman, G.; Henary, M.; Patonay, G. The Effect of Varying Short-Chain Alkyl Substitution on the Molar Absorptivity and Quantum Yield of Cyanine Dyes. *Anal. Chem. Insights* **2011**, *6*, ACI.S6568. https://doi.org/10.4137/ACI.S6568.

(34) Beard, P. Biomedical Photoacoustic Imaging. *Interface Focus* **2011**, *1* (4), 602–631. https://doi.org/10.1098/rsfs.2011.0028.

(35) Cole, L. E.; Vargo-Gogola, T.; Roeder, R. K. Targeted Delivery to Bone and Mineral Deposits Using Bisphosphonate Ligands. *Adv. Drug Deliv. Rev.* **2016**, *99*, 12–27. https://doi.org/10.1016/j.addr.2015.10.005.

(36) Torres Martin de Rosales, R.; Finucane, C.; Mather, S. J.; Blower, P. J. Bifunctional Bisphosphonate Complexes for the Diagnosis and Therapy of Bone Metastases. *Chem. Commun.* **2009**, No. 32, 4847. https://doi.org/10.1039/b908652h.

(37) Verhoeven; Seimbille; Dalm. Therapeutic Applications of Pretargeting. *Pharmaceutics* **2019**, *11* (9), 434. https://doi.org/10.3390/pharmaceutics11090434.

(38) Houghton, J. L.; Membreno, R.; Abdel-Atti, D.; Cunanan, K. M.; Carlin, S.; Scholz, W. W.; Zanzonico, P. B.; Lewis, J. S.; Zeglis, B. M. Establishment of the In Vivo Efficacy of Pretargeted Radioimmunotherapy Utilizing Inverse Electron Demand Diels-Alder Click

Chemistry. *Mol. Cancer Ther.* **2017**, *16* (1), 124–133. https://doi.org/10.1158/1535-7163.MCT-16-0503.

(39) Frampas, E.; Rousseau, C.; Bodet-Milin, C.; Barbet, J.; Chatal, J.-F.; Kraeber-Bodéré, F. Improvement of Radioimmunotherapy Using Pretargeting. *Front. Oncol.* **2013**, *3*. https://doi.org/10.3389/fonc.2013.00159.

(40) de La Serna Higuera, C.; Perez Villoria, A.; Rodriguez Gomez, S.; Martinez Moreno, J.; Betancourt Gonzalez, A.; Martin Arribas, M. Alendronate-Induced Hepatocellular Lesion. *Gastroenterol Hepatol* **2001**, *25* (5), 244–246.

(41) Yanık, B.; Turkay, C.; Atalar, H. Hepatotoxicity Induced by Alendronate Therapy. *Osteoporos. Int.* **2007**, *18* (6), 829–831. https://doi.org/10.1007/s00198-007-0323-2.

(42) Halabe, A.; Lifschitz, B.; Azuri, J. Liver Damage Due to Alendronate. *N. Engl. J. Med.* **2000**, 365–366.

(43) LiverTox: Clinical and Research Information on Drug- Induced Liver Injury. *Natl. Inst. Diabetes Dig. Kidney Dis.* **2012**.

(44) Carrere, C.; Duval, J.; Godard, B.; De Jaureguiberry, J.; Ciribilli, J. Severe Acute Hepatitis Induced by Alendronate. *Gastroenterol Clin Biol* **2002**, *26*, 179–180.

(45) Rathmann, S. M.; Genady, A. R.; Janzen, N.; Anipindi, V.; Czorny, S.; Rullo, A. F.; Sadeghi, S.; Valliant, J. F. A Versatile Platform for the Development of Radiolabeled Antibody-Recruiting Small Molecules. *Mol. Pharm.* **2021**, *18* (7), 2647–2656. https://doi.org/10.1021/acs.molpharmaceut.1c00187.

(46) Usama, S. M.; Park, G. K.; Nomura, S.; Baek, Y.; Choi, H. S.; Burgess, K. Role of Albumin in Accumulation and Persistence of Tumor-Seeking Cyanine Dyes. *Bioconjug. Chem.* **2020**, *31* (2), 248–259. https://doi.org/10.1021/acs.bioconjchem.9b00771.

(47) Thavornpradit, S.; Usama, S. M.; Park, G. K.; Shrestha, J. P.; Nomura, S.; Baek, Y.; Choi, H. S.; Burgess, K. QuatCy: A Heptamethine Cyanine Modification With Improved Characteristics. *Theranostics* **2019**, *9* (10), 2856–2867. https://doi.org/10.7150/thno.33595.

(48) Wan, Z.; Zhang, P.; Lv, L.; Zhou, Y. NIR Light-Assisted Phototherapies for Bone-Related Diseases and Bone Tissue Regeneration: A Systematic Review. *Theranostics* **2020**, *10* (25), 11837–11861. https://doi.org/10.7150/thno.49784.

(49) Yazdani, A.; Janzen, N.; Czorny, S.; Ungard, R. G.; Miladinovic, T.; Singh, G.; Valliant, J. F. Preparation of Tetrazine-Containing [2+1] Complexes of [99mTc] and in Vivo Targeting

Using Bioorthogonal Inverse Electron Demand Diels–Alder Chemistry. *Dalton Trans.* **2017**, *46* (42), 14691–14699. https://doi.org/10.1039/C7DT01497J.

(50) Plaa, G. L. Evaluation of Hepatotoxicity: Physiological and Biochemical Measures of Hepatic Function in Animals. In *Comprehensive Toxicology*; 2010; Vol. 9, pp 129–140.

Chapter 3 : Applying Photoacoustic Imaging for the Detection of Bacterial Infection

3.0 The Current Landscape of Bacterial Infection Diagnostics

Bacterial infection occurs when an exogenous strain of bacteria invades a host organism, eliciting an immune response aimed at controlling and inhibiting proliferation.[1] With the advent of antimicrobial agents into mainstream medicine death and serious disease complications, resulting from bacterial infection, have been significantly reduced. However, the widespread misuse of antibiotics, characterized by over-prescription and premature discontinuation of treatment, has contributed to the rise of antibiotic-resistant strains of bacteria.[2] Consequently, antimicrobial-resistant bacterial infections have become a ubiquitous source of morbidity and mortality in recent years and are projected to become the global leading cause of death by 2050.[3] Accurate diagnosis of early-stage bacterial infection is pivotal for effective disease management, enabling prompt therapeutic intervention and minimization of unnecessary antibiotic prescription.

A significant clinical challenge in diagnosing bacterial infection lies in the similarity of outward presenting symptoms to those of sterile inflammation. This is because bacterial cells elicit a host immune response which activates inflammatory pathways.[4] As a consequence, patients undergoing surgery, medical device implantation, or wound healing, concurrently exhibit symptoms of inflammation, making it challenging to differentiate between sterile and bacteria-induced states based solely on outward manifestations. Furthermore, current diagnostic modalities for bacterial infection, including CT scans, MRI, radiographs, and ultrasonography, are limited by their reliance on later-stage morphological changes as indicators of infection and usually require supplementary verification through blood testing, invasive tissue biopsies and

continued symptom monitoring.[5–7] These methodologies frequently overlook the heterogeneous nature of typical infectious lesions and pose a risk of additional contamination, emphasizing the urgent need for non-invasive, precision diagnostics.

MI for diagnosing bacterial infection holds the potential to generate functional information capable of discerning the presence or absence of bacterial cells. Clinically used PET and SPECT agents, [^{18}F]FDG and [^{99m}Tc]-radiolabeled leukocytes, have demonstrated heightened sensitivity compared with anatomical modalities, but have not been found to offer any advantage in distinguishing between sterile inflammation and bacterial infection.[1,5,7] Therefore, special attention should be placed on the targeting vector to develop highly specific diagnostic tools.

The inherent bacteria-targeting properties of antimicrobial agents have prompted investigations into their potential for directing diagnostic tracers to bacterial cells.[5,6,8,9] One such example, [^{99m}Tc]-labelled Ciprofloxacin, which was a clinically approved antimicrobial-diagnostic agent, was used for some time before it was withdrawn from the market due to late realizations of its lack of specificity.[5,6] Conversely, [^{99m}Tc]-UBI-29-41, an antimicrobial peptide currently undergoing clinical trials, has exhibited promise in both sensitivity and specificity for detecting bacterial infections.[5,10–12]

Early preclinical work assessed the potential of non-specific human immunoglobulins (IgG) but failed to provide conclusive evidence regarding bacterial specificity.[6,13] In contrast, antigen-specific monoclonal and polyclonal antibodies have emerged as promising candidates,[6,14] albeit concerns persist regarding their prolonged circulation times and large molecular sizes.[6] The necessity for early diagnostic intervention after infection onset underscores the potential drawback of utilizing long-circulating antibodies. Additionally, mature biofilms may prevent the

ability of the antibodies to interact with the bacteria cells.

Pathogen-specific small molecule targeting vectors represents another promising avenue as their size and pharmacokinetics will not pose the same concerns as antibodies. Compounds such as maltodextrin and maltotriose, large sugar derivatives that are not immediately utilized by mammalian cells, offer intriguing prospects for localizing diagnostic tracers to bacteria cells without instigating drug resistance.[15,16] These sugar derivatives will not enter mammalian cells until they are metabolized into glucose and have been found to clear quickly from healthy tissues. The unmetabolized derivative is taken up by maltodextrin transporters in the cell membrane of bacteria and is retained for extended periods of time, which provides time for clearance of the glucose metabolites from healthy tissues before imaging.[15] Maltodextrins have demonstrated the ability to penetrate biofilms, rendering them highly effective in detecting more resilient strains of bacterial infection.[15]

Another distinguishing pathogen-specific characteristic is the net negative outer membrane of bacterial cells, primarily comprised of anionic phospholipids, lipoteichoic acids, and lipopolysaccharides.[17,18] This structural feature can be exploited as a bacteria-targeting strategy by employing cationic molecules that engage in electrostatic interactions with the bacterial surface. Dipicolylamine (DPA), first reported in 1964,[19] is a ligand that exhibits notable chelating affinity for cationic metals like zinc (II).[20] Bis(zinc(II)-dipicolylamine) (ZnDPA)-based tracers have been successfully applied in bacterial infection imaging studies, in conjunction with various signalling agents, including SPECT agents indium-111, technetium-99m, and various small molecule fluorophores.[21–24]

Although PAI has been applied in various studies for bacteria imaging,[9,16] there are currently no reports on the use of ZnDPA-directed PIPs. Therefore, the objective of this chapter

is to investigate the potential application of ZnDPA-derived PIPs for the detection of bacterial infections, particularly those manifesting as bacteria-induced myositis and medical device-related infections. Furthermore, this work aims to determine whether bacterial infection imaging holds promise as a viable clinical application for PAI.

3.1 Evaluating ZnDPA-Based PIPs for Targeting Myositis

3.1.1 A Versatile Platform for Developing Infection-Targeting PIPs

3.1.1.1 Research Contributions

This work was performed in collaboration with several lab members. Mohamed E. El-Zaria and Afaf R. Genaday provided pure TCO-ZnDPA (**3-1**) and performed the click reaction with IRTz (**2-5**) prior to biological assessment. Pure IRTz (**2-5**), which was fully investigated in Chapter 2 of this thesis, was prepared by Rowan Swann, and all photoacoustic characterizations were carried out by Rowan Swann and Samantha Slikboer. *In vitro* and *in vivo* studies were performed by Rowan Swann, Samantha R. Slikboer, Amber Faraday and Nancy Janzen.

3.1.1.2 Research Overview

With the recent development of a tetrazine-derived NIR dye, **2-5**,[25] and access to a novel TCO-derived ZnDPA, produced internally, a series of studies were conducted to assess the utility of this biorthogonal reaction-based platform towards the development of bacterial infection-targeted PIPs.

3.1.1.3 Results & Discussion

3.1.1.3.1 Synthesis: Click Reaction

Compound **3-1** was combined with **2-1** to yield **3-2** (**Scheme 3.1**) and was confirmed by mass spectrometry and HPLC (**AII-1** and **AII-2**). Analytical HPLC showed several peaks with a retention time between 11.9 and 14.3 min, which is characteristic of the isomeric pattern of the click product.[26]

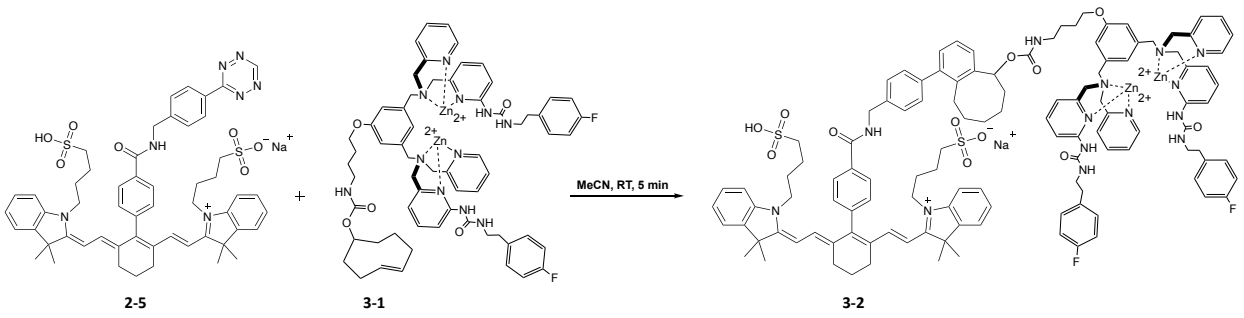

2-5 3-1 3-2

Scheme 3.1. Synthesis of IRTzTCOZnDPA (**3-2**) from a biorthogonal click reaction between IR-Tz (**2-5**) and TCO-ZnDPA (**3-1**).

3.1.1.3.2 Photoacoustic Characterization

Compound **3-2** was found to generate two PA signal maxima at 700 and 765 nm and had some overlap with the PA signal generated by deoxyhemoglobin (**Figure 3.1a**). To ensure the PA system could sufficiently detect the signal of **3-2** from blood, multiwavelength unmixing scans (as outlined in the 'Photoacoustic Phantom Imaging' section) of blood alone, blood with the non-targeted dye **2-5** and the targeted dye **3-2** were performed and the images depicted the differentiation between each of the signals (**Figure 3.1b**). While the results were not quantified, a qualitative increase in the intensity of the green signal attributed to the dye was observed in the samples of blood mixed with the dyes. Additionally, a higher-intensity blue signal was also observed after mixing the blood with the dyes. Without quantifying these intensities, it is not possible to make a definite conclusion on the accuracy of signal unmixing, however, it is hypothesized that the overlap in the PA signal maxima of the dyes and deoxygenated hemoglobin may be reducing the ability of the unmixing algorithm to accurately distinguish between the chromophores, which could cause issues in visualizing low concentrations of the dyes *in vivo*.

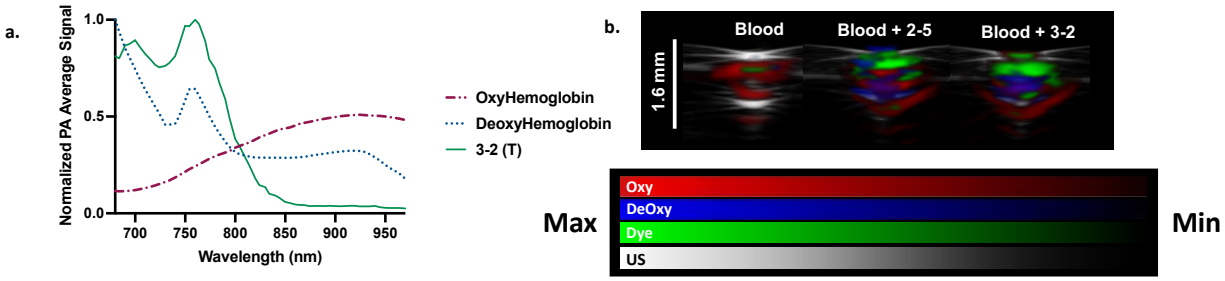

Figure 3.1. Photoacoustic characterization of **3-2**.Normalized PA spectra of **3-2** (50 µM in 10% ethanol in saline) overlaid with the spectra of blood chromophores; oxygenated and deoxygenated hemoglobin. **b.** Unmixed PA images of blood alone or mixed with **2-5** and **3-2** in the PA phantom. Red= oxygenated hemoglobin, blue= deoxygenated hemoglobin, green= **2-5** or **3-2**.

3.1.1.3.3 In Vitro Bacteria Binding Analysis of 2-5 and 3-2 using Fluorescence and Photoacoustic Detection

To test the specificity of the targeted dye for bacteria, samples of *S. aureus* bacteria were incubated with either **3-2** or **2-5** and, after washing the pellet the fluorescence and PA spectra were analyzed (**Figure 3.2a-b**). The anticipated fluorescent and PA maxima (790 nm and 765 nm, respectively) were observed on the bacterial pellet. The signal remaining on the pellet incubated with **3-2** (1291 ± 38.19 a.u.) was found to be significantly higher than that of the pellet incubated with **2-5** (220.3 ± 26.27 a.u., where $P < 0.0001$), and a target-to-nontarget (T/NT) ratio was calculated at 5.86 (**Figure 3.2c**). The same samples were then analyzed on PA phantom (**3-2**: 3.79 ± 0.208 a.u., **2-5**: 0.606 ± 0.073 a.u., where $P < 0.0005$) and a similar T/NT ratio was calculated at 6.25 (**Figure 3.2d**). This demonstrated the specificity of **3-2** to bacteria, as compared with a non-targeted dye.

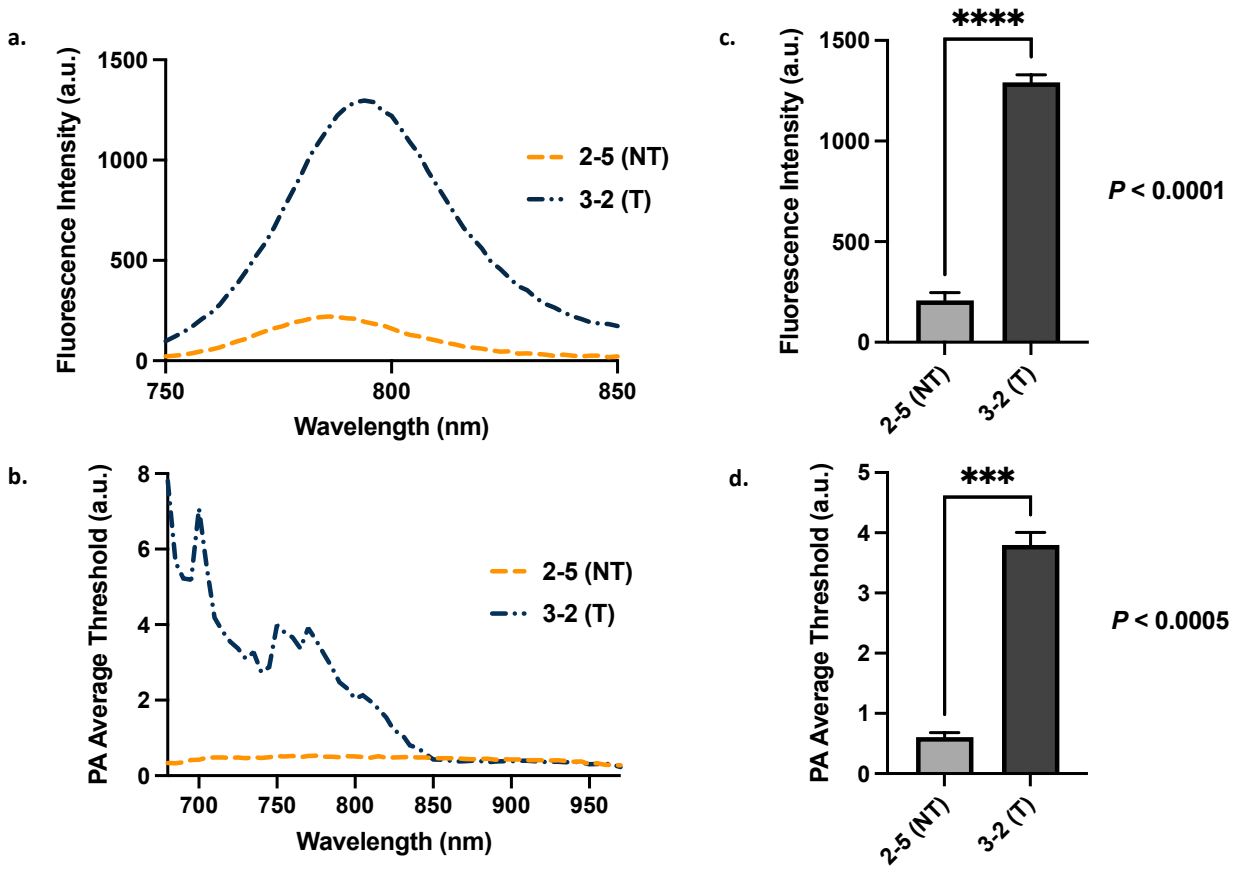

Figure 3.2. *In vitro* bacterial binding analysis of targeted (**3-2**) and non-targeted (**2-5**) dyes (n=3). **a,c.** Fluorescence spectrum (**a**), fluorescence intensity measurements (at 790 nm) (**c**), PA spectrum (**b**), and PA average threshold measurement (at 765 nm) (**d**) of washed *S. aureus* bacterial pellets incubated with **2-5** and **3-2**.

3.1.1.3.4 Assessing the Ability of 3-2 to Detect S. aureus-Induced Myositis, In Vivo using Photoacoustic Imaging

The ability of **3-2** to localize to sites of bacterial infection *in vivo* was assessed using a model of *S. aureus*-induced myositis. 3D multiwavelength unmixing scans depicted a notable PA signal (green) within the infection site at 6 hrs, 12 and 18 hrs post-injection, relative to the background signal in a scan taken prior to injection (**Figure 3.3b**). This was verified by quantifying the PA average signal within the images (**Figure 3.3c**), where the signal was found to be significantly higher at 6 hr (0.399 ± 0.06 a.u., where $P = 0.03$), 12 hr (0.396 ± 0.032 a.u., where P

= 0.01), and 18 hr post-injection (0.353 ± 0.045 a.u., where P = 0.02), than the pre-injection background signal (0.055 ± 0.007). Although this initial study showed that **3-2** localized to sites of bacterial infection, further testing was warranted to confirm that the signal observed was specific to the infection site.

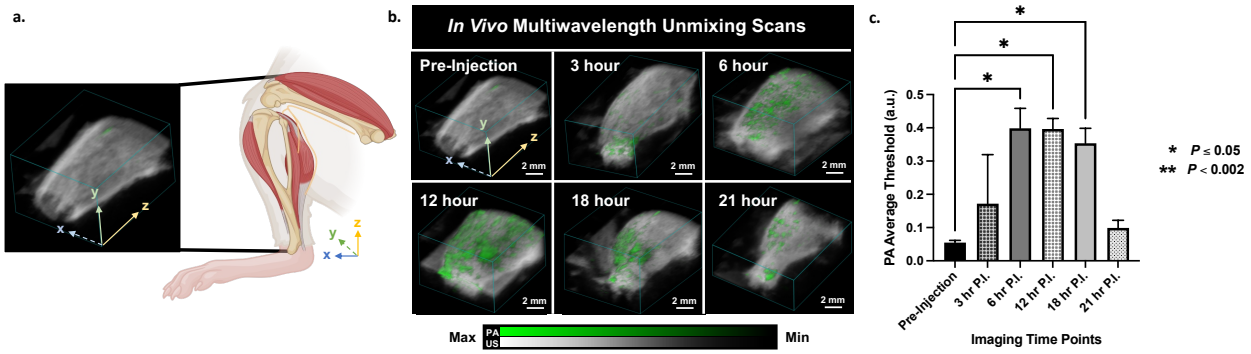

Figure 3.3. Photoacoustic imaging of *S. aureus*-induced myositis using **3-2**. **a**. Image orientation. **b**. Representative *in vivo* PA multispectral unmixing images (at various time points) of mice injected I.V. with **3-2** (1 mM, 200 µL, n=3). **c**. Bar graph representing the quantified 3D PA average signal, derived from the scans in **a**, within the inoculation sites of the mice throughout the study. For all multiwavelength unmixing scans, greyscale= US images overlaid with unmixed PA signal, where green= **3-2**. The signal from oxygenated and deoxygenated hemoglobin has been subtracted from each image.

In a follow-up *in vivo* imaging study, bacterial myositis was induced in one hind limb while the other was inoculated with saline as a vehicle control of the condition. The intended goal of the study was to image both hind limbs pre- and 12 hr post-injection to assess whether the signal was present selectively in the infection site compared to the control limb. For this study, a formulation buffer of 10% ethanol in saline was used in place of 10% ethanol in phosphate-buffered saline (PBS). This change was made following instructions from a product insert of a commercially available Zn-DPA-fluorescent dye kit (MTTI Catalog Number: P-1001, PSVue794) that suggested potential target interaction issues due to the presence of the anionic phosphate in the PBS. However, visible aggregates of **3-2** began to precipitate out of the solution using this new formulation, rendering the material unsuitable for *in vivo* use. It is important to note that

aggregation of this compound was already an ongoing concern and was observed with **2-5** when targeted to bone with a bisphosphonate-TCO, however, the severity of the aggregates precipitating out of solution was not previously observed. Another potential root cause for the unsuccessful dye preparation was also highlighted by the product insert, which indicated a potential shelf-life of 5 days post-zinc coordination. Momentum with this work was halted with the quarantine measures taken during the COVID-19 pandemic and the material allocated for this study was coordinated with zinc months prior to use. While it was not tested beyond this point, we believe the integrity of the material was compromised due to the low solubility of the material in the new formulation buffer in addition to the length of time that **3-1** was stored for. For these reasons, this study was not completed and, while the stability concerns of the zinc coordination could have been easily rectified by employing a 5-day shelf-life for the material, the aggregation issues warranted further consideration.

In previous work with **2-5**, mitigation of dye aggregation was attempted through the utilization of a pre-targeting strategy, where the TCO and Tz constructs were administered separately and anticipated to react *in vivo*. Although this approach was initially considered for the continuation of this work, limitations in the PA signal unmixing algorithm in distinguishing between the dye and deoxygenated hemoglobin justified a shift in focus. Hence, efforts were redirected toward investigating PIPs that generate PA signals at wavelengths that do not overlap so heavily with the predominant peaks of the blood chromophores. To initiate this next phase of work, the commercially available PSVue794, featuring a similar Zn-DPA targeting vector and a heptamethine cyanine dye that absorbs around 800 nm, was utilized, as outlined in section 3.1.2.

3.1.1.4 Conclusion

A novel ZnDPA-based NIR dye was synthesized and evaluated as a photoacoustic imaging agent for detecting bacterial infection. The dye exhibited predominate PA signals at 700 and 765 nm, which overlapped significantly with the PA signal of deoxygenated hemoglobin. The PIP possessed the ability to selectively associate with bacterial cells *in vitro*, compared to the non-targeted dye and initial *in vivo* findings demonstrated localization of the dye to sites of bacterial infection. However, without the proper control groups, such as a vehicle control injected muscle & sterile myositis, the data was not conclusive. Subsequent attempts to address this were impeded by severe dye aggregation. While the stability issues of the zinc-coordinated compound could be easily managed, the low solubility of the PIP and challenges in distinguishing the signal of dye from deoxyhemoglobin prompted the exploration of a commercially available ZnDPA-based NIR dye (discussed in Chapter 3.1.2). Further investigation in Chapter 4 focuses on designing PIPs with enhanced solubility and PA signal generation properties and follows a series of proof-of-concept studies for applying these novel PIPs for the PAI of bacterial infection.

3.1.1.5 Methods & Materials

General Materials & Instrumentation. Unless otherwise noted, all reagents and solvents were ACS grade, purchased from commercial suppliers, and used without further purification. Distilled water was used for all experiments requiring the use of water.

Fluorescence scans were collected on a Tecan Infinite M1000 plate reader using Corning 96-well, clear bottom plates (non-treated surface) (Corning 3631), PerkinElmer film was used to seal any plates containing bacteria cells. High-performance liquid chromatography (HPLC) was performed on a Waters 1525 Binary (Midford, MA), monitored simultaneously with 2998 photodiode array detector at 200/254/700 nm and in line Bioscan (model 106) radioactivity

detector. Analytical HPLC of each compound was performed on a Gemini 5 µm C18 110 Å (250 × 4.6 mm) Column (00G-443-E0, Phenomenex).

HPLC Method A: Solvent A: Water + 0.1% Trifluoroacetic acid (TFA), Solvent B: Acetonitrile + 0.1% TFA. Gradient: 0-2 min 20% B, 2-19 min 20-80% B, 19-21 min 100% B, 21-22 min 20% B.

Synthesis of Compound 3-2: IRTz (**2-5**) (2 equiv.) was dissolved in acetonitrile and TCOZnDPA (**3-1**) (1 equiv.) was added. The mixture was stirred at room temperature for 5 minutes and then characterized by HPLC and MS. **HPLC** (UV 254 and 700 nm); **MS** (ESI^+): *m/z* 2052.9 $[M-2Zn]^+$, 1027.1 $[M-2Zn+2H]^{2+}$.

Photoacoustic Phantom Imaging: PA phantom work was performed using a Vevo Phantom imaging chamber (see **Figure AI-17**) and the Vevo-3100/LAZR-X (FUJIFILM VisualSonics, Inc., Toronto, ON, Canada) imaging system equipped with a 680-970 nm laser. Samples were injected into Vevo Contrast Agent Phantom tubing (PN52807) that was threaded into the Vevo Phantom chamber. A 30 MHz, linear array US transducer equipped with integrated fibre optic cables (MX400 and LZ-400 [15-30 $mJ(cm^3)^{-1}$], FUJIFILM VisualSonics, Inc., Toronto, ON, Canada) was positioned overtop of the tubes.

Spectral analysis was performed using 'Spectro' scans, where the PA signal of a 2D, x,y-cross-section of a sample is quantified at each wavelength (690-970 nm) and is used to plot the spectral curve or 'spectral signature' from a defined ROI. From this, the signal intensity of the chromophore of interest can be quantified by the signal unmixing algorithm utilized in the VevoLAB software (VisualSonics, Inc., Toronto, ON, Canada). The 2D multispectral unmixing scans (oxygenated and deoxygenated hemoglobin unmixed from the spectra of **3-2**) were taken for each material in triplicate. Designated wavelengths (682, 700, 730, and 924 nm), based on notable signals generated within individual chromophore spectra (oxygenated and deoxygenated hemoglobin, or **3-2**), were used by the Vevo-3100/LAZR-X unmixing algorithm. Images from the multiwavelength unmixing scans have been displayed using the render mode with the PA signal overlaid on US B-mode (greyscale) signal of a cross-section of tubing. All image processing was carried out using the VevoLAB software. A ROI was drawn around the US image of the tube and,

using ROIs of the same size and shape, a spectrum was generated from the overlaid PA signal. From the generated spectrum, the PA signal intensity was derived from each sample for analysis.

PA Signal Analysis of 3-2: Samples of **3-2** at 50 μM in 10% ethanol in 0.9% w/v saline and **3-2** and both **3-2** and **2-5** at 1 mM in 10% ethanol in 0.9% w/v saline diluted to 64 μM in whole mouse blood (mixed with 10% EDTA in 0.9% w/v saline [0.15 g/mL]) were prepared alongside appropriate blank controls. The samples were injected into Vevo contrast agent phantom tubing and Spectro scans were taken of the material in triplicate. The data was analyzed as described in 'Photoacoustic Phantom Imaging'.

***In Vitro* Bacteria Binding of 3-2 vs 2-5 using Fluorescence and Photoacoustic Detection: 3-2** or **2-5** (final concentration=10 μM) were incubated with 1×10^9 CFU (50 μL) of *S. aureus* (ATCC; 25923) in HBSS or 50 μL HBSS, for 10 minutes in triplicate. The samples were washed 3 times and the pellet was resuspended in 250 μL of HBSS. 200 μL sample and 200 μL stock solution were transferred to a black flat clear bottom 96-well plate. A fluorescence scan (Ex= 736 nm; Em= 746-850 nm) was performed. The fluorescence intensity at 790 nm of each sample was subtracted from appropriate blanks and the change in intensity was evaluated. The bacterial pellets were fixed with 70% Ethanol, injected (~20 μL) into Vevo contrast agent phantom tubing, and Spectro scans were taken of each sample (as described in the 'Photoacoustic Phantom Imaging' section). The signal intensity at 765 nm was quantified for comparison.

Animal Studies: All procedures were conducted according to the guidelines of the Committee for Research and Ethics Issues of the International Association for the Study of Pain, and guidelines established by the Canadian Council on Animal Care and the McMaster University Animal Research Ethics Board. In each animal study 7-10 week-old female BALB/c mice (Charles River Laboratories, Raleigh, NC), weighing around 20 g, were used. The mice were sterile housed and maintained at 21 ˚C with a 12-hour light/dark cycle and were provided autoclaved food and water *ad libitum*.

***In Vivo* Photoacoustic Imaging Studies:** PAI was performed using the Vevo-3100/LAZR-X imaging system. Mice were anesthetized, and the fur of their right hindlimb was thoroughly

removed before being placed in a prone position on a platform that enabled the monitoring of their respiration and heart rates. A generous amount of US gel was applied before imaging with the transducer (MX400/LX400) positioned overtop of the leg. At each imaging time point, Spectro scans and 3D multispectral unmixing scans were taken of each hindlimb. The transducer was positioned laterally overtop of the hindlimb, corresponding with the inoculation site. Scan distances averaged 20 mm and scans were taken every 0.33 mm.

3D multiwavelength unmixing scans were performed to construct images depicting dye-specific PA signal present within the hindlimb. Designated wavelengths (682, 700, 730, and 924 nm), based on notable signals generated within individual chromophore spectra (oxygenated and deoxygenated hemoglobin, or **3-2**), were used by the Vevo-3100/LAZR-X unmixing algorithm. The series of 2D cross-sectional scans collected were then reconstructed by the instrument into a 3D image, where the signals from each chromophore are assigned a colour and overlaid onto a b-mode ultrasound scan. The scans are displayed as either render mode or texture mapping images where the PA signal is overlaid on US B-mode (greyscale) signal for sections of the hindlimb. Signals from oxygenated and deoxygenated hemoglobin were subtracted from the images to reduce visual complexity. The spectrally unmixed signal of **2**, in the 3D multiwavelength unmixing scans, was quantified using 3D regions of interest (ROI) drawn around the inoculation sites. All signal unmixing algorithms and image processing was carried out using the VevoLAB software. Image processing consisted of signal optimization, with parameters set the same for each image within the study. 3D regions of interest were drawn around the inoculation site.

In vivo spectral analysis was performed using 'Spectro' scans (as described in the "Photoacoustic Phantom Imaging' section) and was used to verify whether the spectral signature of the *in vivo* signal matched that of the exogenous dye. The ROI used for each spectral curve was displayed in a multiwavelength unmixing scan (oxygenated and deoxygenated hemoglobin unmixed from **3**) derived from the Spectro scan.

Assessing the Ability of 3-2 to Detect *S. aureus*-Induced Bacterial Infection Through Photoacoustic Imaging: An aliquot of *S. aureus* (OD_{600}=8.43, 1×10^8 CFUs, 50 μL in HBSS) was injected intramuscularly (I.M.) on the right hindlimb. 6 hours after inoculating mice with *S. aureus* to induce bacterial infection (n=3), the mice were injected intravenously with 200 μL of **3-2** (1 mM) and were imaged, as described in the section titled '*In Vivo* Photoacoustic Imaging Studies',

on the Vevo LAZR X, pre-injection, 3-, 6-, 12-, 18-, and 21-hours post-injection. Animals were end-point monitors throughout the duration of each study.

Statistical Analyses: Data are reported as mean ± standard error of the mean (SEM). Concentration and bacteria-binding data were analyzed by one-way analysis of variance (ANOVA). Differences between test groups and control were assessed using Dunnett's Multiple Comparison Test on GraphPad Prism version 9 (GraphPad Software, San Diego, CA). *In vivo* PAI data were analyzed using a two-way ANOVA. Differences between tested groups and control were assessed using the Tukey Test on GraphPad. Statistical significance was established using * $P \leq 0.05$; ** $P \leq 0.01$; *** $P \leq 0.001$.

Ancillary Information: Supporting data are available in Appendix II: Structural characterization data for **3-1** and **3-2**.

3.1.2 Photoacoustic Imaging of a Cyanine Dye Targeting Bacterial Infection

Rowan Swann[†], Daniel Hernández-Valdés[†], Luis Rafael Silva[†], Yusra Mahmood Marfatia[†], Mohamed E. El-Zaria[†], Afaf R. Genady[†], Jacek M. Kwiecien[‡], John F. Valliant[†], & Saman Sadeghi[†,*]

[†] Department of Chemistry and Chemical Biology, McMaster University, ON L8S 4L8, Canada
[‡] Department of Pathology and Molecular Medicine, McMaster University, Hamilton, ON L8S 4L8, Canada

Manuscript Published in Nature Scientific Reports.
DOI: 10.1038/s41598-024-69148-2

3.1.2.1 Introduction

Healthcare-associated bacterial infections, particularly those that arise in conjunction with medical device implants and surgery, are difficult to distinguish from sterile inflammation without the use of invasive tissue sampling procedures.[27] In recent years, these infections have contributed to extended post-operative hospitalizations and increased patient mortality following routine medical procedures.[28,29] In addition to methods to prevent these infections, there is also a critical demand for non-invasive diagnostic tools that can rapidly and accurately detect and differentiate bacterial infections from sterile inflammation.

Conventional methods used to diagnose bacterial infections include magnetic resonance imaging (MRI), X-ray, ultrasonography and computed tomography (CT).[29] However, these techniques are not specific to infection but rather display anatomical indications of infection-related pathologies. This limits their utility in detecting early stages of infection when notable anatomical signs may not yet be observable and when interventions are most effective. Molecularly targeted photoacoustic imaging (PAI) has emerged as an attractive modality for detecting early-stage infections because it offers the opportunity to develop infection-specific contrast agents. PAI also has improved depth resolution, as compared to purely optical imaging techniques (e.g., fluorescence imaging (FI)) since the generated acoustic waves experience less scattering in tissue

than the photons generated during FI.[30] Additionally, the complimentary prerequisite of light absorption for both PAI and FI, highlights the possible utility of traditional fluorophores for PAI.

Recent reports on optical and PA imaging of infection have successfully utilized fluorophore-conjugated antibiotics,[5,6,8,31] compounds metabolized by bacteria,[15,32,33] and monoclonal antibodies.[6,14] However, antimicrobial resistance may impede the localization of certain probes to the site of infection, and monoclonal antibodies are known to experience long circulation times and could have a limited ability to penetrate mature biofilms due to their size. Zinc (II) dipicolylamine (Zn-DPA)-based bioconjugates can potentially be used to address these limitations as they have been established as suitable bacteria-targeting molecules due to their affinity for the anionic outer surfaces of bacteria cells, as compared to healthy mammalian cells which typically exhibit a net neutral surface.[6,34,35] The fluorescent Zn-DPA-based probe, PSVue794, has been well characterized in the literature for bacterial detection and is commercially available as a reagent for fluorescence imaging of bacteria.[36] Moving beyond fluorescence imaging methods, we evaluated the use of PSVue794 as a PAI probe (PIP) for imaging bacteria. The PA signal properties in phantom studies and *in vitro* bacteria binding were evaluated before radiolabeling the PIP with ^{99m}Tc to assess the biodistribution profile in a mouse model of bacteria-induced myositis. Proof-of-concept *in vivo* PAI studies were pursued to verify that PSVue794 could generate detectable PA signal at sites of infection compared to sites of sterile inflammation.

3.1.2.2 Results

3.1.2.2.1 PA Signal Analysis of 3-4.

Compound **3-4** (**Scheme 3.2**) was found to generate a PA signal within the range of 680-970 nm and possessed a signal maximum at 800 nm (**Figure 3.4a,c**). An overlay of the PA signatures from **3-4** and those of oxygenated and deoxygenated hemoglobin (**Figure 3.4a**) shows

that **3-4** generates a unique signal, distinguishable from both blood chromophores. The signal of **3-4** was quantified in the presence of whole mouse blood using multiwavelength unmixing scans and a significant increase in the signal of **3-4** detected in blood (0.129 ± 0.012 au) was achieved, compared with the background (0.045 ± 0.002 au, where P =0.006) (**Figure 3.4b**). Additionally, the PA maximum of **3-4** was identified in the merged PA spectrum of blood + **3-4** (indicated by the dashed line at 810 nm) while there was no peak observed at ~810 nm in the spectrum of blood alone (**Figure 3.4c**).

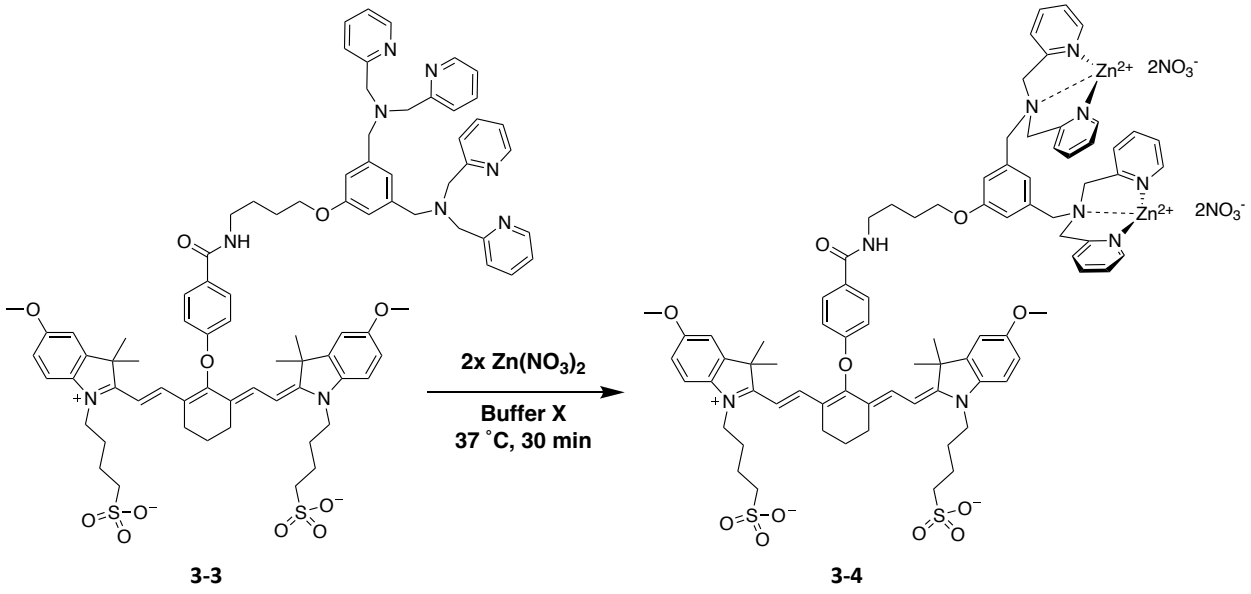

Scheme 3.2. PSVue794 (**3-4**) reagent kit complexation.

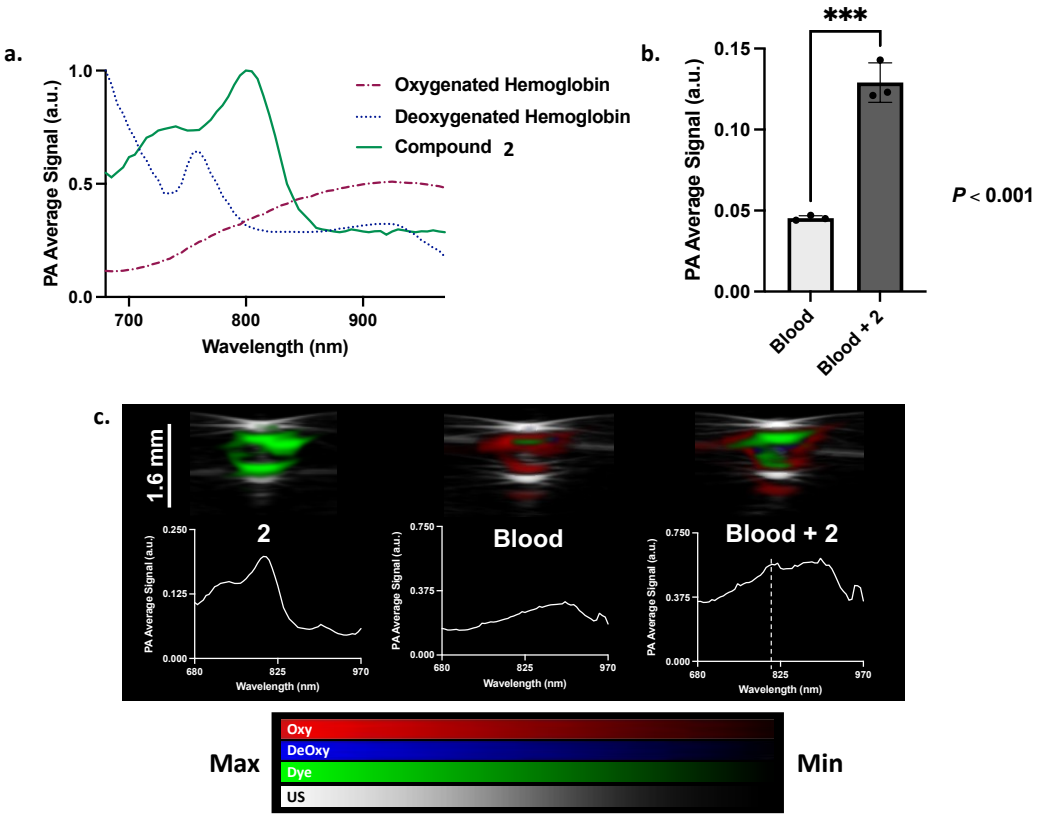

Figure 3.4. Characterization of the PA signal emitted by PSVue794 (**3-4**). **a**. Normalized PA signal of **3-**4 (in Diluent X) overlaid with the PA spectra of oxygenated and deoxygenated hemoglobin. **b.** Quantified PA average single of **3-4** after spectrally unmixing samples of blood with or without **3-4. c**. Multiwavelength unmixing scans of the PA signal for **3-4** (20 µM), blood alone, and **3-4** (64µM) in blood, with the PA spectra below the image. Signal characterization was performed in PA phantom. The white dashed line on the spectrum of blood + **3-4** indicates the peak of **3-4** within the signal generated from blood. Green= 2, red= oxygenated hemoglobin, blue= deoxygenated hemoglobin, grey-scale= ultrasound B-mode.

3.1.2.2.2 In Vitro Bacterial Binding Analysis of 3-4 using Fluorescence & Photoacoustic Detection

After subtraction of the signal observed in a blank sample, the fluorescence intensity of bacterial cell suspension incubated with **3-4** (60263 ± 6136 au) was significantly higher than the no-cell control (20167 ± 701 au, where $P = 0.007$), and the signal-to-background (S/B) ratio was 2.98 ± 0.20 (**Figure 3.5a**). The same samples were then analyzed on a PA phantom, where the bacterial cell suspension was found to have a significantly higher PA signal (0.075 ± 0.014 au)

above the no-cell control (0.024 ± 0.002 au, where $P \leq 0.005$) (**Figure 3.5b**). No significant differences were present between the no-cell control and the blank controls. A visual representation of the PA signal present within each phantom sample is depicted in **Figure 3.5c**, where a green signal, pertaining to **3-4**, was only seen in the bacterial cell suspension that was incubated with **3-4**. A S/B ratio of 3.06 ± 0.30 was calculated from the data displayed in **Figure 3.5b**.

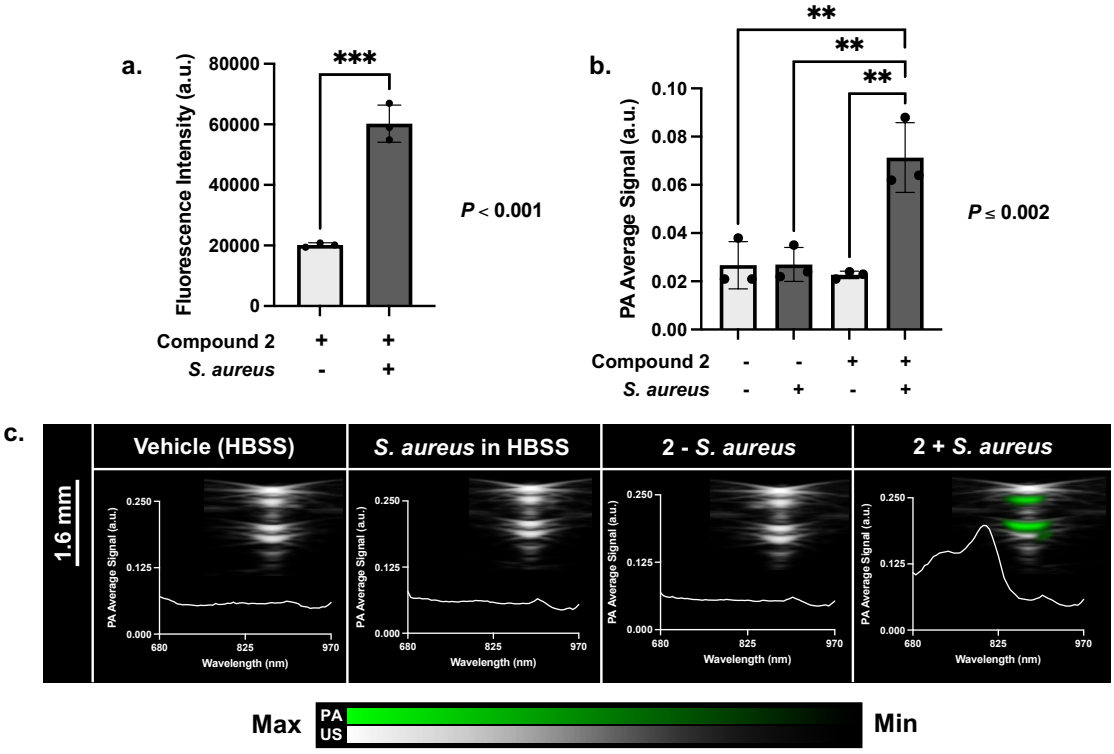

Figure 3.5. Florescent and PA evaluation of *in vitro* bacteria binding of **3-4. a.** Fluorescence intensity measurements of **3-4** incubated with or without bacteria. Signal was normalized by subtracting the values from a blank with or without bacteria. **b.** PA average signal of **3-**4 in each sample. **c.** Phantom PA images of the samples with the PA spectra of each sample overlaid. Where green= **3-4**.

3.1.2.2.3 Radiosynthesis of [^{99m}Tc]Tc-PSVue794 (3-8).

A previously reported method, where technetium tricarbonyl [^{99m}Tc][Tc(CO)$_3$(H$_2$O)$_3$]$^+$ (**3-6**) (**Figure AII-3**) was used to label a dipicolylamine (DPA) ligand,[37,38] was adapted to generate [^{99m}Tc]-TcPSVue794 (**3-8**). Several parameters were explored (**Table AII-1**) to produce **3-8** in high

yield and purity and the optimal conditions involved stirring the Apo-PSS precursor (**3-3**, 0.34 µmol) with **3-6** at room temperature for 1 hour (**Scheme 3.3**). Radio-TLC analysis of the crude material showed a 90% radiochemical conversion to [^{99m}Tc]-TcApo-PSS794 (**3-7**) and a radiochemical purity (RCP) of 99% after passing the reaction mixture through a C-18 cartridge (**Figure AII-4 a,b,d**). Zinc nitrate was then added to **3-7** to form **3-8**, with a RCP of 99%, assessed using radio-TLC and gamma-HPLC (**Figure AII-2 c,e**). The total preparation time was 2 hr and the desired product product was obtained in a non-decay corrected activity yield (**Equation AII-1**) of 52 ± 8% (n=5) (starting activity of 108 ± 9 MBq) and molar activity of 0.76 ± 0.07 MBq/µmol at end of synthesis. The stability of compound **3-8**, incubated in the formulation buffer at room temperature and mouse serum at 37˚C, was assessed over 18 hours. Similar to previous ^{99m}Tc-radiolabeled DPA compounds,[38] **3-8** was stable at all time points (**Figure AII-5 & Table AII-2**).

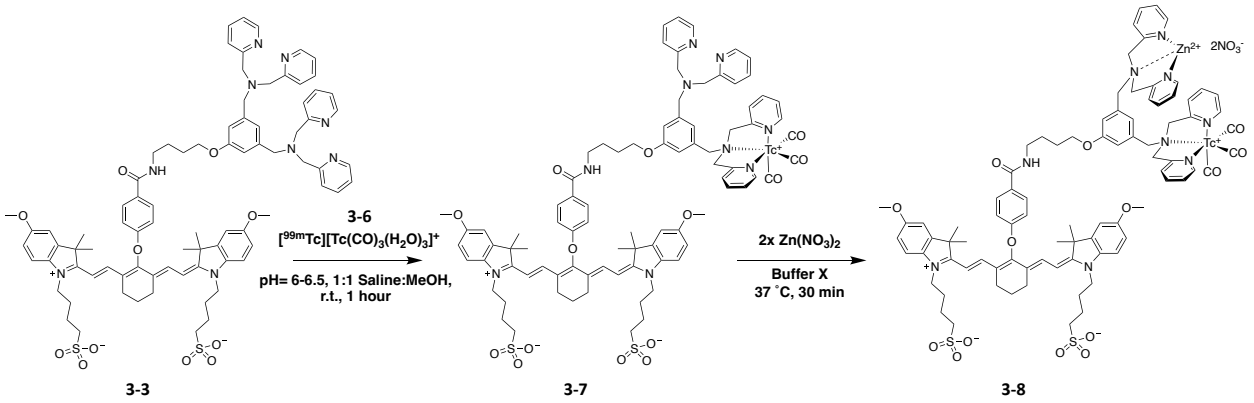

Scheme 3.3. Radiosynthesis of [^{99m}Tc]Tc-PSVue794 (**3-8**) from the Apo-PSS precursor (**3-3**) and [^{99m}Tc][Tc(CO)$_3$(H$_2$O)$_3$]$^+$ (**3-6**). Note that the reaction mixture would also contain **3-3** (not shown here) given the excess of ligand compared to ^{99m}Tc used in a typical radiolabeling experiment.

3.1.2.2.4 In Vitro Bacteria Binding & Quantitative Biodistribution Analysis of 3-8.

An initial *in vitro* test demonstrated that **3-8** (37 kBq) binds to *S. aureus* cells. 15.0 ± 2.1 % of the total activity successfully bound to the bacteria, while the no-cell control percent binding

was 1.3 ± 0.2 % ($P < 0.001$) (**Figure 3.6a**). Subsequently, the whole-body distribution of **3-8** (0.74 MBq/mouse) was assessed in healthy naïve mice and in a mouse model of *S. aureus*-induced myositis (n=4) (**Figure 3.6b & Table AII-3**). A significant increase in the percent injected dose/gram (%ID/g) was noted between the infected muscle tissue (1.68 ± 0.61 % ID/g) and contralateral muscle tissue (0.17 ± 0.07 % ID/g, where $P = 0.01$), generating a target-to-non-target (T/NT) ratio of 10.1 ± 1.1 (**Figure 3.6c**). No significant differences were found in the % ID/g in the spleen in the healthy naïve vs. infected mice. Differences were noted between the gall bladder and large intestine/caecum of the healthy vs. infected mice.

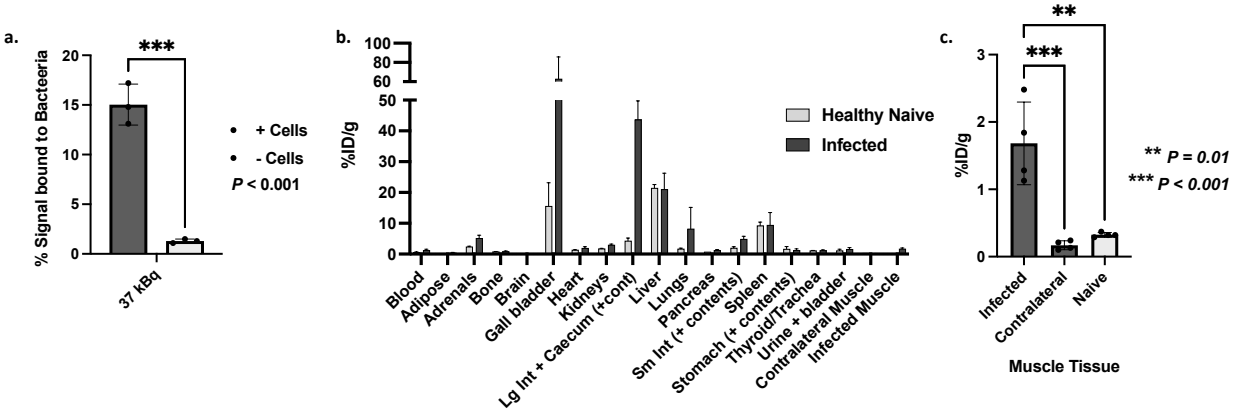

Figure 3.6. a. *In vitro S. aureus* binding analysis of [^{99m}Tc]Tc-PSVue794 (**3-8**). Percentage of total activity (CPM) of **3-8** present after incubation with or without *S. aureus* bacteria cells. Biodistribution analysis of **3-8** in healthy naïve vs. infected mice (n=4 per group) (**b-c**). Infected mice were inoculated with 1×10^8 CFUs of *S. aureus* in the right hindlimb muscle and with an equal volume of HBSS into the left (contralateral) hindlimb muscle. **b.** Percent injected dose/gram (%ID/g) of **3-8** in each tissue. **c.** Comparison of %ID/g of **3-8** in the infected vs contralateral and naïve muscle tissue.

3.1.2.2.5 Bacteria- and LPS-Induced Myositis Models.

A model of sterile inflammation (Lipopolysaccharide [LPS]-induced myositis) was developed, and tissues were analyzed and compared to the previously described bacterial infection

model. The hematoxylin and eosin (H&E) stained tissues (**Figure 3.7**) presented collections of neutrophils in the muscle and perimysium of both LPS- and bacteria-injected tissue, while the spleen of LPS-injected mice exhibited lymphocytic pyknosis and karyorrhexis. The LPS-injected mice were diagnosed with a localized acute inflammation effect, resulting from the injection of material with some immunogenicity, indicated by the observed acute and thrombosing myositis, peri-myositis, and splenic lymphocytolysis. The bacteria-injected mice had acute peri-myositis with intense neutrophilic infiltrations often encompassing bacterial cocci with associated cellular necrosis. Myeloid hyperplasia was present. The contralateral vehicle control-injected muscles had no pathology on histologic analysis.

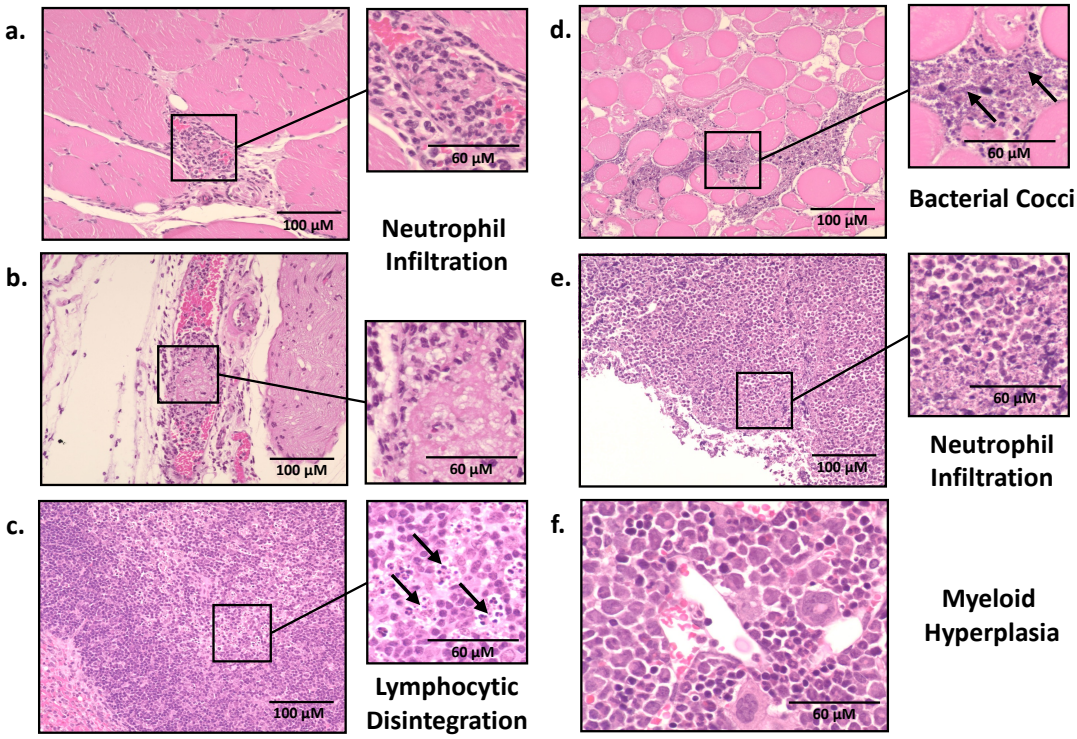

Figure 3.7. Representative images of H&E-stained tissues highlighting key histological features. **a-c.** Tissue fields from LPS-injected mice, including muscle (**a,b**), there are large fibrinous thrombi infiltrated by neutrophils in veins. In the spleen (**c**) a proportion of cells in the lymphoid perivascular cuffs have karyorrhectic or pyknotic nuclei. **d-f**. Tissue fields from the muscle (**d,e**) of bacteria-injected mice, with patchy areas of interstitium markedly widened by severe neutrophilic infiltration (**d**). In some areas, a massive neutrophilic infiltration encompasses large areas of necrosis (**e**). There is myeloid hyperplasia in the bone marrow (**f**).

3.1.2.2.6 Photoacoustic Imaging of LPS-Induced Sterile Inflammation using 3-4.

Following the administration of **3-4** (75 μL, 1 mM) to the LPS model, multiwavelength unmixing scans (**Figure 3.8a**) did not depict a notable PA signal (green) within the inflamed muscle 12 hr post-injection compared to the pre-injection background or the vehicle control muscle (contralateral). Determination of the average PA signal (**Figure 3.8b**) was consistent with this result as the signals within the inflamed muscle (0.062 ± 0.012 a.u.), the pre-injection background (0.058 ± 0.006 a.u.), and the vehicle control muscle (0.066 ± 0.008 a.u.) were not statistically different from one another. The T/NT (inflamed vs. vehicle control muscle) and the S/B (inflamed muscle pre- vs. 12 hr post-injection) ratios were 1.04 ± 0.17 and 1.07 ± 0.11, respectively. The signals of oxygenated and deoxygenated hemoglobin were observed in all the tissues through spectral analysis (**Figure 3.8c**) and no spectral characteristics were noted to indicate the presence of **3-4**.

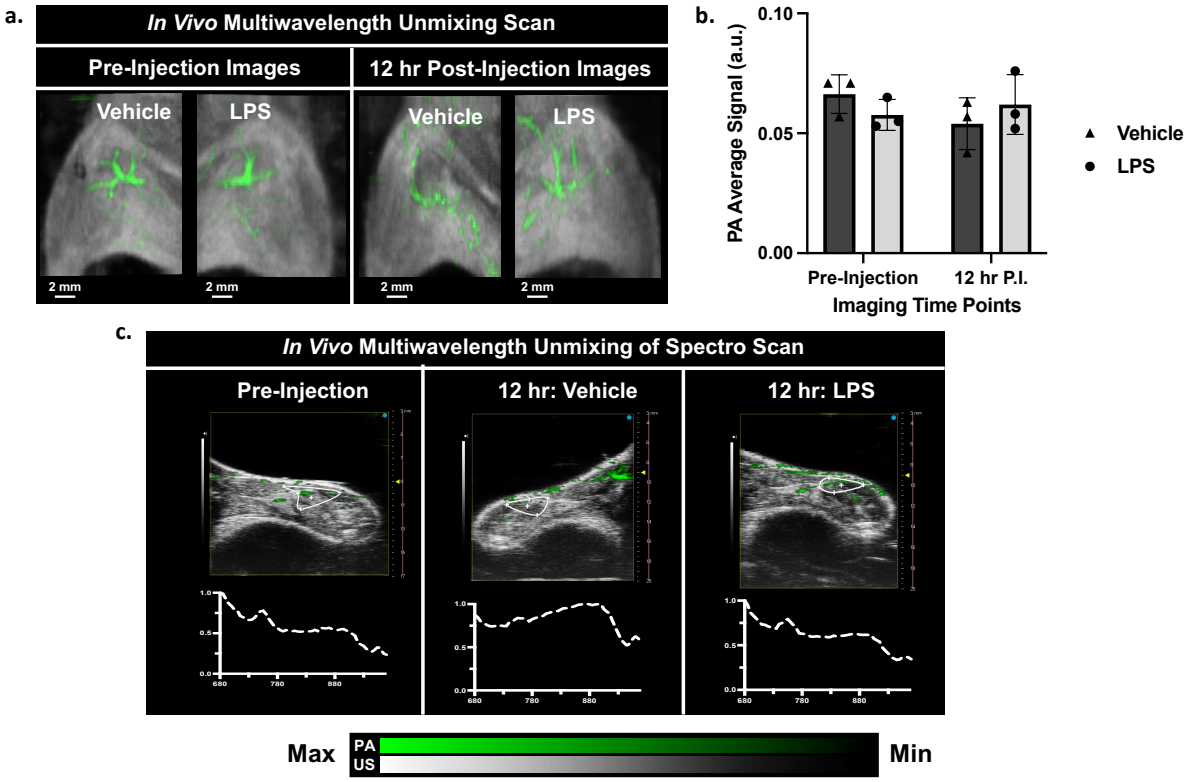

Figure 3.8. PAI of LPS-induced sterile myositis using **3-4. a.** Representative *in vivo* PA multispectral unmixing images (pre-injection and 12 hours post-injection) of mice injected I.V. with **3-4** (1 mM, 75 µL, n=3). **b.** Bar graph representing the quantified 3D PA average signal, derived from the scans in a, within the inoculation sites of the mice throughout the study. **c.** Spectral analysis of the inoculation sites pre-injection & 12 hours post-injection. ROIs drawn over the inoculation sites (white) in the unmixed Spectro scans with the spectral signature with the ROI overlaid (White dashed line indicates the spectral signature of **3-4**). For all multiwavelength unmixing scans, greyscale= Ultrasound (US) images overlaid with unmixed PA signal, where green= **3-4**. The signals from oxygenated and deoxygenated hemoglobin have been subtracted from each image.

3.1.2.2.7 Photoacoustic Imaging of S. aureus-Induced Bacterial Infection using 3-4.

Following administration of **3-4** (75 µL, 1 mM), the multiwavelength unmixing scans depicted a notable PA signal (green) within *S. aureus*-infected muscle (12 hr post-injection) compared to the background (pre-injection) and the vehicle control muscle (contralateral) (12 hr post-injection) (**Figure 3.9a**). This was verified by quantifying the PA average signal within the images (**Figure 3.9b**), where, at 12 hr post-injection, the infected muscle (0.176 ± 0.011 a.u.) was

significantly higher than the pre-injection background (0.081 ± 0.004 a.u., where $P \leq 0.03$) and the vehicle control muscle (0.076 ± 0.017 a.u., where $P \leq 0.03$). The T/NT tissue (infected vs. vehicle control muscle) and S/B (infected muscle pre- vs. 12 hr post-injection) ratios were 2.40 ± 0.49 and 2.17 ± 0.05, respectively. Spectral analysis was used to verify that the signal in the infection site matched the expected spectral signature of **3-4**, with a signal maximum of 810 nm (**Figure 3.9c**). The signal associated with deoxygenated hemoglobin (760 nm) was present in all the tissue.

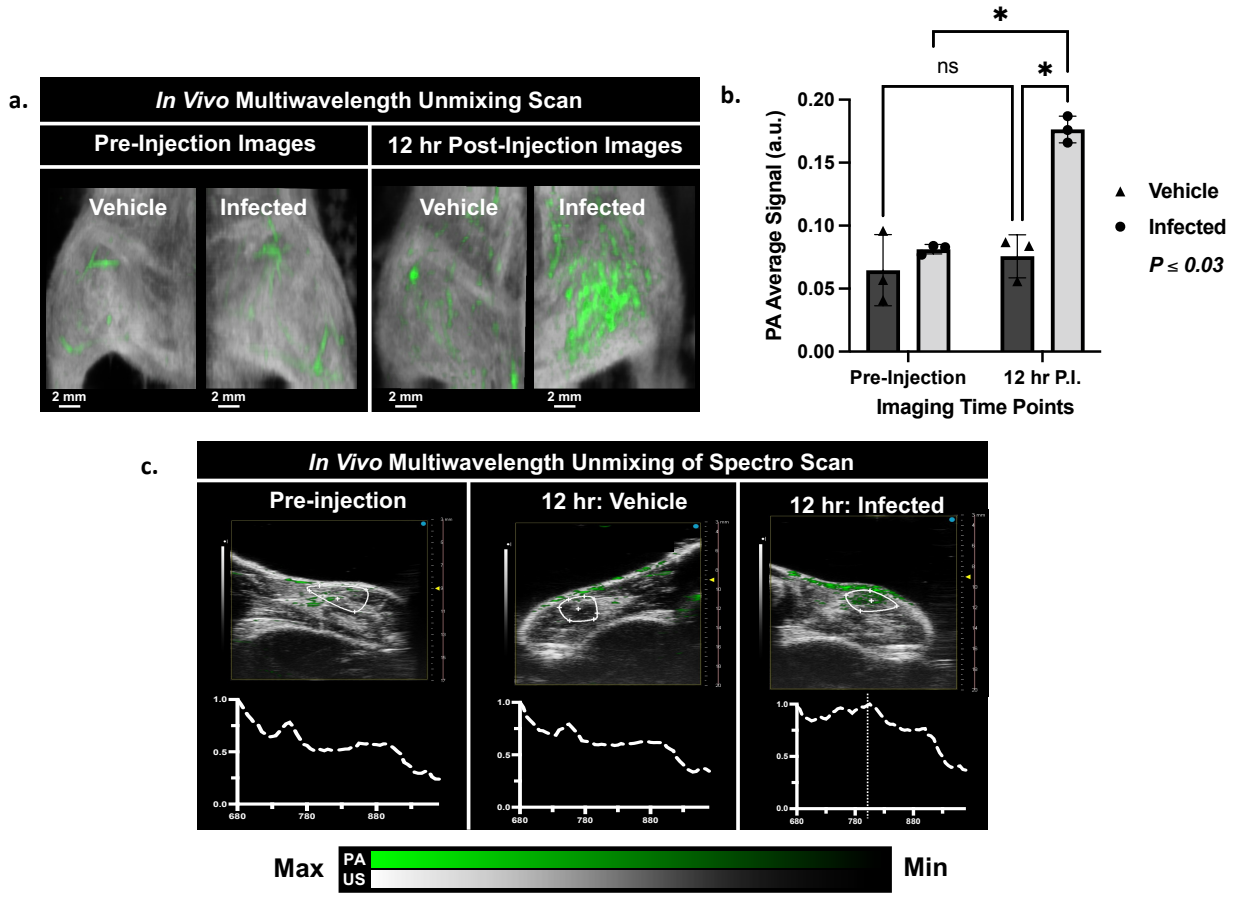

Figure 3.9. PAI of *S. aureus*-induced myositis using **3-4.** a. Representative *in vivo* PA multispectral unmixing images (pre-injection and 12 hours post-injection) of mice injected I.V. with **3-4** (1 mM, 75 µL, n=3). **b**. Quantified 3D PA average signal, derived from the scans in **a**, within the inoculation sites of the mice throughout the study. **c**. Spectral analysis of the inoculation sites pre-injection & 12 hours post-injection. ROIs drawn over the inoculation sites (white) in the unmixed Spectro scans with the spectral signature with the ROI overlaid (White dashed line indicates the spectral signature of **3-4**). For all multiwavelength unmixing scans, greyscale= US images overlaid with unmixed PA signal, where green= **3-4**. The signals from oxygenated and deoxygenated hemoglobin have been subtracted from each image.

3.1.2.3 Discussion & Conclusion:

PA phantom analysis of **3-4** shows that it possesses a unique PA spectrum as compared to endogenous chromophores, oxygenated and deoxygenated hemoglobin. The PA signal of the dye was assessed in whole blood, using a concentration of 64 µM, which represents injecting 75 µL of 1 mM of **3-4**, (a dose recommended in the reagent kit), into the circulating blood volume of a 20g mouse.[39] The signal from **3-4** was observable in the spectrum of the sample and successfully quantified after unmixing it from the blood chromophores, demonstrating that the amount of dye used in this experiment should be sufficient to produce an observable PA signal *in vivo*.

Bacteria binding of **3-4**, using both fluorescence and PAI, was assessed following previously published protocols.[35] Using sealed phantom tubing, a PA S/B ratio of 3.06 ± 0.30 was obtained when comparing the bacterial cell suspension incubated with **3-4** versus the vehicle control. This aligned with the ratio that was determined using fluorescence intensity measurements (S/B= 2.98 ± 0.20), indicating that PA detection is consistent with the fluorescence measurements routinely used for *in vitro* studies.

To facilitate future comparisons using novel optimized PIPs, quantitative biodistribution analysis of PSVue794 was pursued. Reliable quantitation using FI and PAI is highly dependent on the solubility of the constructs and the absence of aggregation. This is because cyanine dyes, such as PSVue794, tend to aggregate in aqueous media, which induces shifts in the photophysical properties of the compound, and could impact the signal intensities observed *in vivo*.[40,41] Building on previous reports that employed DPA as a chelator for the ^{99m}Tc-tricarbonyl core,[37,38] PSVue794 was successfully radiolabelled to generate a gamma-emitting version of PSVue794 (**3-8**). Radiolabeling of PSVue794 enabled quantitative whole-body distribution analysis of the

compound in a mouse model of bacterial infection and will facilitate future quantitative comparisons using different PIPs and models of disease.

The biodistribution of **3-8** in healthy naïve and infected mice were evaluated. By 12 hr post-injection, it was found that the radiolabeled PIP was predominantly processed by the hepatobiliary system, exhibited by the elevated concentrations observed in the gall bladder, large intestine, liver, and spleen. The biodistribution profile of **3-8** was comparable to previously reported data on a ^{99m}Tc-labeled ZnDPA compound, where localization to gastrointestinal organs was observed.[38] No significant differences were found in the % ID/g of the spleen and liver in healthy naive vs. infected mice, which indicated that uptake in these organs was most likely driven by the lipophilic nature of the dye and it's technetium (I) tricarbonyl core. Significantly higher %ID/g was observed in the gall bladder and large intestine/caecum of the infected mice compared to the naïve mice. While this result was not further explored, recent literature reports highlight the possibility of bacteria spreading from the bloodstream into the gall bladder, where it can then seed into the intestines.[42] Additionally, it is possible that the stress of the bacterial infection on the immune system of the mice induced a state of dysbiosis, a phenomenon where imbalances in gut microbiota are commonly observed.[43]

The T/NT ratio of 10.1 ± 1.1, achieved using **3-8**, is somewhat higher than that of a previous ZnDPA derivative that had a T/NT ratio of 6.2, where ^{111}In was chelated to an alternate site on the molecule, maintaining the bis-Zn^{2+} complex.[44] The radiolabeled PIP (**3-8**) retained the ability to target sites of bacterial infection with comparable distribution properties to those of similar published radiolabelled probes.[38]

Subsequent studies utilizing PAI demonstrated the ability of the PIP to localize to and generate detectable PA signal at sites of bacterial infection as compared to sites of sterile

inflammation. Bacterial cells activate inflammatory pathways, typically upon cellular recognition of pathogen-associated molecular pattern molecules produced by the bacteria.[4] Consequently, a model of sterile inflammation was produced to verify that any observed localization of the PIP in the bacterial infection was not due to innate inflammatory processes or cells present. A model of sterile myositis using LPS was adapted from literature to induce muscular and systemic inflammation.[22,45,46] Although PSVue794 has affinity towards the anionic components of apoptotic cells,[47] which has been documented to localize to sites of cell death to a lesser extent than to sites of bacterial infection,[48] the models used here were designed to eliminate this variable in order to showcase the specific interaction of the PIP with bacterial cells over immune cells that are likely also present at the site of bacterial infection. The histological assessment of tissues treated with LPS or with *S. aureus* confirmed that the two conditions effectively induced states of sterile or bacteria-induced myositis, respectively. The T/NT and the S/B ratios derived from the PAI analysis in LPS-induced (T/NT= 1.04 ± 0.17, S/B= 1.07 ± 0.11) and *S. aureus*-induced (T/NT= 2.40 ± 0.49, S/B= 2.17 ± 0.05) myositis showed that the Zn-DPA targeting moiety on **3-4** facilitates the specific localization of the PIP at sites of bacterial infection.

In conclusion, we demonstrated that compounds **3-4** and **3-8** can be used to specifically detect sites of bacterial infection over sites of sterile inflammation and showcased the potential of using PAI as a modality to detect infection. While **3-4** is currently commercially available, further optimization of bacteria-targeting PIPs to achieve superior aqueous solubility and optical absorption could lead to further improvements in T/NT and S/B ratios by facilitating better clearance profiles in healthy tissues along with improved signal unmixing capabilities from blood. Additionally, efforts toward addressing the role of cell death in clinically relevant models of

healthcare-associated bacterial infections will be critical in establishing the utility of ZnDPA-based diagnostic agents for imaging bacterial infection.

3.1.2.4 Methods & Materials:

General Materials, Instrumentation, and Methods. Unless otherwise noted, all reagents and solvents were ACS grade, purchased from commercial suppliers, and used without further purification. Deionized water was used for all experiments requiring the use of water. PSVue794 Reagent Kit was purchased from Cedarlane Labs (25101-1) and was used to prepare PSVue794 (**3-4**) from the Apo-PSS precursor (**3-3**) and a solution of 2 mM Zinc nitrate, 30 minutes before use. Lipopolysaccharide from *Escherichia coli* O55:B5, ready-made solution (1 mg/mL), 0.2 μm filtered, was purchased from Sigma-Aldrich (Cat#L5418-2ML).

Absorbance and fluorescence scans were collected on a Tecan Infinite M1000 plate reader using Corning 96-well, clear bottom plates (non-treated surface) (Corning 3631), PerkinElmer film was used to seal any plates containing bacteria cells. Microwave reactions were performed using a Biotage Initiator 60 microwave reactor under standard settings. Radio-TLC was performed using a Bioscan AR-2000 imaging scanner on iTLC-SG glass microfiber chromatography paper (SG10001, Agilent Technologies) plates and Aluminum oxide plates using 1% HCl in methanol as the eluent. For each TLC performed, plates were spotted with ~3 μL (481 kBq). A background (represented as a blue underline) was integrated on each radio-TLC plate and subtracted from the integration of each peak. Sep-Pak C18 Plus Light Cartridge (55-105 μm) (WAT023501, Waters) was used for isolating radiolabeled products. High-performance liquid chromatography (HPLC) of the radiolabeled compounds was performed on a Waters 1525 Binary (Midford, MA), monitored simultaneously with 2998 photodiode array detector at 245/700 nm and in line radioactivity Bioscan gamma detector with NaI (TI) scintillator using the Empower software package. Analytical HPLC of each compound was performed on a Gemini 5 μm C18 110 Å (250 × 4.6 mm) Column (00G-443-E0, Phenomenex), operating at a flow rate of 1 mL/min. A PerkinElmer Wizard 1470 automatic gamma counter was used to measure the amount of radioactivity in samples from the bacteria binding assay and the biodistribution studies.

Pertechnetate [^{99m}Tc][TcO_4]$^-$ was obtained in 0.9% w/v saline from a ^{99}Mo/^{99m}Tc generator supplied by Lantheus Medical Imaging. ***Caution:*** *these materials are radioactive and should only*

be used in a properly licensed and equipped facility. Potassium boranocarbonate was prepared according to a literature method,[49] as was $[^{99m}Tc(CO)_3(OH_2)_3]^+$.[37]

HPLC Method: Solvent A: Water + 0.1% Trifluoroacetic acid (TFA), Solvent B: Acetonitrile + 0.1% TFA. Gradient: 0-2 min 90% A, 2-6 min 90-40% A, 6-8 min 40% A, 8-10 min 40-10% A, 10-11 min 10-90% A, 11-15 min 90% A.

Photoacoustic Phantom Imaging: PA phantom work was performed using a Vevo Phantom imaging chamber (see **Figure AI-17**) and the Vevo-3100/LAZR-X (FUJIFILM VisualSonics, Inc., Toronto, ON, Canada) imaging system equipped with a 680-970 nm laser. Samples were injected into Vevo Contrast Agent Phantom tubing (PN52807) that was threaded into the Vevo Phantom chamber. A 30 MHz, linear array US transducer equipped with integrated fibre optic cables (MX400 and LZ-400 [15-30 $mJ(cm^3)^{-1}$, 20 Hz repetition rate, 10 ns pulse width], FUJIFILM VisualSonics, Inc., Toronto, ON, Canada) was positioned overtop of the tubes.

Spectral analysis was performed using 'Spectro' scans, where the PA signal of a 2D, x,y-cross-section of a sample is quantified at each wavelength (690-970 nm, step size of 5 nm, ~1 min/spectro scan, axial resolution of 50 μm) and is used to plot the spectral curve or 'spectral signature' from a defined region of interest (ROI). From this, the signal intensity of the chromophore of interest can be quantified by the signal unmixing algorithm utilized in the VevoLAB software (VisualSonics, Inc., Toronto, ON, Canada). This scan was also be used to demonstrate the merged spectra of multiple chromophores mixed. The 2D multispectral unmixing analysis was then performed on the spectrum, where the pre-programmed PA spectra of oxygenated and deoxygenated hemoglobin were unmixed from the spectra of **2**, and were taken for each material in triplicate. Signals generated at 680, 692, 802, 924, and 942 nm were utilized in the signal unmixing algorithm. Images from the multiwavelength unmixing scans have been displayed using the render mode with the PA signal overlaid on US B-mode (greyscale) signal of a cross-section of tubing. All image processing was carried out using the VevoLAB software. A ROI was drawn around the US image of the tube and, applying ROIs of the same size and shape to each image, a spectrum of the PA average signal was generated from the overlaid PA data of each image.

PA Signal Analysis of 3-4: Samples of **3-4** at 20 μM in Diluent X and **3-4** at 1 mM in Diluent X diluted to 64 μM in whole mouse blood (collected from cardiac puncture using EDTA coated syringes & immediately supplemented with 10% EDTA in 0.9% w/v saline [0.15 g/mL]) were prepared alongside appropriate blank controls. The samples were injected into Vevo contrast agent phantom tubing and Spectro scans were taken of the material in triplicate. The data was analyzed as described in 'Photoacoustic Phantom Imaging'.

Preparation of Bacterial Overnight (O/N) Culture: *S. aureus* cells (ATCC; 25923) were incubated in tryptic soy broth (TSB) liquid media at 37 ˚C (450 rpm) for 18 hours. The cells were centrifuged (2 minutes at 10 000 xg) and the pellet was resuspended in Hank's Balanced Salt Solution (HBSS) to an OD_{600}= 19.9 for *in vitro* assay, or to an OD_{600}= 8.43 for *in vivo* studies.

***In Vitro* Bacteria Binding of 3-4 using Fluorescence and Photoacoustic Detection: 3-4** (10 μM, final concentration) was incubated with 50 μL of *S. aureus* suspension (1×10^9 CFU in 50 μL of HBSS) or 50 μL of HBSS (no-cell control), for 10 minutes in triplicate. The samples were washed 3 times and the pellet was resuspended in 250 μL of HBSS. 200 μL sample and 200 μL stock solution were transferred to a black flat clear bottom 96-well plate. A fluorescence scan (Ex= 736 nm; Em= 746-850 nm) was performed. The fluorescence intensities (at 829 nm) of blank samples were subtracted from samples of **3-4** incubated with or without bacteria and the change in intensity was evaluated. Approximately 20 μL of each sample was then injected into Vevo contrast agent phantom tubing. The ends of each tube were sealed with heat and Spectro scans were acquired of each sample in triplicate. The data was analyzed as described in the 'Photoacoustic Phantom Imaging' section.

Radiosynthesis of [^{99m}Tc]Tc-PSVue794 (3-8): 400 μL of Apo-PSS794 (**3-3**) (0.5 mg in 400 μL of methanol [0.87 mM]), was combined with 400 μL of $[^{99m}Tc(CO)_3(OH_2)_3]^+$ (**3-6**) (Prepared using a procedure reported by Causey, *et al*. (2008))[37] (370 MBq, dissolved in 0.9% w/v saline, pH= 6-6.5), and mixed at room temperature for 1 hour. Radio-TLC (1% HCl in methanol eluant) and HPLC (method A, UV=700 nm t_r= 8 min; γ trace t_r= 8.8 min) were used to determine the radiochemical conversion (~85-90%). The material was then diluted in 10 mL of water and loaded onto a C18 cartridge for purification. Water was used to elute any remaining **3-6** from the

cartridge and ethanol was used to elute **3-7** in 99% purity based on Radio-TLC. The ethanol was evaporated, and the material was reconstituted in 171.5 µL mL of Diluent X. 171.5 µL of $Zn(NO_3)_2$ (0.015 M in Diluent X) was added to **3-7** and stirred at 37˚C for 30 minutes. The material was then adjusted to the correct concentration using 10% ethanol in 0.9% w/v saline for subsequent experiments. **HPLC** UV=700 nm t_r= 8 min; γ trace t_r= 8.8 min.

Stability Testing of 3-8: The stability of compound **3-8**, incubated in formulation buffer (Diluent X) (room temperature) and in mouse serum (37˚C), was assessed at 0, 2 and 18 hours. At each time point an aliquot of the material was analyzed by radio-TLC (eluting in 1% HCl in methanol). For serum samples, the aliquot was mixed with cold acetonitrile and pelleted by centrifugation to remove the serum proteins.

***In Vitro* Bacteria Binding of 3-8:** In a clear, conical bottom 96-well plate, 200 µL of **3-8** (37 kBq) in 10% ethanol in 0.9% w/v saline was incubated with *S. aureus* suspension (1×10^9 CFUs in 50 µL of HBSS) or 50 µL of HBSS (no-cell control), for 10 minutes (n=3 per condition). The sealed plate was centrifuged for 1 minute at max speed. The supernatants were removed and 200 µL of HBSS was added to resuspend the pellet. This was repeated a total of 3 times to remove the unbound fraction of **3-8**. The washed pellet was resuspended in 200 µL of HBSS, 150 µL was transferred into gamma counting tubes, and the amount of radioactivity in each tube was determined using a gamma counter. A 100 µL aliquot of **3-8** (from the 0.37 MBq stock) was measured and corrected to represent a 100% signal control for each concentration. The counts per minute (CPM) from each sample were corrected based on the dispensed volume measured and specific binding was calculated by subtracting the non-specific binding (CPM from the samples without bacteria cells) from the total binding (CPM from the samples with bacteria cells). The percent binding of each sample was calculated using **Equation AII-2**.

Animal Studies: All procedures were conducted according to the guidelines of the Committee for Research and Ethics Issues of the International Association for the Study of Pain, and guidelines established by the Canadian Council on Animal Care and the McMaster University Animal Research Ethics Board. In each animal study 7-10 week-old female BALB/c mice (Charles River Laboratories, Raleigh, NC), weighing around 20 g, were used. The mice were sterile housed

and maintained at 21 ˚C with a 12-hour light/dark cycle and were provided autoclaved food and water *ad libitum*.

***Staphylococcus aureus*-Induced Myositis Model:** An aliquot of *S. aureus* suspension (1×10^8 CFUs in 50 µL of HBSS) was innoculated intramuscularly (I.M.) on the right hindlimb. 50 µL of the vehicle control, HBSS, was injected IM into the contralateral hindlimb. 18 hours post-inoculation of the bacteria, tissues were collected and analyzed as described in the section titled 'Histological Analysis'. Animals were end-point monitored throughout the duration of the study.

Biodistribution of 3-8: 4 healthy mice and 4 mice with established *S. aureus*-induced myositis were injected in the lateral tail vein with 200 µL (0.74 MBq) of **3-8** formulated in 10% ethanol in 0.9% w/v saline. Animals tolerated administration of the PIPs well and end-point was not reached throughout the study. 12 hr post-injection, animals were anesthetized and euthanized by cardiac puncture followed by cervical dislocation. Fluids, bone (knee), and select tissues were collected, weighed, and quantified on a gamma counter. Decay correction was used to normalize organ activity measurements to the time of dose preparation for data calculations. Data are expressed as percent injected dose per gram of tissue/fluid (%ID/g).

Lipopolysaccharide-Induced Myositis Model: Lipopolysaccharide (LPS) (1 mg/mL, 100 µL/mouse) was injected intramuscularly (IM) on the right hindlimb. 50 µL of the vehicle control, HBSS, was injected IM into the contralateral hindlimb. 15 hours post-injection of LPS, tissues were collected and analyzed as described in the section titled 'Histological Analysis'. Animals were end-point monitored throughout the duration of the study.

Histological Analysis: Mice were euthanized with sodium pentobarbital and perfused with lactate Ringer's solution and tissues were fixed with 10% formalin. The right and left hind limb, and the spleen were collected and decalcified in a solution of 10% formalin + 8% EDTA. The trimmed tissues were embedded into paraffin, sliced, and stained with hematoxylin-eosin (H&E). A veterinary research pathologist, blinded to the treatments, examined the slides under a Nikon Eclipse 50i light microscope and morphological features of the tissues were described. One slice of each tissue (the treated hindlimb, the contralateral hindlimb, and the spleen) from each mouse

in the LPS- and bacteria-induced myositis groups and 1 naïve mouse were analyzed and contributed to the main diagnoses of each condition. The images selected for the figure are representative for each condition and taken from one mouse per group.

The bone marrow was present within the slices of the hindlimbs due to the decalcification of bone. The microphotographs were only provided for the tissues where pathological morphology was observed. This is true for the spleen as well. While the spleen tissue was analyzed from each mouse within each group, the microphotographs were only provided from tissues that displayed morphological changes relative to healthy tissue.

***In Vivo* Photoacoustic Imaging Studies:** PAI was performed using the Vevo-3100/LAZR-X imaging system. Mice were anesthetized, and the fur of their right hindlimb was thoroughly removed before being placed in a prone position on a platform that enabled the monitoring of their respiration and heart rate. A generous amount of US gel was applied before imaging with the transducer (MX400/LX400) positioned over the leg. At each imaging time point, Spectro scans and 3D multispectral unmixing scans were taken of each hindlimb. The transducer was positioned laterally overtop of the hindlimb, corresponding with the inoculation site. Scan distances averaged 20 mm and scans were taken every 0.33 mm (~ 7min/3D scan).

3D multiwavelength unmixing scans were performed, where the pre-programmed PA spectra of oxygenated and deoxygenated hemoglobin are unmixed from the spectra of **2**, across a defined z,x axis to construct images depicting dye-specific PA signal present within the hindlimb. Designated wavelengths (680, 692, 802, 924, and 942 nm), based on notable signals generated within individual chromophore spectra (oxygenated and deoxygenated hemoglobin, or **3-4**), were used by the Vevo-3100/LAZR-X unmixing algorithm. The series of 2D cross-sectional scans collected were then reconstructed by the instrument into a 3D image, where the signals from each chromophore are assigned a colour and overlaid onto a b-mode ultrasound scan. The scans are displayed as either render mode or texture mapping images where the PA signal is overlaid on US B-mode (greyscale) signal for sections of the hindlimb. Signals from oxygenated and deoxygenated hemoglobin were subtracted from the images to reduce visual complexity. The spectrally unmixed signal of **3-4**, in the 3D multiwavelength unmixing scans, was quantified using 3D ROI drawn around the inoculation sites. All signal unmixing algorithms and image processing were carried out using the VevoLAB software. Image processing consisted of signal optimization,

with parameters set the same for each image within the study. 3D regions of interest were drawn around the inoculation site.

Spectral analysis was performed using 'Spectro' scans (as described in the "Photoacoustic Phantom Imaging' section) and was used to verify whether the spectral signature of the *in vivo* signal matched that of the exogenous dye. The ROI used for each spectral curve was displayed in a multiwavelength unmixing scan (oxygenated and deoxygenated hemoglobin unmixed from **3-4**) derived from the Spectro scan.

Photoacoustic Imaging of LPS-Induced Sterile Inflammation using 3-4: 3 hours after treating mice with LPS (n=4), as described previously, the mice were injected intravenously with 75 µL of **3-4** (1 mM) and were imaged, as described in the section titled '*In Vivo* Photoacoustic Imaging Studies', on the Vevo LAZR X, pre-injection, and 12 hours post-injection. Animals tolerated administration of the PIPs well and end-point was not reached throughout the study.

Photoacoustic Imaging of *S. aureus*-Induced Bacterial Infection using 3-4: 6 hours after inoculating mice (n=4), as described previously, the mice were injected intravenously with 75 µL of **3-4** (1 mM) and were imaged, as described in the section titled '*In Vivo* Photoacoustic Imaging Studies', on the Vevo LAZR X, pre-injection, and 12 hours post-injection. Animals tolerated administration of the PIPs well and end-point was not reached throughout the study.

Statistical Analyses: Data are reported as mean ± standard error of the mean (SEM). Concentration and bacteria-binding data were analyzed by one-way analysis of variance (ANOVA). Differences between test groups and control were assessed using Dunnett's Multiple Comparison Test on GraphPad Prism version 9 (GraphPad Software, San Diego, CA). *In vivo* PAI data were analyzed using a two-way ANOVA. Differences between tested groups and control were assessed using the Tukey Test on GraphPad Prism (Threshold * $P \leq 0.05$; ** $P \leq 0.01$; *** $P \leq 0.001$).

Ancillary Information: Supporting data are available in Appendix II: Radiosynthetic characterizations, stability, and biodistribution tables.

3.2 Evaluating the Clinical Relevance of ZnDPA-Based PIPs through the Development of an Implant Infection Model

Rowan Swann[†], Luis Rafael Silva[†], Yusra Mahmood Marfatia[†], John F. Valliant[†], & Saman Sadeghi[†,*]

[†] Department of Chemistry and Chemical Biology, McMaster University, Hamilton, Ontario, Canada

Unpublished Manuscript

3.2.1 Introduction:

With increasing life expectancies, an aging population, and projections for healthcare-associated infections (HAIs) to become a leading cause of death in the coming years, clinical accessibility to robust diagnostic procedures has become crucial.[3,50,51] Current diagnostic measures, involving invasive tissue sampling procedures, not only increase the risk of additional tissue contaminations but also do not account for the heterogeneity of an infectious lesion, leading to a high rate of false negative results and increased potential to underestimate the bacterial population present.[5–7,52] Successful management of HAI, such as surgical site and implant infections, is dependent on early and accurate diagnosis, and the implementation of bacteria-specific diagnostic tracers will facilitate this goal.

It has become a standard practice to investigate the ability of bacteria-targeting vectors to differentiate between bacterial infection and sterile inflammation, two conditions that present similar outward symptoms and are not mutually exclusive biological pathologies, since bacterial infection is accompanied by an inflammatory response.[4] Previous work, outlined in Chapter 3.1.2 and work by Liu, *et al* (2012),[22] demonstrated that the commercial fluorophore PSVue794 (**3-4**) does not localize to sites of sterile inflammation, and bacterial-specificity of the probe was

concluded based on this result. However, these data sets overlook how cell death might impact accurate imaging and infection diagnosis in clinical HAIs.

Healthy mammalian cells possess a dynamic plasma membrane composed of a non-symmetrical bilayer of critical lipids and proteins that facilitate cellular functions. The outer layer of the cell membrane of healthy mammalian cells is fortified with zwitterionic phospholipids that maintain a net neutral charge, while the inner layer is largely composed of the anionic phospholipid, phosphatidylserine (PS).[53] This bilayer distribution is maintained by the active internalization of anionic phospholipids into the inner leaflet of the cell membrane. However, when apoptosis is initiated by compromised cells, ATP is reallocated to carry out the mechanisms of programmed cell death, attenuating the energy-dependant translocation of PS, and leading to increased anionic surface charges.[34,53]

This phenomenon has prompted researchers to investigate the ability of **3-4** to localize to sites of apoptosis, where cytotoxic agents,[48,54] focal beam radiation,[55] or cryoinjury[56] were used to induce cell death. In each case, a significant uptake of **3-4** was achieved at the site of injury. However, when tested alongside a bacterial infection model, Thakur, *et al* (2012) observed significantly higher uptake in the bacterial infection compared to the turpentine-induced injury.[48] This result points to the possibility that the number of bacterial cells within an infection site greatly outnumbers the apoptotic cells at a site of tissue damage. Considering our objective to validate an infection targeting PIP that can detect the early stages of bacterial infection at a surgical implant site, it is imperative to investigate a biologically representative model of a surgical implantation procedure, where relevant levels of tissue damage are generated compared to the bacterial cells present.

Information surrounding mechanisms of cell death is constantly evolving and the exact details and model generation strategies remain widely debated within the field.[57–60] This indicates the potential that the standard models currently being used to assess bacteria-targeting tracers are unrefined with respect to generating conditions relevant to surgical implantation, and conclusions on their applicability are unreliable. The work outlined here aims to develop a model that establishes the representative biological processes of medical implant infection, which will allow us to form definitive conclusions on the clinical utility of ZnDPA-based tracers and PAI as a diagnostic modality for implant-related infections.

3.2.2 Results & Discussion

3.2.2.1 Assessing the Photoacoustic Signal of Clinically Relevant Implant Materials

Various materials are utilized in the creation of implantable medical devices, tailored to their specific applications. Traditionally, alloys such as 316L stainless steel are common in orthopedic implants. However, due to stainless steel's susceptibility to corrosion and the necessity for joint cushioning, there has been a shift towards materials such as titanium, known for its bone integration properties, and ultra-high molecular weight polyethylene.[61,62] The application of PAI for image-guided assistance of device implantation has recently emerged, particularly for metallic implants, which generate strong PA signals due to their thermal conductivity.[63,64] While advantageous for image-guided implantation, this characteristic could hinder PAI's use in detecting the signal of bacteria-targeting PIPs. Therefore, in developing an implant infection model, it was essential to begin with characterizing the PA signal of potential implant materials and to determine whether the signal of the material and **3-4** could be differentiated.

An initial PA phantom study was designed to assess the PA signal from various gauges and textures of medical-grade stainless steel needles embedded in agar gel (**Figure 3.10a-b**). The PA

images were represented by the signal intensity of the metal at 750 nm, which was selected, not only because a notable signal maxima was not generated within the PA spectrum of the metal, but also due to the vast number of chromophores (including deoxygenated hemoglobin) that emit varying degrees of PA signal at this wavelength. Each gauge of stainless steel generated an intense and broad PA signal and a notable drop in signal intensity was observed as the gauge of the needle increased (a decrease in the outer diameter), and when the surface of the needle was sanded to induce surface roughness, contrary to a publication by Mitcham, *et al* (2013) (**Figure 3.10c**).[63] Although the sanded surface of the needle generated a lower PA signal, a smooth surface was pursued to not induce a charge on the metal, which would raise concerns regarding the specificity since Zn-DPA probes rely on ionic interactions with the target.

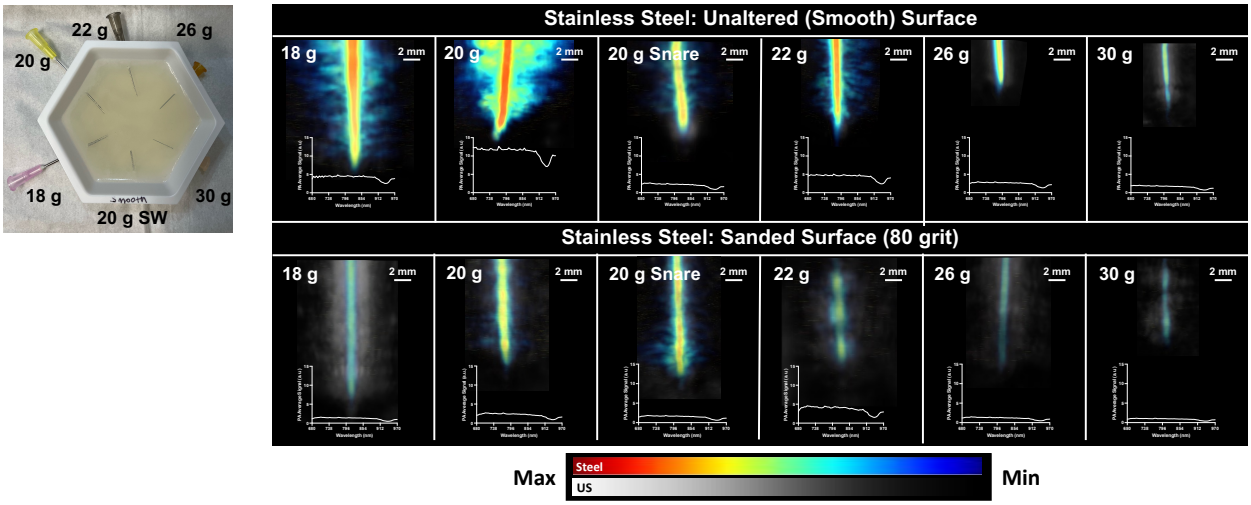

Figure 3.10. Assessing segment gauge and PA Imaging. **a.** Photograph of phantom imaging setup. Medical grade stainless steel needles of various gauges and a 20-gauge stainless steel snare wire (SW) were inserted into a phantom mould and set in an agar gel. **b.** Chart of needle gauges and their outer diameter (OD). **c.** 3D PA scans (750 nm) of the segments in the agar gel phantom and their corresponding PA spectrum. The segments were analyzed unaltered and after being sanded with 80-grit sandpaper.

The intense PA signal generated by the stainless steel can pose a challenge in detecting lower concentrations of **3-4** in the presence of the metal. To characterize the interference and

background PA signal, the metal segment was coated in an even layer of various concentrations of **3-4**. To ensure a uniform coating of dye was achieved around the metal segment, a 30-gauge needle was first inserted into phantom tubing. After embedding the tubing in agar gel, dye was slowly injected to envelop the metal in an even layer (**Figure 3.11a-c**). The PA average signals of **3-4** and the metal (30gSS) were quantified (**Figure 3.11d**) from multiwavelength unmixing scans (**Figure 3.11e**) that were taken of the tubing to capture a 3D section that included the dye alone and the dye with the metal segment. The spectral signature of the components was defined using 'spectro' scans were quantified the average PA signal across the wavelength range of the machine (680-970 nm). In the presence of the metal, the signal of the dye was not detectable above the background for all tested concentrations, and the PA spectrum did not exhibit any notable characteristics of **3-4**. Based on these findings we concluded that PA detection of the dyes is not feasible if stainless steel is used as the implant materials, and alternative materials should be investigated.

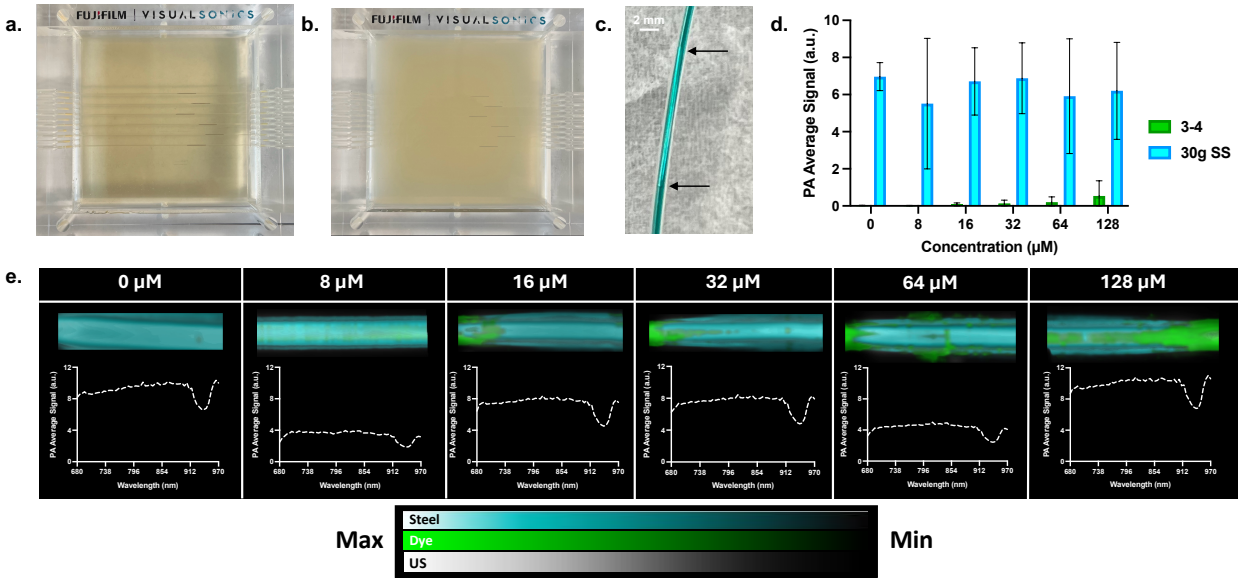

Figure 3.11. Phantom analysis of **3-4** and 30-gauge stainless steel segments. Photographs of the phantom chamber threaded with tubing containing metal segments with freshly poured (**a**.) and fully set (**b**.) agar gel. **c.** Photograph of the tubing containing a metal segment (arrows highlight the segment ends) with an even layer of **3-4** surrounding the segment. **d.** Quantification of the PA average signal of **3-4** (at various concentrations) and the metal segment (30g SS) unmixed from

one another. **e**. Representative 3D multiwavelength unmixing scans and the corresponding spectrum of phantom tubing containing **3-4** with the metal segment. Green= **3-4**, Light Blue= 30g SS.

Considering the clinical shift towards titanium in orthopedic implants, and that it possesses a lower thermal conductivity than stainless steel, indicating that the PA signal generated by the metal may be less intense, titanium was selected as the next implant material to test. The feasibility of detecting **3-4** in the presence of the metal was assessed (**Figure 3.12**), and the results demonstrated that the signal of the dye was detectable in the presence of the metal starting at 64 µM. This was evidenced by the statistically significant signal quantification (**Figure 3.12a**) between 0 µM (0.122 ± 0.013 a.u.) and 64 µM (0.303 ± 0.002 a.u., where $P = 0.05$) in addition to the characteristic signal of **3-4** present in the PA spectra of the samples containing 64, 128, and 256 µM of **3-4**, displayed in **Figure 3.12b**).

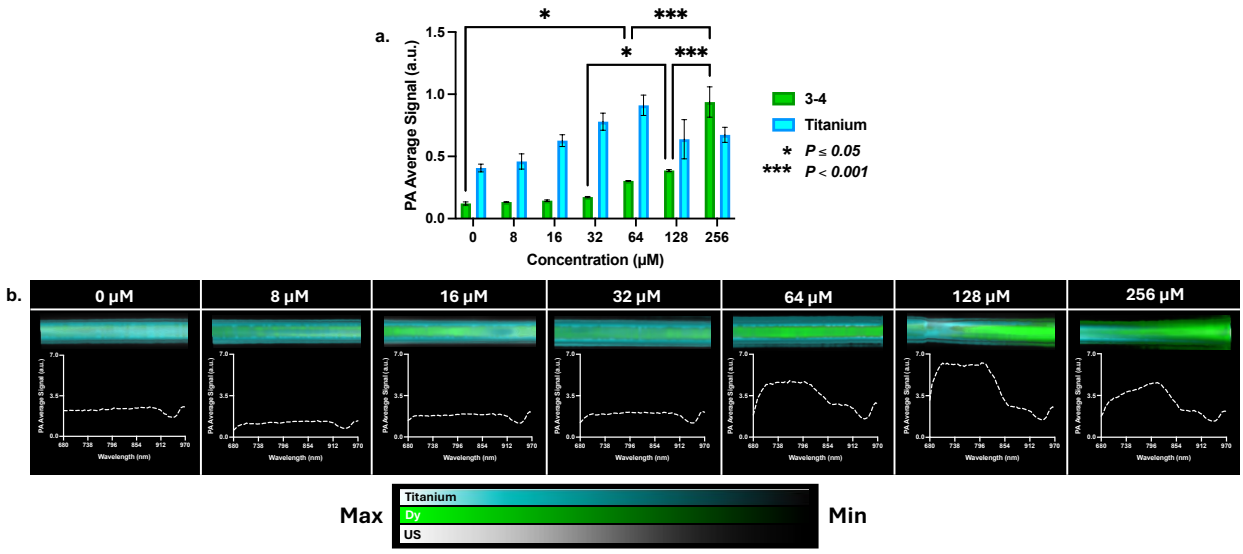

Figure 3.12. Phantom analysis of **3-4** and 30-gauge titanium segments. **a**. Quantification of the PA average signal of **3-4** (at various concentrations) or the metal segment (Titanium) unmixed from one another. **b.** Representative 3D multiwavelength unmixing scans and the corresponding spectrum of phantom tubing containing **3-4** with the metal segment. Green= **3-4**, Light Blue= Titanium.

3.2.2.2 Method of Implantation

To develop a method where the metal segment could be inserted into the gastrocnemius muscle of a mouse reproducibly, US scans were used to establish parameters for successful implantation. To detail, the depth of the metal implant and its location relative to anatomical 'landmarks' such as the tibia, were used (**Figure 3.13**). To prepare the mouse for implantation, a 20-gauge needle was aligned parallel with the tibia and used to perforate the muscle, after which, a 20- or 25-gauge metal segment could be inserted.

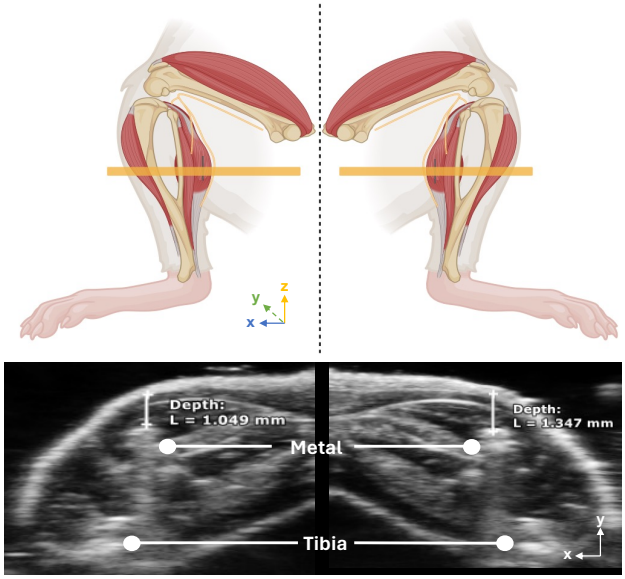

Figure 3.13. Implantation orientation. An orange border designates the approximate cross-section of the hind limb being depicted in the ultrasound scans below. The tibia was used as a visual landmark and the depth of the metal segment was assessed via the ultrasound signal generated by the metal. Figure created with BioRender.

The implantation method was replicated and assessed via US and PAI to ensure reproducibility. Various gauges of stainless steel needles, which were readily available in-house, were used to determine the best-suited size of metal segment to use that would ensure accurate and reproducible implantation in addition to minimizing the level of discomfort imposed on the mice. 3D (**Figure 3.14a**) and 2D (**Figure 3.14b**) US scans were used to depict the placement of the metal

segments, and the depth and length of the segments were consistent between each attempt. 3D multiwavelength unmixing scans were used to set a benchmark for the intensity of signal generated by the metal, *in vivo*. When imaging the left leg, the individual spectra for oxygenated and deoxygenated hemoglobin were unmixed from the metal, while in the right leg, the spectrum of **3-4** was added to the unmixing algorithm (**Figure 3.14c**). Although the dye was not actually present, this was done to determine the ability of the algorithm to distinguish between the signals of each component. The scans showed that the metal generated a high-intensity PA signal and was easily distinguished from oxy- and deoxygenated hemoglobin, and **3-4** (**Figure 3.14c**). From these results the implantation method was deemed successful, however, to minimize discomfort and align with clinical materials, a smaller gauged segment of titanium wire was purchased to carry out the remaining work.

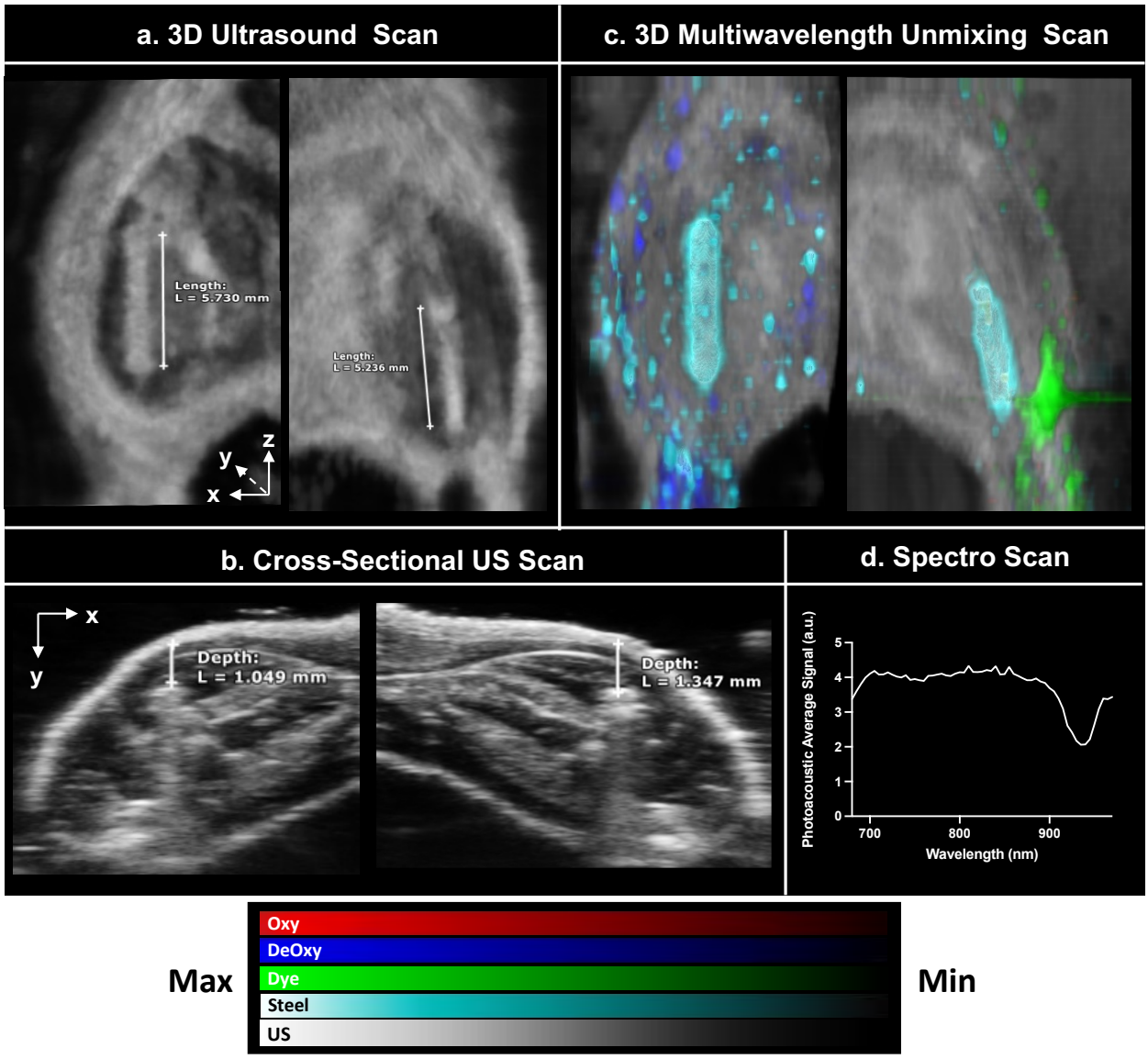

Figure 3.14. Pilot Study 1. Assessing placement of the stainless steel segment and PA signal generated by the metal *ex vivo*. **a**. Representative 3D ultrasound scan of the hindlimb showing a ~5 mm long, 20 gauge segment of stainless steel implanted into the hind limbs of mice. **b.** Cross-sectional view of the implantation. **c.** Representative 3D multiwavelength unmixing scan of the hind limbs, where light blue= stainless steel segment, green= **3-4**, dark blue= deoxygenated hemoglobin. **d**. Spectro scan depicting the PA spectrum produced by the stainless steel segment used for the multiwavelength unmixing scans.

3.2.2.3 Pilot Study 2

A second pilot study was conducted to evaluate the capability of detecting **3-4**, at a biologically relevant concentration, in the presence of the titanium segment *in vivo*. Initially, *S. aureus* cells were incubated with **3-4** (at 10% of our typical injected dose) or vehicle control buffer. After washing to remove the unbound dye, the cells were inoculated into the gastrocnemius muscle of a mouse. Using the previously outlined implantation method, a 25-gauge needle was used to perforate the muscle, followed by insertion of a 20-gauge titanium wire segment (**Figure 3.15**).

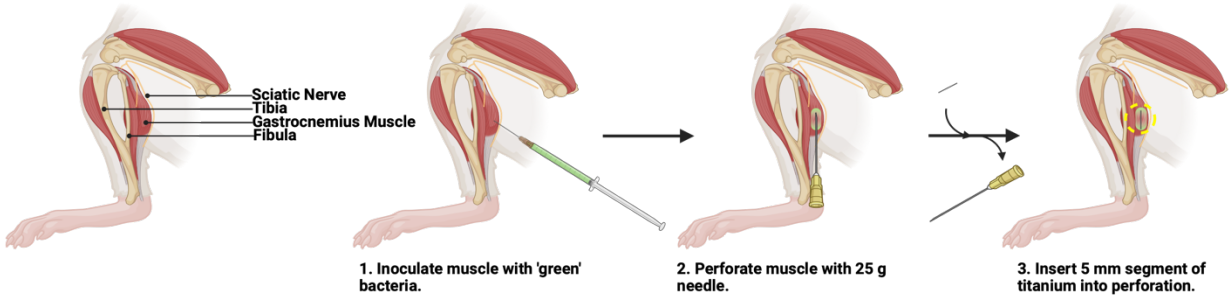

Figure 3.15. Experimental design of the second implant infection pilot study. The figure shows the procedure taken to inoculate the gastrocnemius muscle of the mice with *S. aureus* bacteria neat or pre-incubated with **3-4** ('green') and then implanting the titanium segment into the same muscle. Figure created with BioRender.

The hindlimb was imaged pre- and post-procedure to compare the PA signal and spectra generated by the metal implant & the neat vs 'green' bacteria. Initial images, with an inoculation of 100 µM of dye (~10 % of the ID/g) bound to bacteria (**Figure AII-6**), exhibited an intense PA signal for **3-4**. Subsequently, based on prior biodistribution data, the concentration of 'green' bacteria was diluted to 1% ID/g to simulate the anticipated PA signal of **3-4** reaching the infection site, following systemic circulation (**Figure 3.16**). The signal of **3-4** was detected around the metal implant in the right limb post-procedure (**Figure 3.16a**) with characteristic peaks of **3-4** in the spectrum derived from the ROI in **Figure 3.16b**. This proof-of-concept pilot study demonstrates the ability to discern the signal of **3-4** in the presence of a titanium segment, *in vivo*, and supports

the notion that the titanium signal should not impede the detection of **3-4** in a study where **3-4** is administered I.V.

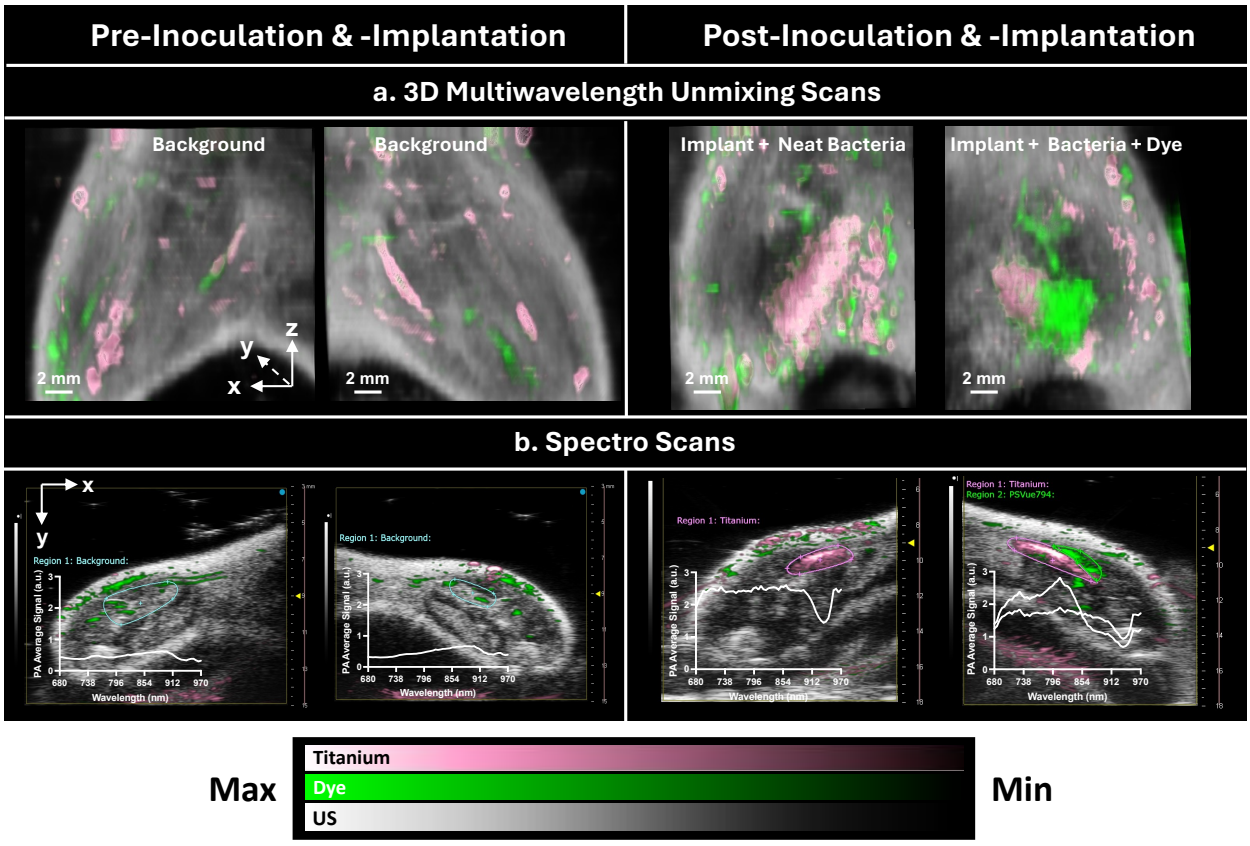

Figure 3.16. Pilot Study 2. **a.** *In vivo* 3D multiwavelength unmixing scans of mice inoculated with *S. aureus*, neat (in left limb) or pre-incubated with **3-4** (1% ID/g) (in right limb), and implanted with a 5 mm, 30-gauge titanium segment. **b.** Spectral analysis of a cross-section of the inoculation/implantation site. Pink= titanium, Green= **3-4**, Greyscale= US B-mode. The signals from oxygenated and deoxygenated hemoglobin have been subtracted from each image.

3.2.3 Conclusion & Future Directions:

Within this work, each study was designed to provide evidence on whether PAI, and more specifically, ZnDPA-based PIPs, are clinically suitable for detecting medical device infections. To this end, the PA signals of various clinically relevant device materials were assessed alongside the feasibility of detecting the signal of a bacteria-targeting dye in their presence. An implantation method was then developed, and a proof-of-concept pilot study was performed. The results

demonstrated the capability of detecting the signal of low concentrations of **3-4** in the presence of the titanium segment, *in vivo*.

Additional studies to validate a clinically relevant implant infection model would involve bacterial inoculation and metal wire implantation of mice 6 hours pre-I.V. injection of **3-4**. PA images of the hind limbs would be collected before the procedure and 12 hours post-injection to provide insight on whether enough **3-4** would localize to the infection site, after systemic circulation, to be detectable in the presence of the metal implant. A control group of mice, implanted with the metal without bacterial inoculation, would be used to demonstrate the specificity of **3-4** to localize to bacterial infection compared to sterile inflammation and cell death. Positive results from this work would support future applications of ZnDPA-based PIPs for imaging implant infection and the development of an implant model, where relevant levels of inflammation, tissue damage, and bacterial infection are generated upon implantation of a contaminated metal segment.

3.2.4 Methods & Materials:

General Materials & Instrumentation. Unless otherwise noted, all reagents and solvents were ACS grade, purchased from commercial suppliers, and used without further purification. Distilled water was used for all experiments requiring the use of water. PSVue794 Reagent Kit was purchased from Cedarlane Labs (25101-1) and was used to prepare PSVue794 (**3-4**) from the Apo-PSS precursor (**3-3**) and a solution of 2 mM Zinc nitrate, 30 minutes before use. Titanium metal wire, 99.7% trace metals basis (OD= 0.25 mm, ~30-gauge) (460400) and glycerol, acs reagent, ≥ 99.5% (G7893), was purchased from Sigma-Aldrich

Photoacoustic Phantom Imaging: PA phantom work was performed using a Vevo Phantom imaging chamber (see **Figure AI-17**) and the Vevo-3100/LAZR-X (FUJIFILM VisualSonics, Inc., Toronto, ON, Canada) imaging system equipped with a 680-970 nm laser. Samples were injected into Vevo Contrast Agent Phantom tubing (PN52807) that was threaded

into the Vevo Phantom chamber. A 30 MHz, linear array US transducer equipped with integrated fibre optic cables (MX400 and LZ-400 [15-30 mJ$(cm^3)^{-1}$], FUJIFILM VisualSonics, Inc., Toronto, ON, Canada) was positioned overtop of the tubes.

Spectral analysis was performed using 'Spectro' scans, where the PA signal of a 2D, x,y-cross-section of a sample is quantified at each wavelength (690-970 nm) and is used to plot the spectral curve or 'spectral signature' from a defined ROI. From this, the signal intensity of the chromophore of interest can be quantified by the signal unmixing algorithm utilized in the VevoLAB software (VisualSonics, Inc., Toronto, ON, Canada). The 2D or 3D multispectral unmixing scans (oxygenated and deoxygenated hemoglobin unmixed from the spectra of **3-4** and the metal) were taken for each material in triplicate. Designated wavelengths (680, 688, 760, 805, 828, 924, and 932 nm), based on notable signals generated within individual chromophore spectra (oxygenated and deoxygenated hemoglobin, or **3-4** and metal), were used by the Vevo-3100/LAZR-X unmixing algorithm. Images from the multiwavelength unmixing scans have been displayed using the texture mapping and render modes with the PA signal overlaid on the US B-mode (greyscale) signal of a cross-section of tubing or in the x,z-plane. All image processing was carried out using the VevoLAB software. A ROI was drawn around the US image of the tube and, using ROIs of the same size and shape, a spectrum was generated from the overlaid PA signal. From the generated spectrum, the PA signal intensity was derived from each sample for analysis.

Agar Gel Preparation: distilled/degassed water (200 mL) glycerol (19.97 g) and agar (7 g) were mixed in a 500 mL Erlenmeyer flask and microwaved in 20-second intervals, stirring in between, until the mixture boils (~3.5 min). The mixture was poured into the desired mould and the bubbles were removed from the top of the gel before leaving to cool and set for 1 hour.

Animal Studies: All procedures were conducted according to the guidelines of the Committee for Research and Ethics Issues of the International Association for the Study of Pain, and guidelines established by the Canadian Council on Animal Care and the McMaster University Animal Research Ethics Board. In each animal study 7-10 week-old female BALB/c mice (Charles River Laboratories, Raleigh, NC), weighing around 20 g, were used. The mice were sterile housed and maintained at 21 ˚C with a 12-hour light/dark cycle and were provided autoclaved food and water *ad libitum*.

***In Vivo* Photoacoustic Imaging Studies:** PAI was performed using the Vevo-3100/LAZR-X imaging system. Mice were anesthetized, and the fur of their right hindlimb was thoroughly removed before being placed in a prone position on a platform that enabled the monitoring of their respiration and heart rates. A generous amount of US gel was applied before imaging with the transducer (MX400/LX400) positioned overtop of the leg. At each imaging time point, Spectro scans and 3D multispectral unmixing scans were taken of each hindlimb. The transducer was positioned laterally overtop of the hindlimb, corresponding with the inoculation site. Scan distances averaged 20 mm and scans were taken every 0.33 mm.

3D multiwavelength unmixing scans were performed to construct images depicting dye-specific PA signal present within the hindlimb. Designated wavelengths (680, 688, 760, 805, 828, 924, and 932 nm), based on notable signals generated within individual chromophore spectra (oxygenated and deoxygenated hemoglobin, or **3-4** and metal), were used by the Vevo-3100/LAZR-X unmixing algorithm. The series of 2D cross-sectional scans collected were then reconstructed by the instrument into a 3D image, where the signals from each chromophore are assigned a colour and overlaid onto a b-mode ultrasound scan. The scans are displayed as either render mode or texture mapping images where the PA signal is overlaid on US B-mode (greyscale) signal for sections of the hindlimb. Signals from oxygenated and deoxygenated hemoglobin were subtracted from the images to reduce visual complexity. All signal unmixing algorithms and image processing was carried out using the VevoLAB software. Image processing consisted of signal optimization, with parameters set the same for each image within the study.

In vivo spectral analysis was performed using 'Spectro' scans (as described in the "Photoacoustic Phantom Imaging' section) and was used to verify whether the spectral signature of the *in vivo* signal matched that of the exogenous dye. The ROI used for each spectral curve was displayed in a multiwavelength unmixing scan (oxygenated and deoxygenated hemoglobin unmixed from **3-4** and the metal) derived from the Spectro scan.

Pilot Study 2- Assessing the PA Signal of 3-4 in the Presence of a Metal Implant, *In Vivo*: 0.75 mL of *S. aureus* bacterial (O/N) culture (1×10^{11} CFUs/mL) was aliquoted into a 1.5 mL microcentrifuge tube and incubated with either 0.1 mL **3-4** (850 μM) or 0.1 mL of HBSS for 10 minutes. The bacterial pellets were washed with HBSS 2 times and resuspended in 0.75 mL of

HBSS. An aliquot of each stock was diluted 10× and 50 μL of each solution was inoculated into the right hind limb (bacteria + Dye) or the left hind limb (bacteria + HBSS, 'neat'). Using a 25-gauge needle, the gastrocnemius muscle was perforated, and a 5 mm segment of titanium wire (30-gauge) was then inserted. The mouse was then PA imaged as described in the *In Vivo* Photoacoustic Imaging section.

Statistical Analyses: Data are reported as mean ± standard error of the mean (SEM). Concentration and bacteria-binding data were analyzed by one-way analysis of variance (ANOVA). Differences between test groups and control were assessed using Dunnett's Multiple Comparison Test on GraphPad Prism version 9 (GraphPad Software, San Diego, CA). *In vivo* PAI data were analyzed using a two-way ANOVA. Differences between tested groups and control were assessed using the Tukey Test on GraphPad Prism (Threshold * $P \leq 0.05$; ** $P \leq 0.01$; *** $P \leq 0.001$).

Ancillary Information: Supporting data are available in Appendix II: *In vivo* pilot study 2 photoacoustic imaging data.

3.3 Conclusions & Future Directions for PAI of Bacterial Infection

In this chapter, two bacteria-targeting PIPs, **3-2** and **3-4**, were investigated for their ability to image sites of bacterial infection. Although **3-2** was able to interact specifically with bacteria *in vitro*, the severe aggregation of the probe in its injectable formulation and the significant PA signal overlap with deoxyhemoglobin prompted us to focus our attention on the assessment of PIPs with fewer solubility issues and better PA properties. A commercially available ZnDPA-based NIR dye, **3-4**, was then sourced and used as an alternative PIP for evaluating the bacterial-specificity of ZnDPA-based probes and the suitability of PAI as a modality for diagnosing bacterial infections.

3-4 was demonstrated to specifically detect sites of bacterial infection compared to sterile inflammation, and PAI was determined to be a suitable modality for detecting soft-tissue infections. A series of proof-of-concept studies were then followed to demonstrate the feasibility of detecting **3-4** in the presence of a titanium implant. Results from these studies suggested that **3-4** could be detected in the presence of the implant, *in vivo*. However, further follow-up studies are required to show *in vivo* localization & detection of **3-4** at the sites of infection, in the presence of the implant.

Overall, PAI remains a promising modality for the detection of HAIs. In the context of implant infection, the PA signal generated by implant materials, such as metals that conduct heat, is anticipated to remain a key challenge. Therefore, the continued development of optimized PIPs, where ideal bacteria-targeting vectors are combined with strong PA contrast agents, will maintain the significance of PAI for applications in diagnosing bacterial infections. Towards this goal, Zn-DPA has thus far provided promising results, however, expanding the scope of targeting vectors used in the design of novel PIPs could improve the percentage of the injected dose that localizes to the bacterial infection, which could improve the ability to image metal-based implant infections.

A promising bacterial targeting vector to consider is the antimicrobial peptide Ubiquicidin (UBI), which has demonstrated specificity to both gram-positive and gram-negative bacterial strains.[65,66] A synthetic derivative of UBI, UBI-29-41, radiolabeled with ^{99m}Tc is currently under clinical investigation and has demonstrated several advantages for infection imaging.[11,67–69] Notably, its rapid localization to infectious lesions within 1-2 hours, and its high bacterial specificity and SPECT sensitivity provide the possibility for quick patient diagnoses with low rates of false negative or positive. Clinical PET studies utilizing a [^{68}Ga]Ga-DOTA-derivative have also yielded promising results.[10,70] While preclinical investigations have explored attaching fluorescent dyes to the protein,[71,72] assessing the utility of these probes for PAI has not been documented.[73] Thus, expanding our investigations to include UBI-derived PIPs is warranted.

Bacteria-specific metabolizable sugars represent another compelling class of targeting vectors for broadening the scope of bacteria imaging work. Although maltodextrin sugar derivatives have yet to advance into clinical trials, preclinical studies have showcased their notable bacterial specificity and signal sensitivity across PET, fluorescence, and PAI modalities.[15,32,33,74,75] Furthermore, their capacity to penetrate bacterial biofilms, a protective polymer matrix produced by bacteria that imparts antimicrobial resistance,[76] is a rare characteristic among bacterial-targeting vectors and adds to their appeal. This could revolutionize the diagnosis of medical implant HAIs, which are notoriously prone to biofilm formation.[77]

The synthesis of novel PA dyes with enhanced aqueous solubility and optimized PA signal generation properties is underway. Parallel to expanding the scope of targeting vectors used, this endeavour will support the ongoing effort to develop the next generation of bacteria-targeting PIPs. Chapter 4 of this thesis is dedicated to the design, synthesis, and evaluation of a general-purpose dye that can be utilized to formulate a diverse array of disease-targeting PIPs.

3.4 References

(1) Signore, A.; Mather, S. J.; Piaggio, G.; Malviya, G.; Dierckx, R. A. Molecular Imaging of Inflammation/Infection: Nuclear Medicine and Optical Imaging Agents and Methods. *Chem. Rev.* **2010**, *110* (5), 3112–3145. https://doi.org/10.1021/cr900351r.

(2) Fiore, D. C.; Fettic, L. P.; Wright, S. D.; Ferrara, B. R. Antibiotic Overprescribing: Still a Major Concern. *J. Fam. Pract.* **2017**, *66* (12), 730–736.

(3) O'Neill, J. *Tackling Drug-Resistant Infections Globally: Final Report & Recommendations*; The Review on Antimicrobial Resistance, 2016. https://amr-review.org/sites/default/files/160525_Final%20paper_with%20cover.pdf.

(4) Chen, L.; Deng, H.; Cui, H.; Fang, J.; Zuo, Z.; Deng, J.; Li, Y.; Wang, X.; Zhao, L. Inflammatory Responses and Inflammation-Associated Diseases in Organs. *Oncotarget* **2018**, *9* (6), 7204–7218. https://doi.org/10.18632/oncotarget.23208.

(5) Eggleston, H.; Panizzi, P. Molecular Imaging of Bacterial Infections in Vivo: The Discrimination of Infection from Inflammation. *Inform. MDPI* **2014**, *1* (1), 72–99. https://doi.org/10.3390/informatics1010072.

(6) van Oosten, M.; Hahn, M.; Crane, L. M. A.; Pleijhuis, R. G.; Francis, K. P.; van Dijl, J. M.; van Dam, G. M. Targeted Imaging of Bacterial Infections: Advances, Hurdles and Hopes. *FEMS Microbiol. Rev.* **2015**, *39* (6), 892–916. https://doi.org/10.1093/femsre/fuv029.

(7) Ordonez, A. A.; Sellmyer, M. A.; Gowrishankar, G.; Ruiz-Bedoya, C. A.; Tucker, E. W.; Palestro, C. J.; Hammoud, D. A.; Jain, S. K. Molecular Imaging of Bacterial Infections: Overcoming the Barriers to Clinical Translation. *Sci. Transl. Med.* **2019**, *11* (508). https://doi.org/10.1126/scitranslmed.aax8251.

(8) Van Oosten, M.; Schäfer, T.; Gazendam, J. A. C.; Ohlsen, K.; Tsompanidou, E.; De Goffau, M. C.; Harmsen, H. J. M.; Crane, L. M. A.; Lim, E.; Francis, K. P.; Cheung, L.; Olive, M.; Ntziachristos, V.; Van Dijl, J. M.; Van Dam, G. M. Real-Time in Vivo Imaging of Invasive- and Biomaterial-Associated Bacterial Infections Using Fluorescently Labelled Vancomycin. *Nat. Commun.* **2013**, *4* (1), 2584. https://doi.org/10.1038/ncomms3584.

(9) Wang, Y.; Thompson, J. M.; Ashbaugh, A. G.; Khodakivskyi, P.; Budin, G.; Sinisi, R.; Heinmiller, A.; Van Oosten, M.; Van Dijl, J. M.; Van Dam, G. M.; Francis, K. P.; Bernthal, N. M.; Dubikovskaya, E. A.; Miller, L. S. Preclinical Evaluation of Photoacoustic Imaging as

a Novel Noninvasive Approach to Detect an Orthopaedic Implant Infection: *J. Am. Acad. Orthop. Surg.* **2017**, *25*, S7–S12. https://doi.org/10.5435/JAAOS-D-16-00630.

(10) Boddeti, D. K.; Kumar, V. Evaluation of 68Ga-DOTA-Ubiquicidin (29–41) for Imaging Staphylococcus Aureus (Staph A) Infection and Turpentine-Induced Inflammation in a Preclinical Setting. *World J. Nucl. Med.* **2021**, *20* (03), 266–272. https://doi.org/10.4103/wjnm.WJNM_103_20.

(11) Flores-Vázquez, J. G.; Rodriguez-Hernandez, L. A.; Becerril-Vega, G.; Rodríguez-Hernández, I. A.; Eguiluz-Melendez, A. G.; Suarez-Rivera, O. Technetium-99m-Ubiquicidin 29–41 SPECT-CT to Detect Postsurgical Spinal Infection: A Case Report. *Surg. Neurol. Int.* **2024**, *15*, 24. https://doi.org/10.25259/SNI_698_2023.

(12) Sathekge, M.; Garcia-Perez, O.; Paez, D.; El-Haj, N.; Kain-Godoy, T.; Lawal, I.; Estrada-Lobato, E. Molecular Imaging in Musculoskeletal Infections with 99mTc-UBI 29-41 SPECT/CT. *Ann. Nucl. Med.* **2018**, *32* (1), 54–59. https://doi.org/10.1007/s12149-017-1219-7.

(13) Nijhof, M. W.; Oyen, W. J. G.; van KÃ, A.; Corstens, F. H. M. Evaluation of Infections of the Locomotor System with Indium-111-Labeled Human IgG Scintigraphy.

(14) Romero Pastrana, F.; Thompson, J. M.; Heuker, M.; Hoekstra, H.; Dillen, C. A.; Ortines, R. V.; Ashbaugh, A. G.; Pickett, J. E.; Linssen, M. D.; Bernthal, N. M.; Francis, K. P.; Buist, G.; Van Oosten, M.; Van Dam, G. M.; Thorek, D. L. J.; Miller, L. S.; Van Dijl, J. M. Noninvasive Optical and Nuclear Imaging of Staphylococcus-Specific Infection with a Human Monoclonal Antibody-Based Probe. *Virulence* **2018**, *9* (1), 262–272. https://doi.org/10.1080/21505594.2017.1403004.

(15) Ning, X.; Lee, S.; Wang, Z.; Kim, D.; Stubblefield, B.; Gilbert, E.; Murthy, N. Maltodextrin-Based Imaging Probes Detect Bacteria in Vivo with High Sensitivity and Specificity. *Nat. Mater.* **2011**, *10* (8), 602–607. https://doi.org/10.1038/nmat3074.

(16) Zlitni, A.; Gowrishankar, G.; Steinberg, I.; Haywood, T.; Sam Gambhir, S. Maltotriose-Based Probes for Fluorescence and Photoacoustic Imaging of Bacterial Infections. *Nat. Commun.* **2020**, *11* (1), 1250. https://doi.org/10.1038/s41467-020-14985-8.

(17) Beveridge, T. J. Structures of Gram-Negative Cell Walls and Their Derived Membrane Vesicles. *J. Bacteriol.* **1999**, *181* (16), 4725–4733. https://doi.org/10.1128/JB.181.16.4725-4733.1999.

(18) Silhavy, T. J.; Kahne, D.; Walker, S. The Bacterial Cell Envelope. *Cold Spring Harb. Perspect. Biol.* **2010**, *2* (5), a000414–a000414. https://doi.org/10.1101/cshperspect.a000414.

(19) Biniecki, S.; Kabzinska, S. Synthesis of Bis-(Pyridylmethyl)-Amines. *Ann. Pharm. Fr.* **1964**, *22*, 685–687.

(20) O'Neil, E. J.; Smith, B. D. Anion Recognition Using Dimetallic Coordination Complexes. *Coord. Chem. Rev.* **2006**, *250* (23–24), 3068–3080. https://doi.org/10.1016/j.ccr.2006.04.006.

(21) Rice, D. R.; Plaunt, A. J.; Turkyilmaz, S.; Smith, M.; Wang, Y.; Rusckowski, M.; Smith, B. D. Evaluation of [111In]-Labeled Zinc–Dipicolylamine Tracers for SPECT Imaging of Bacterial Infection. *Mol. Imaging Biol.* **2015**, *17* (2), 204–213. https://doi.org/10.1007/s11307-014-0758-8.

(22) Liu, X.; Cheng, D.; Gray, B. D.; Wang, Y.; Akalin, A.; Rusckowski, M.; Pak, K. Y.; Hnatowich, D. J. Radiolabeled Zn-DPA as a Potential Infection Imaging Agent. *Nucl. Med. Biol.* **2012**, *39* (5), 709–714. https://doi.org/10.1016/j.nucmedbio.2011.12.006.

(23) Leevy, W. M.; Johnson, J. R.; Lakshmi, C.; Morris, J.; Marquez, M.; Smith, B. D. Selective Recognition of Bacterial Membranes by Zinc(Ii)-Coordination Complexes. *Chem. Commun.* **2006**, No. 15, 1595. https://doi.org/10.1039/b517519d.

(24) Leevy, W. M.; Gammon, S. T.; Johnson, J. R.; Lampkins, A. J.; Jiang, H.; Marquez, M.; Piwnica-Worms, D.; Suckow, M. A.; Smith, B. D. Noninvasive Optical Imaging of Staphylococcus Aureus Bacterial Infection in Living Mice Using a Bis-Dipicolylamine-Zinc(II) Affinity Group Conjugated to a Near-Infrared Fluorophore. *Bioconjug. Chem.* **2008**, *19* (3), 686–692. https://doi.org/10.1021/bc700376v.

(25) Slikboer, S.; Naperstkow, Z.; Janzen, N.; Faraday, A.; Soenjaya, Y.; Le Floc'h, J.; Al-Karmi, S.; Swann, R.; Wyszatko, K.; Demore, C. E. M.; Foster, S.; Valliant, J. F. Tetrazine-Derived Near-Infrared Dye as a Facile Reagent for Developing Targeted Photoacoustic Imaging Agents. *Mol. Pharm.* **2020**, *17* (9), 3369–3377. https://doi.org/10.1021/acs.molpharmaceut.0c00441.

(26) Albu, S. A.; Al-Karmi, S. A.; Vito, A.; Dzandzi, J. P. K.; Zlitni, A.; Beckford-Vera, D.; Blacker, M.; Janzen, N.; Patel, R. M.; Capretta, A.; Valliant, J. F. 125I-Tetrazines and Inverse-Electron-Demand Diels–Alder Chemistry: A Convenient Radioiodination Strategy for Biomolecule Labeling, Screening, and Biodistribution Studies. *Bioconjug. Chem.* **2016**, *27* (1), 207–216. https://doi.org/10.1021/acs.bioconjchem.5b00609.

(27) Fernández-Sampedro, M.; Fariñas-Alvarez, C.; Garces-Zarzalejo, C.; Alonso-Aguirre, M. A.; Salas-Venero, C.; Martínez-Martínez, L.; Fariñas, M. C. Accuracy of Different Diagnostic Tests for Early, Delayed and Late Prosthetic Joint Infection. *BMC Infect. Dis.* **2017**, *17* (1), 592. https://doi.org/10.1186/s12879-017-2693-1.

(28) Widmer, A. F. New Developments in Diagnosis and Treatment of Infection in Orthopedic Implants. *Clin. Infect. Dis.* **2001**, *33* (s2), S94–S106. https://doi.org/10.1086/321863.

(29) Trampuz, A.; Zimmerli, W. Diagnosis and Treatment of Infections Associated with Fracture-Fixation Devices. *Injury* **2006**, *37 Suppl 2*, S59-66. https://doi.org/10.1016/j.injury.2006.04.010.

(30) Weber, J.; Beard, P. C.; Bohndiek, S. E. Contrast Agents for Molecular Photoacoustic Imaging. *Nat. Methods* **2016**, *13* (8), 639–650. https://doi.org/10.1038/nmeth.3929.

(31) Wang, Y.; Thompson, J. M.; Ashbaugh, A. G.; Khodakivskyi, P.; Budin, G.; Sinisi, R.; Heinmiller, A.; van Oosten, M.; van Dijl, J. M.; van Dam, G. M.; Francis, K. P.; Bernthal, N. M.; Dubikovskaya, E. A.; Miller, L. S. Preclinical Evaluation of Photoacoustic Imaging as a Novel Noninvasive Approach to Detect an Orthopaedic Implant Infection: *J. Am. Acad. Orthop. Surg.* **2017**, *25*, S7–S12. https://doi.org/10.5435/JAAOS-D-16-00630.

(32) Zlitni, A.; Gowrishankar, G.; Steinberg, I.; Haywood, T.; Sam Gambhir, S. Maltotriose-Based Probes for Fluorescence and Photoacoustic Imaging of Bacterial Infections. *Nat. Commun.* **2020**, *11* (1), 1250. https://doi.org/10.1038/s41467-020-14985-8.

(33) Takemiya, K.; Røise, J. J.; He, M.; Taing, C.; Rodriguez, A. G.; Murthy, N.; Goodman, M. M.; Taylor, W. R. Maltohexaose-Indocyanine Green (MH-ICG) for near Infrared Imaging of Endocarditis. *PLOS ONE* **2021**, *16* (3), e0247673. https://doi.org/10.1371/journal.pone.0247673.

(34) Rice, D. Imaging and Therapeutic Applications of Zinc(Ii)-Dipicolylamine Molecular Probes for Anionic Biomembranes. *J. Chem. Commun.* **2016**, *52*, 8787. https://doi.org/org/10.1039/C6CC03669D.

(35) Leevy, W. M.; Gammon, S. T.; Jiang, H.; Johnson, J. R.; Maxwell, D. J.; Jackson, E. N.; Marquez, M.; Piwnica-Worms, D.; Smith, B. D. Optical Imaging of Bacterial Infection in Living Mice Using a Fluorescent Near-Infrared Molecular Probe. *J. Am. Chem. Soc.* **2006**, *128* (51), 16476–16477. https://doi.org/10.1021/ja0665592.

(36) Leevy, W. M.; Gammon, S. T.; Johnson, J. R.; Lampkins, A. J.; Jiang, H.; Marquez, M.; Piwnica-Worms, D.; Suckow, M. A.; Smith, B. D. Non-Invasive Optical Imaging of Staphylococcus Aureus Bacterial Infection in Living Mice Using a Bis-Dipicolylamine-Zinc(II) Affinity Group Conjugated to a Near Infrared Fluorophore. *Bioconjug. Chem.* **2008**, *19* (3), 686–692. https://doi.org/10.1021/bc700376v.

(37) Causey, P. W.; Besanger, T. R.; Schaffer, P.; Valliant, J. F. Expedient Multi-Step Synthesis of Organometallic Complexes of Tc and Re in High Effective Specific Activity. A New Platform for the Production of Molecular Imaging and Therapy Agents. *Inorg. Chem.* **2008**, *47* (18), 8213–8221. https://doi.org/10.1021/ic800775w.

(38) wyffels, L.; Gray, B. D.; Barber, C.; Woolfenden, J. M.; Pak, K. Y.; Liu, Z. Synthesis and Preliminary Evaluation of Radiolabeled Bis(Zinc(II)–Dipicolylamine) Coordination Complexes as Cell Death Imaging Agents. *Bioorg. Med. Chem.* **2011**, *19* (11), 3425–3433. https://doi.org/10.1016/j.bmc.2011.04.029.

(39) National Centre for the Replacement Refinement & Reduction of Animals in Research. *Blood sampling: Mouse*. https://nc3rs.org.uk/3rs-resources/blood-sampling/blood-sampling-mouse#2.

(40) Mishra, A.; Behera, R. K.; Behera, P. K.; Mishra, B. K.; Behera, G. B. Cyanines during the 1990s: A Review. *Chem. Rev.* **2000**, *100* (6), 1973–2012. https://doi.org/10.1021/cr990402t.

(41) West, W.; Pearce, S. The Dimeric State of Cyanine Dyes. *J. Phys. Chem.* **1965**, *69* (6), 1894–1903. https://doi.org/10.1021/j100890a019.

(42) Bachta, K. E. R.; Allen, J. P.; Cheung, B. H.; Chiu, C.-H.; Hauser, A. R. Systemic Infection Facilitates Transmission of Pseudomonas Aeruginosa in Mice. *Nat. Commun.* **2020**, *11* (1), 543. https://doi.org/10.1038/s41467-020-14363-4.

(43) Belkaid, Y.; Hand, T. W. Role of the Microbiota in Immunity and Inflammation. *Cell* **2014**, *157* (1), 121–141. https://doi.org/10.1016/j.cell.2014.03.011.

(44) Rice, D. R.; Plaunt, A. J.; Turkyilmaz, S.; Smith, M.; Wang, Y.; Rusckowski, M.; Smith, B. D. Evaluation of [111In]-Labeled Zinc–Dipicolylamine Tracers for SPECT Imaging of Bacterial Infection. *Mol. Imaging Biol.* **2015**, *17* (2), 204–213. https://doi.org/10.1007/s11307-014-0758-8.

(45) Frost, R. A.; Nystrom, G. J.; Lang, C. H. Lipopolysaccharide Regulates Proinflammatory Cytokine Expression in Mouse Myoblasts and Skeletal Muscle. *Am. J. Physiol.-Regul. Integr. Comp. Physiol.* **2002**, *283* (3), R698–R709. https://doi.org/10.1152/ajpregu.00039.2002.

(46) Bivona, J. J.; Crymble, H. M.; Guigni, B. A.; Stapleton, R. D.; Files, D. C.; Toth, M. J.; Poynter, M. E.; Suratt, B. T. Macrophages Augment the Skeletal Muscle Proinflammatory Response through TNFα Following LPS-induced Acute Lung Injury. *FASEB J.* **2021**, *35* (4). https://doi.org/10.1096/fj.202002275RR.

(47) Hanshaw, R. G.; Lakshmi, C.; Lambert, T. N.; Johnson, J. R.; Smith, B. D. Fluorescent Detection of Apoptotic Cells by Using Zinc Coordination Complexes with a Selective Affinity for Membrane Surfaces Enriched with Phosphatidylserine. *ChemBioChem* **2005**, *6* (12), 2214–2220. https://doi.org/10.1002/cbic.200500149.

(48) Thakur, M. L.; Zhang, K.; Paudyal, B.; Devakumar, D.; Covarrubias, M. Y.; Cheng, C.; Gray, B. D.; Wickstrom, E.; Pak, K. Y. Targeting Apoptosis for Optical Imaging of Infection. *Mol. Imaging Biol.* **2012**, *14* (2), 163–171. https://doi.org/10.1007/s11307-011-0490-6.

(49) Alberto, R.; Ortner, K.; Wheatley, N.; Schibli, R.; Schubiger, A. P. Synthesis and Properties of Boranocarbonate: A Convenient in Situ CO Source for the Aqueous Preparation of [99mTc(OH2)3(CO)3]+. *J. Am. Chem. Soc.* **2001**, *123* (13), 3135–3136. https://doi.org/10.1021/ja003932b.

(50) Mitchell, R.; Taylor, G.; Rudnick, W.; Alexandre, S.; Bush, K.; Forrester, L.; Frenette, C.; Granfield, B.; Gravel-Tropper, D.; Happe, J.; John, M.; Lavallee, C.; McGeer, A.; Mertz, D.; Pelude, L.; Science, M.; Simor, A.; Smith, S.; Suh, K. N.; Vayalumkal, J.; Wong, A.; Amaratunga, K. Trends in Health Care–Associated Infections in Acute Care Hospitals in Canada: An Analysis of Repeated Point-Prevalence Surveys. *Can. Med. Assoc. J.* **2019**, *191* (36), E981–E988. https://doi.org/10.1503/cmaj.190361.

(51) Al-Tawfiq, J. A.; Tambyah, P. A. Healthcare Associated Infections (HAI) Perspectives. *J. Infect. Public Health* **2014**, *7* (4), 339–344. https://doi.org/10.1016/j.jiph.2014.04.003.

(52) VanEpps, J. S.; Younger, J. G. Implantable Device-Related Infection. *Shock* **2016**, *46* (6), 597–608. https://doi.org/10.1097/SHK.0000000000000692.

(53) Uchida, Y.; Hasegawa, J.; Chinnapen, D.; Inoue, T.; Okazaki, S.; Kato, R.; Wakatsuki, S.; Misaki, R.; Koike, M.; Uchiyama, Y.; Iemura, S.; Natsume, T.; Kuwahara, R.; Nakagawa, T.; Nishikawa, K.; Mukai, K.; Miyoshi, E.; Taniguchi, N.; Sheff, D.; Lencer, W. I.; Taguchi, T.;

Arai, H. Intracellular Phosphatidylserine Is Essential for Retrograde Membrane Traffic through Endosomes. *Proc. Natl. Acad. Sci.* **2011**, *108* (38), 15846–15851. https://doi.org/10.1073/pnas.1109101108.

(54) Smith, B. A.; Gammon, S. T.; Xiao, S.; Wang, W.; Chapman, S.; McDermott, R.; Suckow, M. A.; Johnson, J. R.; Piwnica-Worms, D.; Gokel, G. W.; Smith, B. D.; Leevy, W. M. In Vivo Optical Imaging of Acute Cell Death Using a Near-Infrared Fluorescent Zinc−Dipicolylamine Probe. *Mol. Pharm.* **2011**, *8* (2), 583–590. https://doi.org/10.1021/mp100395u.

(55) Smith, B. A.; Xiao, S.; Wolter, W.; Wheeler, J.; Suckow, M. A.; Smith, B. D. In Vivo Targeting of Cell Death Using a Synthetic Fluorescent Molecular Probe. *Apoptosis* **2011**, *16* (7), 722–731. https://doi.org/10.1007/s10495-011-0601-5.

(56) Smith, B. A.; Xie, B.-W.; Van Beek, E. R.; Que, I.; Blankevoort, V.; Xiao, S.; Cole, E. L.; Hoehn, M.; Kaijzel, E. L.; Löwik, C. W. G. M.; Smith, B. D. Multicolor Fluorescence Imaging of Traumatic Brain Injury in a Cryolesion Mouse Model. *ACS Chem. Neurosci.* **2012**, *3* (7), 530–537. https://doi.org/10.1021/cn3000197.

(57) Kam, P. C. A.; Ferch, N. I. Apoptosis: Mechanisms and Clinical Implications: Apoptosis. *Anaesthesia* **2000**, *55* (11), 1081–1093. https://doi.org/10.1046/j.1365-2044.2000.01554.x.

(58) Kiechle, F. L.; Zhang, X. Apoptosis: Biochemical Aspects and Clinical Implications. *Clin. Chim. Acta* **2002**, *326* (1–2), 27–45. https://doi.org/10.1016/S0009-8981(02)00297-8.

(59) Krysko, D. V.; Vanden Berghe, T.; D'Herde, K.; Vandenabeele, P. Apoptosis and Necrosis: Detection, Discrimination and Phagocytosis. *Methods* **2008**, *44* (3), 205–221. https://doi.org/10.1016/j.ymeth.2007.12.001.

(60) Van Cruchten, S.; Van den Broeck, W. Morphological and Biochemical Aspects of Apoptosis, Oncosis and Necrosis. *Anat. Histol. Embryol. J. Vet. Med. Ser. C* **2002**, *31* (4), 214–223. https://doi.org/10.1046/j.1439-0264.2002.00398.x.

(61) Edwards, C. Materials Used in Medical Implants: How Is the Industry Breaking the Mould? *Medical Device Network*. August 22, 2018. https://www.medicaldevice-network.com/features/materials-used-medical-implants-industry/?cf-view&cf-closed.

(62) Boutrand, J. P. Efficient Evaluations of Bone Implants Performances. In *Biocompatibility and Performance of Medical Devices*; Elsevier, 2020; pp 305–337. https://doi.org/10.1016/B978-0-08-102643-4.00013-6.

(63) Mitcham, T.; Homan, K.; Frey, W.; Chen, Y.-S.; Emelianov, S.; Hazle, J.; Bouchard, R. Modulation of Photoacoustic Signal Generation from Metallic Surfaces. *J. Biomed. Opt.* **2013**, *18* (5), 056008. https://doi.org/10.1117/1.JBO.18.5.056008.

(64) Lediju Bell, M. A.; Kuo, N. P.; Song, D. Y.; Kang, J. U.; Boctor, E. M. In Vivo Visualization of Prostate Brachytherapy Seeds with Photoacoustic Imaging. *J. Biomed. Opt.* **2014**, *19* (12), 126011. https://doi.org/10.1117/1.JBO.19.12.126011.

(65) Jiang, Y.; Zhang, J. Current Status of and Perspectives on Radiolabelled Ubiquicidin 29-41Derivatives for Bacterial Infection Imaging. *Mini-Rev. Med. Chem.* **2023**, *23* (15), 1500–1506. https://doi.org/10.2174/1389557523666230131100654.

(66) Tegge, W.; Guerra, G.; Höltke, A.; Schiller, L.; Beutling, U.; Harmrolfs, K.; Gröbe, L.; Wullenkord, H.; Xu, C.; Weich, H.; Brönstrup, M. Selective Bacterial Targeting and Infection-Triggered Release of Antibiotic Colistin Conjugates. *Angew. Chem. Int. Ed.* **2021**, *60* (33), 17989–17997. https://doi.org/10.1002/anie.202104921.

(67) Assadi, M.; Vahdat, K.; Nabipour, I.; Sehhat, M. R.; Hadavand, F.; Javadi, H.; Tavakoli, A.; Saberifard, J.; Kalantarhormozi, M. R.; Zakani, A.; Eftekhari, M. Diagnostic Value of 99mTc-Ubiquicidin Scintigraphy for Osteomyelitis and Comparisons with 99mTc-Methylene Diphosphonate Scintigraphy and Magnetic Resonance Imaging. *Nucl. Med. Commun.* **2011**, *32* (8), 716–723. https://doi.org/10.1097/MNM.0b013e3283483fe4.

(68) Gandomkar, M.; Najafi, R.; Shafiei, M.; Mazidi, M.; Goudarzi, M.; Mirfallah, S. H.; Ebrahimi, F.; Heydarpor, H. R.; Abdie, N. Clinical Evaluation of Antimicrobial Peptide [99mTc/Tricine/HYNIC0]Ubiquicidin 29–41 as a Human-Specific Infection Imaging Agent. *Nucl. Med. Biol.* **2009**, *36* (2), 199–205. https://doi.org/10.1016/j.nucmedbio.2008.11.003.

(69) Melendez-Alafort, L.; Rodrıguez-Cortes, J.; Ferro-Flores, G.; Murphy, C. A. D.; Herrera-Rodrıguez, R.; Mitsoura, E.; Martınez-Duncker, C. Biokinetics of 99mTc-UBI 29-41 in Humans. *Nucl. Med. Biol.* **2004**.

(70) Nogueira, S. A.; De Barboza, M. F.; Dell'Aquila, A. M.; Santos, D. C. B.; Osawa, A. Could 68Ga-DOTA-UBI-29-41 Help Identify Chronic Osteomyelitis on PET/CT Images? A Pilot Study. *Clin. Nucl. Med.* **2023**, *48* (11), 982–984. https://doi.org/10.1097/RLU.0000000000004866.

(71) Chen, H.; Liu, C.; Chen, D.; Madrid, K.; Peng, S.; Dong, X.; Zhang, M.; Gu, Y. Bacteria-Targeting Conjugates Based on Antimicrobial Peptide for Bacteria Diagnosis and Therapy. *Mol. Pharm.* **2015**, *12* (7), 2505–2516. https://doi.org/10.1021/acs.molpharmaceut.5b00053.

(72) Bunschoten, A.; Welling, M. M.; Termaat, M. F.; Sathekge, M.; van Leeuwen, F. W. B. Development and Prospects of Dedicated Tracers for the Molecular Imaging of Bacterial Infections. *Bioconjug. Chem.* **2013**, *24* (12), 1971–1989.

(73) Lu, X.; Chen, R.; Lv, J.; Xu, W.; Chen, H.; Ma, Z.; Huang, S.; Li, S.; Liu, H.; Hu, J.; Nie, L. High-Resolution Bimodal Imaging and Potent Antibiotic/Photodynamic Synergistic Therapy for Osteomyelitis with a Bacterial Inflammation-Specific Versatile Agent. *Acta Biomater.* **2019**, *99*, 363–372. https://doi.org/10.1016/j.actbio.2019.08.043.

(74) Gowrishankar, G.; Hardy, J.; Wardak, M.; Namavari, M.; Reeves, R. E.; Neofytou, E.; Srinivasan, A.; Wu, J. C.; Contag, C. H.; Gambhir, S. S. Specific Imaging of Bacterial Infection Using 6″- ^{18} F-Fluoromaltotriose: A Second-Generation PET Tracer Targeting the Maltodextrin Transporter in Bacteria. *J. Nucl. Med.* **2017**, *58* (10), 1679–1684. https://doi.org/10.2967/jnumed.117.191452.

(75) Takemiya, K.; Ning, X.; Seo, W.; Wang, X.; Mohammad, R.; Joseph, G.; Titterington, J. S.; Kraft, C. S.; Nye, J. A.; Murthy, N.; Goodman, M. M.; Taylor, W. R. Novel PET and Near Infrared Imaging Probes for the Specific Detection of Bacterial Infections Associated With Cardiac Devices. *JACC Cardiovasc. Imaging* **2019**, *12* (5), 875–886. https://doi.org/10.1016/j.jcmg.2018.02.011.

(76) Høiby, N.; Ciofu, O.; Johansen, H. K.; Song, Z.; Moser, C.; Jensen, P. Ø.; Molin, S.; Givskov, M.; Tolker-Nielsen, T.; Bjarnsholt, T. The Clinical Impact of Bacterial Biofilms. *Int. J. Oral Sci.* **2011**, *3* (2), 55–65. https://doi.org/10.4248/IJOS11026.

(77) Veerachamy, S.; Yarlagadda, T.; Manivasagam, G.; Yarlagadda, P. K. Bacterial Adherence and Biofilm Formation on Medical Implants: A Review. *Proc Inst Mech Eng H* **2014**, *228* (10), 1083–1099. https://doi.org/10.1177/0954411914556137.

Chapter 4 : Development of a General-Purpose Dye & Methodology for Photoacoustic Imaging

Rowan Swann[†], Yusra Mahmood Marfatia[†], Mohamed E. El-Zaria[†], Afaf R. Genady[†], Luis Rafael Silva[†], John F. Valliant[†], & Saman Sadeghi[†,*]

[†] Department of Chemistry and Chemical Biology, McMaster University, Hamilton, Ontario, Canada

Unpublished Manuscript

4.1 Introduction

Photoacoustic Imaging (PAI) is a dual-modal technique combining optical and acoustic imaging that employs pulsed light absorption to create detectable ultrasound waves. PAI offers detection sensitivity comparable to FI with enhanced depth-resolution capabilities resulting from the reduced scattering of acoustic waves in tissue.[1] Spectral unmixing algorithms facilitate the visualization of target-specific signals amidst interfering signals generated by endogenous chromophores, enabling simultaneous detection of multiple chromophores. Furthermore, anatomical mapping, using conventional US signal, can supplement the PA images by contextualizing signal location.[2]

Currently, 'label-free' imaging techniques dominate clinical PA research, offering valuable chemical and functional insights into disease pathology without the need for FDA-approved exogenous contrast agents. However, the use of exogenous chromophores, combined with specific disease-targeted moieties (PIPs), has become prevalent in preclinical research to facilitate the expansion of PAI applications. These PIPs enable the detection of biomarkers of disease that lack intrinsic light absorption properties.[3,4]

Photophysical and biological properties of molecularly targeted PIPS play a significant role in their design. For PA characteristics, the PIP should feature a unique absorbance spectrum in the

NIR region to ensure that it can be distinguished in the presence of endogenous chromophores such as oxygenated and deoxygenated hemoglobin. Additionally, a high molar extinction coefficient will optimize light absorption, while a low quantum yield will maximize the energy converted to heat that is used to generate PA signal.[1] From a biological standpoint, the implemented targeting vector should overcome circulatory and cellular barriers in order to maximize localization to the intended site. The PIP should generate a low background signal and exhibit minimal uptake in non-target organs to generate a strong signal, with minimal adverse side effects.[1]

The use of small molecule dyes for PAI applications is warranted by their commercial availability, easily functionalized structures, and biocompatibility. Many commercial NIR dyes, marketed for FI applications, possess relatively low fluorescence quantum yields, offering intriguing potential for PAI applications. However, utilizing these dyes in the synthesis of novel PIPs requires careful consideration of the pharmacokinetic and photophysical influence that the addition of a linker group and targeting vector can have on the overall construct.

The conjugated backbone and flanking electron donor/cationic electron acceptor, that constitute the heptamethine cyanine dyes explored in this work, are responsible for the light absorption properties of these molecules but also perpetuate the formation of aggregates in aqueous media. High dielectric constant solvents, such as water, have been documented to diminish ionic repulsion among similarly charged species, and coupled with the hydrophobic nature of the pi-conjugated backbone, instigate aggregate formation.[5–7] These aggregates are undesirable for *in vivo* use, not only because I.V administration could lead to venous thromboembolism, but also because aggregates could cause high levels of off-target uptake that could lead to toxicity and lower signal-to-background ratios for imaging.[8,9] Thus, a key aspect of this work involved employing hydrophilic linkers to enhance the aqueous solubility of the PIPs.

The presence of intrinsic chromophores, namely oxygenated and deoxygenated hemoglobin, is essential to consider in the design of new PIPs as they produce NIR PA signal which could interfere with the detection of lower-intensity exogenous signal. Additionally, if the PA signal maximum of the exogenous chromophore overlaps with the predominant peaks generated by the endogenous chromophores, multiwavelength signal unmixing algorithms will not be able to differentiate the chromophores. Thus, it is critical to design a PIP to generate signals with a PA maximum that minimally overlaps with the signal of the blood chromophores to improve the accuracy of the signal unmixing algorithm.

In this work, a novel 'general-purpose' dye, IRyne800PEG$_{12}$ (**4-4**), was designed to improve aqueous solubility and optimize PA signal generation. To detail, a commercially available heptamethine cyanine dye, IR783 (**2-1**) was selected as the chromophore for the PIP, as it offered a baseline absorbance maximum (783 nm) and PA signal (775 nm) within the working wavelength range of the Vevo LAZR-X PAI system (680-970 nm). The design of the general-purpose dye includes a poly(ethylene)glycol (12) (PEG$_{12}$) linker to improve solubility in aqueous media and a central benzoic-ethynyl group, purposefully placed to induce an anticipated bathochromic shift in absorption from 783 nm to ~ 800 nm.[10] This shift in absorption is expected to shift the PA signal maximum to a wavelength that offers greater separation from the signal of endogenous blood chromophores, which could improve PA signal quantification and sensitivity. Finally, a carboxylic acid handle on the PEG linker was implemented into the design to allow for the functionalization of the PIP with amine-containing targeting vectors.

The work presented here outlines the synthesis of the 'general-purpose' dye with a proof-of-concept functionalization to a Zn-DPA moiety for targeting bacterial infection. To evaluate the implemented structural features of the PIPs, commercially available PSVue794, which possesses

the same targeting vector, was used for comparative studies. The design and implementation of assays to determine aqueous solubility and the accuracy of unmixing the signals from blood are detailed and a final series of proof-of-concept were conducted to demonstrate the specificity of the targeted PIP.

4.2 Results & Discussion

4.2.1 Synthesis & Characterization

The synthesis of **4-4** (**Scheme 4.1**) was initiated by performing a Sonogashira coupling between IR783 (**2-1**) and 4-ethynylbenzoic acid (**4-1**), in an isolated yield of 70%. The product (**4-2**) was characterized by HPLC and HRMS (ESI^-) and ^1H- & ^{13}C-NMR analysis (**Figures AIII-1-4**). A coupling reaction between amino-PEG_{12}-propanoic acid *t*-Butyl ester (**4-3**) and **4-2**, was then performed and subsequent acid-deprotection of the tBu-protected carboxylic acid was carried out using 1:5 trifluoroacetic acid (TFA) in dichloromethane (DCM) (25% yield) (structural characterizations: **Figures AIII-5-8**).

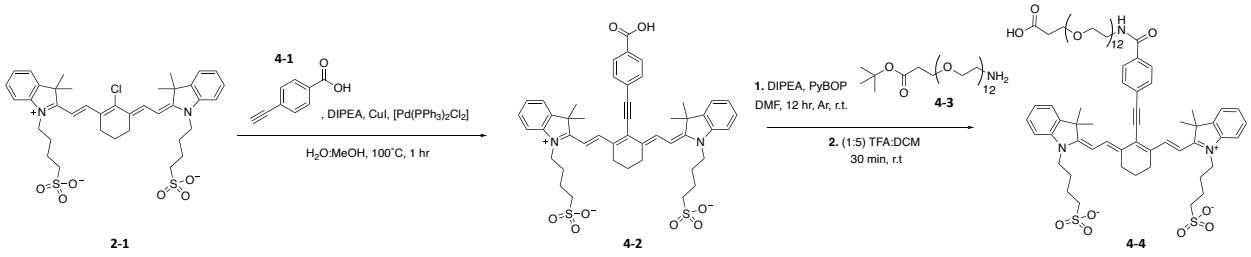

Scheme 4.1. 2-step synthesis of **4-4** from IR783 (**2-1**).

ZnDPA was chosen as the first amine-containing targeting vector to functionalize compound **4-4**. The addition of the DPA-NH_2 (**4-5**) moiety to **4-4** was carried out using a PyBOP coupling reaction to yield **4-6** (60%) (structural characterizations: **Figures AIII-9-12**). IR-ZnDPA-1 (**4-7**) was obtained after incubating **4-6** with $Zn(NO_3)_2$ for 30 minutes at 37˚C. The HPLC trace

of the product (**4-7**) did not display a shift in the retention time compared to the starting dye **4-6** (**Figure AIII-13**). Based on low-resolution mass spectrometry, the doubly and triply charged species of the dye coordinated to 1 and 2 zinc moieties were present (**Figure AIII-14-16**).

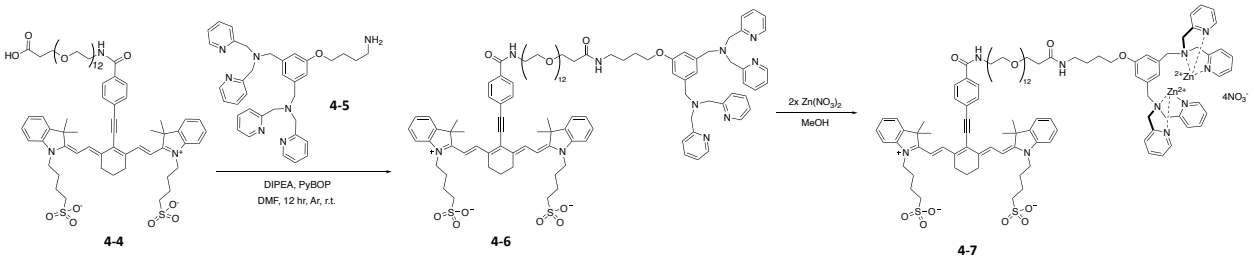

Scheme 4.2. Synthesis of IR-ZnDPA-1 (**4-7**).

4.2.2. Photophysical Characterizations of 4-4 & 4-7.

The photophysical properties of **4-4** and **4-7** were characterized via absorbance and emission spectra, PA signal, quantum yield and molar absorptivity (**Figure 4.1 & Table 4-1**). Two prominent peaks were observed in the absorbance (740 and 800 nm) and PA (735 and 790 nm) spectra of **4-4**, corresponding to the dimeric and monomeric species of the dye, respectively. Upon functionalizing the dye with **4-5** and coordination with zinc nitrate, a notable decrease in dimeric species intensity was observed, leading to a single prominent peak at in both the absorbance (810 nm) and PA (805 nm) spectra of **4-7**.

A biocompatible solvent of 10 % ethanol in saline was used in all measurements, except when calculating the fluorescence quantum yield where methanol was used to allow for a direct comparison to the literature value found for **2-1**.[11] Comparative analysis with **2-1** (**Table 4.1**) demonstrated decreased molar absorptivity for **4-4** and **4-7**, yet within expected ranges for heptamethine cyanine dyes.[12] Low fluorescence quantum yields suggest efficient conversion of absorbed energy to thermal or vibrational energy, ideal for PA signal generation.[13] The sharper

monomer peak of **4-7** suggests potential superiority over **4-4** in the PA signal unmixing algorithm, particularly in the presence of blood.

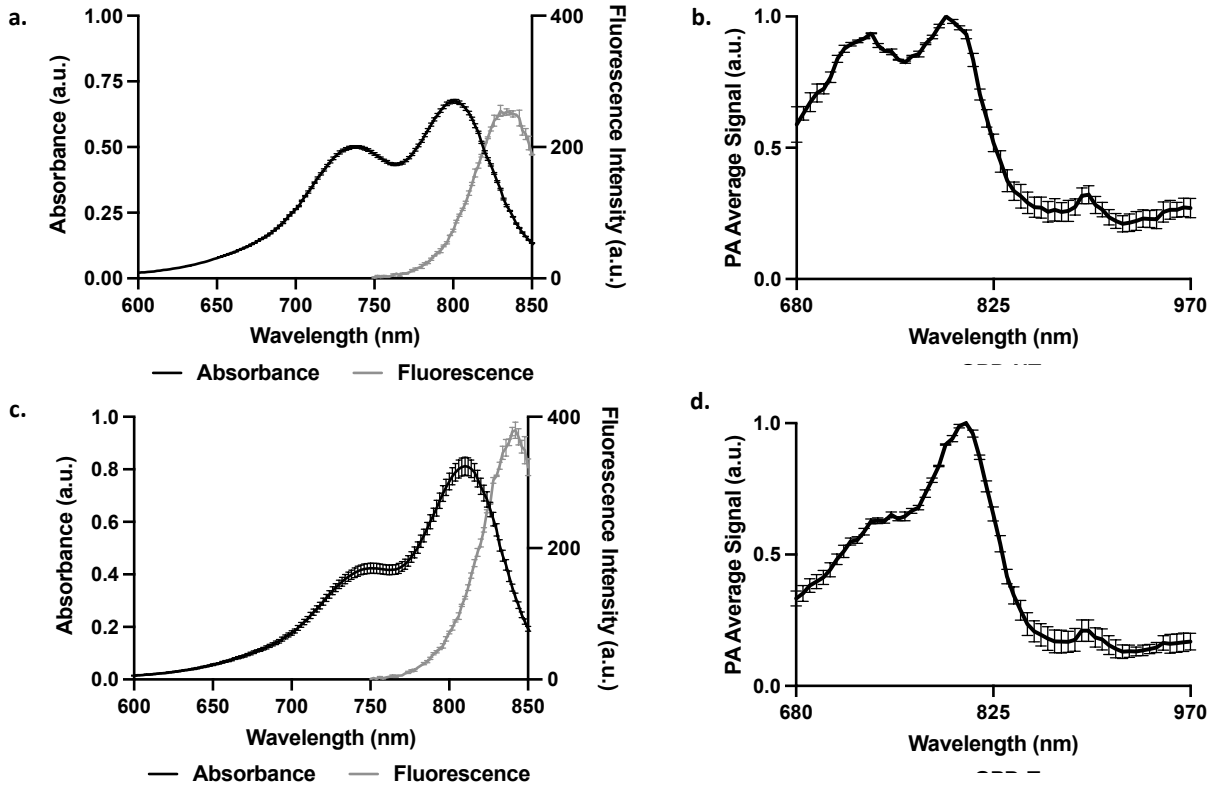

Figure 4.1. Spectral characterization of **4-4** and **4-7**: **a.** Absorbance & emissions spectra of **4-**4 (20 µM, 10% ethanol in saline), $\boldsymbol{\lambda_{exc}}$= 746 nm. b. PA spectrum of **4-4** (20 µM, 10% ethanol in saline). **c.** Absorbance & emissions spectra of **4-**7 (20 µM, 10% ethanol in saline), $\boldsymbol{\lambda_{exc}}$= 746 nm. **d**. PA spectrum of **4-7** (20 µM, 10% ethanol in saline).

Table 4.1. Photophysical characteristics comparison of **2-1**, **4-4**, & **4-7**.

Construct	Solvent	PA λ_{max} (nm)	Absorbance λ_{max} (nm)	Emission λ_{max} (nm)	Fluorescent Quantum Yield (φ_f)	Molar Absorptivity (ε) ($cm^{-1}M^{-1}$)
2-1	Methanol	760	783	808	0.084*	282 200*
4-4	Methanol	-	802	834	0.036	177 998
	10% Ethanol in Saline	735/790	800	834	-	-
4-7	Methanol	-	804	840	0.015	202 913
	10% Ethanol in Saline	805	810	842	-	-

*Data derived from James, *et al*., 2013.[11]

4.2.3. Solubility Analysis.

To evaluate the effect of the PEG linker addition, a solubility study was conducted using the absorbance spectra of probes **4-4**, **4-7,** and **3-4** in solvents of varying polarity. It has been well characterized in the literature that various states of dye aggregation can be observed in the absorbance spectra, where H- and J-aggregates species possess a respective hypsochromic and bathochromic shift in absorbance compared to the monomeric species.[5] An illustrative example of these shifts is provided in **Figure 4.2**, displaying the differing absorbance spectra of **2-5** in methanol (MeOH) and saline.

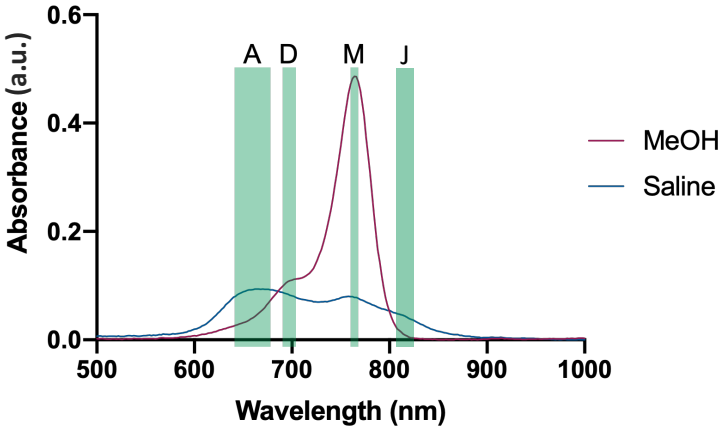

Figure 4.2. Assessing solubility of a dye using the absorbance characteristics of monomeric, dimeric, H- and J-aggregated dye species. **2-5** dissolved in methanol or saline.

Methanol was employed to dissolve the dyes to define the spectrum of a fully solubilized dye, while 10% ethanol in saline and 100% saline were used to evaluate probe solubility in injectable formulations. Absorbance scans of each formulation were acquired, and the spectra were plotted (**Figure 4.3**). In the absorbance spectra of **3-4** (**Figure 4.3a**), a propensity to aggregate was observed with increasing aqueous solvent content, as indicated by diminished monomer intensity and broadening of the spectrum in saline. Notably, the formation of J-aggregates was evident due

to the bathochromic shift in absorbance out to ~850 nm. Similarly, a reduction in monomer intensity was observed in the spectra **4-4** in 10% ethanol in saline and saline alone, relative to the spectra in methanol (**Figure 4.3b**). However, development of the dimeric species appeared to occur in place of the formation of the aggregate species, which suggest that the PEG linker contributes to higher solubility in aqueous solvent. Interestingly, the absorbance spectra of **4-7** (**Figure 4.7c**) showed a less extensive decrease in monomer intensity with increasing aqueous solvent content. Similar to **4-4**, the intensity of the dimer peak increased, without development of the aggregate species. These results indicate that not only the addition of the PEG linker but also further functionalization to form **4-7**, substantially improved the aqueous solubility of the novel heptamethine cyanine dye compared to a commercially available dye, **3-4**, with similar targeting properties.

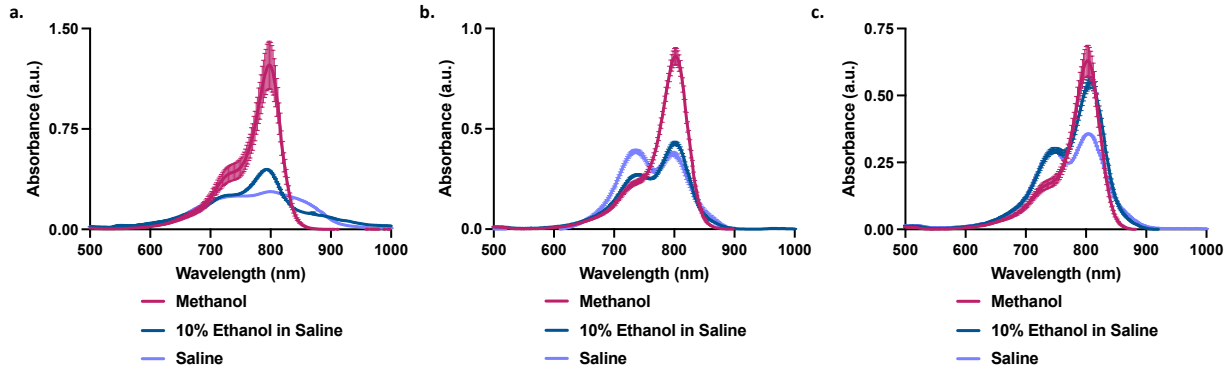

Figure 4.3. Solubility analysis of **3-4 (a), 4-4 (b),** and **4-7 (c)** in methanol, 10% ethanol in saline, and saline (15 μM).

4.2.4. Blood Signal Unmixing Analysis.

An integral feature of the Vevo LAZR-X imaging system is the multispectral unmixing algorithm that allows for the simultaneous detection of multiple chromophores. This component is especially important for *in vivo* PAI applications due to the presence of intrinsic chromophores

that interfere with NIR signal detection. Specifically, the spectra of oxygenated and deoxygenated hemoglobin generate distinct signals in the instrument's wavelength range (680-970 nm), which are essential to consider in the design of new PIPs. To improve the accuracy of the signal unmixing algorithm, it is proposed that a PIP should generate a signal with a PA maximum at a location that overlaps minimally with the signal maxima of the blood chromophores. Accordingly, two wavelength ranges were proposed as ideal for signal unmixing (**Figure 4.4**), guiding the design of the dyes synthesized in this work.

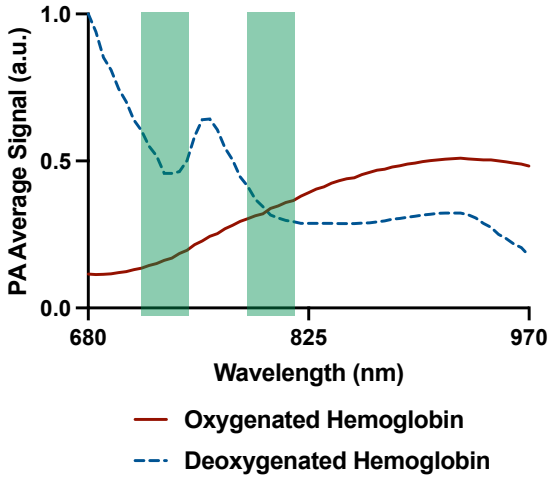

Figure 4.4. Proposed ideal wavelength ranges for dyes to emit PA signal for optimal unmixing capabilities from blood chromophores.

To assess the ease of unmixing PA spectra of **4-4** and **4-7** from blood chromophores, two studies were designed, the first of which utilized whole mouse blood mixed with the dyes *in situ*. Accuracy in distinguishing between deoxygenated hemoglobin and dye was gauged by comparing samples of neat blood and blood mixed with dye, from which the detected signals of deoxygenated hemoglobin and dye were quantified. Hypothetically, in the absence of dye, the baseline signal of deoxyhemoglobin and the background level of dye can be determined. Further, in samples containing both blood and dye, the signal of deoxyhemoglobin should not change, while the signal

of dye should be detected at significantly higher levels than the background. Detection of a deoxyhemoglobin signal higher than the baseline in this sample would suggest that the algorithm is unable to accurately distinguish between the signals.

As with the solubility assay, **3-4** was compared to the non-targeted dye, **4-4**, and the targeted dye, **4-7** (**Figure 4.5**). As anticipated a significantly higher signal of each dye was observed between the samples of neat blood and blood mixed with each dye (**3-4**: 0.106 ± 0.020 a.u. and 0.327 ± 0.044 a.u., where $P< 0.001$; **4-4**: 0.109 ± 0.006 a.u. and 0.196 ± 0.008 a.u, where $P< 0.001$; **4-7**: 0.057 ± 0.007 a.u. and 0.176 ± 0.025 a.u., where $P= 0.002$). However, the signal of deoxyhemoglobin was also detected at levels significantly higher than the baseline in the samples of blood mixed with **3-4** (0.060 ± 0.007 a.u. and 0.139 ± 0.018 a.u., where $P=0.03$) and **4-4** (0.048 ± 0.010 a.u. and 0.139 ± 0.003 a.u., where $P< 0.001$), indicating that the algorithm was not able to accurately distinguish between deoxyhemoglobin and the dyes. Importantly, the detected signal from deoxyhemoglobin did not increase above baseline in the sample of blood mixed with **4-7** (0.069 ± 0.009 a.u. and 0.060 ± 0.016 a.u.). A limitation of this study was the non-biologically relevant levels of deoxyhemoglobin present in the drawn blood samples, as what would be expected *in vivo*. This prompted the accompanying *in vivo* signal unmixing study to assess a biologically relevant make-up of intrinsic chromophore interference.

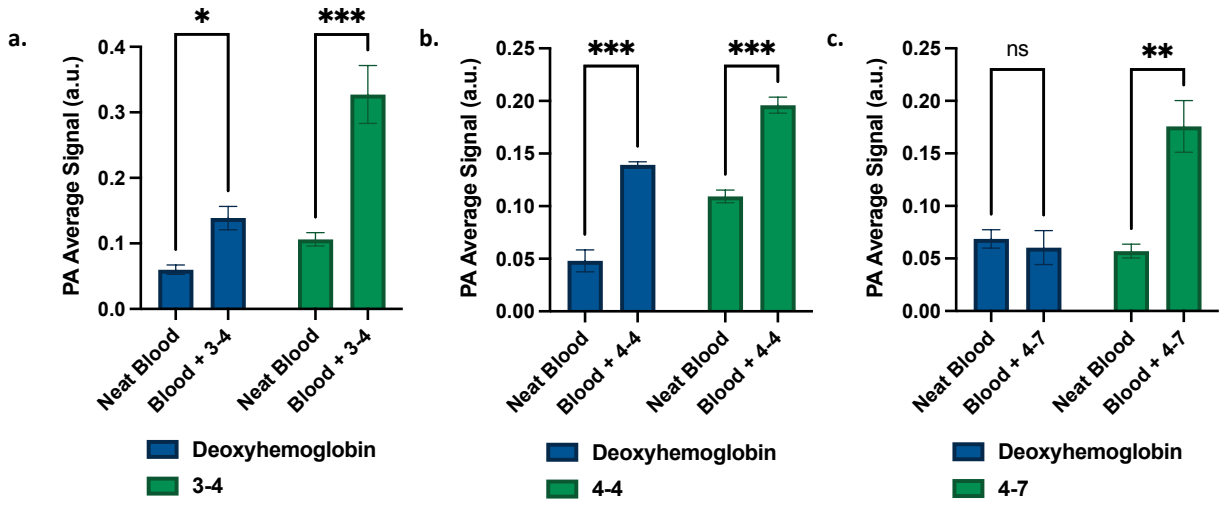

Figure 4.5. *In vitro* blood unmixing analysis of **3-4 (a), 4-4 (b),** and **4-7 (c**), where the quantified signals of dye (green) and deoxyhemoglobin (blue) were unmixed from samples containing neat blood or blood mixed with dye.

To assess the accuracy of the algorithm in a biologically relevant environment, naïve mice were imaged using the multiwavelength unmixing algorithm, where oxygenated and deoxygenated hemoglobin were unmixed from predetermined spectra for **3-4**, **4-4**, or **4-7**. The objective was to assess how the PA spectral characteristics of each dye impacted the background levels detected in the absence of injected dye. **Figure 4.6a-c** shows the overlay of the pre-determined spectral signatures for oxygenated and deoxygenated hemoglobin with **4-4**, **3-4**, and **4-7**, respectively, and the subsequent hindlimb images with the unmixed signals. Additionally, the green signal from each 3D scan was quantified (**Figure 4.6d**), demonstrating that the background signal of **4-4** (0.077 ± 0.004 a.u.) was significantly higher than that of **3-4** (0.066 ± 0.007 a.u., where P=0.05) and that of **4-7** (0.049 ± 0.001 a.u., where P< 0.001). A significant difference was also observed between **3-4** and **4-7** (P= 0.009). Upon further analysis, the background signal between the dyes decreases as the monomer-to-dimer peak ratio of the dyes (**4-4**: 1.07, **3-4**: 1.18, and **4-7**: 1.67) increases. This result points to the importance of maintaining a single PA signal maximum, unique from the PA signal of blood chromophores, for accurate signal unmixing *in vivo*, and highlights how the

improved solubility of **4-7**, compared to a similarly designed construct, **3-4**, contributes to optimized *in vivo* PAI.

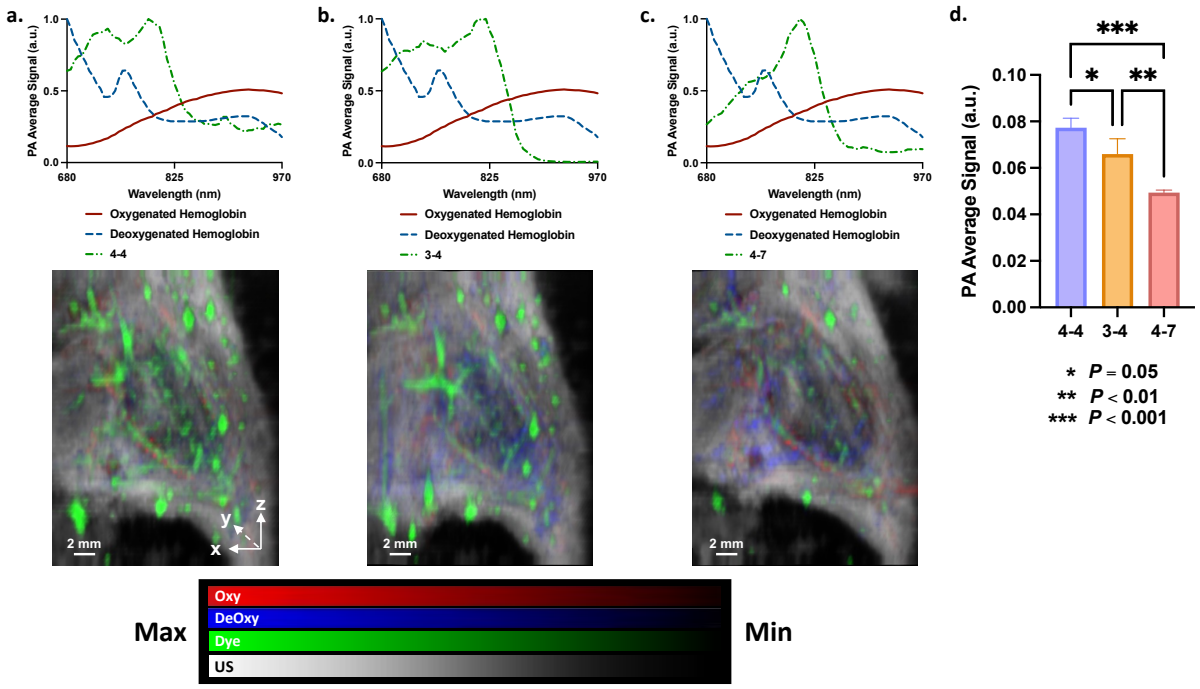

Figure 4.6. *In vivo* blood unmixing analysis of **4-4 (a), 3-4 (b),** and **4-7 (c).** Where the quantified background signals for each dye (green) (**d**) were unmixed from blood chromophores using pre-determined PA spectra, in the hindlimb of a naïve mouse. Blue= deoxygenated hemoglobin, red= oxygenated hemoglobin.

4.2.5. Proof-of-Concept *In Vitro* Bacteria Binding Assay.

To assess the targeting ability of the PIP, an *in vitro* bacteria binding assay was performed, comparing the fluorescence intensity of *S. aureus* bacterial pellets incubated with or without the non-targeted (**4-4**) or the targeted (**4-7**) dyes (**Figure 4.7**). The fluorescence intensity of the bacterial pellets incubated with **4-4** (919 ± 1111 a.u.) was not found to be different from the intensity of the no-cell control (3850 ± 865 a.u.), whereas the intensity of the bacterial pellet incubated with **4-7** (18169 ± 2279 a.u.) was significantly higher than the no-cell control (4378 ± 1325 a.u., where $P < 0.001$), as well as the intensity of the bacterial pellet incubated with **4-4** ($P <$

0.001). A signal-to-background (S/B) ratio of 4.15 and targeted-to-non-targeted (T/NT) ratio of 19.7 were calculated, indicating that the construct was able to bind to the anionic outer membrane of bacteria, as anticipated.

A sample of dye alone, at 10 μM, that was not treated through centrifugation, was measured to determine the intensity of the signal that would be generated if all the dye remained in solution. This control group represents situations where no bacteria-binding occurred and no dye crashed out of the solution through centrifugation. It was used to assess the degree of bacterial binding based on the initial supernatants and the washed bacterial pellets (**Figure 4.7b-c**). It was observed that no significant drop in the fluorescence intensity occurred between the 10 μM control (236573 ± 13655 a.u.) and the initial supernatant (217893 ± 10451 a.u.) of **4-4**, indicating no non-specific bacterial binding occurred (**Figure 4.7b**). Additionally, there was a significant decrease in the signal intensity of the dye remaining on the washed bacterial pellet (919 ± 1112 a.u., where $P <$ 0.001). A similar result was observed when comparing the 10 μM control to the no-cell control for **4-4** (**Figure AIII-17a**). A significant drop was observed between the 10 μM control (405344 ± 4020 a.u.) and the supernatant of the sample incubated with **4-7** (284202 ± 18376 a.u., where $P <$ 0.001), which was not observed with the no-cell control (**Figure AIII-17b**), indicating that the drop in signal was attributed to the bacterial binding affinity of the dye and not to a crash-out of dye during centrifugation. However, a significant drop was also noted between the initial supernatant and the washed bacterial pellet (18170 ± 2280 a.u., where $P < 0.001$) (**Figure 4.7c**). Although it was not tested beyond this result, it was hypothesized that the increased aqueous solubility of the dye may have caused the dye to possess a higher affinity to diffuse back into solution compared to its electrostatic affinity of the cationic zinc for the anionic outer membrane of the bacteria as the pellet was being washed. The significant difference between the 10 μM

control signal of **4-7** and the signal in the initial supernatant, along with the significant differences between the washed bacterial pellets of **4-4** and **4-7**, provide evidence that a specific interaction between the targeted dye and the bacteria was maintained.

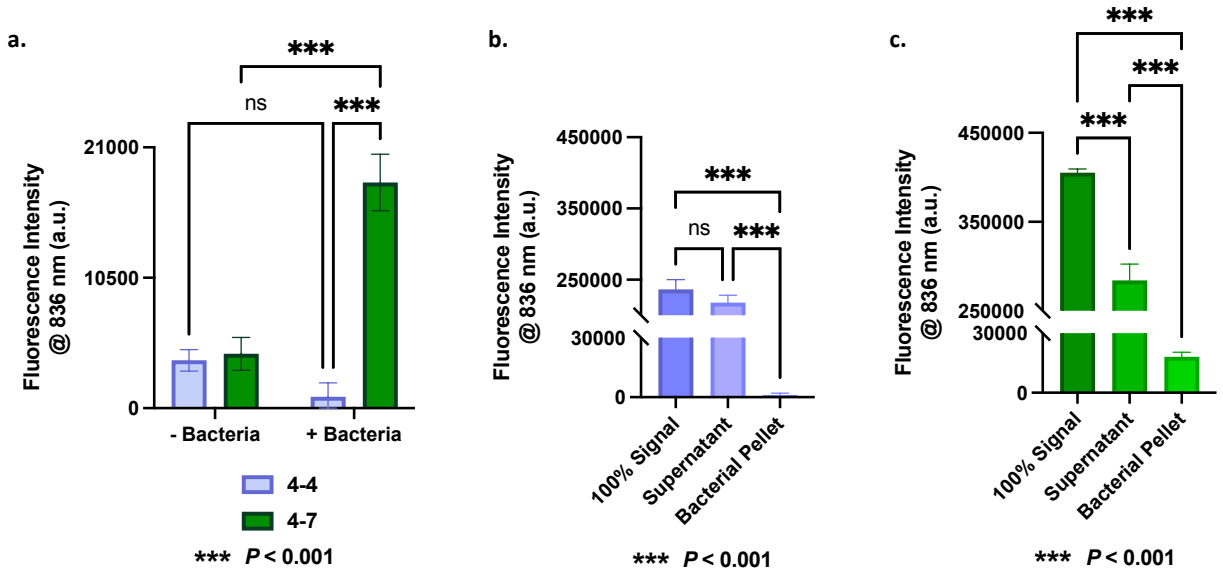

Figure 4.7. *In vitro S. aureus* binding assay. **a.** Quantified fluorescence intensity measurements, at 836 nm, of the washed 'pellets' with or without cells incubated with **4-4** or **4-7.** Fluorescence intensity measurements of samples with bacteria cells, including the supernatant, the washed pellet, and a 10 µM control of 4-4 (**b**), and **4-7** (**c**).

4.2.6. Proof-of-Concept *In Vivo* PAI of *S. aureus*-Induced Bacterial Infection.

A final *in vivo* PAI study was pursued to assess the ability of the dye to localize to sites of bacterial infection. Mice were inoculated with *S. aureus* ($1x10^8$ CFUs) in the right hindlimb and the vehicle control in the left hindlimb, and then split into two cohorts. The mice were injected with either the non-targeted dye (**4-4**) or the targeted dye (**4-7**) (n=4 per cohort) and imaged pre-injection and 12 hours post-injection (**Figure 4.8a**). No differences were observed in either hindlimb pre- (vehicle: 0.097 ± 0.028 a.u.; infected: 0.145 ± 0.014 a.u.) or post-injection (vehicle: 0.188 ± 0.031 a.u.; infected: 0.097 ± 0.004 a.u.) of the non-targeted cohort (**Figure 4.8b**). The spectrum of the signal generated from within the inoculation site did not show indication to the

presence of the dye, specifically in the anticipated 735 and 790 nm regions (**Figure 4.8d**). The cohort injected with the targeted dye (**4-7**) showed a significantly higher signal in both hindlimbs post-injection (vehicle: 0.437 ± 0.063 a.u., where $P = 0.005$; infected: 0.378 ± 0.057 a.u., where $P = 0.02$) compared to the pre-injection signal (vehicle: 0.110 ± 0.017 a.u.; infected: 0.115 ± 0.023 a.u.) (**Figure 4.8c**), and a characteristic peak at 805 nm was observed in the spectrum of the signal present in both hindlimbs at 12 hours, that was not present pre-injection (**Figure 4.8e**). The PA signal in the vehicle control limb was not expected to be significantly higher than the background signal since bacterial infection was not established in that location. Therefore, a histological examination of the tissues is currently underway and will be necessary to analyze before an official conclusion on these unanticipated results can be made.

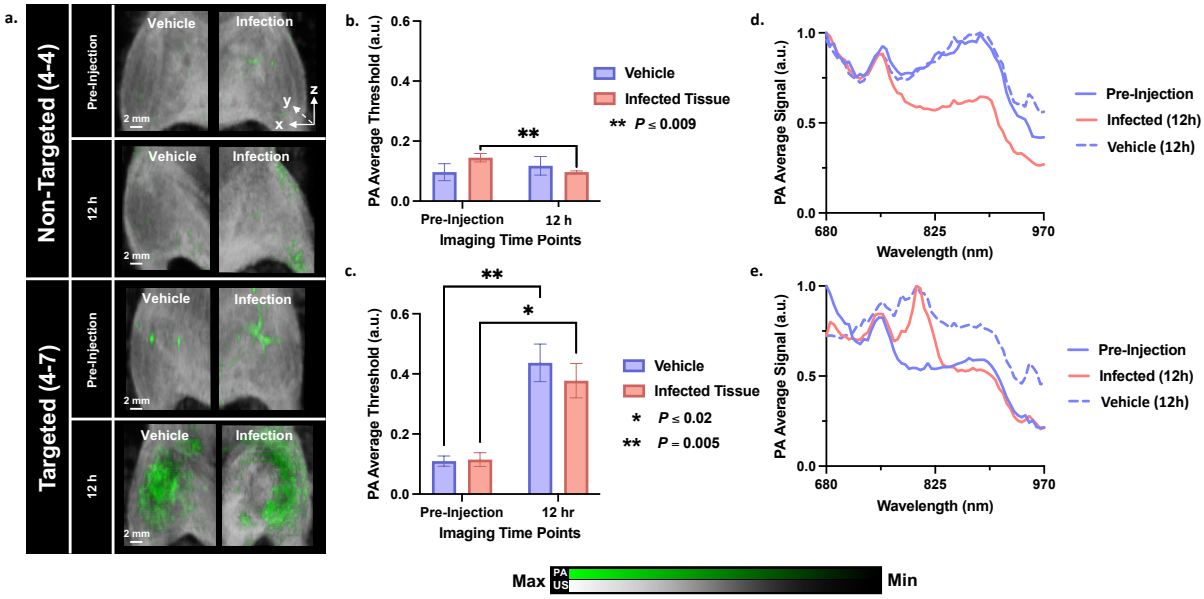

Figure 4.8. PAI of *S. aureus*-induced myositis using **4-4** or **4-7**: **a.** Representative PA multispectral unmixing images (pre-injection and 12 hours post-injection (12h) of mice injected I.V. with **4-4** or **4-7** (1 mM, 100 µL, n=4). **b-c.** Quantified 3D PA average signal, derived from the scans in a. of mice injected with **4-4** and **4-7**, respectively, within the inoculation sites of the mice. **d-e.** Spectral analysis of the inoculation sites pre-injection and 12h of mice injected with **4-4** and **4-7**, respectively. For all multiwavelength unmixing scans, greyscale= US images overlaid with unmixed PA signal, where green= **4-4** or **4-7**. The signals from oxygenated and deoxygenated hemoglobin have been subtracted from each image.

4.3 Conclusion

Compound **4-4**, a novel NIR dye designed to possess properties ideal for *in vivo* PAI, features a PEG-linker for enhanced aqueous solubility and a shifted absorbance maximum to for more accurate signal unmixing. To evaluate these modifications, the dye was conjugated with a Zn-DPA targeting vector to form **4-7**, which was tested alongside the non-targeted counterpart and a commercially available Zn-DPA NIR dye, PSVue794 (**3-4**). In aqueous solvent, where **3-4** demonstrated a tendency to aggregate, **4-4** and **4-7** primarily formed dimeric species, with **4-7** exhibiting the highest monomer intensity out of the three constructs in the prominently used injectable formulation of 10% ethanol in saline. These results suggest that the addition of the PEG linker and conjugation with a targeting vector to form **4-**7 conferred high solubility in aqueous solvent, potentially improving *in vivo* biodistribution. The high solubility of **4-7** also led to a single PA maximum at 805 nm, which was found to enhance the accuracy of the signal unmixing algorithm in distinguishing **4-7** from endogenous blood chromophores compared to **4-4** and **3-4**, which displayed lower monomer-to-dimer peak ratios.

Proof-of-concept bacteria targeting studies were conducted to assess the specificity of **4-7** for the anionic membrane of bacteria compared to **4-4**. An *in vitro* binding assay demonstrated **4-7**'s ability to bind to bacteria, while **4-4** did not. However, **4-7** also exhibited a tendency to diffuse back into solution upon washing of the bacterial pellet. In an *in vivo* model of bacterial infection, **4-7** generated a low background level and a clear post-injection signal, while **4-4** did not produce a signal above background. Unfortunately, a significant signal was also detected in the vehicle control limb, which indicated that the *in vivo* bacteria-targeting ability of the PIP was inconclusive. It is currently hypothesized that the high aqueous solubility of the dye may hinder the comparatively weak electrostatic forces that drive the bacterial targeting mechanism. Future

investigations will focus on blood circulation studies and exploration of the relationship between solubility and target affinity. Alternative Zn-DPA derivatives, such as those containing phenethyl- or butyl-ureido substituents, offer documented improvements for anionic membrane affinity over **4-5**,[14,15] and may be tested to continue evaluations of ZnDPA-based PIPs. Additionally, substituting the Zn-DPA for other bacteria-targeting vectors is outlined in Chapter 3 is warranted. Finally, functionalization of **4-4** with a similar PSMA targeting vector that was used in YC-27,[16] will be investigated for PAI of prostate cancer.

4.4 Experimental Section

General Materials, Instrumentation, & Methods: Unless otherwise noted, all reagents and solvents were ACS grade, purchased from commercial suppliers, and used without further purification. Distilled water was used for all experiments requiring the use of water. Amino-PEG_{12}-propanoic acid t-Butyl ester was purchased from Conju-Probe, LLC (CP-1019). Distilled water was used for all experiments requiring the use of water. Deuterated solvents for NMR samples were purchased from Cambridge Isotope Laboratories.

Nuclear magnetic resonance (NMR) spectra (^{1}H, ^{13}C) were recorded on a Bruker AV600 MHz spectrometer at ambient temperature. Mass spectrometry analyses were provided by the McMaster Regional Center for Mass Spectrometry on an Agilent 6340 Ion Trap LC/MS mass spectrometer operating in electrospray ionization (ES) mode. High-resolution mass spectrometry (HRMS) was collected on a Waters/Micromass Q-Tof Global Ultima spectrometer. Absorbance and fluorescence scans were collected on a Tecan Infinite M1000 plate reader using Corning 96-well, clear bottom plates (non-treated surface) (Corning 3631). Solvents were evaporated using reduced pressure with a rotary evaporator. Unless otherwise stated, flash chromatography purifications were carried out on a CombiFlash®Rf+. Compounds were dried using a VirTis Benchtop lyophilizer equipped with an Edwards RV5 pump. High-performance liquid chromatography (HPLC) was performed on a Waters 1525 Binary (Midford, MA), monitored simultaneously with 2998 photodiode array detector at 245/700 nm using the Empower software package. Analytical HPLC of each compound was performed, using the HPLC method described below, on a Gemini 5 μm C18 110 Å (250 × 4.6 mm) Column (00G-443-E0, Phenomenex),

operating at a flow rate of 1 mL/min. The same HPLC method was used for preparatory HPLC of **4-6**, performed on a Gemini 5 μM NX-C18 110 Å (250 × 10 mm) Column (00G-4454-N0, Phenomenex), operating at a flow rate of 4 mL/min.

CombiFlash®Rf+ Method A: Using the Prep HPLC Column: C18Aq Dimensions: 30 mm x 150 mm 5μm. Solvent A: Acetonitrile, Solvent B: Water. 1-10 min 100% B, 10-20 min 100-70% B, 20-30 min 70% B, 30-40 min 70-50% B, 40-50 min 50% B.

HPLC Method: Solvent A: Water + 0.1% Trifluoroacetic acid (TFA), Solvent B: Acetonitrile + 0.1% TFA. Gradient: 0-2 min 90% A, 2-6 min 90-40% A, 6-8 min 40% A, 8-10 min 40-10% A, 10-11 min 10-90% A, 11-15 min 90% A.

Synthesis of IRyne-800 (4-2): IR-783 (**2-1**) (0.130 g, 0.17 mmol), 4-ethynylbenzoic acid (**4-1**) (0.05 g, 0.34 mmol), *N,N*-diisopropylethylamine (DIPEA) (0.08 mL, 0.44 mmol), copper (I) iodide (0.0064 mL, 0.034 mmol), Bis(triphenylphosphine)palladium (II) dichloride (0.012 g, 0.017 mmol) and 40 mL of water: acetonitrile (1:1) (sparged with argon gas) were added to a round bottom flask under inert atmosphere and equipped with a magnetic stir bar. The mixture was refluxed for 1 hour and then cooled to room temperature. The mixture was filtered through a pad of celite, washed with water, and the solvent was evaporated. CombiFlash®Rf+ Method A was used to purify the material yielding the **4-2** as a DIPEA salt (70% yield). **HPLC** (UV 700 nm) t_r= 9.87 min. **HRMS** (ESI$^-$) m/z calculated for $C_{47}H_{51}N_2O_8S_2^-$: 835.3081 $[M-H]^-$, found 835.3104; 417.151 $[M-2H]^{2-}$, found 417.1522. **^{1}H NMR** (600 MHz, CD_3OD) δ= 8.452 (d, J=13.8 Hz, 2H), 8.103 (d, J=7.8 Hz, 2H), 7.723 (d, J=7.8 Hz, 2H), 7.460 (d, J=7.2 Hz, 2H), 7.365 (dt, J=7.8, 1.2 Hz, 2H), 7.307 (d, J=7.8 Hz, 2H), 7.203 (t, J=7.8 Hz, 2H), 6.328 (d, J=14.4 Hz, 2H), 4.162 (t, J=7.2 Hz, 4H), 3.628 (sep, J=6.6 Hz, 2H), 3.184 (q, J=7.2 Hz, 2H), 2.855 (t, J=7.2 Hz, 4H), 2.685 (t, J=6 Hz, 4H), 1.997-1.887 (m, 10H), 1.705 (s, 12H) ppm, 1.335 (t, J=6.3,15H) ppm; **^{13}C NMR** (150 MHz, CD_3OD) δ=173.5, 147.0, 143.7, 142.5, 142.1, 134.2, 132.4, 131.2, 129.9, 126.2, 126.1, 123.5, 112.2, 103.1, 102.1, 87.9, 55.8, 51.8, 50.5, 44.9, 43.8, 28.6, 27.3, 25.5, 23.6, 21.9, 18.6, 17.3, 13.1 ppm.

Synthesis of IRyne-800-PEG$_{12}$Ca (4-4): To a dry microwave vial equipped with a magnetic stir bar, compound **4-2** (0.035 g, 0.042 mmol), PyBOP (0.048 g, 0.097 mmol) and *N,N*-

diisopropylethylamine (DIPEA) (0.015 mL, 0.084 mmol) were added. The vial was capped, and a nitrogen atmosphere was induced. The mixture was dissolved in 2 mL of DMF. In a separate, dry microwave vial, Amino-PEG_{12}-propanoic acid t-Butyl ester (**4-3**) (0.042 g, 0.063 mmol) was added and dissolved in 3 mL of anhydrous DMF once the vial was capped and under nitrogen. Once fully dissolved, **4-3** was added dropwise to the vial containing the reaction mixture. The reaction was sparged with argon then shielded from light and stirred at room temperature for 12 hours. The solvent was evaporated and placed on a high vacuum for 20 minutes. The material was then redissolved in 1 mL of DCM, and 100 µL of trifluoroacetic acid (TFA) was slowly added to the mixture and stirred for 1 hour at room temperature. The solvent was evaporated and then diluted in 10 mL of water and loaded onto a C18 cartridge. 5 mL of water was used to wash the cartridge and ethanol was used to elute the dye. The material was purified using a prep-TLC (normal phase) eluted in 12.5% methanol in DCM (product Rf=0) (25 % yield). **HPLC** (UV 700 nm) t_r= 8.96 min. **HRMS** (ESI^-) m/z calculated for $C_{74}H_{105}N_3O_{21}S_2$: 1435.6609 $[M-H]^-$, found 1434.6631; 716.8268 $[M-2H]^{2-}$, found 716.827. **^{1}H NMR** (600 MHz, CD_3OD) δ= 8.453 (d, J=14.04 MHz, 2H), 7.949 (d, J=8.34 MHz, 2H), 7.724 (d, J=8.4 MHz, 2H), 7.397 (d, J=7.44 MHz, 2H), 7.331 (dt, J=8.1, 0.84 MHz, 2H), 7.278 (d, J=7.92 MHz, 2H), 7.167 (t, J=7.44 MHz, 2H), 6.296 (d, J=14.1 MHz, 2H), 4.129 (t, J=7.08 MHz, 4H), 3.635 (m, 6H), 3.589 (m, 6H), 3.545 (m, 38H), 2.808 (t, J=7.32 MHz, 4H), 2.639 (t, J= 5.94 MHz, 4H), 2.421 (t, J=6.12, 2H), 1.899 (m, 10H), 12.339 (s, 12H) ppm; **^{13}C NMR** (150 MHz, CD_3OD) δ=173.5, 169.2, 147.1, 143.9, 142.6, 141.9, 136.7, 134.4, 132.9, 130.1, 129.4, 126.5, 126.4, 123.6, 112.4, 102.7, 102.3, 88.4, 71.7, 71.6, 71.5, 71.49, 71.47, 71.45, 71.4, 71.37, 71.36, 71.33, 71.30, 71.23, 70.7, 68.7, 58.5, 51.9, 50.7, 45.1, 41.2, 37.4, 33.2, 33.1, 30.9, 30.8, 30.6, 28.8, 27.5, 25.7 23.9, 23.8, 22.1, 18.5, 14.6 ppm.

Synthesis of IRyne-800-PEG_{12}-DPA (4-6): To a dry microwave vial equipped with a magnetic stir bar, compound **4-4** (0.012 g, 0.0085 mmol), PyBOP (0.01 g, 0.017 mmol) and *N,N*-diisopropylethylamine (DIPEA) (2.0 µL, 0.017 mmol) were added. The vial was capped, and a nitrogen atmosphere was induced. The mixture was dissolved in 1.5 mL of DMF. In a separate, dry microwave vial, DPA-NH_2 (**4-5**) (0.01 g, 0.017 mmol) was added and dissolved in 1 mL of anhydrous DMF once the vial was capped and under nitrogen. Once fully dissolved, DPA-NH_2 was added dropwise to the vial containing the reaction mixture. The reaction was shielded from light and stirred at room temperature for 12 hours. The solvent was evaporated, and the material

was purified by prep-HPLC (dissolved in 2 mL of water) (60% yield). **HPLC** (UV 700 nm) t_r= 8.08 min. **HRMS** (ESI^+) m/z calculated for $C_{110}H_{144}N_{10}O_{21}S_2$: 2006.022 $[M+H]^+$, found 2005.9974; 1003.5047 $[M+2H]^{2+}$, found 1003.5083; 681.9919 $[M+Na-H+3H]^{3+}$, found 681.9928. **^{1}H NMR** (600 MHz, CD_3OD) δ= 8.63 (d, J=4.8 MHz, 4H), 8.39 (d, J=13.9 MHz, 2H), 7.99 (dt, J= 7.8, 1.8 MHz, 4H), 7.96 (d, J=8.4 MHz, 2H), 7.72 (d, J=8.4 MHz, 2H), 7.57 (d, J=8.4 MHz, 4H), 7.51 (t, J=6.6 MHz, 4H), 7.42 (d, J=7.2 MHz, 2H), 7.33 (t, J=7.2 MHz, 2H), 7.29 (d, J=8.4 MHz, 2H), 7.18 (t, J=7.8 MHz, 2H), 6.94 (s, 1H), 6.73 (s, 2H), 6.32 (d, J=13.8, 2H), 4.26 (s, 8H), 4.16 (t, J=6.7 MHz, 4H), 3.92 (s, 4H), 3.89 (s, 1H), 3.80 (t, J=6.2 MHz, 2H), 3.64-3.62 (m, 3H), 3.61-3.59 (m, 6H), 3.58-3.3.55 (m, 5H), 3.54-3.52 (m, 3H), 3.51-3.45 (m, 37H), 3.14 (t, J=7.0 MHz, 2H), 2.87 (t, J=7.2 MHz, 4H), 2.55 (t, J=6 MHz, 4H), 2.33 (t, J=6 MHz, 2H), 1.93 (m, 10H), 1.78 (t, J=6 MHz, 2H), 1.65 (s, 15H), 1.55 (q, J=7.2 MHz, 2H) ppm; **^{13}C NMR-UDEFT** (150 MHz, CD_3OD) δ= 174.1, 169.2, 161.0, 154.7, 147.6, 143.8, 142.7, 137.4, 136.8, 132.9, 130.2, 129.5, 126.6, 126.1, 125.3, 123.7, 117.8, 71.8, 71.7, 71.6, 71.5, 71.4, 70.7, 68.9, 68.5, 60.3, 58.6, 57.6, 52.1, 50.7, 45.1, 41.4, 39.9, 37.9, 30.9, 28.9, 28.5, 27.5, 27.3, 26.4, 25.7, 23.8, 17.4 ppm.

Synthesis of IR-ZnDPA-1 (4-7): Compound **4-6** (0.001 g, 0.0005 mmol) and $Zn(NO_3)_2$ (0.00019 g, 0.001 mmol) were dissolved in methanol (490 µL) and stirred at 37˚C for 30 minutes. The solvent was evaporated, and the material was redissolved in a suitable solvent (chosen based on the application) and used without purification. **HPLC** (UV 700 nm) t_r= 8.08 min. **LRMS** (ESI^+) m/z: 1035 $[M+Zn+2H]^{2+}$, 1068 $[M+2Zn+2H]^{2+}$, 690 $[M+Zn+3H]^{3+}$, 712 $[M+2Zn+3H]^{3+}$.

Sample Preparation: Compounds **4-4** and **4-7** were dissolved in methanol to create stock solutions at 1 mM, from which aliquots were taken and the solvent evaporated. The material was then redissolved in an appropriate solvent (Methanol, 10% Ethanol in 0.9% w/v saline, or 0.9% w/v saline) and at an appropriate concentration for the desired application (10, 15, 20 µM or kept at 1 mM).

Absorption/Emission Spectra & Solubility Analysis: Each sample (10 µM in 10% ethanol in 0.9% w/v saline) was aliquoted, in triplicate, into a 96 well plate and the absorption (600-950 nm) and emission (excitation at 736 nm, emission from 746-850 nm) spectra were collected on a Tecan Infinite M1000 plate reader. Blank scans, of neat 10% ethanol in 0.9% w/v

saline, were subtracted from the data to correct for any solvent effects. The same method was applied for the solubility analysis using samples at 15 μM and dissolved in methanol, 10% ethanol in 0.9% w/v saline, or 0.9% w/v saline. Absorption coefficients and quantum yields were calculated using procedures that can be found in **AI-1: Supporting Methods**.

Photoacoustic Phantom Imaging: PA phantom work was performed using a Vevo Phantom imaging chamber (see **Figure AI-17**) and the Vevo LAZR-X (FUJIFILM VisualSonics, Inc., Toronto, ON, Canada) imaging system equipped with a 680-970 nm laser. Samples (20 μM, 10% ethanol in 0.9% w/v saline) were injected into Vevo Contrast Agent Phantom tubing (PN52807) that was threaded into the Vevo Phantom chamber. A 30 MHz, linear array US transducer equipped with integrated fibre optic cables (MX400 and LZ-400 [15-30 $mJ(cm^3)^{-1}$], FUJIFILM VisualSonics, Inc., Toronto, ON, Canada) was positioned overtop of the tubes.

Spectral analysis was performed using Spectro scans, where the PA signal of a 2D, x,y-cross-section of a sample is quantified at each wavelength (690-970 nm) and is used to plot the spectral curve from a defined ROI. From this, the signal intensity of the chromophore of interest can be quantified by the signal unmixing algorithm utilized in the VevoLAB software (VisualSonics, Inc., Toronto, ON, Canada). Additionally, 2D multispectral unmixing scans (oxygenated and deoxygenated hemoglobin unmixed from the spectra of **4-4** or **4-7**) were taken for the desired sample in triplicate. Designated wavelengths based on notable signals generated within individual chromophore spectra (oxygenated and deoxygenated hemoglobin: 680, 924, 936 nm; **3-4**: 692 and 802 nm; **4-4**: 735 and 802 nm; or **4-7**: 806 nm), were used by the Vevo-3100/LAZR-X unmixing algorithm. Images from the Spectro and multiwavelength unmixing scans are displayed to show the PA signal overlaid on the US B-mode (greyscale) signal of a cross-section of the tubing. All image processing was carried out using the VevoLAB software. A ROI was drawn around the US image of the tube and, applying ROIs of the same size and shape to each image, a spectrum of PA average signal was generated from the overlaid PA data of each image.

Animal Studies: All procedures were conducted according to the guidelines of the Committee for Research and Ethics Issues of the International Association for the Study of Pain, and guidelines established by the Canadian Council on Animal Care and the McMaster University

Animal Research Ethics Board. In each animal study 7-10 week-old female BALB/c mice (Charles River Laboratories, Raleigh, NC), weighing around 20 g, were used. The mice were sterile housed and maintained at 21 ˚C with a 12-hour light/dark cycle and were provided autoclaved food and water *ad libitum*.

***In Vivo* Photoacoustic Imaging Studies:** PAI was performed using the Vevo-3100/LAZR-X imaging system. Mice were anesthetized, and the fur of their right hindlimb was thoroughly removed before being placed in a prone position on a platform that enabled the monitoring of their respiration and heart rate. A generous amount of US gel was applied before imaging with the transducer (MX400/LX400) positioned over the leg. At each imaging time point, Spectro scans and 3D multispectral unmixing scans were taken of each hindlimb. The transducer was positioned laterally overtop of the hindlimb, corresponding with the inoculation site. Scan distances averaged 20 mm and scans were taken every 0.33 mm.

3D multiwavelength unmixing scans were performed to construct images depicting dye-specific PA signal present within the hindlimb. Designated wavelengths based on notable signals generated within individual chromophore spectra (oxygenated and deoxygenated hemoglobin: 680, 924, 936 nm; **3-4**: 692 and 802 nm; **4-4**: 735 and 802 nm; or **4-7**: 806 nm), were used by the Vevo-3100/LAZR-X unmixing algorithm. The series of 2D cross-sectional scans collected were then reconstructed by the instrument into a 3D image, where the signals from each chromophore are assigned a colour and overlaid onto a b-mode ultrasound scan. The scans are displayed as either render mode or texture mapping images where the PA signal is overlaid on US B-mode (greyscale) signal for sections of the hindlimb. Signals from oxygenated and deoxygenated hemoglobin were subtracted from the images to reduce visual complexity. The spectrally unmixed signal of **4-4** or **4-7**, in the 3D multiwavelength unmixing scans, was quantified using 3D ROI drawn around the inoculation sites. All signal unmixing algorithms and image processing were carried out using the VevoLAB software. Image processing consisted of signal optimization, with parameters set the same for each image within the study. 3D regions of interest were drawn around the inoculation site.

Spectral analysis was performed using ‘Spectro’ scans (as described in the “Photoacoustic Phantom Imaging’ section) and was used to verify whether the spectral signature of the *in vivo* signal matched that of the exogenous dye.

Signal Unmixing Analysis

Phantom PA Signal Unmixing: 12.8 µL of **4-4** or **4-7** (1 mM in 10% ethanol in 0.9% w/v saline) were added to 187.2 µL of whole mouse blood (mixed with 10% EDTA in PBS). The samples (including 12.8 µM of 10% ethanol in 0.9% w/v saline added to 187.2 µL of blood) were injected into Vevo contrast agent phantom tubing and Spectro scans were taken of the material in triplicate. The signals from the spectra scans were unmixed and analyzed as described in 'Photoacoustic Phantom Imaging'.

***In Vivo* PA Signal Unmixing:** Naïve Balb/C mice (n=4) were imaged as described in the section titled '*In Vivo* Photoacoustic Imaging Studies', on the Vevo LAZR X pre-injection. 3D multiwavelength unmixing scans were taken of the same tissue where the signals of **3-4**, **4-4**, or **4-7** were unmixed from oxygenated and deoxygenated hemoglobin, as outlined in '*In Vivo* Photoacoustic Imaging Studies'.

Proof-of-Concept Bacteria-Binding Analysis of 4-7 Compared to 4-4

***In Vitro* Bacteria Binding Assay: 4-4** or **4-7** (12 µM) were incubated with 1×10^9 CFU (50 µL) of *S. aureus* (ATCC; 25923) in HBSS or 50 µL of HBSS (no-cell control), for 10 minutes in triplicate. The samples were washed 3 times and the pellet was resuspended in 250 µL of HBSS. 200 µL sample and 200 µL stock solution were transferred to a black flat clear bottom 96-well plate. A fluorescence scan (Ex= 736 nm; Em= 746-850 nm) was performed. The fluorescence intensities (at 829 nm) of blank samples were subtracted from samples of **4-4** and **4-7** incubated with or without bacteria and the change in intensity was evaluated.

***Staphylococcus aureus*-Induced Myositis Model:** An aliquot of *S. aureus* (OD_{600}=8.43, 1×10^8 CFUs, 50 µL in HBSS) was injected intramuscularly (I.M.) on the right hindlimb. 50 µL of the vehicle control, HBSS, was injected IM into the left hindlimb. 18 hours post-inoculation of the bacteria, tissues were collected and analyzed as described in the section titled 'Histological Analysis'. Animals were end-point monitored throughout the study.

Photoacoustic Imaging of *S. aureus*-Induced Bacterial Infection using 4-4 or 4-7: 6 hours after inoculating mice (n=4), as described previously, the mice were injected intravenously with 100 µL of **4-4** or **4-7** (1 mM) and were imaged, as described in the section titled '*In Vivo* Photoacoustic Imaging Studies', on the Vevo LAZR X, pre-injection, and 12 hours post-injection. Animals tolerated administration of the PIPs well and end-point was not reached throughout the study.

Statistical Analyses: Data are reported as mean ± standard error of the mean (SEM). Concentration and hydroxyapatite binding data were analyzed by one-way analysis of variance (ANOVA). Differences between test groups and control were assessed using Dunnett's Multiple Comparison Test on GraphPad Prism version 9 (GraphPad Software, San Diego, CA). Each experiment was performed and validated at least 3 times. *In vivo* PAI data were analyzed using a two-way ANOVA. The Tukey Test on GraphPad was used to assess the differences between the test and control groups. Statistical significance was established using * $P \leq 0.05$; ** $P \leq 0.01$; *** $P \leq 0.001$ vs. control or appropriate diluent.

Ancillary Information: Supporting data are available in Appendix III: Supporting methods & calculations for molar absorptivity and fluorescence quantum yield, HPLC, HRMS, and ^{1}H & ^{13}C-NMR data of all compounds.

4.5 References

(1) Weber, J.; Beard, P. C.; Bohndiek, S. E. Contrast Agents for Molecular Photoacoustic Imaging. *Nat. Methods* **2016**, *13* (8), 639–650. https://doi.org/10.1038/nmeth.3929.

(2) Emelianov, S. Y.; Li, P.-C.; O'Donnell, M. Photoacoustics for Molecular Imaging and Therapy. *Phys. Today* **2009**, *62* (8), 34–39. https://doi.org/10.1063/1.3141939.

(3) Steinberg, I.; Huland, D. M.; Vermesh, O.; Frostig, H. E.; Tummers, W. S.; Gambhir, S. S. Photoacoustic Clinical Imaging. *Photoacoustics* **2019**, *14*, 77–98. https://doi.org/10.1016/j.pacs.2019.05.001.

(4) Sivaramakrishnan, M.; Maslov, K.; Zhang, H. F.; Stoica, G.; Wang, L. V. Limitations of Quantitative Photoacoustic Measurements of Blood Oxygenation in Small Vessels. *Phys. Med. Biol.* **2007**, *52* (5), 1349–1361. https://doi.org/10.1088/0031-9155/52/5/010.

(5) West, W.; Pearce, S. The Dimeric State of Cyanine Dyes. *J. Phys. Chem.* **1965**, *69* (6), 1894–1903. https://doi.org/10.1021/j100890a019.

(6) Mishra, A.; Behera, R. K.; Behera, P. K.; Mishra, B. K.; Behera, G. B. Cyanines during the 1990s: A Review. *Chem. Rev.* **2000**, *100* (6), 1973–2012. https://doi.org/10.1021/cr990402t.

(7) Watson, A. D. Binding Studies of Near Infrared Cyanine Dyes with Human Serum Albumin and Poly-L-Lysine Using Optical Spectroscopy Methods. Dissertation, Georgia State University, 2008. h9p://scholarworks.gsu.edu/chemistry_diss/15.

(8) Usama, S. M.; Park, G. K.; Nomura, S.; Baek, Y.; Choi, H. S.; Burgess, K. Role of Albumin in Accumulation and Persistence of Tumor-Seeking Cyanine Dyes. *Bioconjug. Chem.* **2020**, *31* (2), 248–259. https://doi.org/10.1021/acs.bioconjchem.9b00771.

(9) Thavornpradit, S.; Usama, S. M.; Park, G. K.; Shrestha, J. P.; Nomura, S.; Baek, Y.; Choi, H. S.; Burgess, K. QuatCy: A Heptamethine Cyanine Modification With Improved Characteristics. *Theranostics* **2019**, *9* (10), 2856–2867. https://doi.org/10.7150/thno.33595.

(10) König, S. G.; Krämer, R. Accessing Structurally Diverse Near-Infrared Cyanine Dyes for Folate Receptor-Targeted Cancer Cell Staining. *Chem. - Eur. J.* **2017**, *23* (39), 9306–9312. https://doi.org/10.1002/chem.201700026.

(11) James, N. S.; Chen, Y.; Joshi, P.; Ohulchanskyy, T. Y.; Ethirajan, M.; Henary, M.; Strekowsk, L.; Pandey, R. K. Evaluation of Polymethine Dyes as Potential Probes for Near Infrared Fluorescence Imaging of Tumors: Part - 1. *Theranostics* **2013**, *3* (9), 692–702. https://doi.org/10.7150/thno.5922.

(12) Chapman, G.; Henary, M.; Patonay, G. The Effect of Varying Short-Chain Alkyl Substitution on the Molar Absorptivity and Quantum Yield of Cyanine Dyes. *Anal. Chem. Insights* **2011**, *6*, ACI.S6568. https://doi.org/10.4137/ACI.S6568.

(13) Beard, P. Biomedical Photoacoustic Imaging. *Interface Focus* **2011**, *1* (4), 602–631. https://doi.org/10.1098/rsfs.2011.0028.

(14) Plaunt, A. J.; Harmatys, K. M.; Wolter, W. R.; Suckow, M. A.; Smith, B. D. Library Synthesis, Screening, and Discovery of Modified Zinc(II)-Bis(Dipicolylamine) Probe for

Enhanced Molecular Imaging of Cell Death. *Bioconjug. Chem.* **2014**, *25* (4), 724–737. https://doi.org/10.1021/bc500003x.

(15) Rice, D. R.; Vacchina, P.; Norris-Mullins, B.; Morales, M. A.; Smith, B. D. Zinc(II)-Dipicolylamine Coordination Complexes as Targeting and Chemotherapeutic Agents for Leishmania Major. *Antimicrob. Agents Chemother.* **2016**, *60* (5), 2932–2940. https://doi.org/10.1128/AAC.00410-16.

(16) Chen, Y.; Dhara, S.; Banerjee, S. R.; Byun, Y.; Pullambhatla, M.; Mease, R. C.; Pomper, M. G. A Low Molecular Weight PSMA-Based Fluorescent Imaging Agent for Cancer. *Biochem. Biophys. Res. Commun.* **2009**, *390* (3), 624–629. https://doi.org/10.1016/j.bbrc.2009.10.017

Chapter 5 : Conclusions & Future Directions

5.1 Summary & Conclusions

MI techniques are a critical aspect of clinical research and medical practice, as they enable the non-invasive visualization of cellular biochemistry which facilitates the advancement of our understanding of disease pathology. PAI is an emerging MI modality that utilizes the non-radiative relaxation of contrast agents excited by pulsed light absorption, to generate detectable ultrasound waves. PAI offers the capability to take real-time images, with superior depth resolution compared to fluorescence imaging, and without the use of ionizing radiation.[1] Although light penetration is a limiting factor in the clinical translation of PAI, there are many suitable disease imaging applications for this modality, including localized diseases accessible via the various tomographic, handheld, and endoscopic transducer configurations. Despite these mechanical advancements, there is a current paucity of clinically relevant molecularly targeted agents. Therefore, to meet this demand, the work presented within this thesis aimed to evaluate suitable combinations of light-absorbing small molecule dyes, disease-targeting molecules, and *in vivo* targeting strategies.

First, a near-infrared photoacoustic probe was used to image bone and was assessed via active and pre-targeting strategies. To do this a tetrazine-derived cyanine dye and a *trans*-cyclooctene-modified bisphosphonate, were synthesized. *In vitro* hydroxyapatite binding of the probe via active and pre-targeting strategies showed comparable binding to hydroxyapatite versus a non-targeted control. Intrafemoral injection of the bisphosphonate-dye conjugate showed retention out to 24 hours post-injection, with a 14-fold increase in signal over background, while the non-targeted dye exhibited negligible binding to bone and signal washout by 4 hours post-injection. Accumulation in the bone was demonstrated as early as 4 hours post-intravenous injection using both active and pre-targeting strategies, where the signal was found to be 3.6- and

1.5-fold higher, respectively, than the signal from the non-targeted dye. The described bone-targeted PIP enabled *in vivo* photoacoustic imaging and the synthetic strategy provided a convenient building block for developing PIPs from other TCO-based targeting vectors.

The tetrazine dye was then tested alongside a ZnDPA-derived TCO, to explore the utility of PAI for diagnosing bacterial infections. This first-generation probe demonstrated poor aqueous solubility and overlapping photoacoustic (PA) signal with deoxyhemoglobin, which prompted the exploration of a commercially available bacteria-targeting fluorophore, PSVue794. A radiolabeled version of the dye, [^{99m}Tc]Tc-PSVue794, was developed to facilitate quantitative biodistribution studies beyond what is currently feasible to generate with optical imaging methods, which showed a target-to-non-target ratio of 10.1 ± 1.1, 12 hrs post-injection. The ability of the PIP to differentiate between bacterial infection, sterile inflammation, and healthy tissue in a mouse model, was then evaluated via PAI. The T/NT and the S/B ratios derived from the PAI analysis in LPS-induced (T/NT= 1.04 ± 0.17, S/B= 1.07 ± 0.11) and *S. aureus*-induced (T/NT= 2.40 ± 0.49, S/B= 2.17 ± 0.05) myositis showed that the Zn-DPA targeting moiety facilitates the specific localization of the PIP at sites of bacterial infection and that the commercially available fluorophore could be used to generate a detectable PA signal, *in vivo*.

Since inflammation and cell death are pathologies that often accompany medical implant infections, a series of proof-of-concept studies were then executed to demonstrate the feasibility of detecting PSVue794 in the presence of a PA signal-emitting metallic implant. The signal of the PIP was identifiable against the signal of the implant and the spectral signature of the PIP was verified. Although the work requires a follow-up study, where the PIP is administered I.V. and assessed for its ability to distinguish between sterile and infected implants, Zn-DPA-based PIPs have remained promising candidates for PAI of bacterial infection.

In consideration of the challenges faced by the bone and infection-targeted PIPs, namely their solubility and the capacity to accurately unmix their PA signals from the signal generated by blood, a novel NIR dye was designed to possess properties ideal for *in vivo* PAI. The PIP featured a PEG-linker for enhanced aqueous solubility and a shifted absorbance maximum to facilitate accurate signal unmixing from endogenous blood chromophores. To evaluate these modifications, the general-purpose dye was conjugated with a Zn-DPA-based bacteria targeting vector, which was tested alongside the non-targeted counterpart and the previously discussed commercially available dye, PSVue794. The novel dyes primarily formed dimeric species in aqueous solution, a notable improvement from the aggregate formation of PSVue794, and the targeted PIP exhibited a high monomer intensity in all solvents. This ideal solubility also led to a single PA maximum at 805 nm, which was found to contribute to the accuracy of the signal unmixing algorithm in distinguishing the target dye from endogenous blood chromophores. *In vivo*, the novel PIP did not demonstrate target-specificity, potentially resulting from the weak electrostatic forces that drive the bacterial targeting mechanism in combination with the high aqueous solubility of the PIP. The rationale that contributed to the design of the general-purpose dye did lead to high solubility and promising PA properties of the targeted PIP and will remain a key aspect of future work, which will aim to investigate the dye with higher affinity targeting vectors for PA-compatible diseases.

5.2 Future Directions

5.2.1 Continued Investigation of Photoacoustic Imaging for Diagnosing Bacterial Infection

With the general-purpose dye described in Chapter 4, the infection imaging work will be continued by assessing the dye alongside various bacteria-targeting vectors. Although our initial studies with **4-7** were inconclusive on the targeting ability of the construct, it will be valuable to assess ZnDPA moieties that possess phenethyl- or butyl-ureido substituents, which have been

documented to strengthen the probe's interaction with the outer membrane of the bacteria by implementing secondary non-covalent interactions between the substituents and phosphatidylserine in the membrane.[2,3] Alternative bacteria-targeting vectors, including the antimicrobial peptide, UBI, and bacteria-metabolizable sugars, such as maltodextrins, are also currently under consideration for moving forward with the work.

With the final PIPs, a series of *in vitro* and *in vivo* studies will be performed to assess their utility. To detail, evaluation of bacterial binding will be conducted for each of the probes using the *in vitro S. aureus* assay described in Chapters 3 and 4. Additionally, the probes may be tested against various other bacterial strains that are commonly associated with implant and surgical site infections, namely *Escherichia coli, Pseudomonas aeruginosa, Klebsiella pneumoniae,* Methicillin-resistant *S. aureus* (MRSA) and *Staphylococcus epidermidis.*[4–8] The *S. aureus*- and LPS-induced myositis models (described in Chapters 3 and 4) will be used to evaluate the probe's specificity to sites of infection over sterile inflammation.

Once the targeting ability of the probes has been demonstrated, follow-up studies can be performed to assess the detectability of the PA signal generated by the PIPs in the presence of an infected titanium implant. Mice will be inoculated with bacteria and implanted with the titanium rod in the gastrocnemius muscle (as described in Chapter 3.2), after which, the PIP will be injected intravenously. Once enough time has passed, to allow for localization of the PIP to the infection site, the mice will be imaged and the PA signal of the PIP will be unmixed from the signal generated by both blood chromophores and the metal implant, and quantified. If the PIPs can preferentially localize to sites of infected implants, at detectable concentrations, compared to sites of non-infected implants, a focus will then be placed on evaluating the use of the PIPs for detecting early-stage infections. While the infection models described in this work utilized higher

concentrations of bacteria for proof-of-concept, lower concentrations of bacteria, starting with 1.0×10^6 CFUs and 1.0×10^4 CFUs, will be inoculated into the muscle and the signal-to-background ratios will be used to conclude on the PIPs sensitivity towards lower levels of bacteria to represent earlier-stages of infection. The data generated from these studies will be used toward the greater goal of developing non-invasive methods to accurately diagnose early stages of healthcare-associated bacterial infections, enabling precise therapeutic intervention and a reduction in the misuse of antibiotics.

5.2.2 Other Applications of PAI

Many articles have discussed projected clinical applications of PAI with a consensus surrounding the promise of PAI towards screening for and treatment monitoring of various cancers.[1,9–12] It is evident how the continued advancement of tomographic, handheld, and endoscopic PA transducers warrants the development of PIPs targeted towards prostate, breast, and ovarian cancers. Within our group, progress has already been made toward the development of a prostate cancer-targeted PIP that utilizes glutamate-ureido-lysine (GUL) to target prostate-specific membrane antigen (PSMA), a biomarker overexpressed on the surface of prostate cancer cells.[13] The probe, which utilizes the general purpose dye, **4-4** targeted with GUL, will be compared to YC-27 a similarly designed probe reported by Chen, *et al*.[13,14] The aqueous solubility of the probes will be compared before assessing the *in vivo* prostate cancer-targeting capabilities of each PIP using patient-derived LNCaP (PSMA+) and PC3 (PSMA-) xenografts. Additional efforts should be dedicated to determining breast and ovarian cancer-targeting agents, to be used alongside **4-4,** and the most suitable biological models of disease to validate the utility of these probes.

As it currently exists, PAI has discernible advantages over other optical techniques, such as fluorescent imaging, and has been used extensively in the preclinical study of disease. Nevertheless, the adoption of 'label-free' PAI methods in clinical practice has only recently gained traction, while the availability of translational exogenous contrast agents has been limited. Progress in developing exogenous PIPs with optimal synthetic, photophysical, and biological properties, alongside the establishment of robust validation methodologies to ensure efficacy and safety, will enhance the recognition and clinical utility of PAI.

5.3 References

(1) Mehrmohammadi, M.; Joon Yoon, S.; Yeager, D.; Y. Emelianov, S. Photoacoustic Imaging for Cancer Detection and Staging. *Curr. Mol. Imaging* **2013**, *2* (1), 89–105. https://doi.org/10.2174/2211555211302010010.

(2) Plaunt, A. J.; Harmatys, K. M.; Wolter, W. R.; Suckow, M. A.; Smith, B. D. Library Synthesis, Screening, and Discovery of Modified Zinc(II)-Bis(Dipicolylamine) Probe for Enhanced Molecular Imaging of Cell Death. *Bioconjug. Chem.* **2014**, *25* (4), 724–737. https://doi.org/10.1021/bc500003x.

(3) Rice, D. R.; Vacchina, P.; Norris-Mullins, B.; Morales, M. A.; Smith, B. D. Zinc(II)-Dipicolylamine Coordination Complexes as Targeting and Chemotherapeutic Agents for Leishmania Major. *Antimicrob. Agents Chemother.* **2016**, *60* (5), 2932–2940. https://doi.org/10.1128/AAC.00410-16.

(4) Council of Canadian Academies. *When Antibiotics Fail: The Expert Panel on the Potential Socio-Economic Impacts of Antimicrobial Resistance in Canada.*; 2019.

(5) Stavrakis, A. I.; Niska, J. A.; Loftin, A. H.; Billi, F.; Bernthal, N. M. Understanding Infection: A Primer on Animal Models of Periprosthetic Joint Infection. *Sci. World J.* **2013**, *2013*, 1–6. https://doi.org/10.1155/2013/925906.

(6) Fulkerson, E.; Valle, C. J. D.; Wise, B.; Walsh, M.; Preston, C.; Di Cesare, P. E. Antibiotic Susceptibility of Bacteria Infecting Total Joint Arthroplasty Sites. *J. Bone Joint Surg. Am.* **2006**, *88* (6), 1231–1237. https://doi.org/10.2106/JBJS.E.00004.

(7) Salgado, C. D.; Dash, S.; Cantey, J. R.; Marculescu, C. E. Higher Risk of Failure of Methicillin-Resistant Staphylococcus Aureus Prosthetic Joint Infections. *Clin. Orthop.* **2007**, *461*, 48–53. https://doi.org/10.1097/BLO.0b013e3181123d4e.

(8) Walls, R. J.; Roche, S. J.; O'Rourke, A.; McCabe, J. P. Surgical Site Infection with Methicillin-Resistant Staphylococcus Aureus after Primary Total Hip Replacement. *J. Bone Joint Surg. Br.* **2008**, *90* (3), 292–298. https://doi.org/10.1302/0301-620X.90B3.20155.

(9) Beard, P. Biomedical Photoacoustic Imaging. *Interface Focus* **2011**, *1* (4), 602–631. https://doi.org/10.1098/rsfs.2011.0028.

(10) de la Zerda, A. Photoacoustic Molecular Imaging and Its Biomedical Applications. Doctoral Dissertation, Stanford University, 2011. http://purl.stanford.edu/rc934jq3457.

(11) Luke, G. P.; Yeager, D.; Emelianov, S. Y. Biomedical Applications of Photoacoustic Imaging with Exogenous Contrast Agents. *Ann. Biomed. Eng.* **2012**, *40* (2), 422–437. https://doi.org/10.1007/s10439-011-0449-4.

(12) Attia, A. B. E.; Balasundaram, G.; Moothanchery, M.; Dinish, U. S.; Bi, R.; Ntziachristos, V.; Olivo, M. A Review of Clinical Photoacoustic Imaging: Current and Future Trends. *Photoacoustics* **2019**, *16*, 100144. https://doi.org/10.1016/j.pacs.2019.100144.

(13) Zhang, H. K.; Chen, Y.; Kang, J.; Lisok, A.; Minn, I.; Pomper, M. G.; Boctor, E. M. Prostate-Specific Membrane Antigen-Targeted Photoacoustic Imaging of Prostate Cancer *in Vivo*. *J. Biophotonics* **2018**, *11* (9), e201800021. https://doi.org/10.1002/jbio.201800021.

(14) Chen, Y.; Dhara, S.; Banerjee, S. R.; Byun, Y.; Pullambhatla, M.; Mease, R. C.; Pomper, M. G. A Low Molecular Weight PSMA-Based Fluorescent Imaging Agent for Cancer. *Biochem. Biophys. Res. Commun.* **2009**, *390* (3), 624–629. https://doi.org/10.1016/j.bbrc.2009.10.017.

Appendix I: Supporting Information for Chapter 2

A Tetrazine-Derived Near-Infrared Dye for Targeted Photoacoustic Imaging of Bone

Rowan Swann[†], Samantha Slikboer[†], Afaf Genady[†], Luis Rafael Silva[†], Nancy Janzen[†], Amber Faraday[†], John F. Valliant[†,], & Saman Sadeghi[†,*]

[†] Department of Chemistry and Chemical Biology, McMaster University, Hamilton, Ontario, L8S 4L8, Canada

Corresponding author
* Phone: (905) 525-9140 ext. 22537; Email: sadegs10@mcmaster.ca

Table of Contents

AI-1: Supporting Methods

Molar Absorptivity Calculation of Dyes: Molar absorptivity (ε, $M^{-1}cm^{-1}$) of the dyes were calculated using **equation 1** from absorbance measurements of **2-1**, **2-5**, and **2-7** (concentration, C=5 μM, dissolved in methanol; optical path length, b= 1cm) acquired from the Ultrospec 2100 *pro* spectrophotometer.

Equation AI-1: $\varepsilon = \frac{A}{bC}$

Quantum Yield Calculation of Dyes: The relative fluorescence quantum yield (Φ_x) was determined for **2-5** and **2-7** (5 μM, methanol) using **equation 2**, with Φ_{ref}= quantum yield of **2-1** as a reference.[1] A_x and A_{ref} are the absorbance at the fluorescence excitation wavelength (736 nm), of **2-5** or **2-7** and of **2-1**, respectively. F_x and F_{ref} are the areas under the curves of the fluorescence emission spectra for **2-5** or **2-7** and of **2-1**, respectively. Because the material was dissolved in the same media as the reference material (methanol), $\left(\frac{n_x}{n_{ref}}\right)^2 = 1$.

Equation AI-2: $\Phi_x = \Phi_{ref} \bullet \left(\frac{A_{ref}}{A_x}\right) \bullet \left(\frac{F_x}{F_{ref}}\right) \bullet \left(\frac{n_x}{n_{ref}}\right)^2$

Limit of Detection (LOD) Calculation:

Equation AI-3: $LOD = 3 \times \frac{Standard\ Deviation\ of\ a\ low\ concentration}{Slope\ of\ the\ line}$

Hydroxyapatite (HA) Binding Equation: The percent binding of the probe to HA was calculated using **equation 4**,[2] where Abs_{withHA} is the absorbance (770 nm) of the supernatant of the sample incubated with HA and $Abs_{withoutHA}$ is the absorbance (770 nm) of the supernatant of the sample incubated without HA.

Equation AI-4: $\%\ Binding = [1 - \frac{(Abs_{with\ HA})}{(Abs_{without\ HA})}] \times 100$

AI-2: Supporting Data

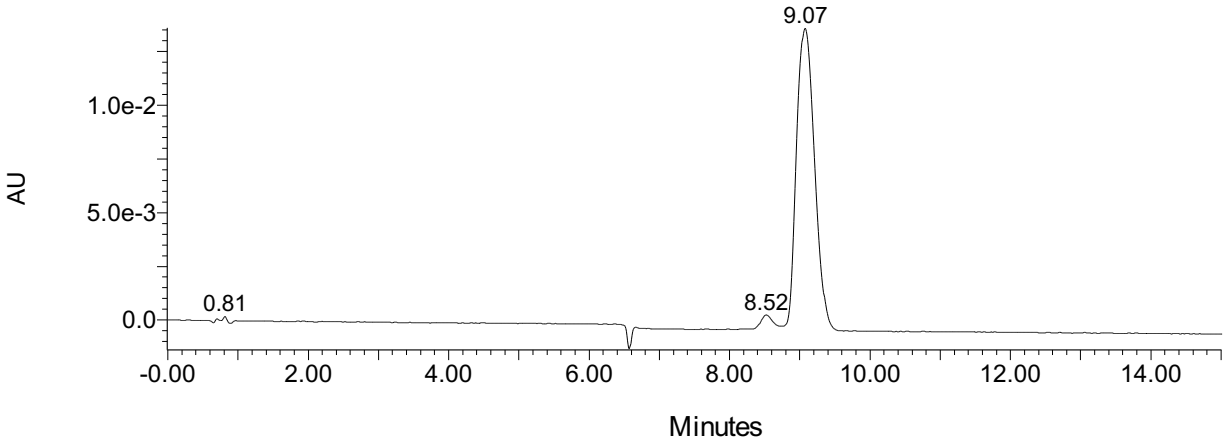

Figure AI-1. UV-HPLC trace (700 nm) of **2-3**, HPLC Method A.

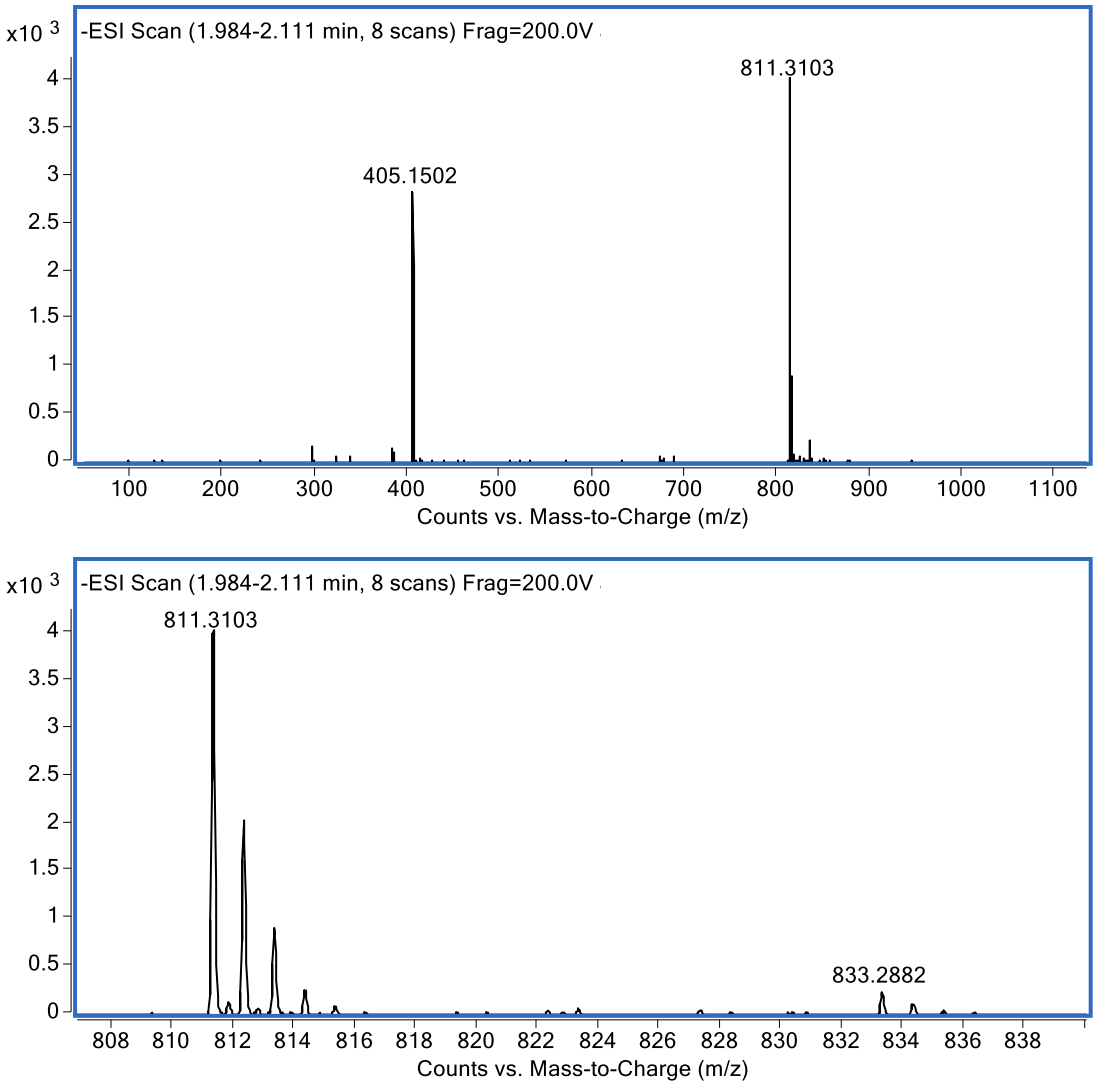

Figure AI-2. HRMS (ESI^-) of **2-3**.

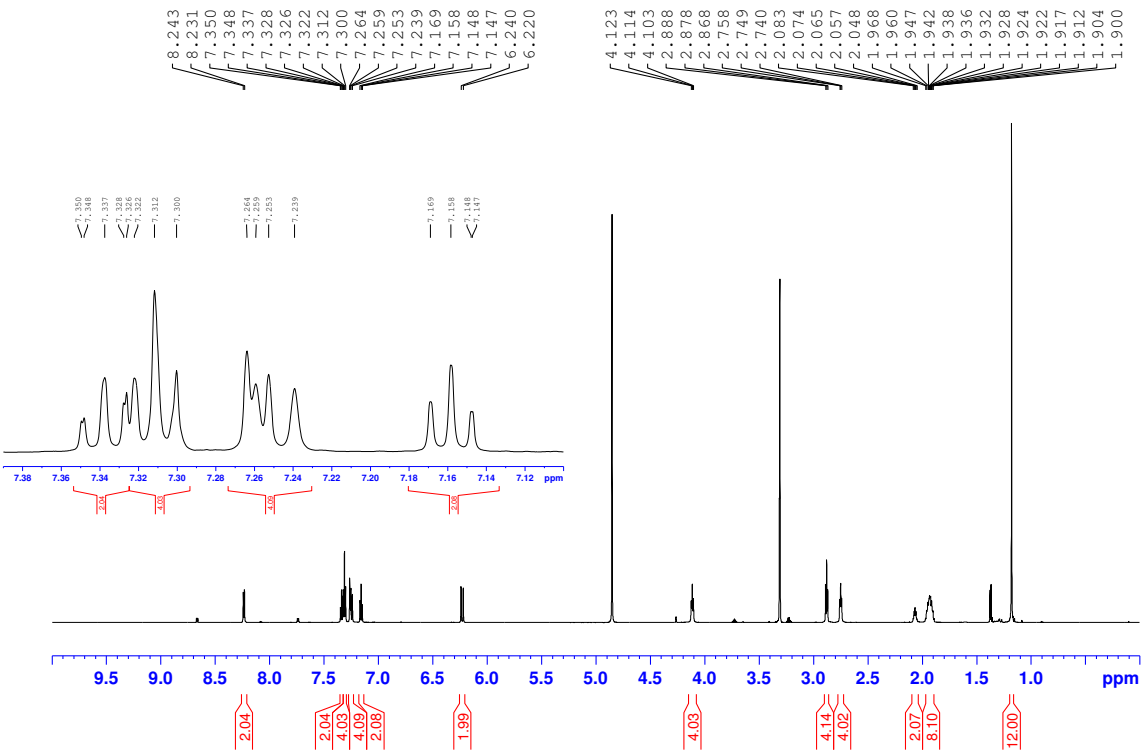

Figure AI-3. ^{1}H NMR (600 MHz, CD_3OD) of **2-3**.

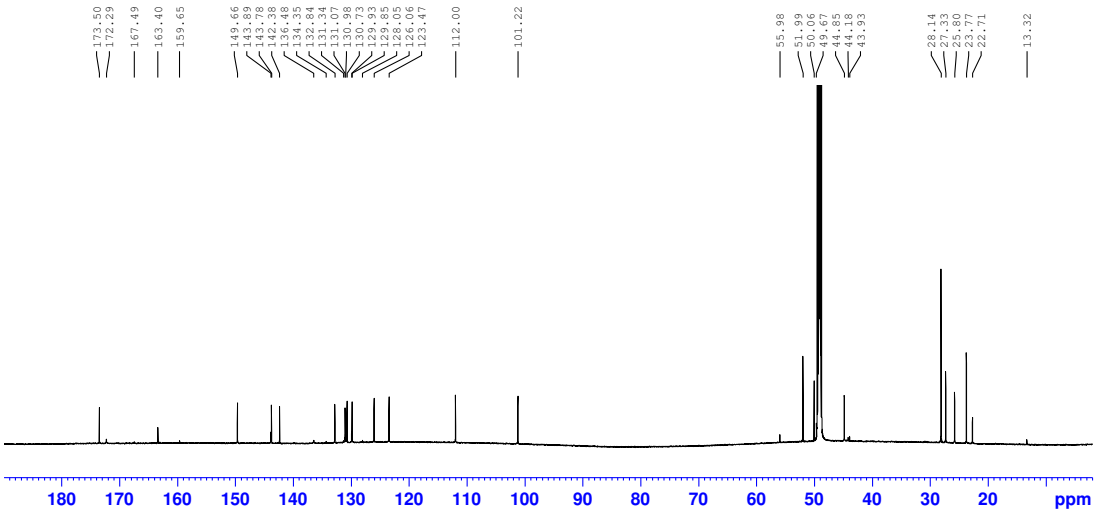

Figure AI-4. ^{13}C NMR (150 MHz, CD_3OD) of **2-3**.

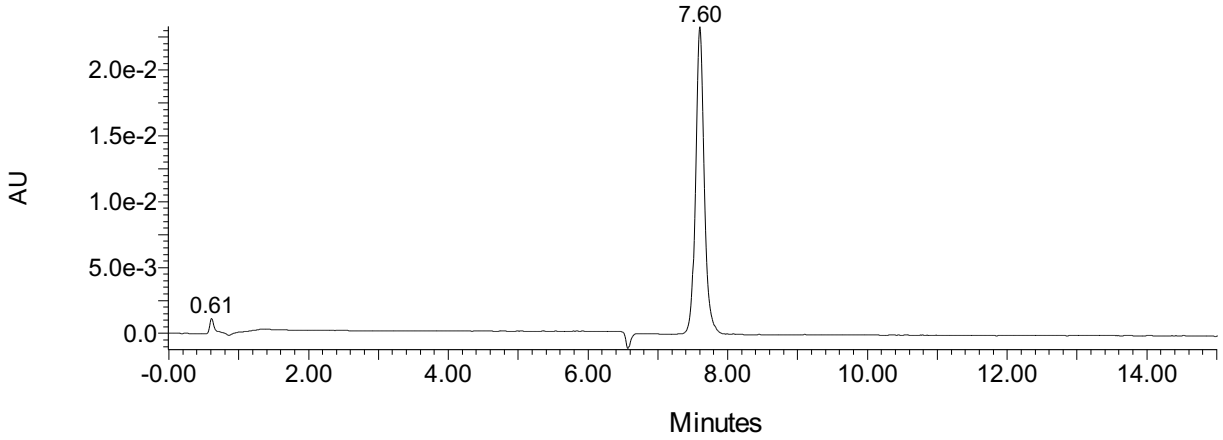

Figure AI-5. UV-HPLC trace (700 nm) of **2-5**, HPLC Method A.

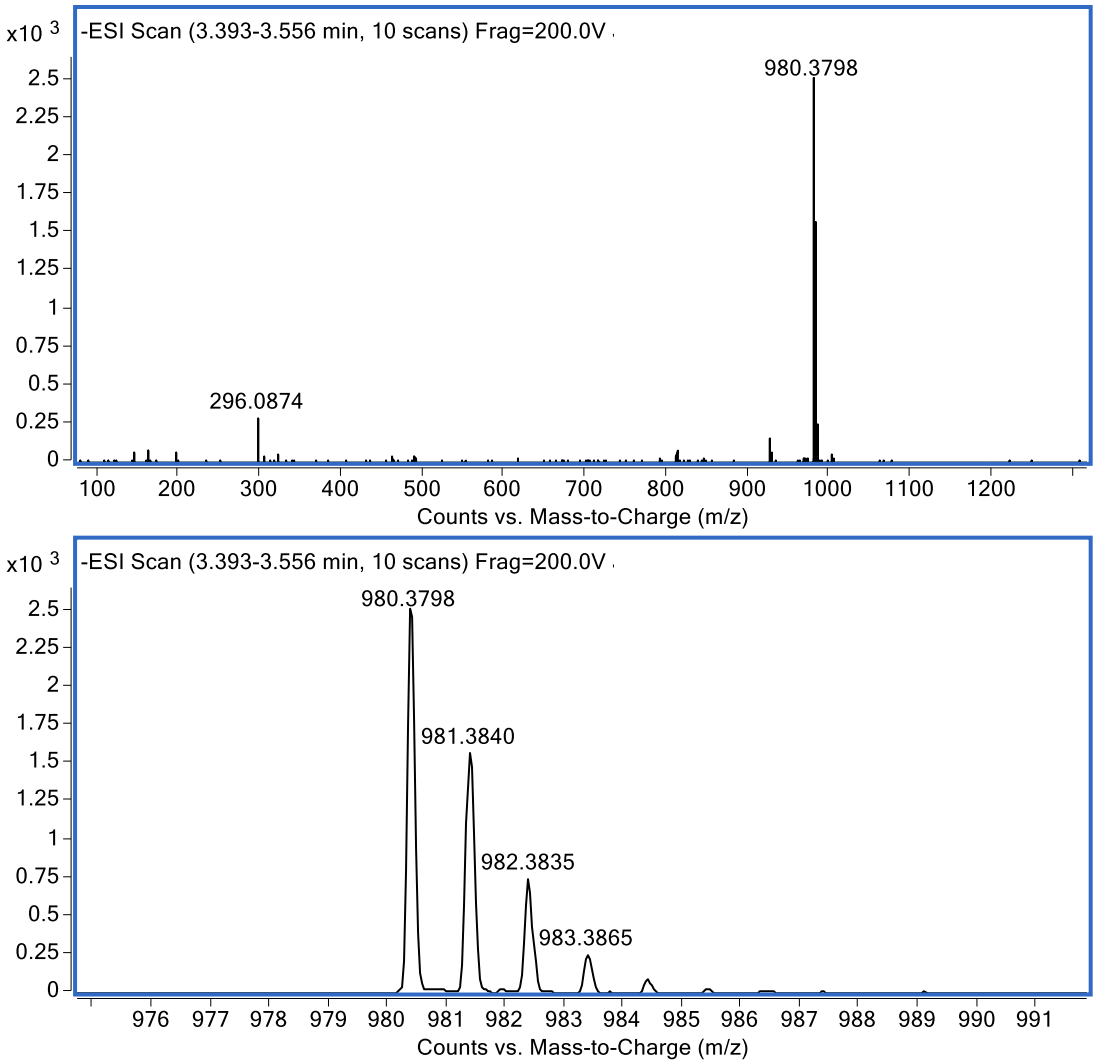

Figure AI-6. HRMS (ESI^-) of **2-5**.

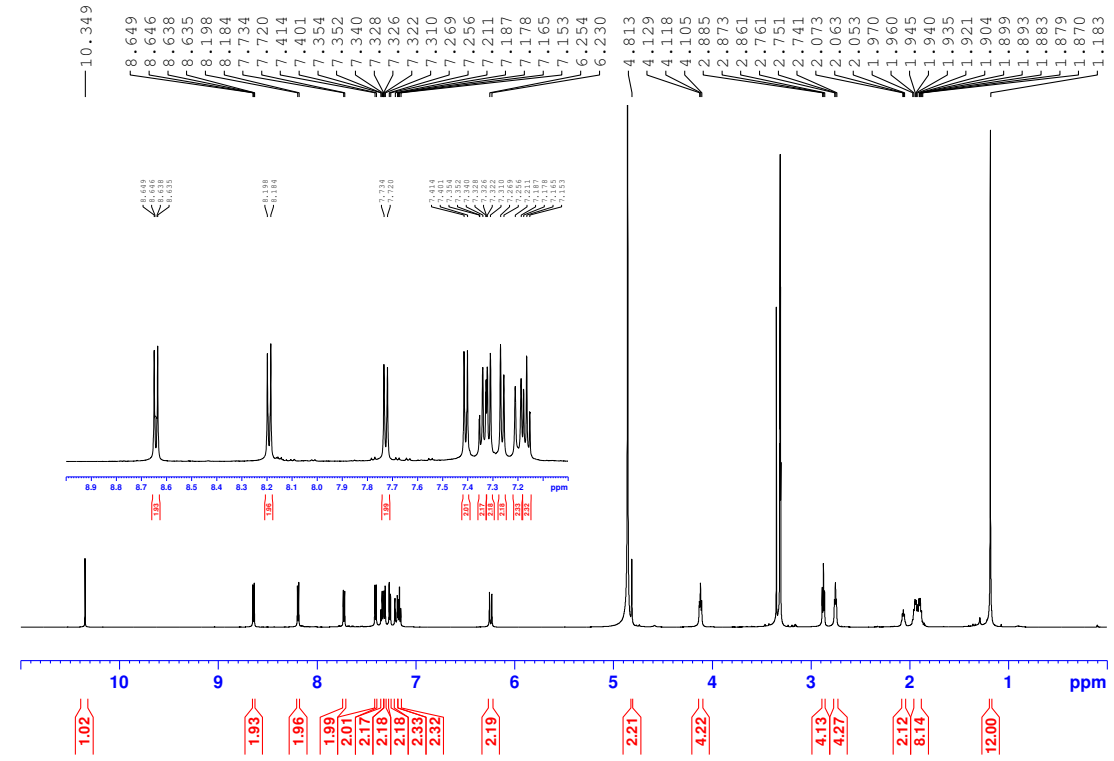

Figure AI-7. ^{1}H NMR (600 MHz, CD_3OD) of **2-5**.

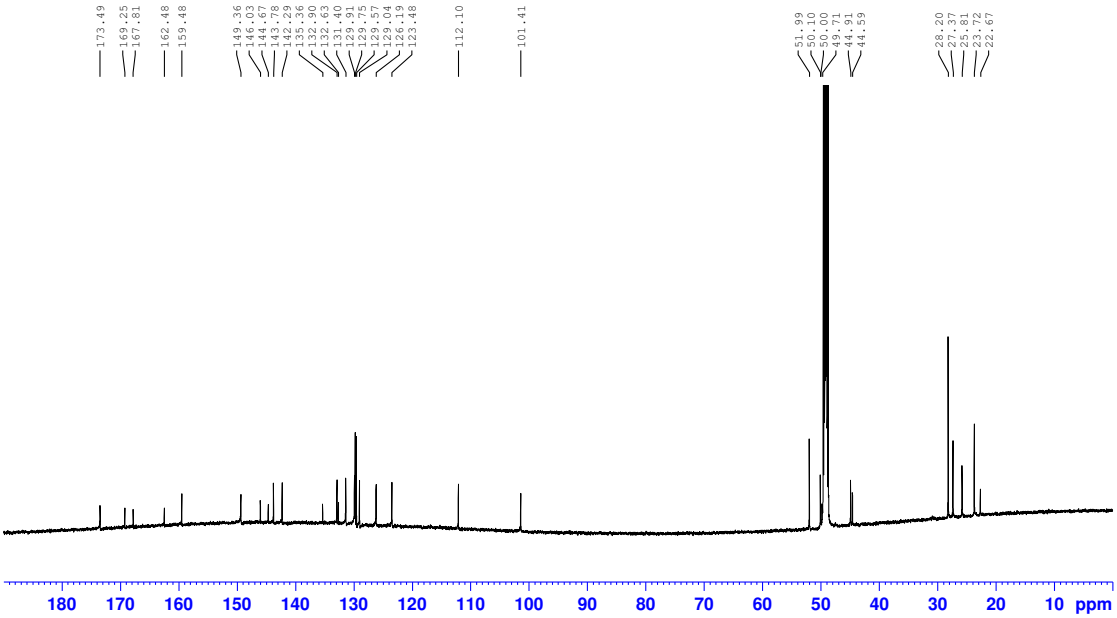

Figure AI-8. ^{13}C NMR (150 MHz, CD_3OD) of **2-5**.

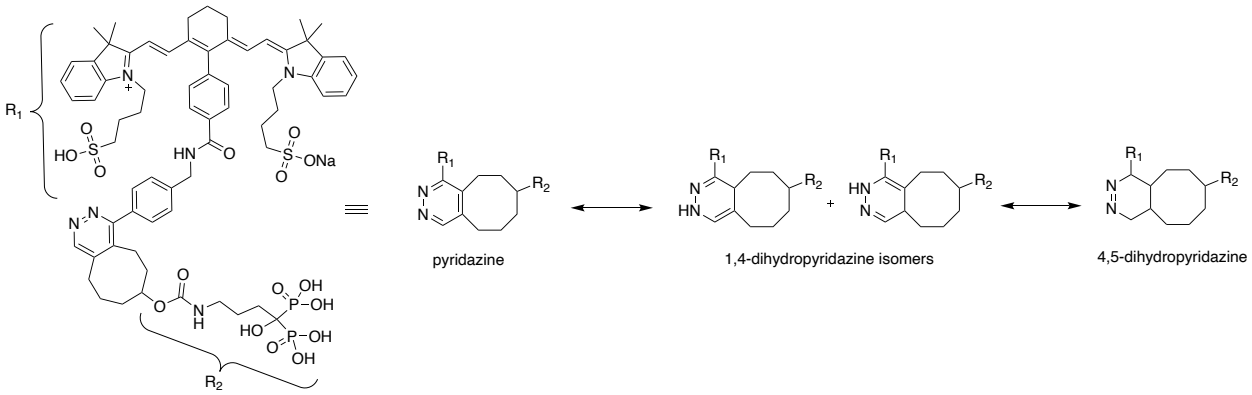

Scheme AI-1. Expected Inverse electron demand Diels-Alder (IEDDA)-products.

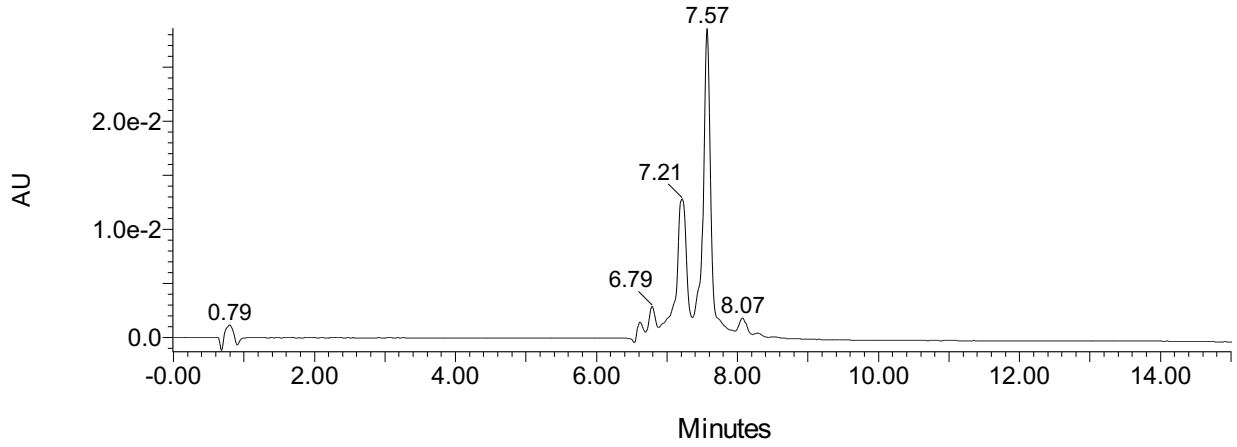

Figure AI-9. UV-HPLC trace (700 nm) of **2-7**, HPLC Method A. Where the peak at 7.57 min most likely corresponds to the thermodynamic pyridazine product (Refer to **Scheme S1**).

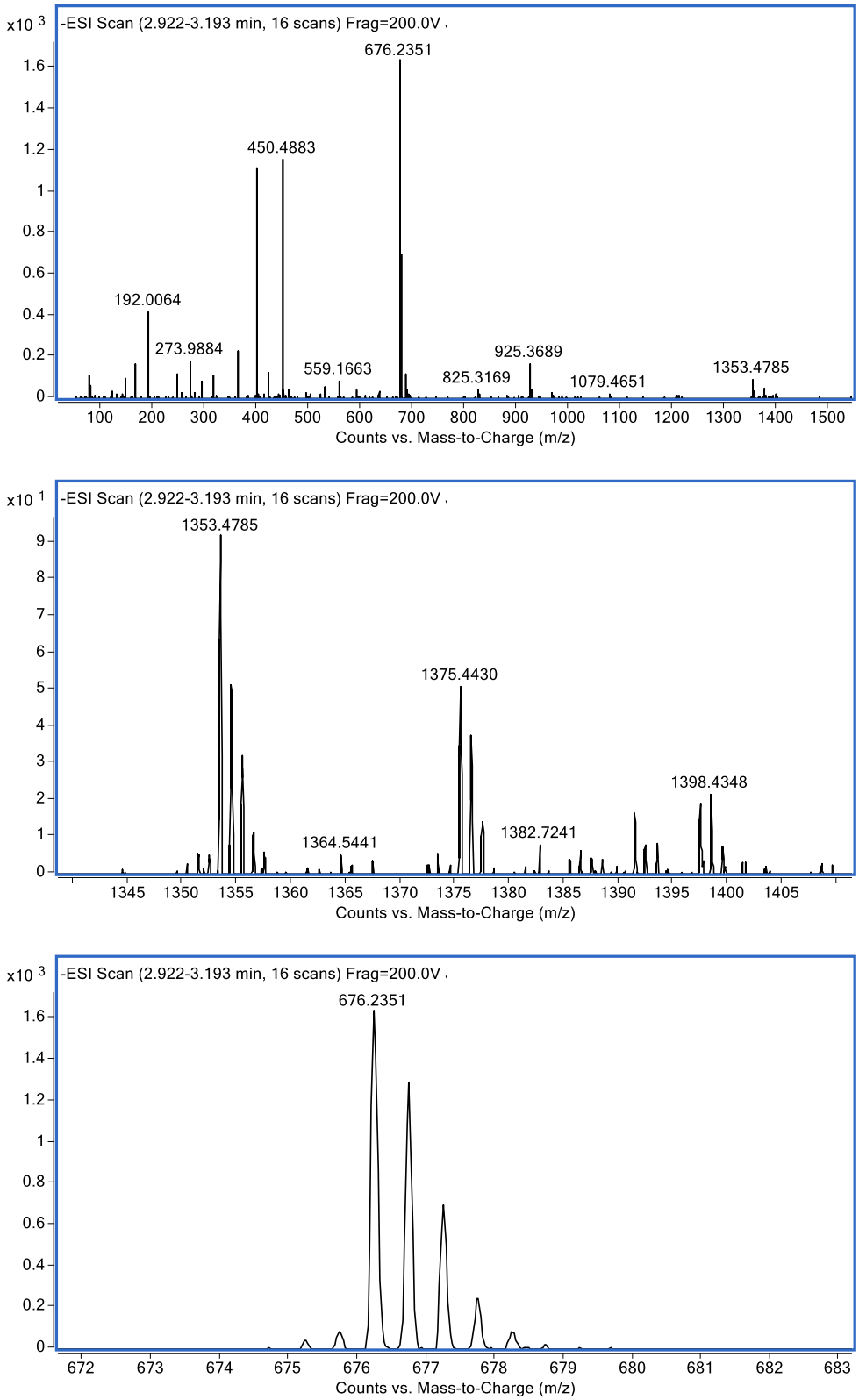

Figure AI-10. HRMS (ESI^-) of **2-7**.

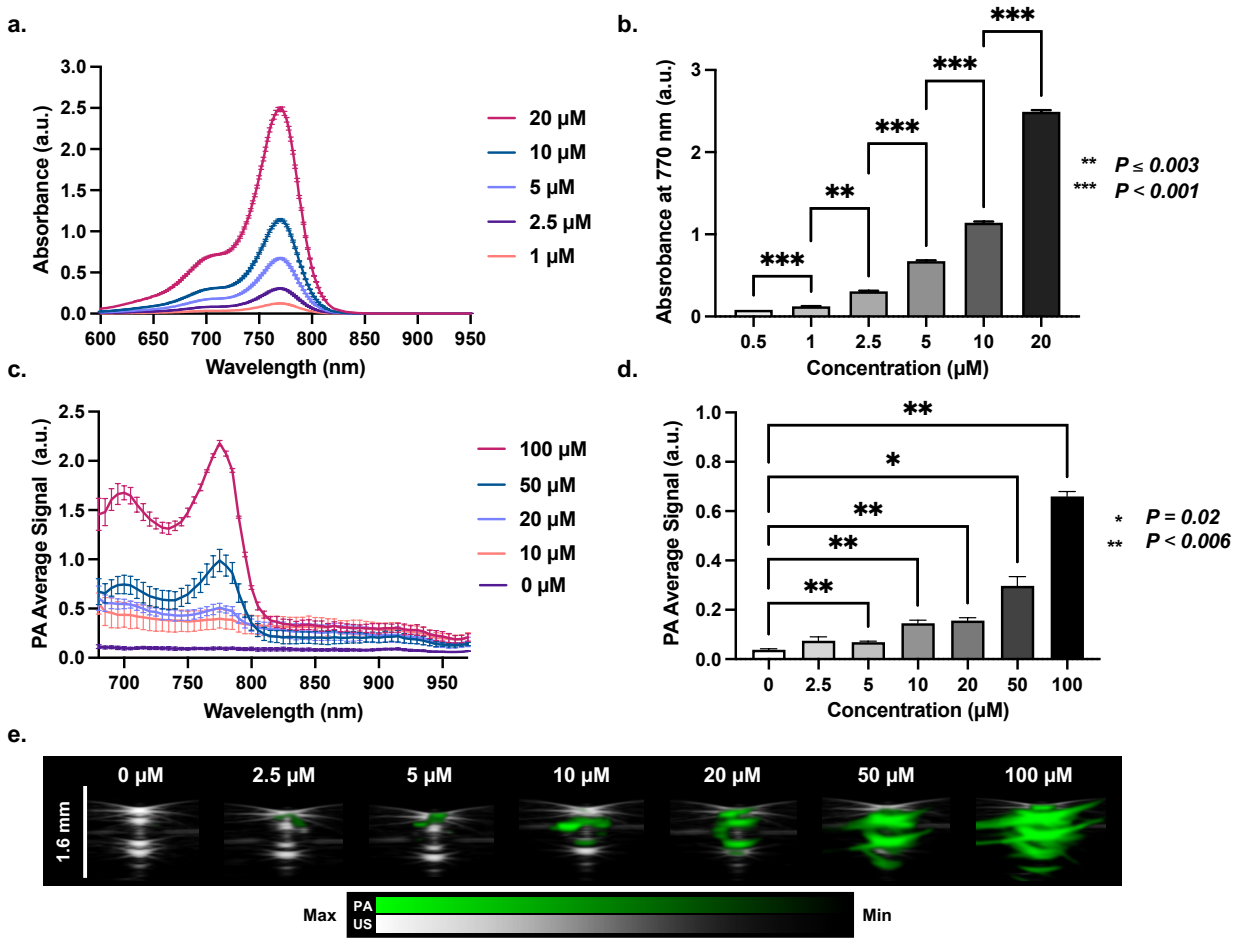

Figure AI-11. Absorbance & photoacoustic signal analysis **2-5** in neat solvent 10% ethanol in saline, as a function of concentration: **a.** Absorbance spectra of **2-5**. **b.** Absorbance intensity of **2-5** at 770 nm. **c.** PA spectra of **2-5**. **d**. PA average signal of **2-5** at 770 nm. **e.** Corresponding PA images of **2-5** in PA phantom.

a.

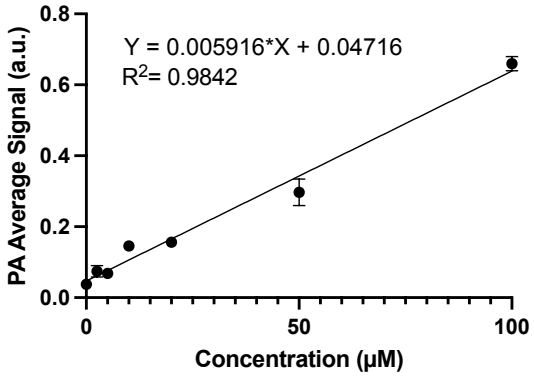

b.

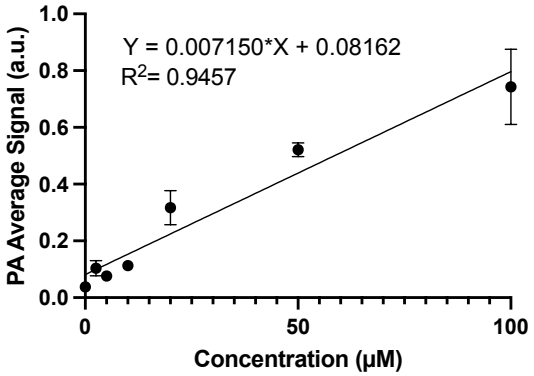

c.

Concentration (μM)	PA Average Signal Values (a.u)
0	0.0377 ± 0.00451
2.5	0.0743 ± 0.0159
5	0.0683 ± 0.00493
10	0.146 ± 0.0120
20	0.157 ± 0.0110
50	0.297 ± 0.0374
100	0.660 ± 0.0199

d.

Concentration (μM)	PA Average Signal Values (a.u)
0	0.0377 ± 0.00451
2.5	0.104 ± 0.0268
5	0.0760 ± 0.0113
10	0.113 ± 0.00862
20	0.317 ± 0.0605
50	0.521 ± 0.0241
100	0.743 ± 0.133

Figure AI-12. Linear regression analysis of **2-5** and **2-7** in 10% ethanol in saline. **a-b.** Linear regression fitting of **2-5** and **2-7**, respectively. **c-d.** Table of values of **2-5** and **2-7**, respectively, as a function of concentration.

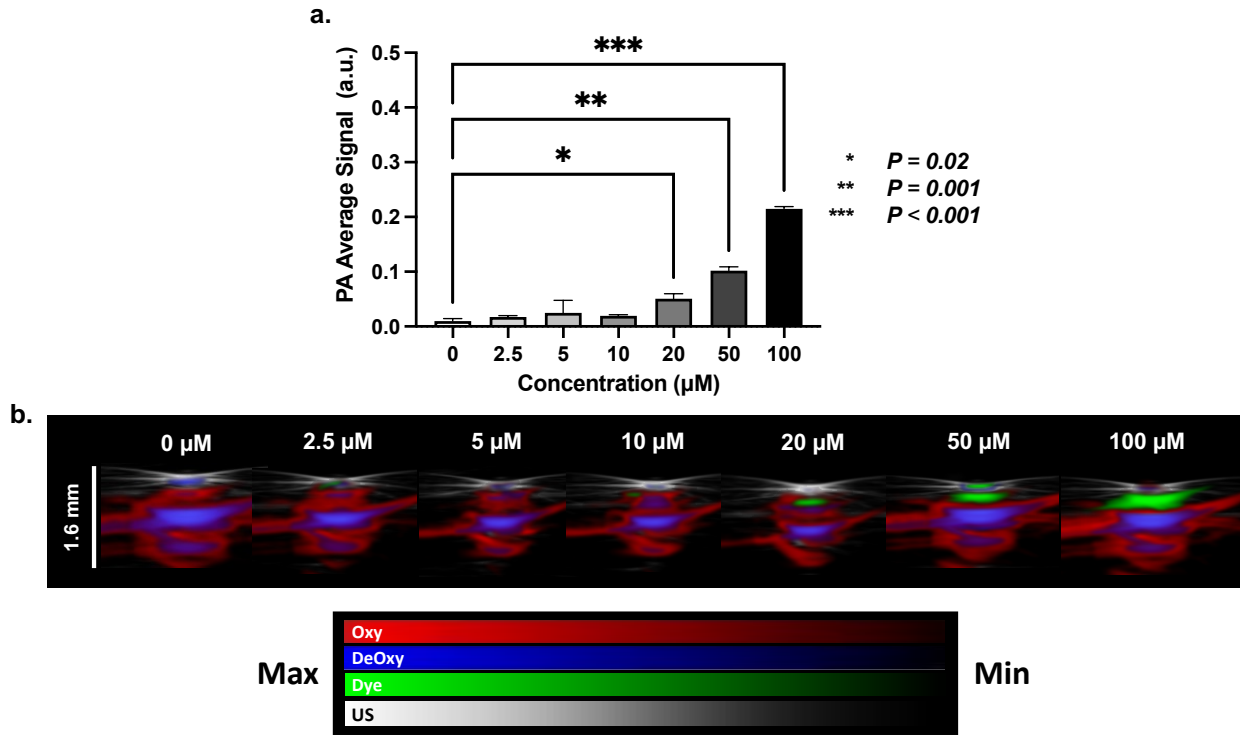

Figure AI-13. Photoacoustic signal analysis of **5** in whole murine blood: **a.** Analysis of the PA average signal of **2-5** unmixed from blood, as a function of concentration. **b.** Corresponding unmixed PA images of the samples in PA phantom. Red= oxygenated hemoglobin, blue= deoxygenated hemoglobin, green= **2-5**.

a.

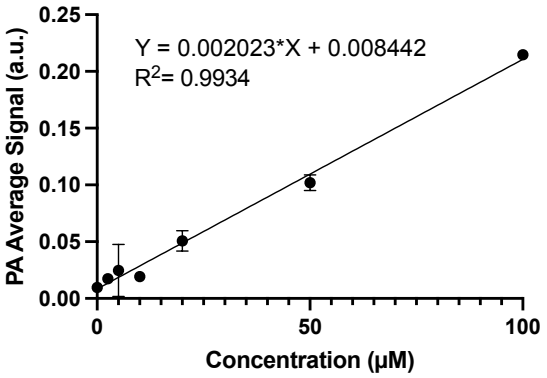

b.

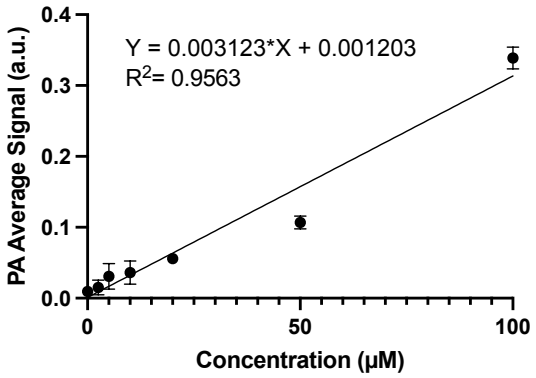

c.

Concentration (μM)	PA Average Signal Values (a.u)
0	0.00967 ± 0.00451
2.5	0.0173 ± 0.00231
5	0.0247 ± 0.0232
10	0.0193 ± 0.00231
20	0.0507 ± 0.00907
50	0.102 ± 0.00700
100	0.215 ± 0.00416

d.

Concentration (μM)	PA Average Signal Values (a.u)
0	0.00967 ± 0.00451
2.5	0.0153 ± 0.0105
5	0.0310 ± 0.0183
10	0.0360 ± 0.0166
20	0.0560 ± 0.00529
50	0.107 ± 0.00917
100	0.339 ± 0.0155

Figure AI-14. Linear regression analysis of **2-5** and **2-7** in murine blood. **a-b.** Linear regression fitting of **2-5** and **2-7**, respectively. **c-d.** Table of values of **2-5** and **2-7**, respectively, as a function of concentration.

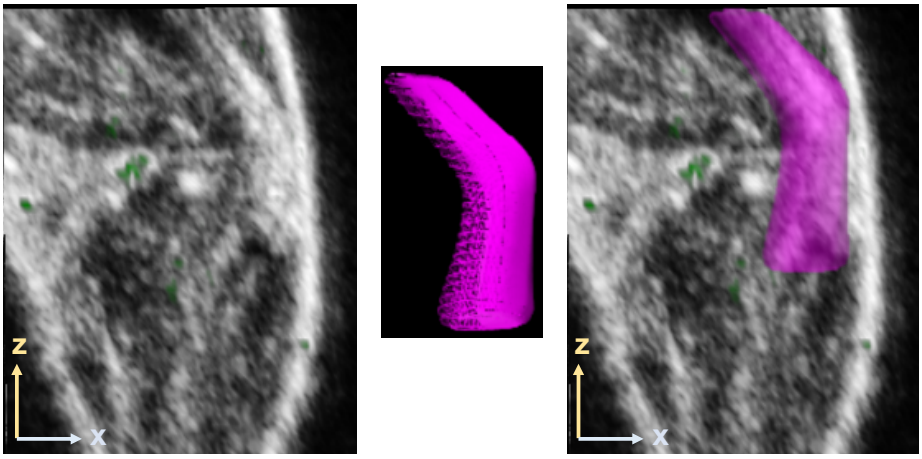

Figure AI-15. An example of a 3D ROI used for *in vivo* PA signal quantifications: A 30 mm^3 volume (pink) represents the approximate size and location, when superimposed on a texture mapping image of a hindlimb, of the ROIs used throughout all quantitative *in vivo* PA average signal analyses.

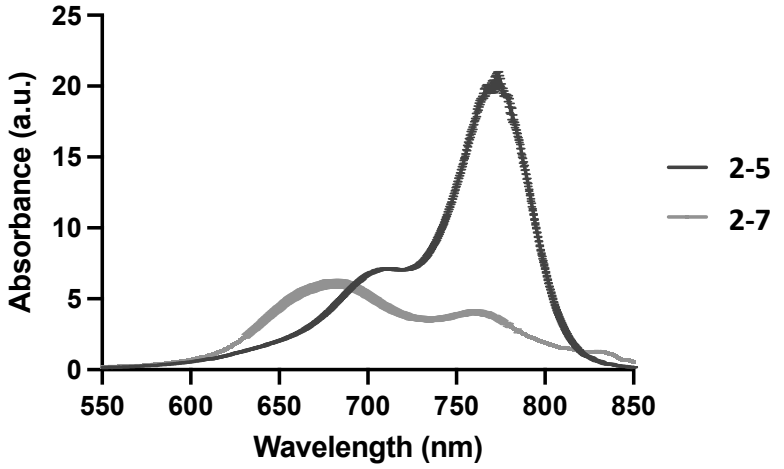

Figure AI-16. Absorbance analysis of **2-5** & **2-7** at an extended concentration (100 μM). Analysis was performed using the Nanodrop 1, where 1 μL of each dye (formulated in 10% ethanol in saline) was pipetted onto the pedestal for analysis. Samples were measured in triplicate. Based on literature reports on the altered absorbance properties of cyanine dyes in various states of aggregation,[3] the absorbance spectra were interpreted as follows: The spectrum of **2-5** shows that the dye remains non-aggregated with a monomer peak at 760 nm and a dimer peak at 710 nm. The spectrum of **2-7** shows that the dye formed H-aggregates at a hypsochromic shift in absorbance (675 nm), and a small intensity of J-aggregates at a bathochromic shift in absorbance (840 nm), relative to the monomer peak.

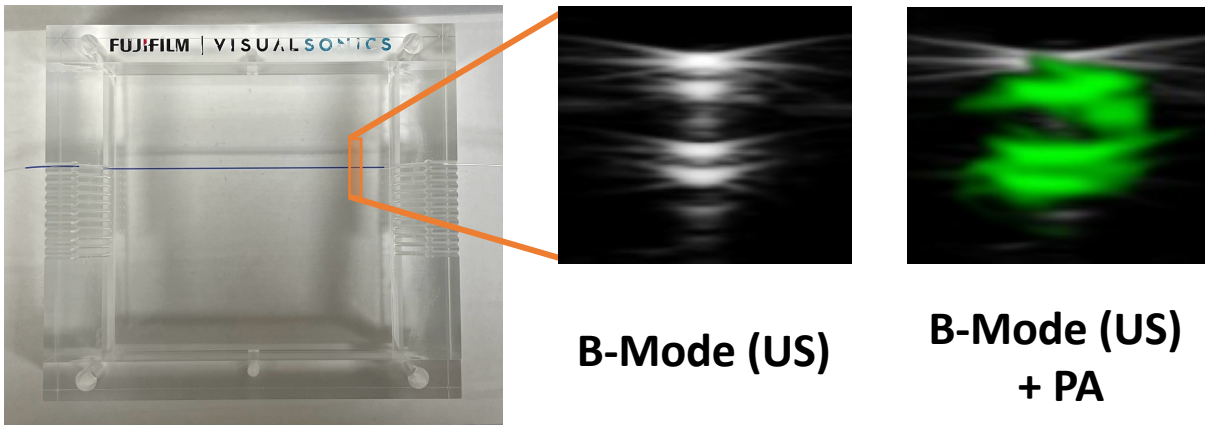

Figure AI-17. Example of the PAI phantom set-up & images acquired from tubing.

AI-3: Supporting References

(1) James, N. S.; Chen, Y.; Joshi, P.; Ohulchanskyy, T. Y.; Ethirajan, M.; Henary, M.; Strekowsk, L.; Pandey, R. K. Evaluation of Polymethine Dyes as Potential Probes for Near Infrared Fluorescence Imaging of Tumors: Part - 1. *Theranostics* **2013**, *3* (9), 692–702. https://doi.org/10.7150/thno.5922.

(2) Torres Martin de Rosales, R.; Finucane, C.; Mather, S. J.; Blower, P. J. Bifunctional Bisphosphonate Complexes for the Diagnosis and Therapy of Bone Metastases. *Chem. Commun.* **2009**, No. 32, 4847. https://doi.org/10.1039/b908652h.

(3) Mishra, A.; Behera, R. K.; Behera, P. K.; Mishra, B. K.; Behera, G. B. Cyanines during the 1990s: A Review. *Chem. Rev.* **2000**, *100* (6), 1973–2012. https://doi.org/10.1021/cr990402t.

Appendix II: Supporting Information for Chapter 3

Applying Photoacoustic Imaging for the Detection of Bacterial Infection

Table of Contents

AII-1: Supporting Methods

Equation AII-1: Activity Yield Calculation (non-decay corrected):

$$Activity\ Yield = \left(\frac{A_f}{A_0}\right) \times 100$$

Where A_0 is the initial amount of radioactivity (at t=0) added to the reaction and A_f is the final activity remaining after purification of the product.

Equation AII-2: Bacterial Percent Binding Calculation:

$$\%\ Binding = [\frac{\left(A_{pellet}\right)}{\left(A_{100\%\ signal}\right)}] \times 100$$

Where A_{pellet} is the counts per minute (CPM) measured in the washed pellet and $A_{100\%\ signal}$ is the CPM measured in the sample that represents 100 % of the signal possible from the amount of **7** that was added to the bacteria and no-cell controls.

AII-2: Supporting Data

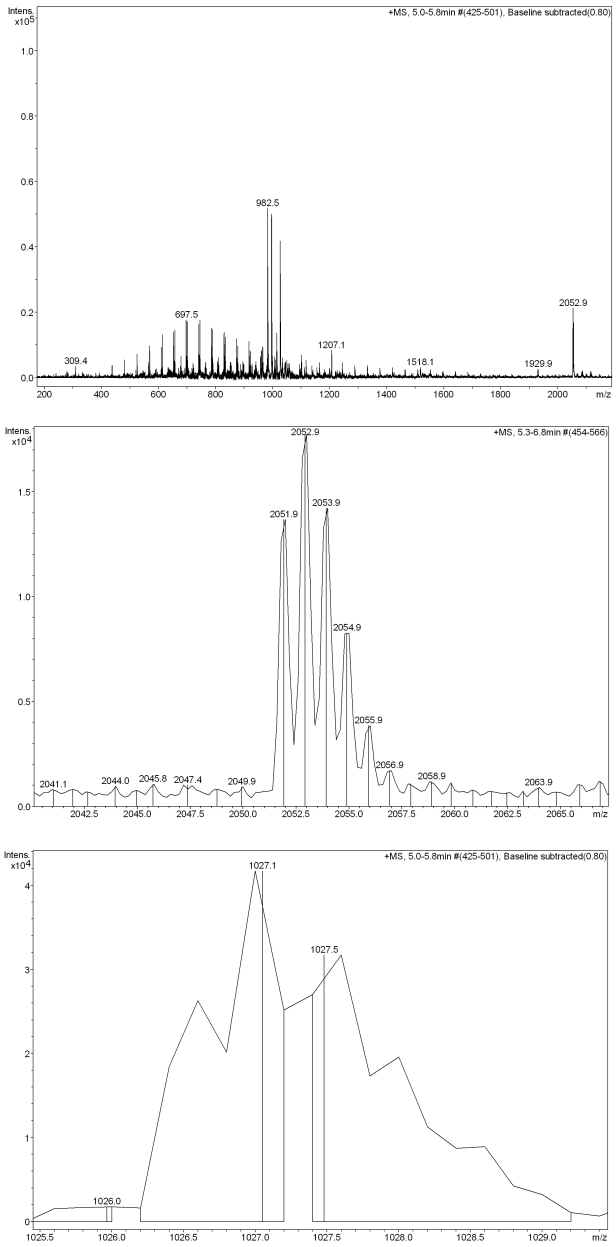

Figure AII-1. Mass spectrum of **3-2**.

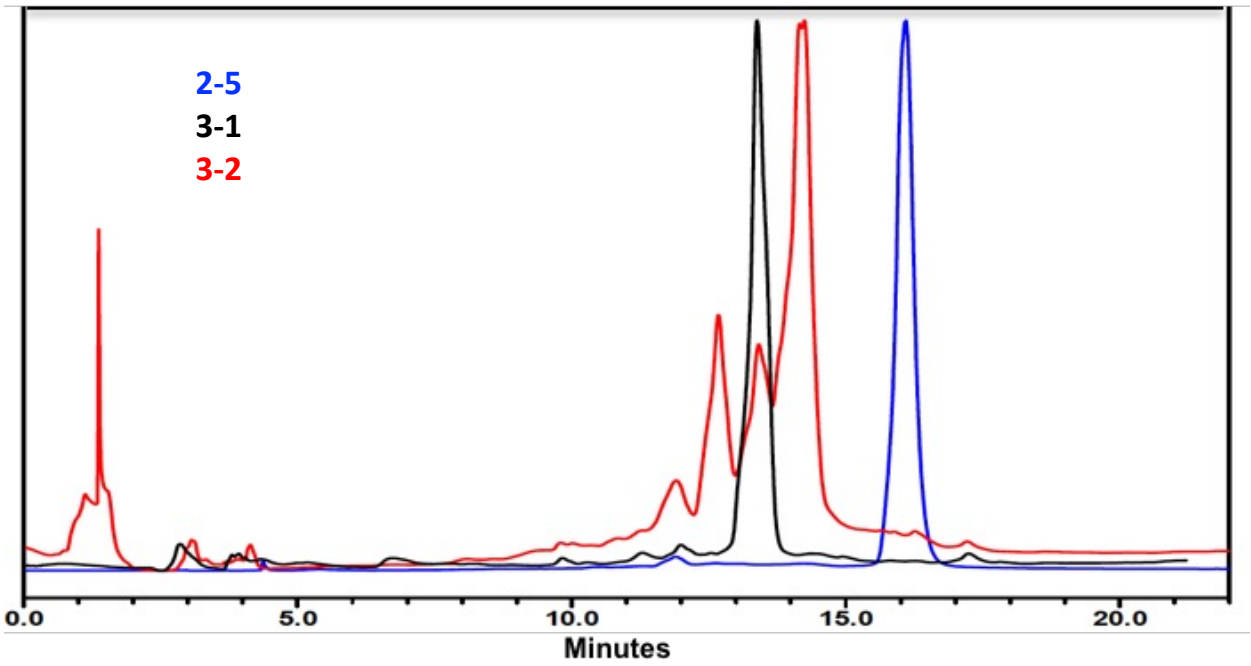

Figure AII-2. UV-HPLC trace (700 nm) of **2-5**, **3-1**, and **3-2**, overlayed, HPLC Method A.

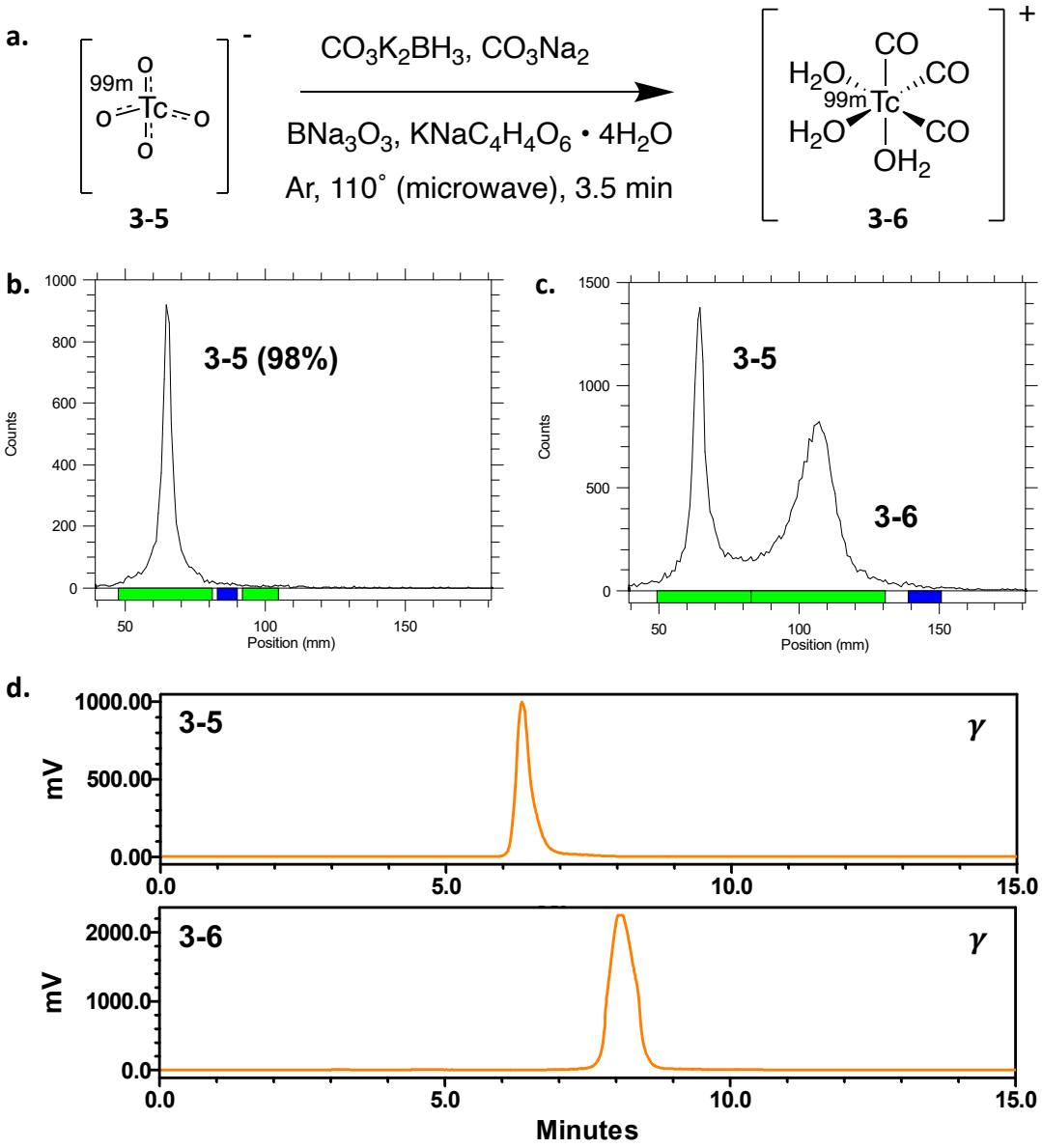

Figure AII-3. **a.** Radiosynthesis of $[^{99m}Tc][Tc(CO)_3(H_2O)_3]^+$ (**3-6**) from $[^{99m}Tc][TcO_4]^-$ (**3-5**), as reported by Causey, *et al.* (2008).[1] **b.** Radio-TLC analysis of **3-6** on aluminum oxide plate, eluted with 1% HCl in MeOH. **c.** Radio-TLC analysis of **3-6** with a co-spot of **3-5** on aluminum oxide plate, eluted with 1% HCl in MeOH. **d.** HPLC gamma traces of **3-5** and **3-6** using HPLC method A.

Table AII-1. Summary of reaction conditions tested in the synthesis of **3-8**.

Reaction Number	$Zn(NO_3)_2$ Added*	Temperature (˚C)	Time (min)	Radio-TLC Conversion	Degradation**
1	After	90	20	96 %	Yes
2	After	110	3.5	>99 %	Yes
3	After	37	60	96 %	Yes
4	After	r.t.	60	90 %	No
5	Before	r.t.	90	70 %	No

* Zinc Nitrate was either added before or after the coordination of $[^{99m}Tc][Tc(CO)_3(H_2O)_3]^+$.
** Degradation observed by gamma and uv HPLC.

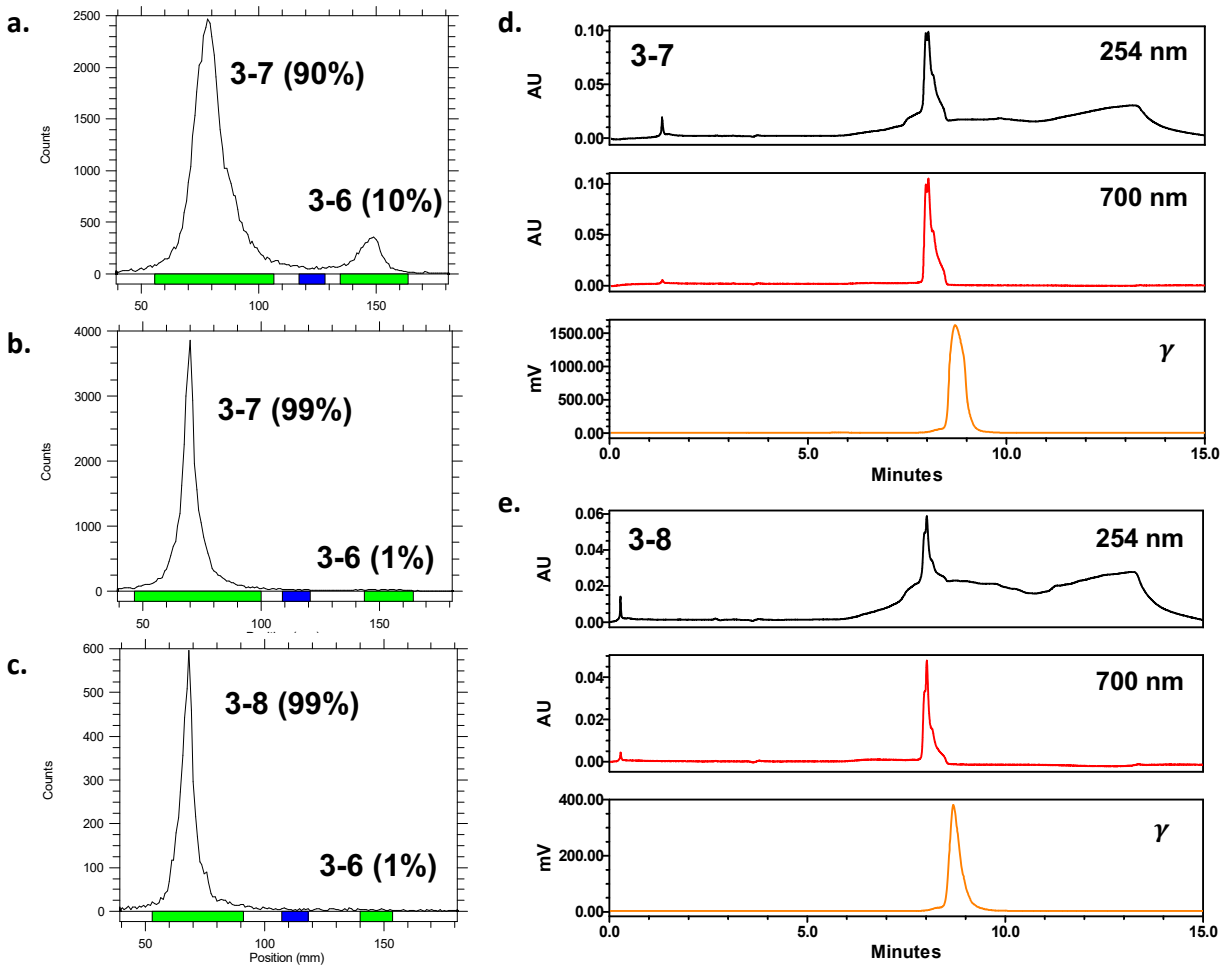

Figure AII-4. Characterization of [^{99m}Tc]-TcPSVue794 (**3-8**) radiolabeling, resulting in 90% crude radiochemical conversion, 99% RCP, and 57 MBq activity yield starting from 108 MBq at end of synthesis. Radio-TLC and gamma HPLC analysis of **3-7** (crude) (**a**), **3-7** isolated by C18 SepPak extraction (**b,d**), and **3-8** after 30-minute incubation (37˚C) (**c,e**). Radio-TLC plates eluted with 1% HCl in MeOH.

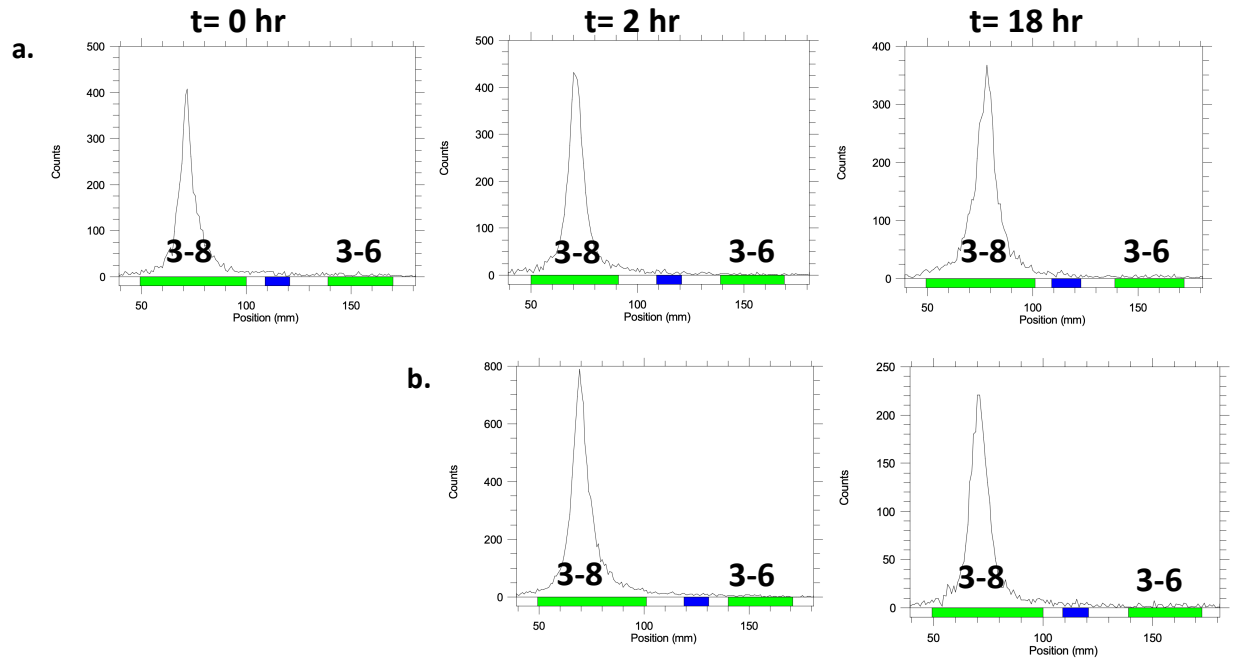

Figure AII-5. Stability analysis of **3-8** in formulation buffer (r.t.) (**a**) and mouse serum (37 ˚C) (**b**) at 0, 2, and 18 hours, assessed by radio-TLC using 1% HCl in methanol as an eluent.

Table AII-2. Stability analysis of **3-8**, quantified from radio-TLC.

[^{99m}Tc]TcPSVue794 (3-8)	Duration of Incubation		
	0 h	**2 h**	**18 h**
Formulation Buffer	98.7 %	98.7 %	97.7 %
Mouse Serum	-	98.7 %	97.1 %

Table AII-3. Biodistribution Data for **3-8** in (**a**) mice with bacterial infection and (**b**) healthy mice.

a.

Bacterial Myositis	**12 hr Post-Injection**					
Organs	**1**	**2**	**3**	**4**	**Mean**	**SEM**
Blood	0.63	0.96	2.05	1.40	1.26	0.31
Adipose	0.59	0.16	0.65	0.42	0.45	0.11
Adrenals	3.66	3.20	6.37	7.29	5.13	1.00
Bone	1.01	0.54	0.79	1.09	0.86	0.12
Brain	0.03	0.02	0.03	0.03	0.03	0.00
Gall bladder	126.94	49.91	55.33	19.55	62.93	22.74
Heart	1.76	0.75	3.08	2.03	1.90	0.48
Kidneys	3.08	2.17	3.59	3.09	2.98	0.30
Lg Int + Caecum (+cont)	55.78	32.83	33.54	52.53	43.67	6.09
Liver	26.78	6.88	20.05	30.48	21.05	5.19
Lungs	1.48	0.73	29.04	1.64	8.22	6.94
Pancreas	1.35	0.42	1.58	1.51	1.22	0.27
Sm Int (+ contents)	5.75	2.87	6.97	3.92	4.88	0.92
Spleen	11.84	0.60	5.69	19.54	9.42	4.08
Stomach (+ contents)	2.32	0.51	1.58	0.57	1.24	0.43
Thyroid/Trachea	1.21	0.52	1.58	1.30	1.15	0.23
Urine + bladder	0.57	1.47	3.02	1.29	1.59	0.51
Contralateral Muscle	0.24	0.10	0.13	0.21	0.17	0.03
Infected Muscle	2.48	1.13	1.28	1.84	1.68	0.31

b.

Healthy Mice	**12 hr Post-Injection**					
Organs	**1**	**2**	**3**	**4**	**Mean**	**SEM**
Blood	0.88	0.69	0.45	0.46	0.62	0.10
Adipose	0.20	0.18	0.18	0.21	0.19	0.01
Adrenals	2.14	2.47	1.95	2.90	2.36	0.21
Bone	0.89	0.63	0.76	0.84	0.78	0.06
Brain	0.03	0.02	0.03	0.01	0.02	0.00
Gall bladder	12.00	37.86	5.40	7.04	15.58	7.56
Heart	1.42	1.18	1.28	1.43	1.33	0.06

Kidneys	2.00	1.67	1.60	1.79	1.76	0.09
Lg Int + Caecum (+cont)	6.89	2.79	2.99	4.45	4.28	0.94
Liver	23.39	19.97	23.45	18.96	21.44	1.16
Lungs	2.26	1.31	1.36	1.79	1.68	0.22
Pancreas	0.78	0.65	0.73	0.72	0.72	0.03
Sm Int (+ contents)	3.20	1.61	1.54	1.61	1.99	0.40
Spleen	7.83	6.77	10.76	11.58	9.23	1.15
Stomach (+ contents)	3.19	0.32	0.27	2.86	1.66	0.79
Thyroid/Trachea	1.27	0.98	1.19	1.11	1.14	0.06
Urine + bladder	0.58	2.41	0.76	0.76	1.13	0.43
Healthy Naïve Muscle	0.32	0.29	0.37	0.32	0.33	0.02

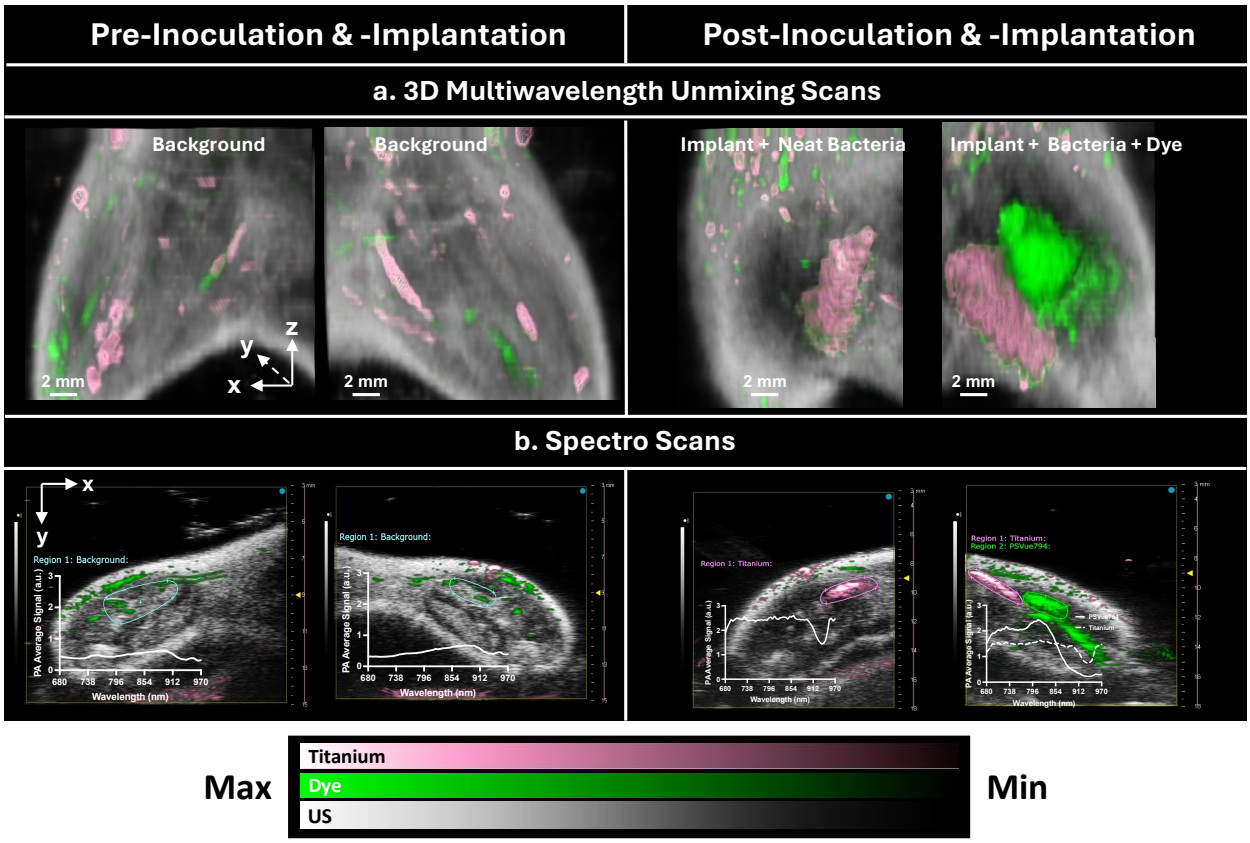

Figure AII-6. Pilot Study 2. **a.** *In vivo* 3D multiwavelength unmixing scans of mice inoculated with *S. aureus*, neat (in left limb) or pre-incubated with **3-4** (10% ID/g) (in right limb), and implanted with a 5 mm, 30-gauge titanium segment. **b.** Spectral analysis of a cross-section of the inoculation/implantation site. Pink= titanium, Green= **3-4**, Greyscale= US B-mode. The signals from oxygenated and deoxygenated hemoglobin have been subtracted from each image.

AII-3: Supporting References

(1) Causey, P. W.; Besanger, T. R.; Schaffer, P.; Valliant, J. F. Expedient Multi-Step Synthesis of Organometallic Complexes of Tc and Re in High Effective Specific Activity. A New Platform for the Production of Molecular Imaging and Therapy Agents. *Inorg. Chem.* **2008**, *47* (18), 8213–8221. https://doi.org/10.1021/ic800775w.

Appendix III: Supporting Information for Chapter 4

Development of a General-Purpose Dye & Methodology for Photoacoustic Imaging

Rowan Swann[†], Yusra Mahmood Marfatia[†], Mohamed E. El-Zaria[†,§], Afaf R. Genady[†], Luis Rafael Silva[†], John F. Valliant[†], & Saman Sadeghi[†,*]

[†] Department of Chemistry and Chemical Biology, McMaster University, Hamilton, Ontario, Canada
[§]Biotechnology Program, Faculty of Health Sciences & Wellness, Humber College, Toronto, Ontario, Canada

Corresponding Author

* Phone: (905) 525-9140 ext. 22537; Email: sadegs10@mcmaster.ca

Table of Contents

AIII-1: Supporting Methods

Molar Absorptivity Calculation of Dyes: Molar absorptivity (ε, $M^{-1}cm^{-1}$) of the dyes were calculated using **equation AIV-1** from absorbance measurements of **4-4** and **4-7** (concentration, C=5 μM, dissolved in methanol; optical path length, b= 1cm) acquired from the Ultrospec 2100 *pro* spectrophotometer.

Equation AIII-1: $\varepsilon = \frac{A}{bC}$

Relative Fluorescence Quantum Yield Calculation of Dyes: The relative fluorescence quantum yield (Φ_x) was determined for **5** and **7** (5 μM, methanol) using **equation AIV-2**, with Φ_{ref}= quantum yield of **1** as a reference.[1] A_x and A_{ref} are the absorbance at the fluorescence excitation wavelength (746 nm), of **4-4** or **4-7** and of **2-1**, respectively. F_x and F_{ref} are the areas under the curves of the fluorescence emission spectra for **4-4** or **4-7**, and of **2-1**, respectively. Because the material was dissolved in the same media as the reference material (methanol), $\left(\frac{n_x}{n_{ref}}\right)^2 = 1$.

Equation AIII-2: $\Phi_x = \Phi_{ref} \bullet \left(\frac{A_{ref}}{A_x}\right) \bullet \left(\frac{F_x}{F_{ref}}\right) \bullet \left(\frac{n_x}{n_{ref}}\right)^2$

AIII-2: Supporting Data

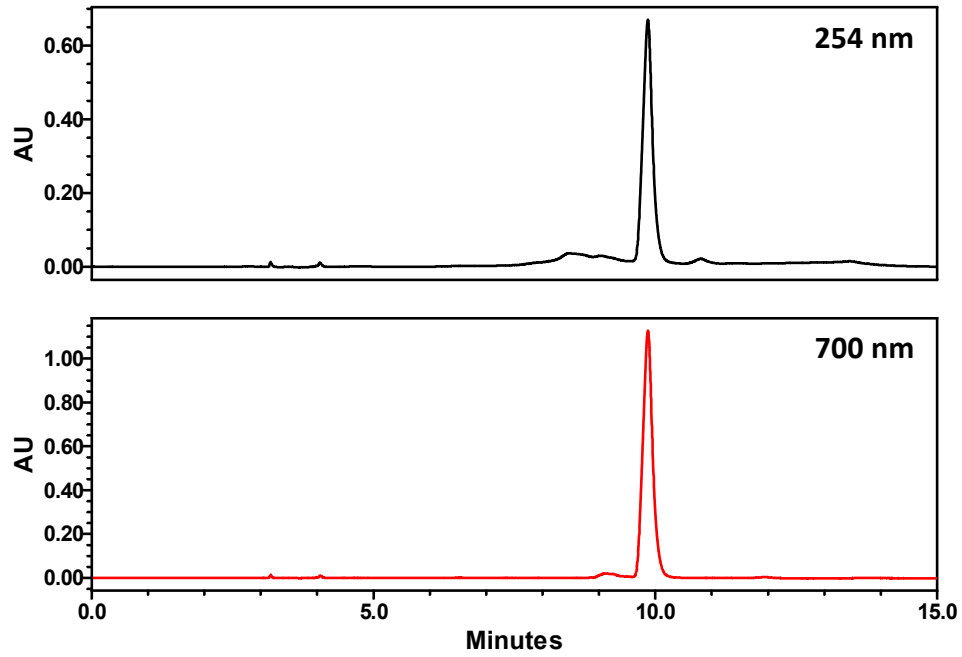

Figure AIII-1. UV-HPLC trace (254 & 700 nm) of **4-2**.

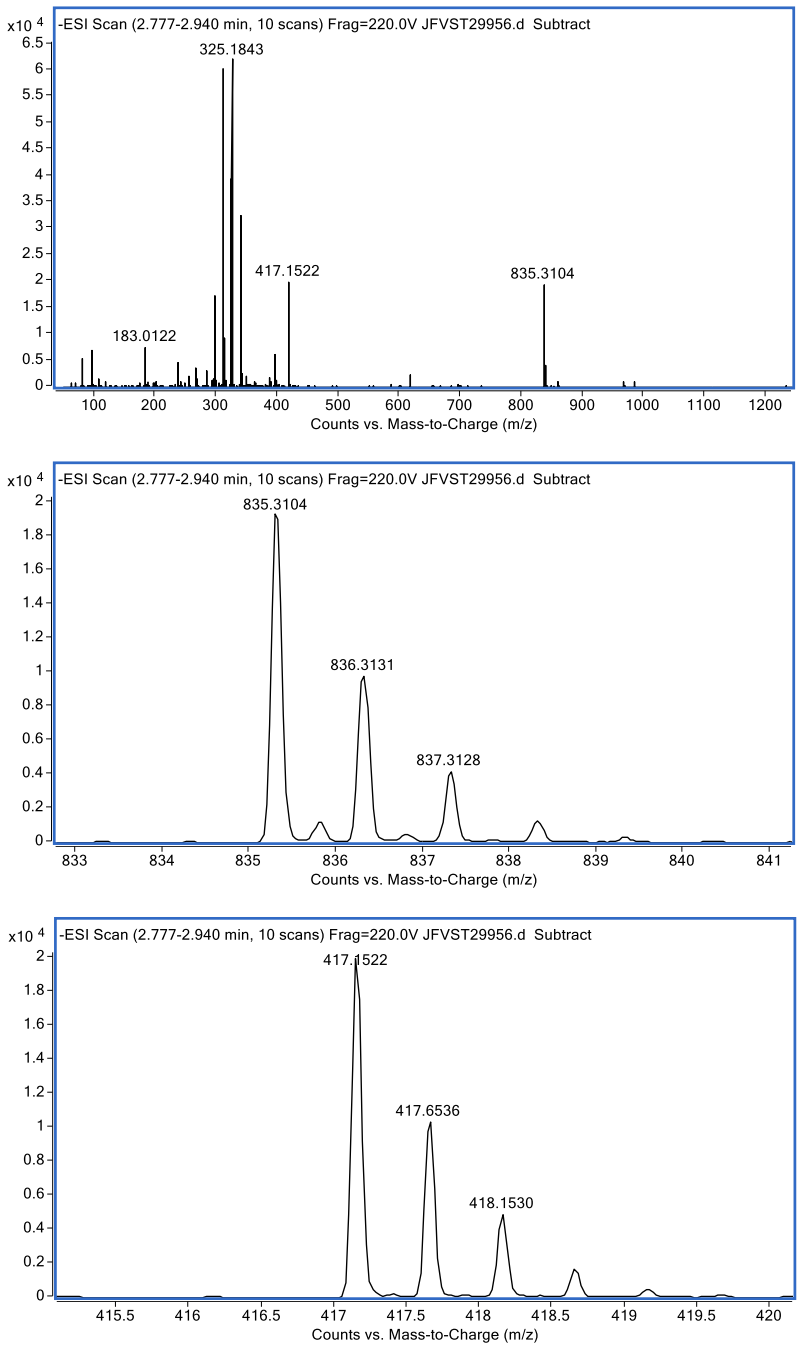

Figure AIII-2. HRMS (ESI$^-$) of **4-2**.

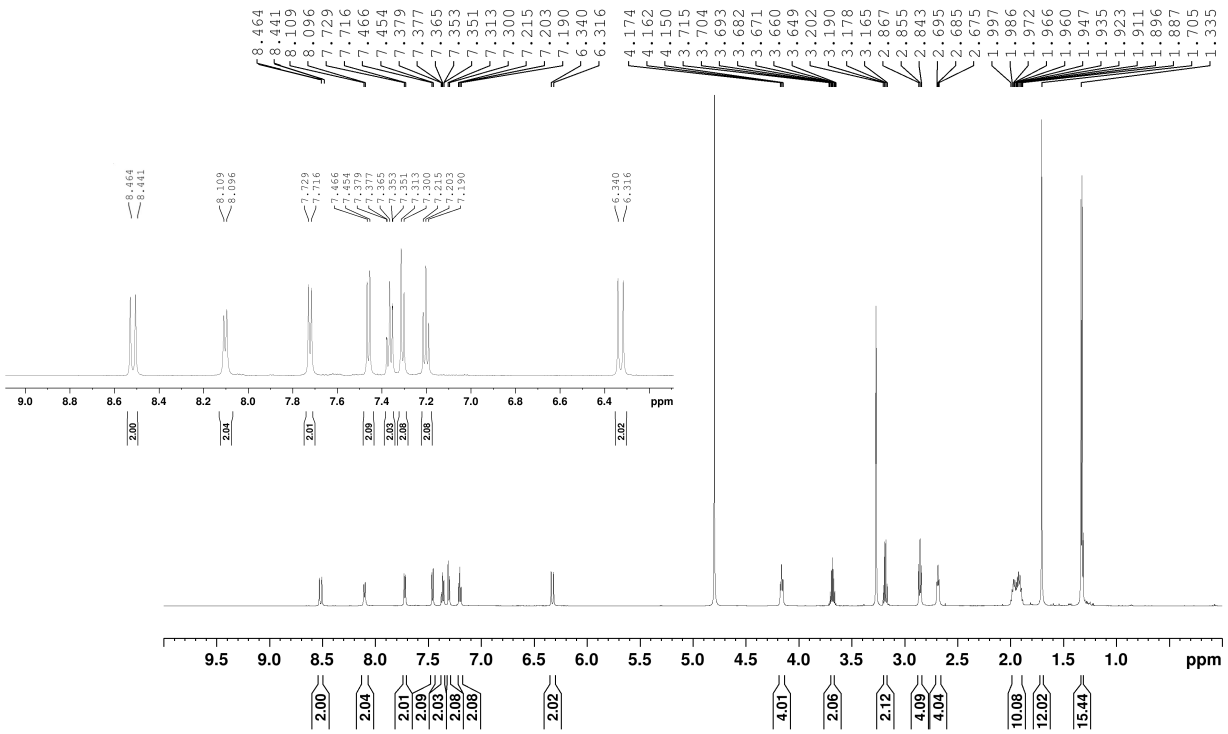

Figure AIII-3. ^{1}H NMR (600 MHz, CD_3OD) of **4-2**.

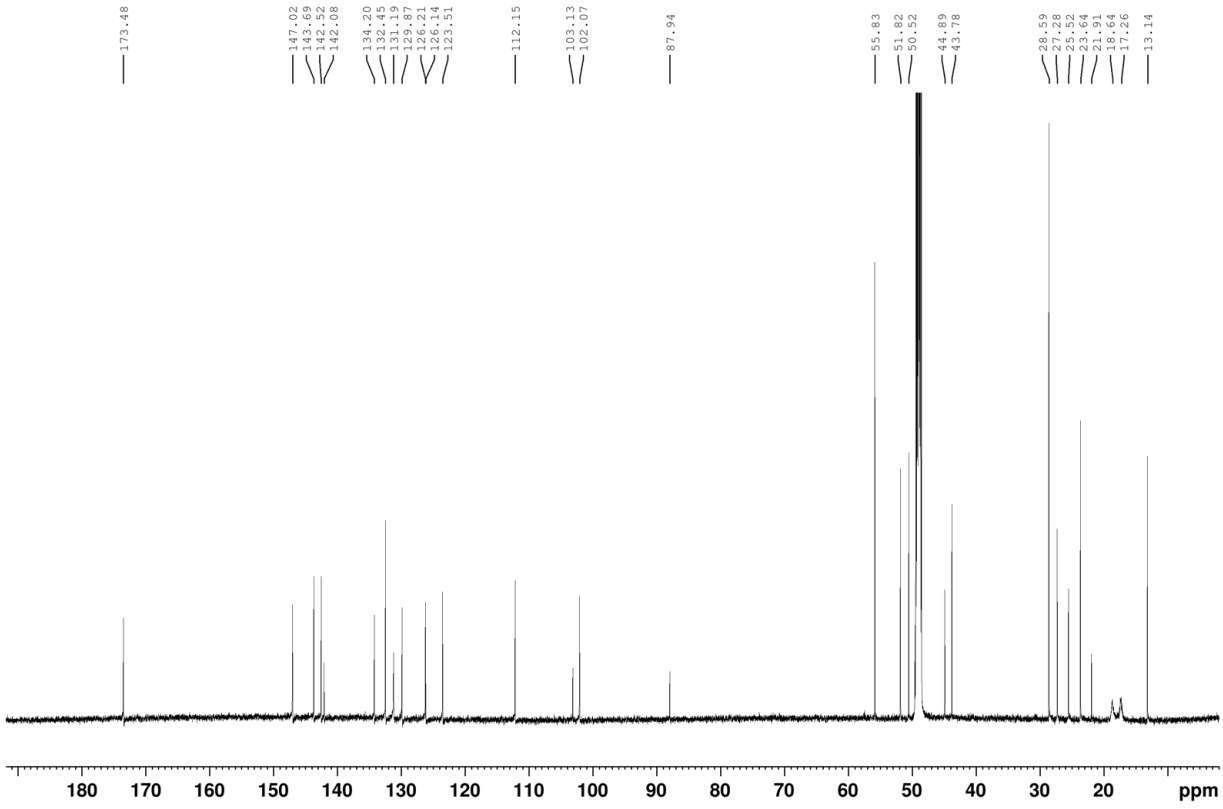

Figure AIII-4. ^{13}C NMR (150 MHz, CD_3OD) of **4-2**.

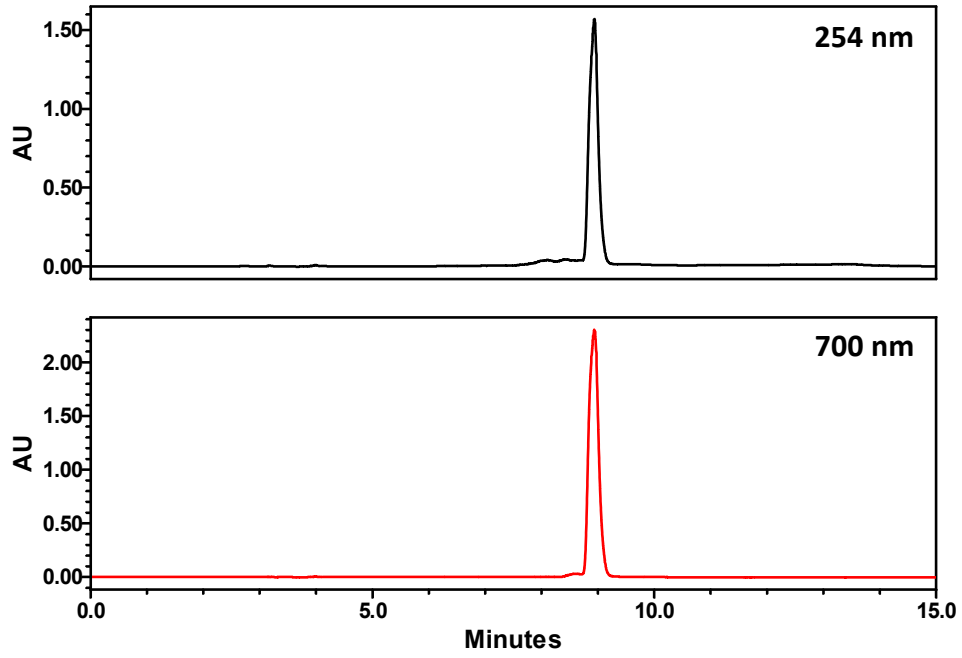

Figure AIII-5. UV-HPLC trace (254 & 700 nm) of **4-4**.

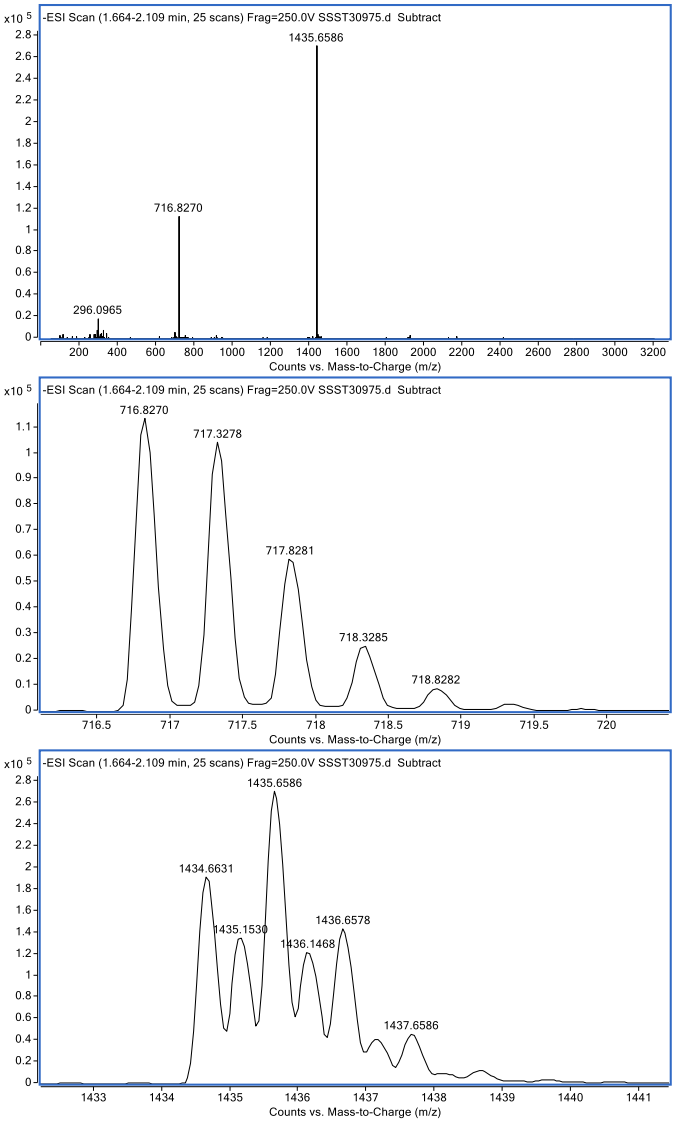

Figure AIII-6. HRMS (ESI$^-$) of **4-4**.

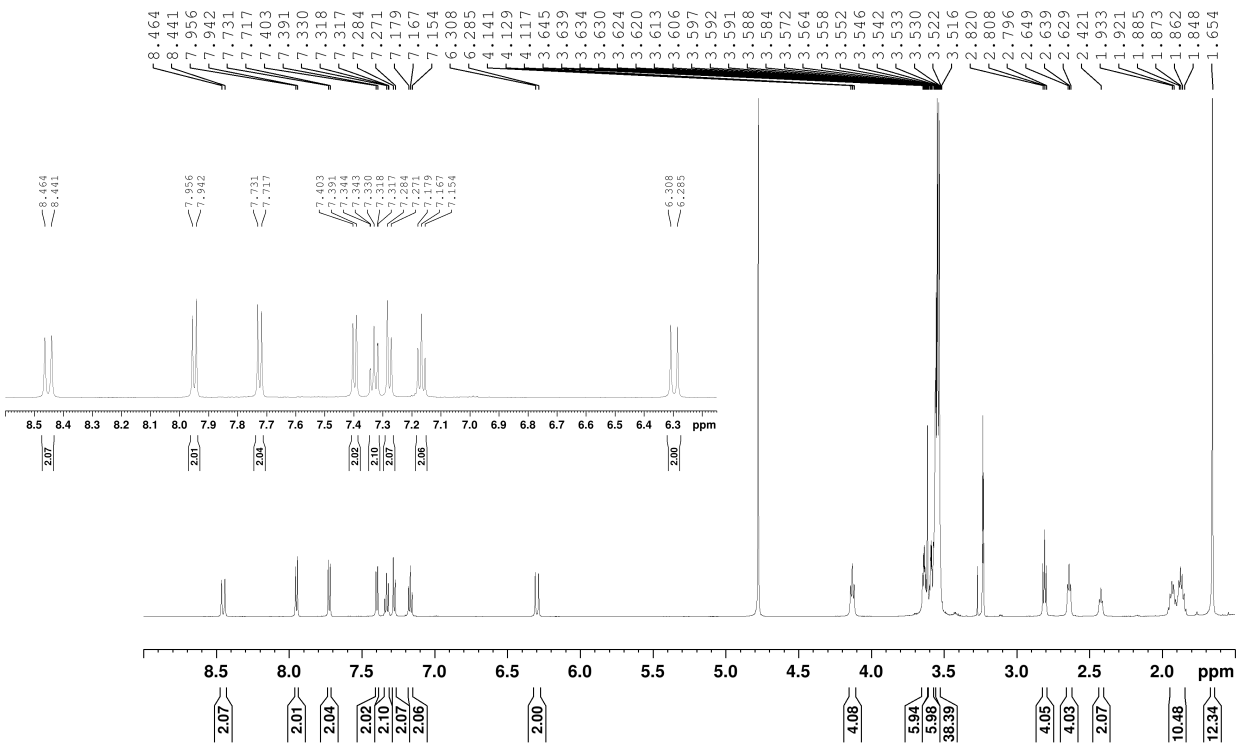

Figure AIII-7. ^{1}H NMR (600 MHz, CD_3OD) of **4-4**.

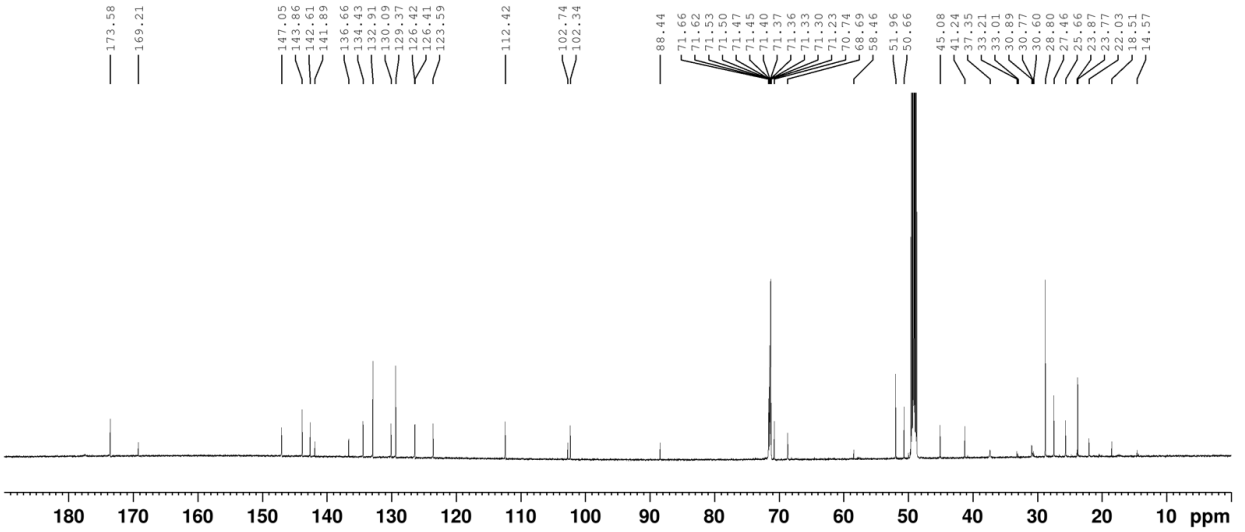

Figure AIII-8. ^{13}C NMR (150 MHz, CD_3OD) of **4-4**.

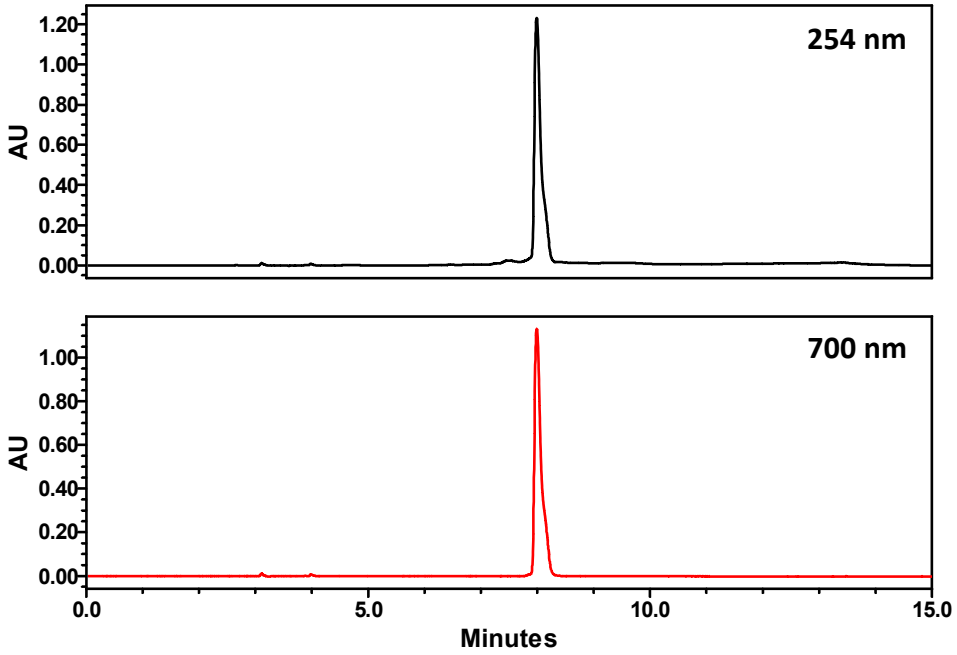

Figure AIII-9. UV-HPLC trace (254 & 700 nm) of **4-6**.

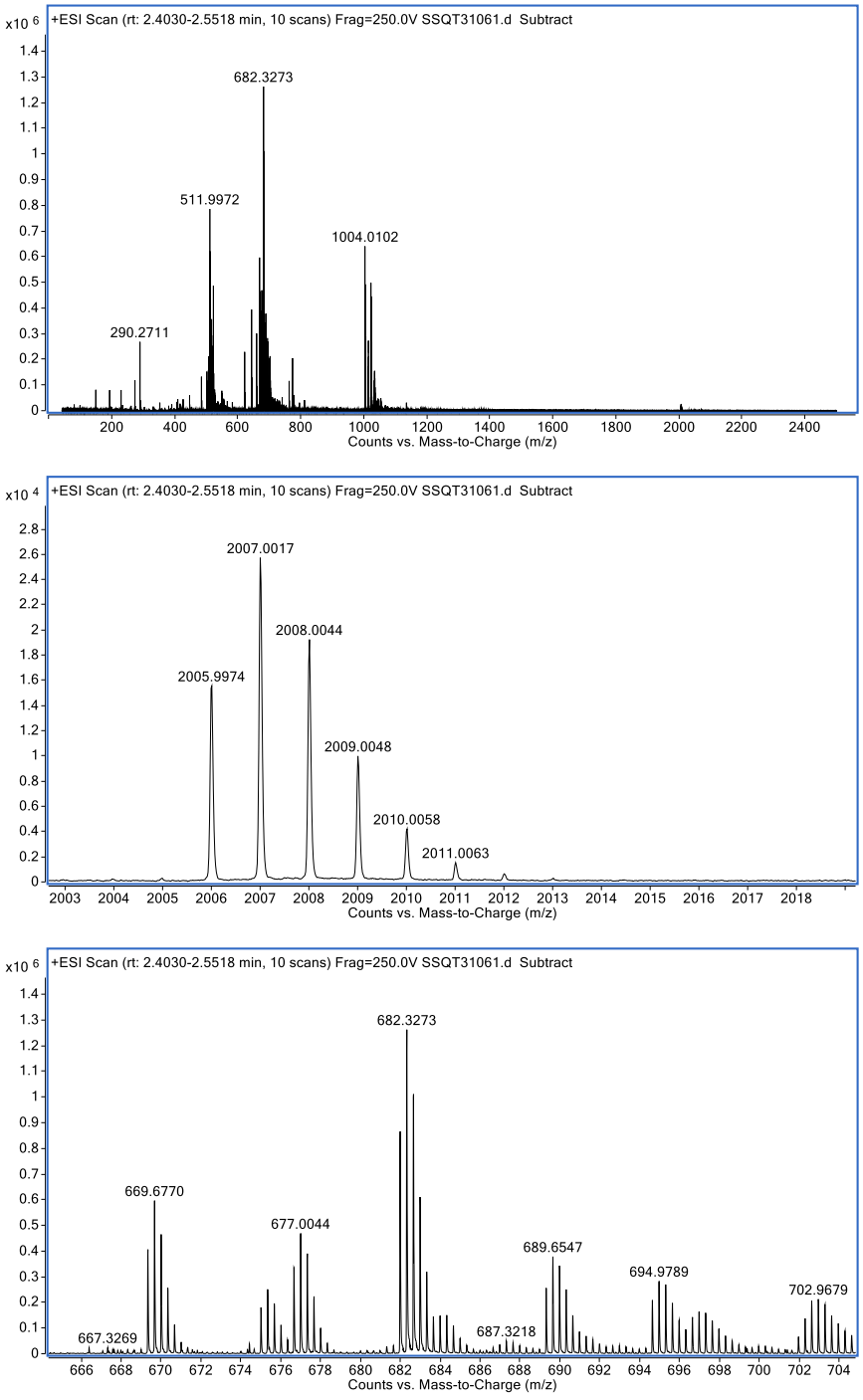

Figure AIII-10. HRMS (ESI^+) of **4-6**.

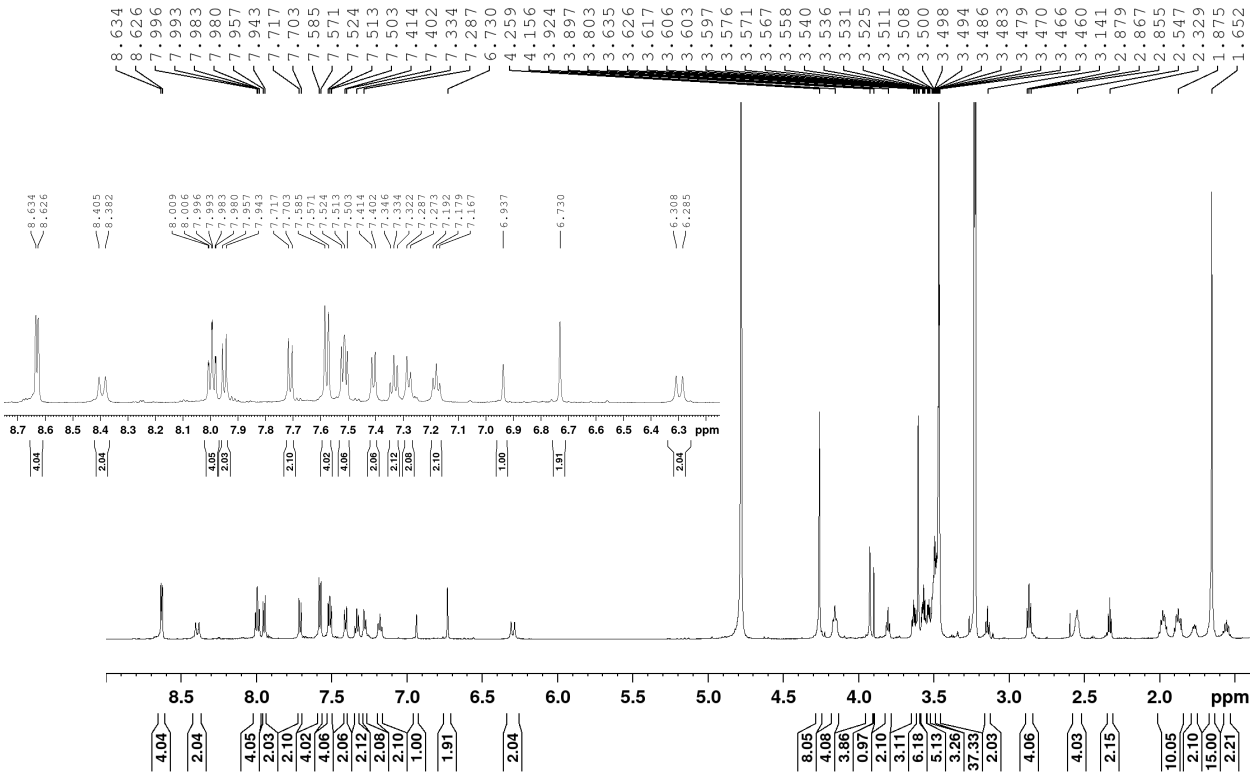

Figure AIII-11. ^{1}H NMR (600 MHz, CD_3OD) of **4-6**.

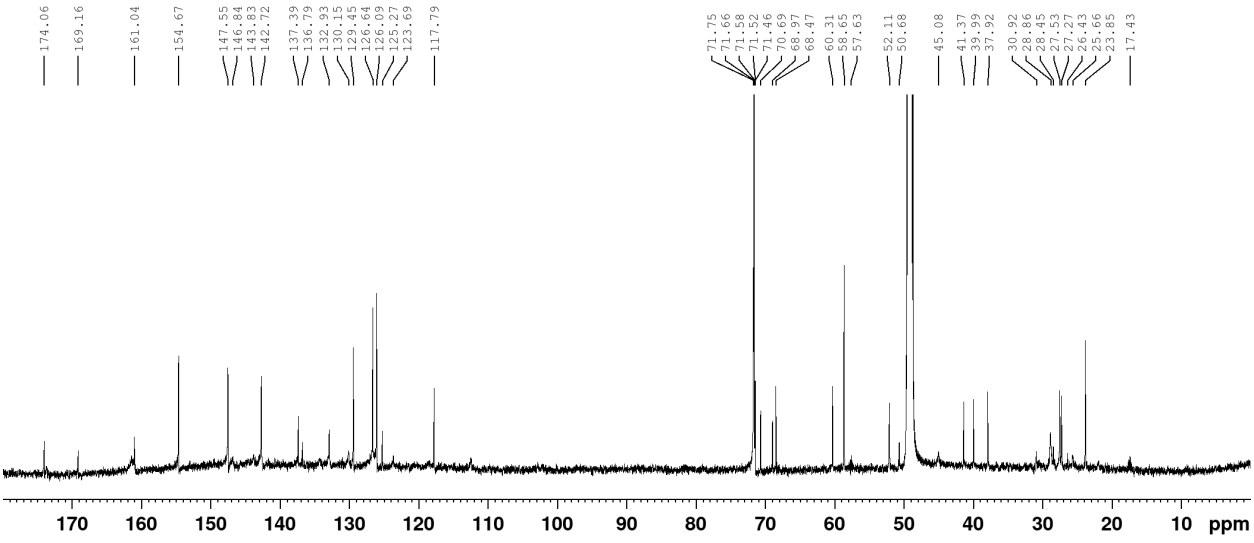

Figure AIII-12. ^{13}C NMR-UDEFT (150 MHz, CD_3OD) of **4-6**.

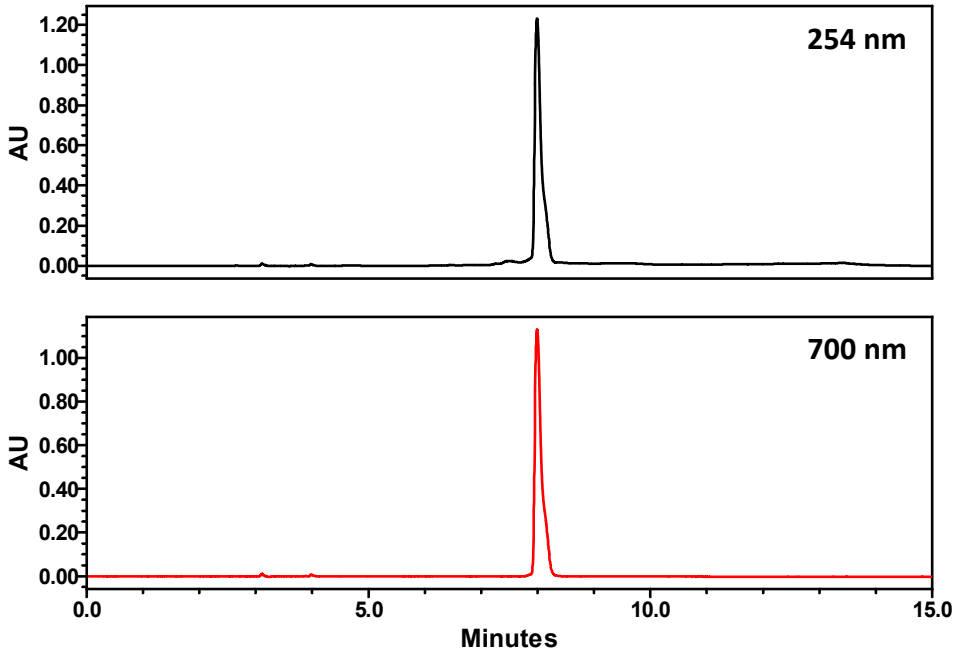

Figure AIII-13. UV-HPLC trace (254 & 700 nm) of **4-7**.

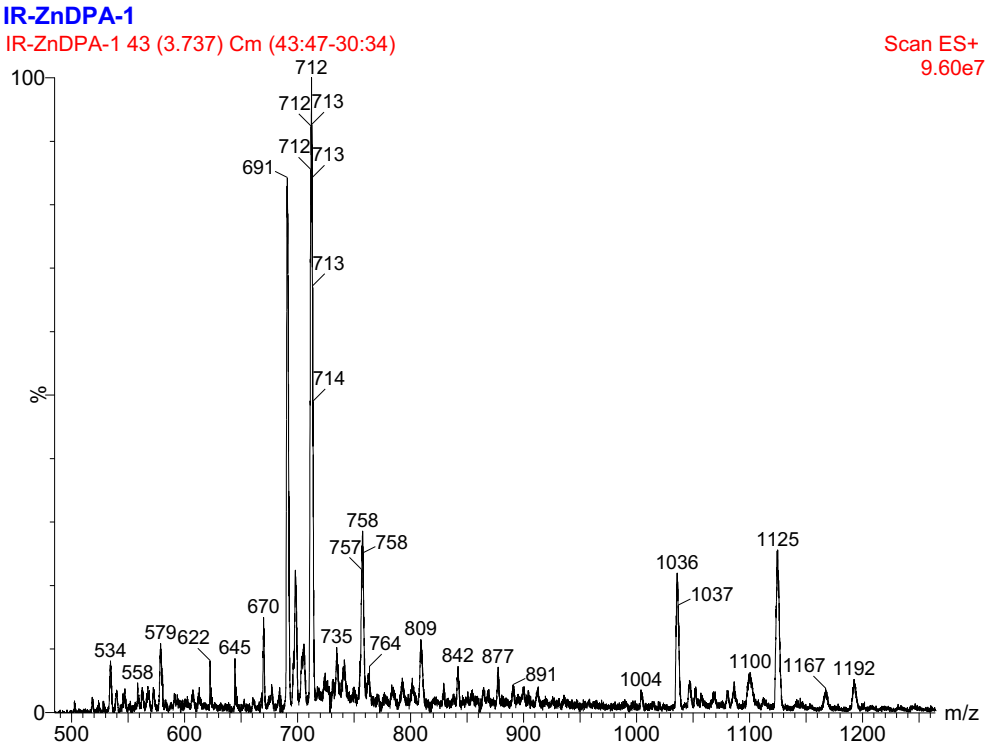

Figure AIII-14. Low-Resolution (LR) MS (ESI^+) of **4-7**.

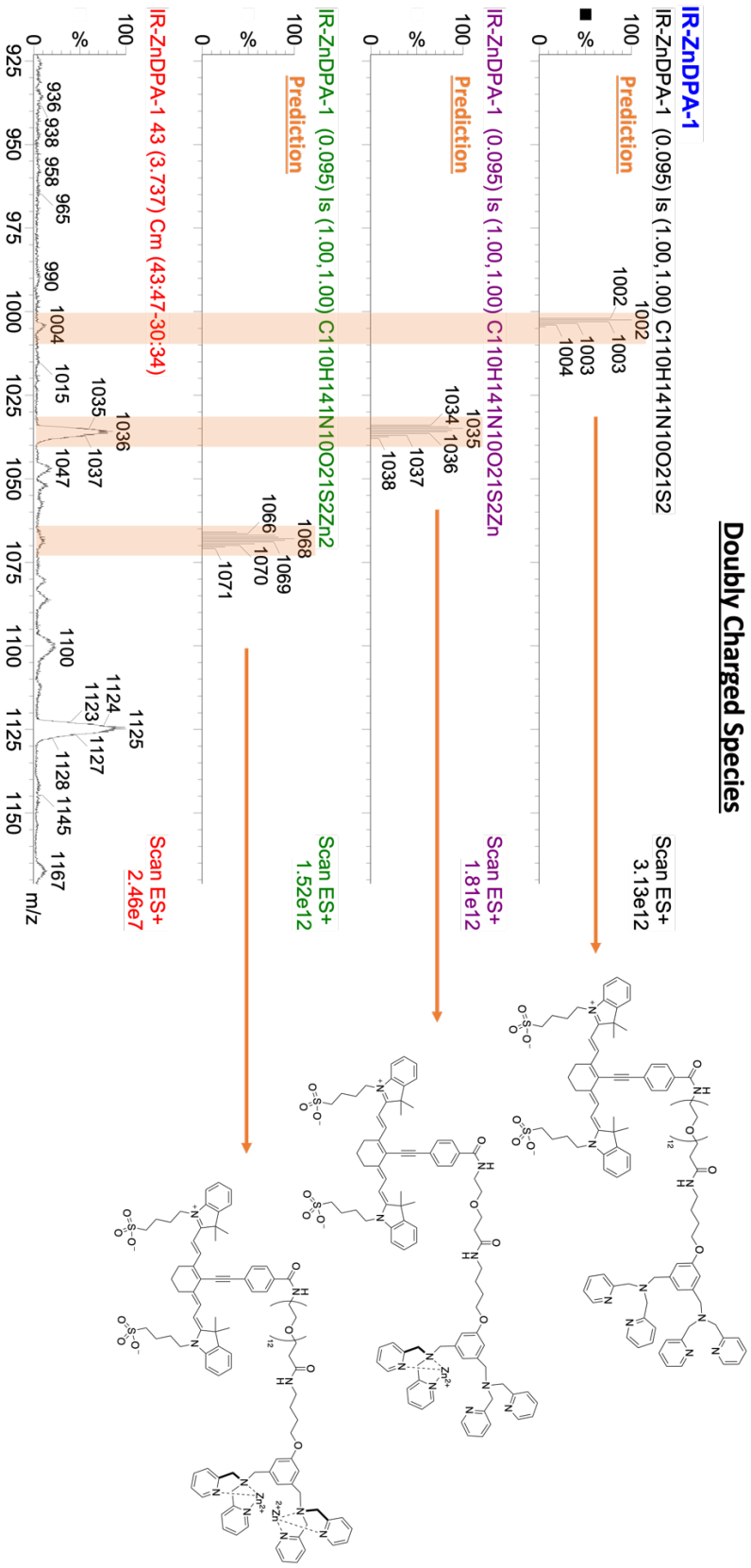

Figure AIII-15. LRMS (ESI^+) analysis of doubly charged species of **4-7**.

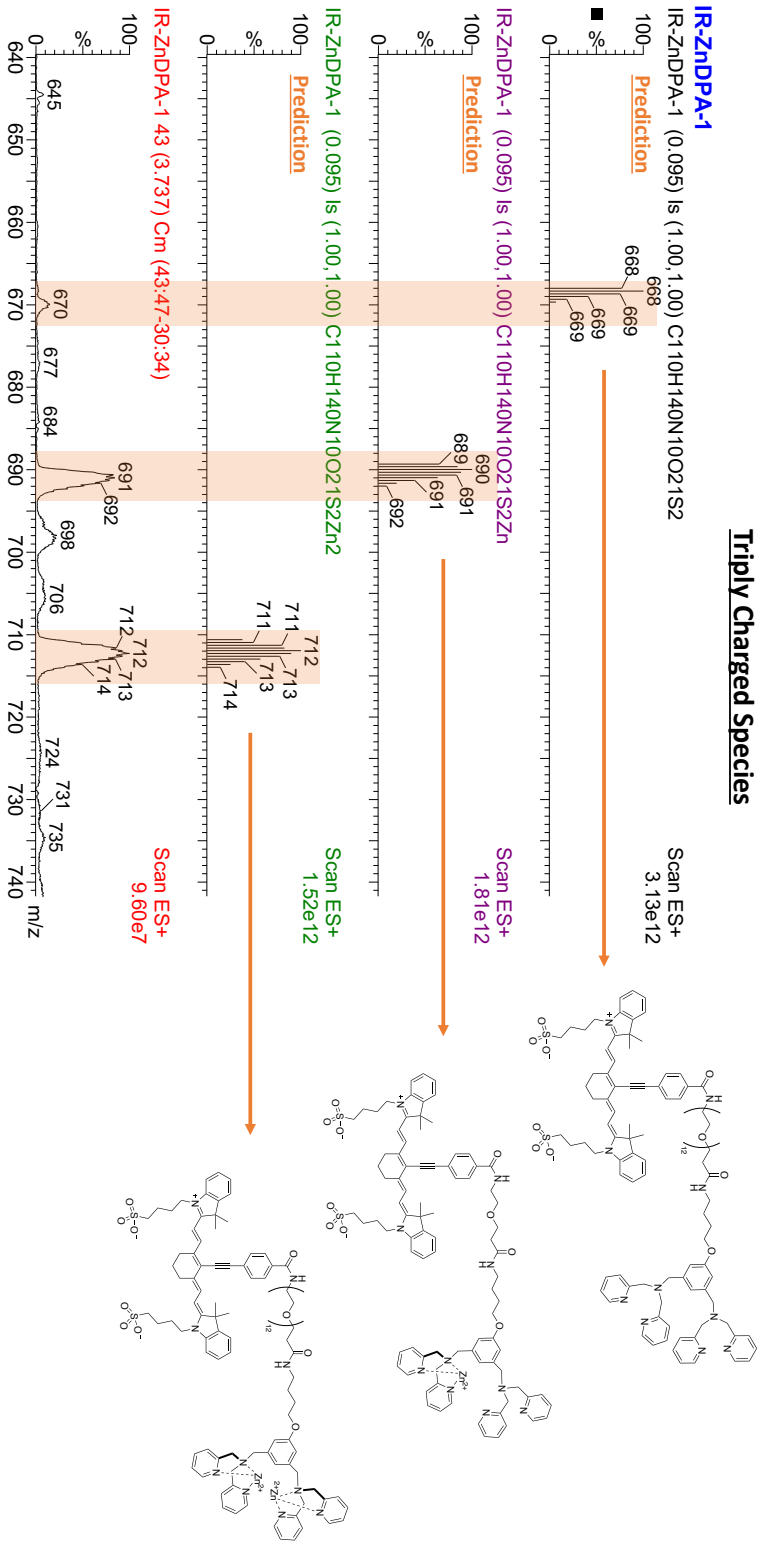

Figure AIII-16. LRMS (ESI^+) analysis of triply charged species of **4-7**.

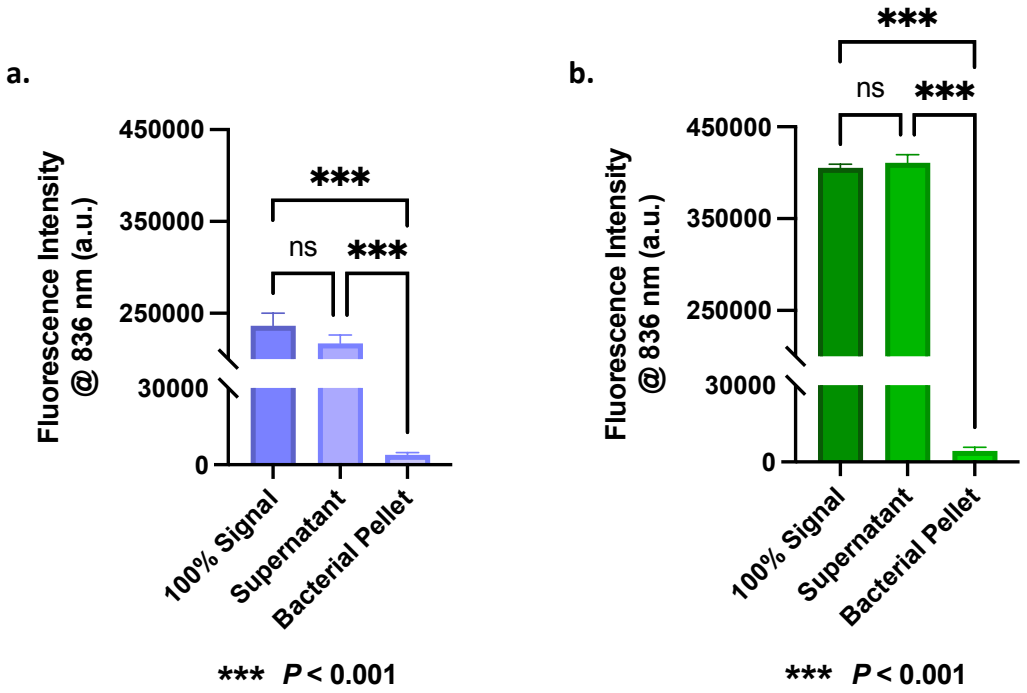

Figure AIII-17. *In vitro S. aureus* binding assay. Fluorescence intensity measurements of samples without bacteria cells (no-cell control), including the supernatant, the sample after 3 washes, and a 10 µM signal control of **4-4** (**a**), and **4-7** (**b**).

AIII-3: Supporting References

(1) James, N. S.; Chen, Y.; Joshi, P.; Ohulchanskyy, T. Y.; Ethirajan, M.; Henary, M.; Strekowsk, L.; Pandey, R. K. Evaluation of Polymethine Dyes as Potential Probes for Near Infrared Fluorescence Imaging of Tumors: Part - 1. *Theranostics* **2013**, *3* (9), 692–702. https://doi.org/10.7150/thno.5922.